Summer 8-2-2012

Computational Scheme Guided Design of a Hybrid Mild Gasifier

You Lu
ylv2@uno.edu

Computational Scheme Guided Design of a Hybrid Mild Gasifier

A Thesis

Submitted to the Graduate Faculty of the
University of New Orleans
in partial fulfillment of the
requirements for the degree of

Master of Science
in
Engineering
Mechanical

By

You Lu

B.S. Central South University, 2009

August, 2012

ACKNOWLEDGEMENT

It is my honor to take this opportunity to thank my advisor, Dr. Ting Wang, for his guidance and support while I worked under him as a graduate student. None of this would be made possible without Dr. Wang's hard work and dedication to his students and the University of New Orleans. I would also like to thank Drs. Kazim M. Akyuzlu, Martin J. Guillot, and Carsie A. Hall, III for being a part of my thesis committee.

I would also like to thank my fellow colleagues, students and researchers Monayem Mazumder, Dr. Jobaidur Rahman Khan, Reda Ragab, Xijia Lu, Hank Long, III, Scott Richard, and others from the Energy Conversion and Conservation Center (ECCC) for their help, support, and valuable suggestions.

Again, I would like to thank my parents for their support during the years in which I was pursuing my Master’s degree in Mechanical Engineering. In addition, I would like to thank my older sister Xiuhong Bao. She has always been there for me during both good and bad times.

TABLE OF CONTENTS

LIST OF FIGURES

LIST OF TABLES

NOMENCLATURE

a	local speed of sound (m/s)
c	concentration (mass/volume, moles/volume)
c_p	heat capacity at constant pressure (J/kg-K)
c_v	heat capacity at constant volume (J/kg-K)
D	mass diffusion coefficient (m^2/s)
D_H	hydraulic diameter (m)
D_{ij}	mass diffusion coefficient (m^2/s)
D_t	turbulent diffusivity (m^2/s)
E	total energy (J)
g	gravitational acceleration (m/s^2)
G	linear-anisotropic phase function coefficient
Gr	Grashof number ($L^3\rho^2 g\beta\Delta T/ \mu^2$)
H	total enthalpy (W/m^2-K)
h	specific enthalpy (W/kg-m^2-K)
J	mass flux; diffusion flux (kg/m^2-s)
k	turbulence kinetic energy (m^2/s^2)
k	thermal conductivity (W/m-K)
m	mass (kg)
M_W	molecular weight (kg/kgmol)
M	Mach number
p	pressure (atm)
Pr	Prandtl number (ν/α)
q	heat flux
q_r	radiation heat flux
R	universal gas constant (8314.34 J/Kmol-K)
S	source term for mass, energy, species concentration
Sc	Schmidt number (ν/D)
S_G	user-defined radiation source

t	time (s)
T	temperature (K)
U	mean velocity (m/s)
X	mole fraction (dimensionless)
Y	mass fraction (dimensionless)
x, y, z	coordinates

Greek letter

β	coefficient of thermal expansion (K^{-1})
ε	turbulence dissipation (m^2/s^3)
ε_w	wall emissivity
κ	von Karman constant
μ	dynamic viscosity (kg/m-s)
μ_k	turbulent viscosity (kg/m-s)
v	kinematic viscosity (m^2/s)
v'	stoichiometric coefficient of reactant
v''	stoichiometric coefficient of product
ρ	density (kg/m^3)
ρ_w	wall reflectivity
σ	Stefan-Boltzmann constant
σ_s	scattering coefficient
τ	stress tensor ($kg/m\text{-}s^2$)

Subscript

i	reactant i
j	product j
r	reaction r

ABSTRACT

A mild gasification method has been developed to provide an innovative clean coal technology. The objectives of this study are to (a) incorporate a fixed rate devolatilization model into the existing 2D multiphase reaction model, (b) expand the 2D model to 3D and (c) utilize the improved model to investigate the mild-gasification process and guide modification of the mild-gasifier design. The Eulerain-Eulerian method is employed to calculate both the primary phase (air) and secondary phase (coal particles). The improved 3D simulation model, incorporated with a devolatilization model, has been successfully developed and employed to determine the appropriate draft tube dimensions, entrained flow residence time, The simulations also help determine the appropriate operating fluidization velocity range to sustain the fluidized bed depth without depleting the chars or blowing the char away. The results are informative, but require future experimental data for verification.

Keywords: Clean coal technology, coal gasification, fluidized-bed, mild gasifier, CFD, multi-phase flow

CHAPTER ONE
INTRODUCTION

1.1 Background

1.1.1 Introduction of Coal

China was the first country to utilize coal, alongside Greece and ancient Rome. The Greek scholar, Theophrastus, documented the nature of coal in the book "STONE" around 300 BC. The 12th century is when Native Americans started to use coal in their pottery industry.

Coal's formation is a continuous process. Coal is formed from the remains of vegetation that grew as many as 400 million years ago. It is often referred to as "buried sunshine," since the plants which formed coal captured energy from the sun through photosynthesis to create the compounds that make up plant tissues and eventually become a part of the coal structure. The most important element in the plant material is carbon, which gives coal most of its energy. Most of the coal we are using right now was formed about 300 million years ago, when much of the earth was covered by steamy swamps. As plants and trees died, their remains sank to the bottom of the swampy areas, accumulating layer upon layer of biodegraded material and eventually forming a soggy, dense material called peat. Over long periods of time, the makeup of the earth's surface changed, and seas and greater rivers caused deposits of sand, clay, and other mineral matter to accumulate, burying the peat. Sandstone and other sedimentary rocks were formed, and the pressure caused by their weight squeezed water from the peat. Increasingly deeper burial and the heat associated with it gradually changed the material into coal.

1.1.2 Methods of Using Coal

The different uses of coal can be separated into four main categories: (a) combustion, (b) pyrolysis, (c) liquefaction, and (d) gasification. In combustion, coal is directly burned to produce heat. In pyrolysis, coal is decomposed through heating in the absence of oxygen. Coal will release volatiles matter while it absorbing the heat from outside, Volatile leaving only carbon (char) and tar. In

liquefaction, coal is converted into liquid fuel. In gasification, coal is converted into synthetic gas (syngas).

Gasification is a process that converts any carbon-based materials, such as coal, pet-coke, biomass, or various wastes, into a synthetic gas (syngas) through an oxygen-limited environment. The clean syngas can be used as a fuel to produce electricity or valuable products such as chemicals, fertilizers, and transportation fuels. Compared to a combustion process that takes place in abundant oxidant conditions, a gasification process takes place under sub-stoichiometric conditions. Roughly, the amount of O_2 used is only 35% or less of the amount required for complete combustion. The main differences between combustion and gasification are listed in Table 1.1.

Table 1.1 Comparisons between combustion and gasification

Combustion	**Gasification**
✓ Occurs in excess-oxidant conditions ✓ Releases heat (exothermic) ✓ Produces heat	✓ Occurs in oxidant-lean conditions ✓ Less production of air pollutants gas ✓ Absorbs heat (endothermic) ✓ Produces syngas

Gasification has a lower environmental impact compared to traditional combustion technologies because of the following reasons:

1. Gasification can recover the available energy from low energy density materials, such as municipal solid waste and pet-coke.
2. Syngas is cleaned before combustion, thus reducing air pollutants such as NO_x and SO_x.
3. By-products of gasification (sulfur and slag) are nonhazardous and marketable.
4. Higher efficiency.
5. Low CO_2 production per kW of output due to higher efficiency.
6. Carbon dioxide (CO_2) can be captured prior to syngas combustion. It gives the least costly and most efficient way of capturing CO_2 from a fossil-fuel based power plant.

1.1.3 IGCC System Description

A very efficient way to use the syngas as fuel in electricity generation is by employing the Integrated Gasification Combined Cycle (IGCC). A schematic of a typical IGCC system is presented in Fig. 1.1. IGCC combines the gasification system with the gas clean-up system and the combined power system. The syngas produced by the gasifier is cleaned and used as a fuel for the gas turbines. The high-pressure and -temperature gases produced in the combustor then expand through the gas turbines to drive the air compressor and an electric generator. The hot exhaust gases from the gas turbines are sent to an HRSG (Heat Recovery Steam Generator), producing steam that expands through a steam turbine to drive another electric generator.

Integrated Gasification Combined Cycle (IGCC) also provides a more efficient method of capturing carbon dioxide (CO_2) than in the conventional pulverized coal burning power plants. IGCC demonstration plants have been operating since the early 1970's and some of the plants constructed in the 1990's are now entering successful commercial services.

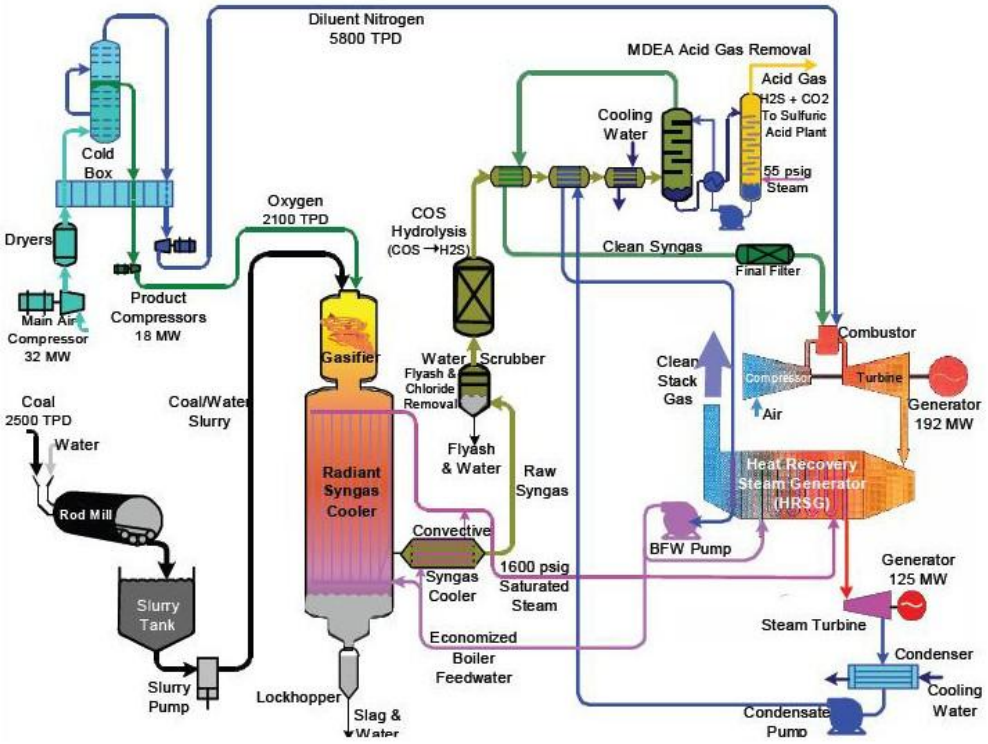

Figure 1.1 Schematic of Tampa Electric IGCC System (Source: DOE).

1.2 Literature Review

1.2.1 Clean Coal Technology

Clean coal technology was dedicated to developing new and innovative technologies to reduce the negative impacts from utilizing coal for energy generation. If the coal is used as a fuel through combustion, SO_x, NO_x, CO_2, and other trace elements (e.g., Hg and Ar), are generated by thermal decomposition and released into air simultaneously. These emissions have been discovered to have a detrimental impact on the environment: e.g. acid rain and climate changes. Various clean coal technologies have been developed to reduce power plants' emissions and increase their thermal efficiency. Among them, coal gasification technology possesses the greatest potential for achieving these goals. A detailed description of the coal gasification process and technology follows.

1.2.2 Detailed Description of the Coal Gasification Process

Figure 1.2 presents the typical processes undergone by coal particles in gasification. The gasification of coal particles involves two major steps: (a) thermal decomposition (demoisturization, pyrolysis, and devolatilization) and (b) combustion of solid residue from the first step. Coal particles undergo demoisturization and pyrolysis while facing the hot combustion environment.

The volatiles are then released as the particle temperature continues to increase. The process by which this occurs is called devolatilization. The volatiles are then thermally cracked into lighter gases, such as H_2, CO, C_2H_2, CH_4, etc. These lighter gases can further react with O_2, releasing some of the heat needed for the pyrolysis.

With only char and ash left, the particles undergo combustion to produce CO and CO_2, leaving only ash. The thermal decomposition occurs relatively slowly, while the combustion of carbon is faster so the combustion heat can continuously support the devolatilization and gasification processes. More specific explanations for each process are given bellow.

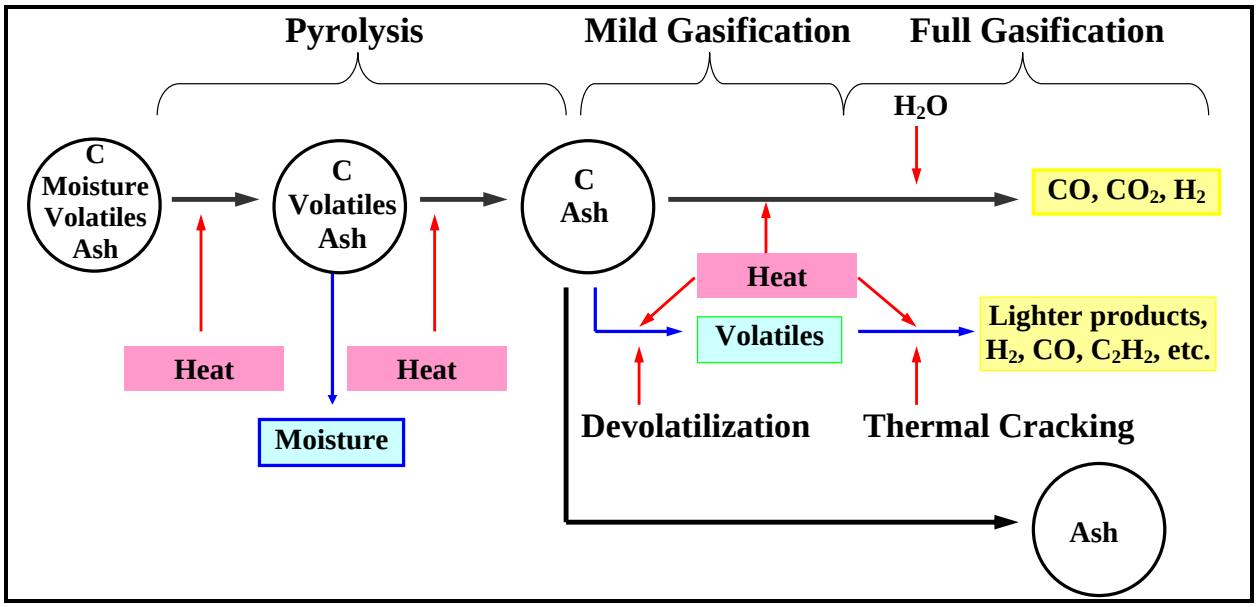

Figure 1.2 Simplified global gasification processes of coal particles (sulfur and other minerals are not included in this figure). Heat can be provided externally or internally through combustion of char, volatiles, and CO.

1.2.2.1 Pyrolysis

The word pyrolysis is generated from the Greek word "pyro," meaning "fire," and "lysys," meaning "to separate." It is the chemical decomposition of condensed substances by heating that occurs spontaneously at high temperatures. Pyrolysis differs from other high temperature processes such as combustion and hydrolysis in that it does not involve reactions with oxygen, water, or any other reagents. It's a special case of thermolysis which is most commonly used for organic materials. In general, pyrolysis of organic substances produces gas and liquid products and leaves a solid residue that is rich in carbon content. The word carbonization is known as extreme pyrolysis, which leaves mostly carbon as the residue. In the chemical industry, this chemical process is heavily used, for example, to produce charcoal, to produce coke from coal, to convert biomass into syngas, to produce methanol from wood, to turn waste into safely disposable substances, and for transforming medium-weight hydrocarbons from oil into lighter ones like gasoline. The specialized uses of pyrolysis are known by different names, such as dry distillation, destructive distillation, or thermal cracking. It also plays an important role in several cooking procedures, such as baking, frying, grilling, and caramelizing. Figure 1.3 presents a general idea of carbonaceous fuel undergoing pyrolysis.

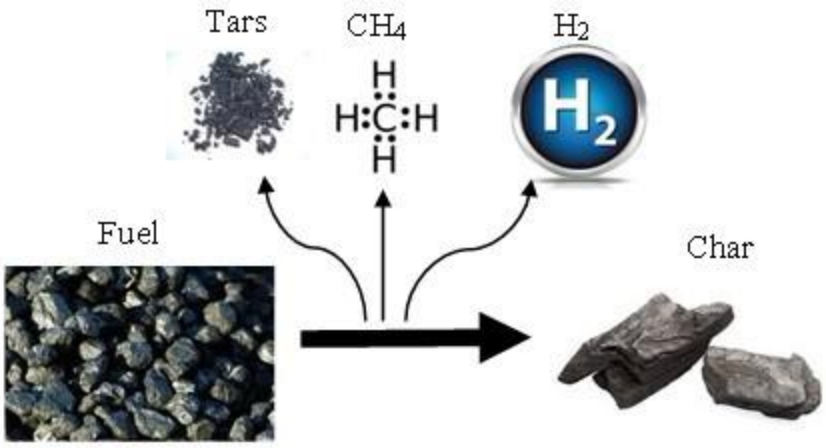

Figure 1.3 Schematic drawing of Pyrolysis of Carbonaceous Fuels

1.2.2.2 Devolatilization

Devolatilization process takes place while hydrocarbon materials are absorbing heat. Temperature, residence time, particle size, and coal type all can influence devolatilization rates. The heating causes chemical bonds to rupture and both the organic and mineral parts of coal to thermally decompose. Such a process starts at a temperature around 100 °C (212 °F) with desorption of gases, for example, water/steam, CO_2, CH_4, and N_2, which are stored in the coal pores. When the temperature goes beyond 300 °C (572 °F), the released liquid hydrocarbon consists primarily of tar. Gaseous hydrocarbons such as CO, CO_2, and water/steam are also released. From here, coal particles are in a plastic state, where they undergo drastic changes in size and shape, while the temperature rises above 500 °C (932 °F). The coal particles then become hard again, and together are called char, when the temperature reaches around 550 °C (1022 °F). As heating continues, H_2 and CO are released.

Coal particles undergo swelling when they are heated. Small particles don't share the same behaviors as larger particles. Smaller ones expand at lower temperatures than the larger ones. Aside from expanding, the particles' shape keeps varying during swelling. Generally, the sharp edges of the particles become rounded off. The structure of the coal particles at the end of devolatilization is influenced by the amount of volatiles contained in the coal. Intensive volatiles released in high volatile

coal results in larger particle porosity, while low volatile particles have smaller porosity and burn on the surface.

The pyrolysis conditions affect the physical properties of coal chars. Gale et al. (1995) conducted an experiment with maximum particle temperatures between 570 °C (1058 °F) and 1355 °C (2471 °F) and heating rates between 10^4 and 2 x 10^5 K/s, to prove that micro-pore (CO_2) surface area generally increases with increasing residence time and mass releases for lignite and bituminous coals. It also indicated that the micro-pore surface area of char increases with increasing maximum particle temperature and heating rate.

Temperature distribution in the particle depends on volatile matters generated during heating. The volatiles generated near the center of the particle travel to the particle surface and escape. The flow of these volatiles from the particle center to the particle surface can reduce the convective heat transfer from the surroundings to the particles surface. It has been found that the heat transfer coefficient decreases by 10 times during fast heating of coal particles mixed with a hot solid heat carrier. This reduced heat transfer rate to the particle surface results in a temperature plateau of the particle surface on the level of about 400 °C (752 °F) and lasts during the whole time of volatile release. Davies and Brown (1969) gave another explanation for this temperature plateau is that this is caused by a strong effect of devolatilization.

In general, the larger the particle size, the smaller amount the volatile yields. This is due to the fact that, in larger particles, more volatiles may crack, condense, or polymerize with some carbon deposition occurring during their migration from the inside to the particle surface. High pressure has an identical effect on the devolatilization rates. Anthony et al. (1975) reported that devolatilization rates are higher at lower pressures. An increase in pressure increases the transit time of volatiles to diffuse to particle surface.

Seebauer et al. (1997) employed thermogravimetric analysis to investigate the effects of pressure, particle size, and heating rate on coal pyrolysis. The pressure used in the study ranged from 1 to 40 atm and heating rate from 0.03 to 0.1 K/s. Seebauer et al. found that the total volatile yield decreased with increasing pressure. Sun et al. (1997) studied the pyrolysis of two Chinese coals under

pressure ranging from 1 to 13 atm with a heating rate as low as 0.33 K/s. It was reported that, at high pressure, the total volatile yield decreases with increasing pressure. The total weight loss is almost independent of pressure at low temperatures (less than 837 K).

Fatemi et al. (1987) studied the pressure effects on devolatilization of pulverized coal with operation temperatures of up to 1373 K and a pressure of 68 atm in an entrained bed reactor. They found that the tar yield decreases significantly with increasing pressure up to 13.8 atm. Weight loss and gas yield both decrease with increasing pressure up to 13.8 atm, but there is no significant effect above this pressure.

Wall et al. (2002) reviewed the pressure effect on variety aspects of coal reactions reported in open literature. In general, the total volatile and tar yields decrease with increasing pressure. This effect is more pronounced at higher temperatures than high pressures. Increasing pressure improves the fluidity of the coal melting and reduces char reactivity.

1.2.2.3 Carbon Particle Combustion/Gasification

The steps involved in a reaction between a gas and a solid particle are as follows:

1. Transport of reactants to solid surface by convection and/or diffusion.
2. Adsorption of reactant molecules on the particle surface.
3. Reaction steps involving various combinations of adsorbed molecules, the surface, and the gas-phase molecules.
4. Desorption of product molecules from the surface.
5. Transport of product molecules away from the solid surface by convection and/or diffusion.

Chemical reactions occur between gases and solids due to the porous structure of the char particles' outer and inner surfaces. Reacting gases diffuse from the free space to the particle outer surface and then diffuse into the particle through the porous structure. As the reaction proceeds, the size of the available pores increases, which increases the inner particle surface area. The particle active

surface area reaches a maximum at burnout of about 40%. The total active surface area is then decreased as a result of the interconnection of enlarging neighboring pores.

1.2.3 Particle Combustion Model

(a) Random Pore Model

The random pore model (Bhatia and Perlmutter, 1980) accounts for the evolution of the particle reactive surface during the combustion. The rate of mass change of the particle is defined as follow,

$$\frac{dm_p}{dt} = R_k m_{po}\left(S + A_o\right) \tag{1.1}$$

Where m_p is the particle mass, m_{po} is the initial particle mass, R_k is the kinetic rate, and A_0 is the initial particle surface area. S is the instantaneous internal reactive surface area, which is defined as follow,

$$\frac{S}{S_o} = 1 - x\sqrt{1 - \psi \ln\left(1 - x\right)} \tag{1.2}$$

Where S_o is the initial reactive area, x is the conversion factor, and ψ is the structure parameter for the particular char/coal type.

(b) Kinetics/Diffusion Fixed-Core Model

The kinetics/diffusion fixed-core model considers the diffusion and kinetic rates of the combustion. The size of the particle during the combustion is assumed to be constant. The particle consumption rate is defined as follow,

$$\frac{dm_p}{dt} = \frac{P_g}{\frac{1}{k_d} + \frac{1}{k_s}} A_0 \tag{1.3}$$

Where m_p is the particle mass, P_g is the partial pressure of the gas phase species, A_0 is the original particle surface area, k_d is the diffusion rate constant, and k_s is the kinetic rate constant.

(c) Shrinking Core Model

The shrinking core model accounts for the reduction in the particle radius as the combustion occurs. The effect of diffusion through the ash layer surrounding the particle is also taken into account. The particle consumption rate is defined as follow,

$$\frac{dm_p}{dt} = \frac{P_g A_0}{\frac{1}{k_d} + \frac{1}{k_s}\left(r_p / R_p\right)^2 + \frac{1}{k_{dash}}\left(\frac{R_p}{r_p} - 1\right)} \quad (1.4)$$

Where m_p is the particle mass, P_g is the partial pressure of the gas phase species, A_0 is the initial particle surface area, k_d is the diffusion rate constant, k_s is the kinetics rate constant, $k_{d,ash}$ is the ash diffusion constant, r_p is the instantaneous radius of the particle, and R_p is initial radius of the particle.

1.2.4 Gasification Reactions Summary

Coal gasification occurs when the coal is absorbing energy from a limited amount of oxygen and steam in a gasification reaction chamber. The gasification process is very complicated: however, a simplified list of main global reactions involved in the gasification process can be modeled as follows:

Heterogeneous reactions:

$C(s) + ½\ O_2 \rightarrow CO$	$\Delta H°_R$ = -110.5 MJ/kmol	(R1.1)
$C(s) + CO_2 \rightarrow 2CO$	$\Delta H°_R$ = +172.0 MJ/kmol (Gasification, Boudouard reaction)	(R1.2)
$C(s) + H_2O\ (g) \rightarrow CO + H_2$	$\Delta H°_R$ = +131.4 MJ/kmol (Gasification)	(R1.3)

Homogeneous reactions:

$CO + ½\ O_2 \rightarrow CO_2$	$\Delta H°_R$ = -283.1 MJ/kmol	(R1.4)
$CO + H_2O\ (g) \rightarrow CO_2 + H_2$	$\Delta H°_R$ = -41.0 MJ/kmol (Water-shift)	(R1.5)

The gasification of char by the CO_2 and H_2O, reactions (R1.2) and (R.1.3), respectively, are endothermic reactions. The exothermic, two-step char combustion reactions, (R1.1) and (R1.4), are needed to supply the energy needed in the gasification reactions. The synthetic gas produced mainly consists of CO and H_2 with minor CH_4.

1.2.5 Introduction of Different Gasifiers

There are four main gasifier types: (a) fluidized bed gasifier, (b) entrained flow gasifier, (c) transport gasifier, and (d) moving bed gasifier. Explanations of each type and its examples are presented below. The comparisons of these gasifiers are summarized in Table 1.2.

1.2.5.1 Fluidized Bed Gasifier (FBG)

A fluidized bed gasifier (FBG) employs a similar principle of a conventional combustion fluidized bed, but with only partial oxidant to convert carbonaceous feedstock to produce steam, process heat, chemicals, electric power etc. The functional requirements of the fluidized bed gasifier are to convert efficiently and reliably the carbonaceous fuel into raw reducing gas, ash, char, and possibly raw liquid products by combining carbonaceous fuel with oxidant, steam, and/or an external heat source. For solids transport, aeration and the inert gases, such as nitrogen and recycled product gas also fed to the gasifier.

In a fluidized bed gasifier, air or oxygen is injected upward at the bottom of solid fuel bed, suspending the fuel particles. A schematic of a fluidized bed gasifier is presented in Fig. 1.4. The size (5-10mm) and weight of the particles prevent them from blowing out. The fuel feed rate and the gasifier temperature are lower compared to those of entrained bed gasifiers. The operating temperature of a fluidized bed gasifier is around 1000 °C (1830 °F), which is roughly only half of the operating temperature of a coal burner. This lower temperature has several advantages:

- ✓ Lower NO_x emission. The temperature is not hot enough to break apart the nitrogen molecules and cause the nitrogen atoms to join with oxygen atoms to form NO_x.
- ✓ No slag formation. The temperature is not hot enough to melt ash. It is suitable for coals of any rank (high or low ash content.)
- ✓ Lower syngas temperature, which means a cheaper syngas cooling system prior to gas clean up.

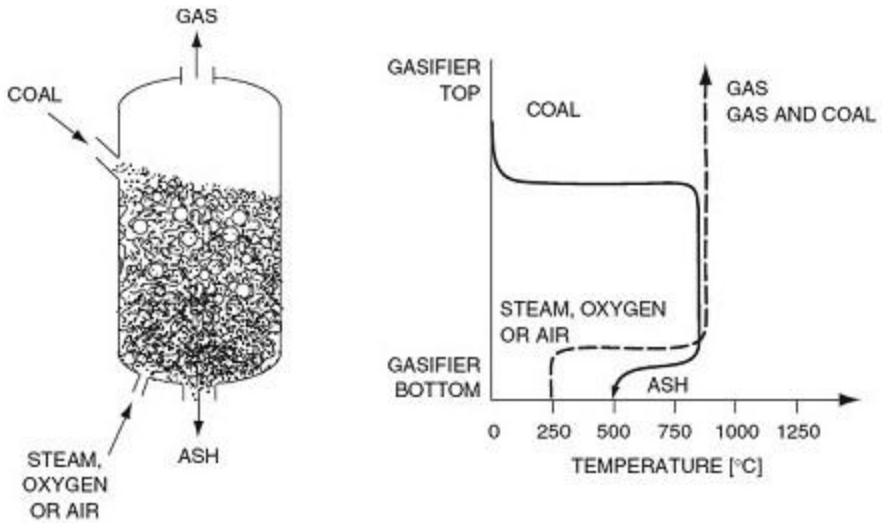

Figure 1.4 Schematic of fluidized bed gasifier (Source: Enggcyclopedia)

Fluidized bed gasifiers require a moderate supply of oxygen and steam. Examples of commercial fluidized bed gasifiers are:

(i) High Temperature Wrinkler (HTW)

The High Temperature Wrinkler (HTW) gasifier was developed by Rheinbraun in Germany to gasify lignite for the production of a reducing gas for refining iron ore. A schematic of an HTW gasifier is presented in Fig. 1.5. The gasifier is a refractory-lined vessel equipped with a water jacket. Coal is dropped into the fluidized bed which consists of particles, semi-coke, and coal. The gasifier is fluidized by the injection of air or oxygen/steam from the bottom. The temperature of the bed is kept at around 800 °C (1470 °F), which is below the ash fusion temperature. An additional gasification gas is added at the freeboard to decompose undesirable byproducts formed during gasification. The operating pressure can vary from 1 to 3 MPa. The raw syngas exiting the top of gasifier is then passed through a cyclone to remove particulates and then cooled. Particulates recovered in the cyclone are recycled back into the gasifier.

The HTW technology was successfully applied to produce methanol from lignite at Berrenrath, Germany, between 1986 and 1997. The plant was shut down at the end of 1997 because the process was

no longer considered economically viable. In 1989, a 140 ton/day plant was commissioned in Wesseling, Germany, to supplement research and development of the HTW technology, including the study to future applications for power generation through an Integrated Gasification Combined Cycle system (IGCC). There is presently a project to build a 400 MW IGCC plant in the Czech Republic using the HTW technology developed at the Wesseling plant.

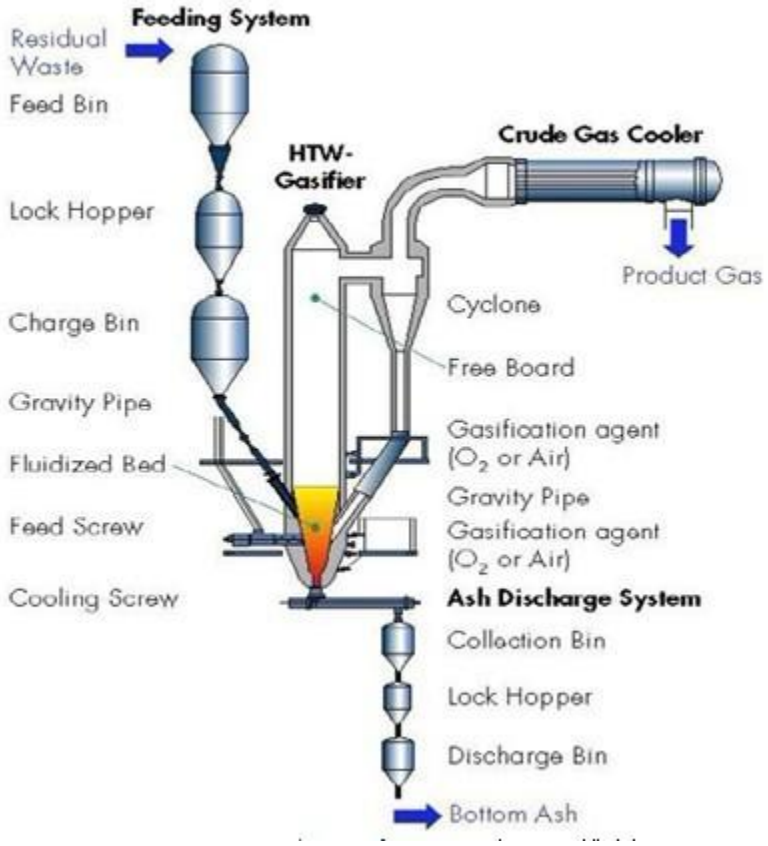

Figure 1.5 Schematic of the High Temperature Wrinkler (HTW) Gasifier (Source: DOE)

(ii) Kellogg-Rust-Westinghouse (KRW)

A schematic of a Kellogg-Rust-Westinghouse (KRW) gasifier is shown in Fig. 1.6. The fuel and oxidant enter the bottom of the gasifier through concentric high-velocity jets, ensuring thorough mixing of the fuel and oxidant and of the bed of char and limestone that collects in the gasifier. Upon entering the gasifier, the coal releases its volatiles, which then immediately burn, releasing heat needed for the gasification. The combusted volatiles form large bubbles that rise up to the center of the gasifier. This

causes the char and the sorbent in the bed to move down the sides of the gasifier and back into the central jet. The char in the bed reacts with the steam, which is injected together with the oxidant and also through multiple other injections on the bottom of the gasifier, to form syngas. The ash particles formed are denser than the coal, thus they settle down to the bottom of the gasifier and are then removed. Any particles that escaped the gasifier through the exit at the top is recaptured in the cyclone gas clean-up system and is then injected back into the gasifier.

In 1997 through 2000, a 965MW Integrated Gasification Combined Cycle (IGCC) demonstration plant using the KRW technology was carried out in Pinon Pine, Nevada, by Sierra Pacific Resources and was sponsored by the U.S. Department of Energy (DOE) as part of its Clean Coal Technology Program. It was the only large-scale coal-based IGCC plant using the KRW technology. Unfortunately, the plant faced numerous problems. It had 18 gasifier start-ups and all of them failed due to equipment design.

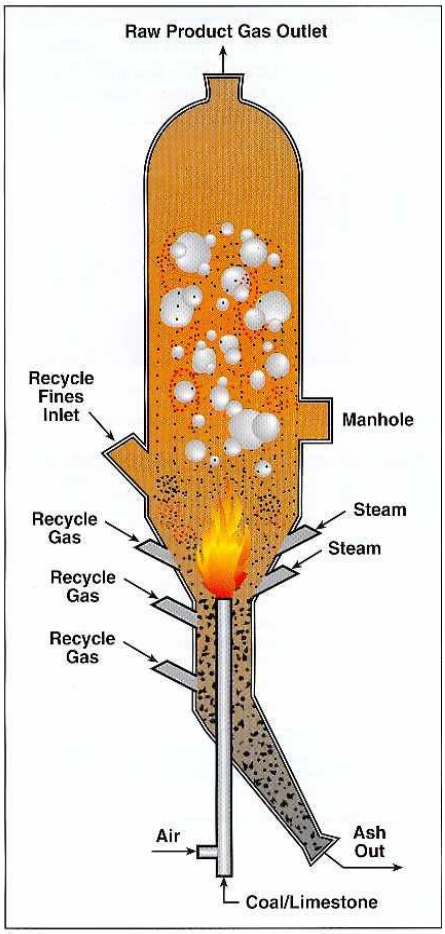

Figure 1.6 Schematic of a Kellogg-Rust-Westinghouse (KRW) gasifier. (Source: DOE)

1.2.5.2 FBG Design Considerations

The design of fluidized bed gasifiers requires developing the transport models of conservation of mass, momentum, and energy. The mass and energy balances are closely coupled and their solutions provide estimates of gas and solids composition, temperature profiles, and input and output stream conditions by applying empirical reaction kinetic and multiple phase mixing models. The momentum balances provide the gasifier pressure profile and total pressure drop by applying appropriate fluidized bed phase density models. The design of fluidized bed gasifiers is related to the selection of several interrelating design, operating, and performance parameters and requires the consideration of performance and cost trade-offs for any specific application. The fluidized bed gasifier is designed to promote a reaction environment having good gas-particle contacting, good particle-particle mixing, and relatively uniform temperature conditions and to avoid operational difficulties resulting from the agglomeration, deposition, erosion, and corrosion of carbonaceous fuels.

1.2.5.3 Fluidization Velocity

A chemical engineering as well as mechanical engineering operation commonly involves the use of fluidized beds. These are devices where a large surface area for contact between a liquid and a gas (absorption, distillation) or a solid and a gas or liquid (adsorption, catalysis) is obtained for achieving rapid mass and heat transfer, and particularly in the case of fluidized beds, catalytic chemical reactions. The theory and empirical correlations associated with thermal-flow fundamentals in a packed bed are reviewed first, followed by the same in a fluidized bed.

1.2.5.3.1 Minimum Fluidization Velocity of Packed Beds

A typical packed bed is a cylindrical column that is filled with a suitable packing material. The liquid is distributed as uniformly as possible at the top of the column and flows downward, wetting the packing material. A gas is admitted at the bottom, and flows upward, contacting the liquid in a countercurrent model. An example of a packed bed is an absorber. Here, the gas contains some carrier species that is insoluble in the liquid (such as air) and a soluble species such as carbon dioxide or

ammonia. The soluble species is absorbed in the liquid, and the lean gas leaves the column at the top. The liquid, rich in the soluble species, is taken out at the bottom.

From a fluid dynamics point of view, the most important issue is that of the pressure drop required for the liquid or the gas to flow through the column at a specified flow rate. To calculate this quantity we count on a friction factor correlation dedicated by Ergun. Other fluid dynamics issues involve the proper distribution of the liquid across the cross-section, and developing models of the velocity profile in the liquid film around a piece of packing material so that heat and mass transfer calculations can be made. Design of packing materials to achieve uniform distribution of the fluid across the cross-section throughout the column is an important subject as well. Here, only the pressure drop issue is reviewed.

The **Ergun equation** that is commonly used is given below,

$$f_p = \frac{150}{Re_p} + 1.75 \qquad (1.5)$$

Here, the friction factor f_p for the packed bed, and the particle Reynolds number Re_p, are defined as follows.

$$f_p = \left(\frac{\Delta p}{L}\right)\left(\frac{D_p}{\rho V_s^2}\right)\left(\frac{\varepsilon^3}{1-\varepsilon}\right) \qquad (1.5a)$$

$$\text{And } Re_p = \frac{D_p\ \rho\ V_s}{(1-\varepsilon)\,\mu} \qquad (1.5b)$$

Using the above friction factor f_p and the particle Reynolds number Re_p relations, the **Ergun equation** becomes,

$$\left(\frac{\Delta p}{L}\right)\left(\frac{D_p}{\rho_f\ V_s^2}\right)\left(\frac{\varepsilon^3}{1-\varepsilon}\right) = \frac{150(1-\varepsilon)\mu}{D_p\ \rho_f\ V_s} + 1.75 \qquad (1.6)$$

The various symbols appearing in the above equations are defined as follows.

Δp = Pressure Drop

L = Length of the Bed

ρ_p = Density of the particle

ρ_f = Density of the fluid

μ = Dynamic viscosity of the fluid

D_p = Equivalent spherical diameter of the particle defined by, $D_p = 6\dfrac{volume of\ the\ particle}{surface area of\ the\ particle} = \dfrac{6V_p}{A_p}$

ε = Void fraction of the bed (ε is the ratio of the void volume to the total volume of the bed)

$$\varepsilon \equiv \frac{volume voids}{volume of\ entire bed}$$

$$\varepsilon \equiv \frac{volume of\ entire bed - volume of\ particles}{volume of\ entire bed}$$

$$\varepsilon \equiv \frac{\pi R^2 L - \dfrac{weight of\ all\ particles}{particles density}}{\pi R^2 L}$$

Where, R = inside radius of the column

V_s= Superficial velocity ($V_s = \dfrac{Q}{A}$, where Q is the volumetric flow rate of the fluid and A is the cross-sectional area of the bed, the theoretical velocity of the fluid assuming no particles)

1.2.5.3.2 Minimum Fluidization Velocity of Fluidized Beds

A fluidized bed is a bed through which fluid flows at such a high velocity that the bed is loosened and the particle-fluid mixture behaves as though it is a fluid. Thus, when a bed of particles is fluidized, the entire bed can be transported like a fluid. Both gas and liquid flows can be used to fluidize a bed of particles. The most common reason for fluidizing a bed is to obtain vigorous agitation of the solids in contact with the fluid, leading to excellent contact between the solid and the fluid and between the solid and the wall. This means that nearly uniform temperatures can be maintained even in highly exothermic reaction situations where the particles are used to catalyze a reaction in the species contained in the fluid. As a matter of fact, fluidized beds were used in catalytic cracking in the petroleum industry

in the past. The catalyst is suspended in the fluid by fluidizing a bed of catalytic particles so that intimate contact can be achieved between the particles and the fluid. Nowadays, fluidized beds are used in catalyst regeneration, solid-gas reactors, combustion of coal, roasting of ores, drying, and gas adsorption operations.

First, consider the behavior of a bed of particles when the upward superficial fluid velocity is gradually increased from zero past the point of fluidization, and back down to zero then calculate the minimum fluidization velocity. The superficial velocity is the velocity of the fluid in the bed if no particles are present.

At first, when there is no flow, the pressure drop is zero, and the bed has a certain height, as shown in Fig. 1.7. The superficial velocity increases along the right arrow, tracing the path ABCD. At first, the pressure drop gradually increases while the bed height remains fixed. When the point B is reached, the bed starts expanding in height while the pressure drop levels off and no longer increases as the superficial velocity is increased. This is happing when the upward force (or upward drag force, F_d) exerted by the fluid on the particles is sufficient to balance the net weight of the bed (or gravitational force, F_g) and the particles begin to separate from each other and float in the fluid. As the velocity is increased further, the bed continues to expand in height, but the pressure drop remains constant. It is possible to reach large superficial velocities without having the particles carried out with the fluid at the exit. This would occur if the superficial velocity is equal to the terminal settling velocity of the particles. The terminal settling velocity is explained later in this section.

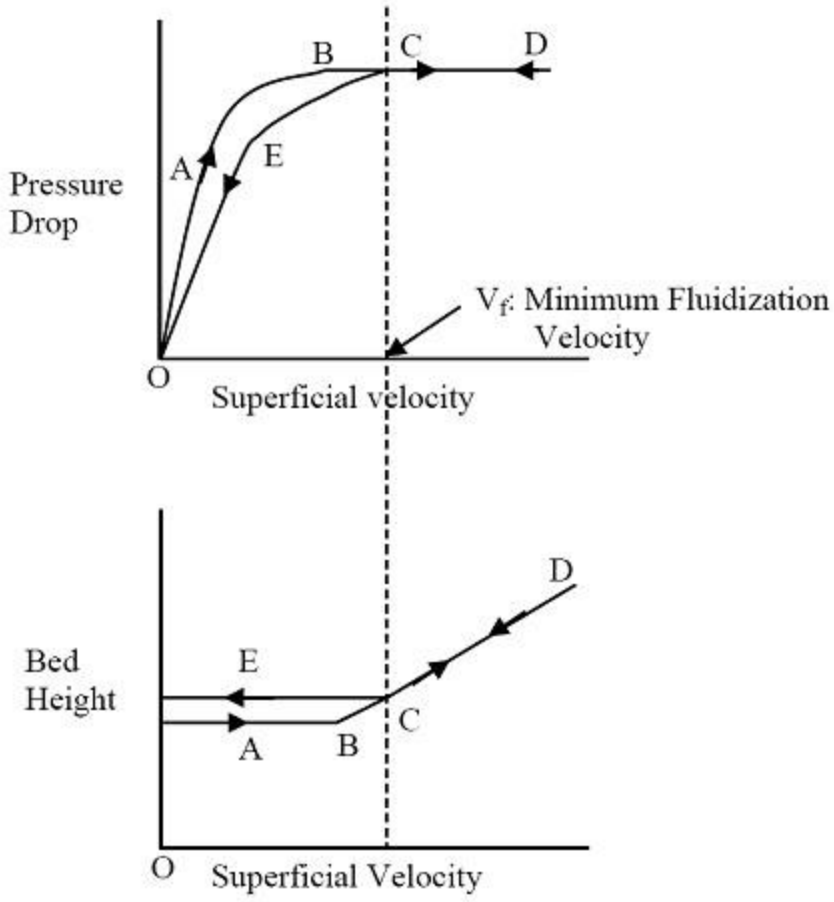

Figure 1.7 Schematic drawing of Minimum Fluidization Velocity

Now, if the path is traced backward by gradually decreasing the superficial velocity in the direction of the reverse arrows in the figure, it is found that the behavior of the bed follows the curves DCE. At first, the pressure drop stays fixed while the bed settles back down, and then begins to decrease when the point C is reached. The bed height no longer decreases while the pressure drop follows the curve CEO. A bed of particles, left alone for a sufficient length of time, becomes consolidated, but it is loosened when it is fluidized. After fluidization, it settles back into a more loosely packed state; this is why the constant bed height on the return loop is larger than the bed height in the initial state. If the experiment is now repeated by increasing the superficial velocity from zero, the path will follow the set of curves ECD in both directions. Because of this reason, the velocity at the point C in the Fig. 1.7 is defined as the **minimum fluidization velocity,** V_{mf}.

1.2.5.3.3 Calculation of V_{mf}

One can calculate minimum fluidization velocity, V_{mf}, by balancing the net weight of the bed against the upward force exerted on the bed, namely the pressure drop across the bed (Δp) multiplied by the cross-sectional area of the bed (A). Ignoring the small frictional force exerted on the wall of the column by the flowing fluid, the force balance can be formulated as fallows

Upward force on the bed = Δp A (1.7)

If the height of the bed at this point is "L" and the void fraction is "ε", the volume of particles can be written as

Volume of particles = (1-ε)AL (1.8)

If the acceleration due to gravity is g, the net gravitational force on the particles (net weight) is

Net Weight of the particles, $W = (\rho_p - \rho_f)(1-\varepsilon)ALg$ (1.9)

Balancing the equation 1.5 and equation 1.7 yields the following relation,

$$(\Delta p)\,A = W = (1-\varepsilon)(\rho_p - \rho_f)ALg$$
$$\frac{\Delta p}{L} = (1-\varepsilon)(\rho_p - \rho_f)g \qquad (1.10)$$

The various symbols appearing in the above equations are defined as follows.

Δp = Pressure Drop

L = Length of the Bed

A = cross-sectional area of the column

ρ_p = Density of the particle

ρ_f = Density of the fluid

ε = Void fraction of the bed (ε is the ratio of the void volume to the total volume of the bed)

The point of maximum pressure drop shown in Fig. 1.7 is the point of minimum fluidization. The force balanced equations for the point of minimum fluidization are:

$$(\Delta p)\,A = W = (1-\varepsilon_{mf})(\rho_p - \rho_f)AL_{mf}\,g$$
$$\frac{\Delta p}{L_{mf}} = (1-\varepsilon_{mf})(\rho_p - \rho_f)g \qquad (1.11)$$

According to **Ergun equation** (Eq. 1.6), the pressure drop increases with the fluid velocity through the following correlation. The first part of the right hand side of Eq. 1.12 is the viscous effect and second part is the inertial effect of fluid.

$$\left(\frac{\Delta p}{L}\right)\left(\frac{D_p}{\rho_f V_s^2}\right)\left(\frac{\varepsilon^3}{1-\varepsilon}\right) = \frac{150(1-\varepsilon)}{N_{\mathrm{Re}}} + 1.75 \qquad (1.12)$$

Where, $N_{\mathrm{Re}} = \dfrac{D_p\,\rho_f\,V_s}{\mu_f}$ = average Reynolds number based upon superficial velocity

D_p = Equivalent spherical diameter of the particle

V_s = Superficial velocity

$$\left(\frac{\Delta p}{L}\right)\left(\frac{D_p}{\rho_f\,V_s^2}\right)\left(\frac{\varepsilon^3}{1-\varepsilon}\right) = \frac{150(1-\varepsilon)\mu_f}{D_p\,\rho_f\,V_s} + 1.75 \qquad (1.13)$$

At minimum fluidization, the superficial velocity, V_s, is equal to the minimum fluidization velocity, V_{mf}. At this condition, the above Ergun equation (1.13) is rearranged with V_s being substituted by V_{mf}, L substituted by L_{mf}, and ε substituted by ε_{mf}.

$$\left(\frac{\Delta p}{L_{mf}}\right)\left(\frac{D_p}{\rho_f\,V_{mf}^2}\right)\left(\frac{\varepsilon_{mf}^3}{1-\varepsilon_{mf}}\right) = \frac{150(1-\varepsilon_{mf})\mu_f}{D_p\,\rho_f\,V_{mf}} + 1.75$$
$$\left(\frac{\Delta p}{L_{mf}}\right) = \frac{150\,\mu_f\,V_{mf}}{D_p^2}\frac{(1-\varepsilon_{mf})^2}{\varepsilon_{mf}^3} + \frac{1.75\,\rho_f\,V_{mf}^2}{D_p}\frac{(1-\varepsilon_{mf})}{\varepsilon_{mf}^3} \qquad (1.14)$$

The minimum fluidization velocity, V_{mf}, at which fluidization begins can be calculated by combining Eq. 1.11 and Eq. 1.14 to obtain the following quadratic equations

$$(1-\varepsilon_{mf})(\rho_p-\rho_f)g=\frac{150\mu_f V_{mf}}{D_p^2}\frac{(1-\varepsilon_{mf})^2}{\varepsilon_{mf}^3}+\frac{1.75\rho_f V_{mf}^2}{D_p}\frac{(1-\varepsilon_{mf})}{\varepsilon_{mf}^3}$$

$$(\rho_p-\rho_f)g=\frac{150\mu_f V_{mf}}{D_p^2}\frac{(1-\varepsilon_{mf})}{\varepsilon_{mf}^3}+\frac{1.75\rho_f V_{mf}^2}{D_p\,\varepsilon_{mf}^3} \tag{1.15}$$

$$\frac{g\rho_f(\rho_p-\rho_f)D_p^3}{\mu_f^2}=\frac{150(1-\varepsilon_{mf})}{\varepsilon_{mf}^3}\left(\frac{D_p\rho_f V_{mf}}{\mu_f}\right)+\frac{1.75}{\varepsilon_{mf}^3}\left(\frac{D_p\rho_f V_{mf}}{\mu_f}\right)^2 \tag{1.16}$$

Consider the Archimedes number, $Ar=\dfrac{g\rho_f(\rho_p-\rho_f)D_p^3}{\mu_f^2}$ (1.17)

and the Reynolds number at minimum fluidization, $Re_{mf}=\dfrac{D_p\rho_f V_{mf}}{\mu_f}$ (1.18)

Substituting the Eq. 1.17 and Eq. 1.18 to Eq. 1.16, "Ar" is obtained as,

$$Ar=\frac{150(1-\varepsilon_{mf})}{\varepsilon_{mf}^3}Re_{mf}+\frac{1.75}{\varepsilon_{mf}^3}Re_{mf}^2 \tag{1.19}$$

By solving the above quadratic Eq. 1.19 the Reynolds number can be obtained and from Eq. 1.18, the minimum fluidization velocity, V_{mf}, can be obtained. For large particles ($D_p \geq 1$ mm), inertial effects are important, and the full Ergun Equation, Eq. 1.19, must be used to determine V_{mf}.

For a bed of small particles ($D_p \leq 0.1$ mm), the flow conditions at this stage are such that the Reynolds number is relatively small ($Re \leq 10$) so that the Kozeny-Carman Equation can be used to establish the point of minimum fluidization. The Kozeny-Carman Equation is the simplified version of

Ergun equation (Eq. 1.12), which is applicable to viscous flow dominant regimes by removing the inertial part (second part of the right hand side of Eq. 1.12). This yield is given by Eq. 1.20:

$$V_{mf} = \frac{(\rho_p - \rho_f) g D_p^2}{150 \mu_f} \frac{\varepsilon_{mf}^3}{(1-\varepsilon_{mf})} \tag{1.20}$$

The state of the bed is one of incipient fluidization, when the superficial velocity V_s is equal to V_{mf}. The void fraction, ε, at this state depends upon the particle material, shape, and size. For nearly spherical particles, McCabe, Smith, and Harriott (2001) suggested that ε lies in the range 0.40 to 0.45, increasing a bit with particle size.

1.2.5.3.4 Terminal Setting Velocity

Consider the upward flow of a gas through a bed of particles. At some superficial velocity, the upward drag force (F_d) exerted by the gas on the particles balances the downward body force of gravity (F_g). This is the condition of minimum fluidization (where, $F_d = F_g$). For particles with diameters in the range of 50 to 500 microns and densities in range of 0.2 to 5,000 kg/m^3, fluidization usually can be achieved smoothly with increasing gas velocity. As denoted by Geldart (1972), these characteristics embrace the majority of particles encountered in fluidized beds applications. For such particles, gas velocities above the minimum fluidization velocity result in the occurrence of gas bubbles in the bed, wherein some fraction of the gas flows through the suspension of particles as a continuum phase, while the remaining fraction flows as discrete bubbles rising through the suspension. This is the regime commonly called dense bubbling fluidization. The upper limit of the gas velocity for this regime is related to the terminal settling velocity of the particles, beyond which interfacial drag becomes sufficient to entrain the particles out of the bed. To establish the appropriate fluidization regime for any given application, one needs to calculate the minimum fluidization velocity and the terminal settling velocity of the bed particles.

The superficial velocity of the gas for minimum fluidization (V_{mf}) can be calculated by solving the following quadratic equation for Re_{mf} :

$$Ar = \frac{150(1-\varepsilon_{mf})}{\varepsilon_{mf}^3} Re_{mf} + \frac{1.75}{\varepsilon_{mf}^3} Re_{mf}^2$$

Where, the Archimedes number, $Ar = \frac{g\,\rho_f\,(\rho_p - \rho_f) D_p^3}{\mu_f^2}$

and the particle Reynolds number at minimum fluidization, $Re_{mf} = \frac{D_p\,\rho_f\,V_{mf}}{\mu_f}$

When a free-falling object accelerates downwards due to gravity, the upward drag force acting on the object increases, causing the acceleration to decrease. At a particular speed, the downward gravitational force (F_g) will be equal to the upward drag force (F_d). This causes the net force on the object to be zero, resulting in an acceleration of zero. This particular speed is known as terminal velocity (also called settling velocity).

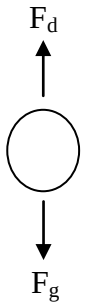

The terminal velocity (V_{ts}) is given by the expression:

$F_d = F_g$

$$\frac{1}{2}\rho_f\,V_{ts}^2\left(\frac{\pi}{4}D_p^2\right)C_D = (\rho_p - \rho_f)\left(\frac{\pi}{6}D_p^3\right)g$$

$$V_{ts} = \sqrt{\frac{4\,g\,D_p\,(\rho_p - \rho_f)}{3\,\rho_f\,C_D}} \qquad (1.21)$$

where C_D is the drag coefficient for a single particle.

The drag coefficient, C_D is equal to 0.44, in the case of spherical particles. But in the case of near-spherical particles, over the range $1 < Re_{ts} < 1{,}000$, C_D is given by the relationship:

$$C_D = 18.5\,Re_{ts}^{-3/5} \qquad (1.22)$$

where the Reynolds number at terminal velocity (Re_t) is defined by the following equation:

$$Re_{ts} = \frac{D_p \, \rho_f \, V_{ts}}{\mu_f} \tag{1.23}$$

Substituting Eq. 1.22 into Eq. 1.21, an explicit equation for the terminal settling velocity is

Obtained: $V_{ts} = \left[0.072\, g \, \frac{D_p^{8/5} \left(\rho_p - \rho_f \right)}{\rho_f^{2/5} \, \mu_f^{3/5}} \right]^{5/7}$

Now, consider the condition one must impose on the superficial velocity so that particles are not carried out with the fluid at the exit. This would occur if the superficial velocity is equal to the terminal settling velocity of the particles.

If one's attention is restricted solely to small particles ($D_p \leq 0.1$ mm), Stokes's Law can then be used to calculate their terminal settling velocity as:

$$V_{ts} = \frac{\left(\rho_p - \rho_f \right) g \, D_p^3}{18 \, \mu_f} \tag{1.24}$$

By using the result for the minimum fluidization velocity for the case of small particles, as in Eq. 1.20, the ratio of Eq. 1.24 and Eq. 1.20 can be found as:

$$\frac{V_{ts}}{V_{mf}} = \left(\frac{25}{3} \right) \frac{\left(1 - \varepsilon_{mf} \right)}{\varepsilon_{mf}^3} \tag{1.25}$$

For all "ε" in the range of 0.40 to 0.45, which yields a ratio ranging from 78 to 50.

1.2.5.3.5 Calculation Results of Minimum Fluidization Velocity

In this study, a fluidized bed is loaded with spherical, granular carbon solid whose particles are 250 micrometers (2.5×10^{-4}m) in diameter. Assuming that these particles are to be fluidized by

ambient air, the minimum fluidization velocity needs to be calculated as a reference value for the purpose of simulating coal gasification. The approaches that have been used are given below.

Table 1.2: Properties of the two phases

Properties	Gas (air)	Particles (carbon solid)
Density, ρ (kg/m^3)	1.225	2000
Heat capacity, c_p (kJ/kg K)	1006.43	0.71
Thermal conductivity, k (W/m K)	0.0242	119
Viscosity, μ (kg/m s)	1.7894 x 10^{-5}	1.72 x 10^{-5}

According to Geldart's classification, the carbon solid belongs to type B. The void fraction at the point of minimum fluidization is found to be $\varepsilon_{mf} = 0.60$. Assuming the sphericity of the carbon solid to be $\Phi_s = 1.0$, the Archimedes number must first be found by solving Eq. 1.17, yield Ar = 2097.40. Then, the Reynolds number at the minimum fluidization is found by solving the equation Eq. 1.19, and then the value $Re_{mf} = 6.62$ is obtained. From this Reynolds number, the minimum fluidization velocity can be obtained in terms of solving Eq. 1.18, yielding: $U_{mf} = 0.3868$ m/s. The following are other equations that can be used to find out the minimum fluidization velocity of carbon solid that are used in this study.

Todes and Ciovich (1981) suggested:

$$U_{mf} = \frac{\mu_g}{d_p \rho_g}\left(\frac{Ar}{1400 + 5.25\sqrt{Ar}}\right) \tag{1.26}$$

Saxena and Vogel (1977) recommended:

$$U_{mf} = \frac{\mu_g}{d_p \rho_g}\left[\left\{(25.28)^2 + 0.0571 \times Ar\right\}^{0.5} - 25.28\right] \tag{1.27}$$

Finally, Kumer and Gupta (1980) indicated:

$$U_{mf} = 0.005\frac{\mu_g}{d_p \rho_g}\, Ar^{0.78} \tag{1.28}$$

1.2.5.4 Review of FBG History

In 1952, Ergun reviewed and studied the existing information on the flow field through beds of granular solids. In his research work, he described experimental results obtained for the purpose of testing the validity of the various equations and numerous other pieces of data taken from the literature. He found that pressure drops are due to simultaneous kinetic energy and viscous energy losses, and gave the following comprehensive equation for all types of flow.

$$\left[\frac{\Delta p}{L}\right]=\left[150\frac{(1-\varepsilon)^2}{\varepsilon^3}\frac{\mu_f\ V_m}{D_p^2}\right]+\left[1.75\frac{(1-\varepsilon)}{\varepsilon^3}\frac{\rho_f\ V_m^2}{D_p}\right] \tag{1.29}$$

Viscous energy losses per unit length are expressed by the first term of the right hand side of the above equation, and the kinetic energy losses are expressed by the second term of right hand side. Ergun also examined the above equation from the prospective of its dependence upon the fluid flow rate, properties, and fractional void volume (ε) and the orientation, size, shape, and surface of the granular solids. Whenever possible, conditions were chosen so that the effect of one variable at a time could be considered. A transformation of the general equation points out that the Blake-type friction factor has the following form:

$$f_v=1.75+150\frac{(1-\varepsilon)}{N_{Re}} \tag{1.30}$$

In Ergun's report, a new concept of friction factor, f_v, representing the ratio of pressure drop to the viscous energy term is discussed as well.

Due to high rates of heat and mass transfer and solid mobility throughout the coal gasification process inside a hot fluidized bed, Syamlal and Gidaspow (1985) developed a computational model. Even though fluidized beds can be used to combust coal in order to produce electric power, one of the main concerns of using fluidized beds to fulfill commercialization how the operating parameters will change when the reactor is scaled up. This is because the existing hydrodynamic theory used to describe the complicated transient gas and solid motion in a fluidized bed is lacking experimental verification. For combustion inside a fluidized bed, Adams and Welty (1979) provided a model and it's been proven

to be very useful for explaining heat transfer coefficients from a horizontal tube to a fluidized bed. The Illinois Institute of Technology (IIT) developed a fluidized bed model for a two dimensional bed in cold flow only, which was able to predict void distribution, solids circulation, and bubbling behaviors. Further, this model was extended to a heated fluidized bed. Their results show that, in a bubbling bed, the large heat transfer coefficients can be computed from their hydrodynamic model without the use of any turbulence. This model computes a transient type behavior caused by the formation of bubbles, their propagation, and their eruption at the top of the bed. All of the computed variables including the void fraction, the gas and solid velocities, and the temperatures exhibit a complex oscillatory behavior.

Syamlal (1987) developed a multi-particle model of fluidization phenomena. He simulates fluidization, for example, as segregation, elutriation, and solids mixing. The concept known as particle-particle drag is required for his model as it accounts for the momentum transfer between the particulate phases due to collisions. Earlier researchers developed empirical correlations and measured the particle-particle drag for dilute systems, such as pneumatic conveyors. Similar measurements, however, are not possible to be completed in dense systems, such as a fluidized bed. Therefore, based on the kinetic theory of dense gases, he derived an expression for the particle-particle drag, and then compared the predictions of the model with Yang's and Keairns's experimental data in order to test the accuracy of that expression. Yang and Keairns (1982) used uniform mixtures of dolomite and acrylic particles in a fluidized bed many times. They also measured the rate of separation of the dolomite particles from the acrylic particles. They found that the dolomite particles settled rapidly due to it being heavier and larger than the acrylic particles. Yang and Keairns's experimental data suggest that the rate of settling is strongly dependent upon the particle-particle drag. Therefore, for determining the accuracy of the equation for particle-particle drag, duplicating Yang and Keairns experiments is a necessary endeavor. He found that the model predicts the initial rate of separation reasonably well. But, the predicted equilibrium concentrations of dolomite particles in the upper layer of acrylic particles do not agree with the experimental data. He thought this is because of the absence of granular stress from the model. Hence, further refinement of the particle-particle drag term can be sought only after including realistic granular stress in the multi-particle model.

Syamlal and O'Brien (1989) studied bubble behavior. The hydrodynamic model of a fluidized medium as a mixture of a gas and a granular (solid) phase was used in their study. The bubbles in

fluidized beds of various particle sizes, with and without jets can also be modeled. They found that the predicted characteristics of bubble formation, bubble motion, bubble eruption at the surface, bubble shape, bubble coalescence phenomena, and also the dynamics of the bed surface are in good qualitative agreement with experimental data. They compared the bubble volume, bubble rise velocities, bubble frequency, wake angle, wake fraction, and pressure profile with experimental data and simpler theories. They tested the predicted gas and solids mixing by using a new graphical technique and found that the data is in good agreement with experimental results.

Benyahia et al. (2004) investigated the capability of three gas-solid flow models (standard granular kinetic theory and two gas-solid turbulence models) to estimate the core-annular flow behavior usually observed in dense gas/solid flows. Their study proved that the granular kinetic theory, Balzer et al. 1996, and Cao and Ahmadi 1995 give similar estimation of a dense, fully-developed flow in a vertical channel and that the gas turbulence may not have a dominant effect in relatively dense gas/solid flows. Eventually, the core-annular flow behavior in which the maximum concentration of solids occurred at the walls was not observed if the boundary conditions cause production of granular energy at the wall. Boundary conditions that dissipate granular energy near the wall are needed to induce a core-annular flow structure.

Gunn (1978) experimentally measured the heat transfer to and from particles in fixed beds and showed that either the Nusselt number decreases to zero if axial dispersion has been neglected, or the Nusselt number remains at a constant value as the Reynolds number is reduced. A quantitative analysis of particle to fluid heat transfer upon a stochastic model of the fixed bed leads to a constant value of the Nusselt group at low Reynolds number. When the analytical equation contains an asymptotic condition, he derived an expression which describes the dependence of the Nusselt group upon Reynolds number. In addition, he extended this expression to describe mass and heat transfer to fixed and fluidized beds of particles within the porosity range of 0.35 to 1.0. Both the gas and liquid phase transfer groups were correlated up to a Reynolds number of 10^5.

Lun et al. (1984) used statistical methods analogous to those used in the kinetic theory of gases to model the flow of an idealized granular material consisting of uniform, smooth, inelastic spherical particles. They developed two theories: one for the Couette flow of particles having arbitrary

coefficients of restitution (inelastic particles) and a second for the general flow of particles with coefficients of restitution near one (slightly inelastic particles). The study of inelastic particles in Couette flow duplicated the method of Savage & Jeffrey (1981). An ad hoc distribution function was used to simulate the collisions between particles. They compared the results of this first analysis with other theories of granular flow, with the Chapman-Enskog dense-gas theory, and with experiments. Their theory agreed moderately well with experimental data, and it is found that the asymptotic analysis of Jenkins & Savage (1983), which was developed for slightly inelastic particles, gave wonderful results that are similar to the first theory even for highly inelastic particles. Thus, the "nearly elastic" approximation is pursued as a second theory using an approach that is closer to the established methods of the Chapman-Enskog dense-gas theory. By defining the collisional distribution functions through a rational approximation scheme, their new approach is not only applicable to normal flow fields, but to simple shear flows as well. It incorporates kinetic as well as collisional contributions to the constitutive equations for stress and energy flux and is thus appropriate for dilute as well as dense concentrations of solids. While the collisional contributions are dominant, it predicts stresses similar to the first analysis for the simple shear case.

Ding and Gidaspow (1990) indicated that, for a better understanding of tube erosion in fluidized bed combustors, detailed knowledge of bubble motion, solid circulation, and the frequencies of porosity oscillations is required. They suggested a predictive two-phase flow model starting with the Boltzmann equation for the velocity distribution of the particles. This model is a generalization of the Navier-Stokes equations of the type proposed by R. Jackson, except that the solid viscosities and stresses are computed by simultaneously solving a fluctuating energy equation for the particulate phase. Predictions from this model agree with the time-averaged and instantaneous porosities measured in two-dimensional fluidized beds. They also estimated the bubbles and observed flow patterns.

Kuipers et al. (1992) developed a computational model for a hot gas fluidized bed using the two-fluid model (TFM) approach. In their approach, both phases are treated as continuous and fully interpenetrating. They calculated the local wall-to-bed heat transfer coefficients by solving the two-fluid model (TFM) conservation of mass, momentum, and energy equations simultaneously. Their preliminary calculations suggest that the experimentally-observed high wall-to-bed heat transfer coefficients of gas fluidized beds can be predicated with the present hydrodynamic model without the

incorporation of turbulence terms in the transport equation. Their calculation clearly showed the enhancement of the wall-to-bed heat transfer process due to the bubble-induced bed-material refreshment along the heated wall. The model proved its usefulness and distinguished itself advantageously from former theoretical models by offering detailed information on the local behavior of the wall-to-bed heat transfer coefficients. The local wall-to-bed heat transfer coefficient is relatively large in the wake of the bubbles rising along the heated wall because of the vigorous solid circulation in the bubble wake.

Enwald et al. (1999) investigated a validation of the two-fluid model for a bubbling fluidized bed application and a mesh refinement study for the same. They calculated the simulated statistical bubble quantities from voidage signals derived from the transient multidimensional solution of two-fluid models. The algorithm for computing these quantities was taken directly from the evaluation program treating the measurement signals. They developed a parallel version of the two-fluid model solver to remedy the long simulation times required to obtain acceptable statistical values. This version was based on a domain decomposition method for distributed memory computers. The mesh refinement study indicates that a higher degree of mesh refinement is required for atmospheric than for pressurized fluidization. They evaluated statistical bubble parameters (bubble frequency, mean bubble rise velocity, mean pierced bubble length, and mean bubble volume fraction). They investigated a number of problems related to the parallelization. These problems are related to the optimal treatment of the velocity components with respect to the frequency of data exchange at multi-block boundaries, local errors at multi-block boundaries, and simulation time requirements.

Mathiesen et al. (2000) developed a computational study of the flow behavior in a cold-flow, pilot-scale circulating fluidized-bed. They presented a multi-fluid Computational Fluid Dynamics (CFD) model and verified it against experimental data reported in the literature. The flow model is based on an Eulerian description of the phases where the kinetic theory of granular flow forms the basis for the turbulence modeling in the solid phases. The model is generalized for one gas phase and "N" number of solid phases to enable a realistic description of the particle size distributions in gas/solids flow systems. Each solid phase is characterized by a diameter, density, and restitution coefficient. They operated the simulations with different initial solid concentrations, superficial gas velocities, and standard deviations within the particle size distribution. They emphasize studying the effects of different particle size

distributions and the fluctuating behavior of the dilute gas/solids flow system. Altogether, their simulation results in very good agreement with the experimental data. They also calculated mean diameters, axial and radial mean and turbulent velocities, and mass fluxes successfully.

Huilin et al. (2003) investigated the dynamic behavior of gas-solids flow in a 6 m high riser using a transient, two-dimensional (2-D) hydrodynamic model based on the kinetic theory of granular flows. They obtained the void fraction(s), turbulent parameters, and instantaneous and local gas-particle velocities. The typical core-annular flow structure was reflected by predicted time-averaged particle concentrations and velocities, which were in agreement with experimental measurements, specifically with those reported by Miller and Gidaspow (1992). Predicted total granular temperature and instantaneous solids concentration frequencies compared well with the experimental data for various regions of the riser. They predicted high thermal conductivities of fluidized powders from the kinetic theory without adjusting the parameters. They assessed the effects of riser diameter, initial conditions, inlet geometry, and riser vertical inclination. They predicated the unexpectedly strong distortions of solid concentrations and vertical fluxes for small inclination angles on the order of 2°. Thus, analysis of experimental data should be carefully conducted to ensure that the riser inclination is not too important over the length of the riser in order to eliminate potential computational artifacts due to this geometric parameter.

Jiradilok et al. (2006) studied the turbulent fluidization regime, which is described by the co-existence of a dense, bottom region and a dilute, top bed. CFD code combined with kinetic theory with a drag corrected for clusters captured the basic features of this flow regime: the dilute and dense regions, high dispersion coefficients, and strong anisotropy. The computed energy spectrum captures the observed gravity wave and the Kolmogorov -5/3 law at high frequencies. The computed turbulent kinetic energy is close to the measurements for Fluidized Catalytic Cracking (FCC) particles. The CFD simulations compared reasonably well with the measured core-annular flow experiments at very high solid fluxes. The computed solid pressures, granular temperatures, FCC viscosities, and frequencies of oscillations were close to the measurements reported in the literature. Their computations suggested that, unlike for the flow of group B particles, the oscillations for the FCC particles in the center of the riser are primarily due to the oscillations of clusters and not due to oscillations of individual particles. Therefore, mixing is not on the level of individuals particles.

Panneerselvam, Savithri, and Surender (2007) carried out CFD simulations to predict flow patterns in a liquid-solid fluidized bed using Eulerian-Eulerian framework. They compared the CFD results with the experimental findings reported by Limtrakul et al. (2005) and showed a good agreement. Further, they extended the CFD model to compute the solid mass balance in the core and annular regions for verifying conservation of mass and energy flows due to various dissipation mechanisms. They also compared the energy required for solid expansion in a liquid fluidized bed with the energy required for solid suspension in an equivalent stirred tank contactor at similar operating conditions. They investigated the influence of various inter-phase drag models proposed by Di Felice et al. (1994), Gidaspow (1994), and Syamlal and O'Brien (1988) on solid in liquid fluidized beds. Even though the models proposed by Syamlal and O'Brien predicted the flow pattern of solid motion inside the fluidized bed only with reasonable accuracy, the model proposed by Gidaspow showed a better quantitative agreement with experimental data. Their grid sensitivity indicates time step sensitivity and effects of inlet feed conditions for ensuring the accuracy of the numerical simulation's predicted result.

Wang et al. (2008) numerically analyzed the hydrodynamics of three-dimensional gas-solid bubbling fluidized beds. They simulated the particle-particle interactions from the kinetic theory for flow of dense, slightly inelastic, slightly rough spheres proposed by Lun (1991) to account for rough sphere binary collisions and the frictional stress model proposed by Johnson et al. (1990) to consider the frictional contact forces between particles. Their model was evaluated by comparing with the measured particle distributions and velocities of Yuu et al. (2001) and the experimental bed expansion of Taghipour et al. (2005). Their computed results indicated that their model gave better agreement with the experimental data than the results from the original kinetic theory for frictionless, slightly inelastic spheres of Ding and Gidaspow (1990) with and without a solid friction stress model.

Reuge et al. (2008) verified a CFD model before they used it for designing fluidized bed reactors. They collected the validation data from a fluidized bed of (Geldart's group B, 1972) alumina particles operated at different gas velocities involving two fluidization hydrodynamic regimes (bubbling and slugging). They measured the height of bed fluctuations, bed expansion, and frequency of fluctuations from videos of the fluidized bed. To simulate the experiments, they used the Eulerian-Eulerian two-fluid model MFIX (website: http://www.mfix.org). They evaluated two different models for the particle stresses: the Schaeffer model developed by Syamlal, Rogers, and O'Brien (1993) and

Schaeffer (1987) and the Princeton model developed by Srivastava and Sundaresan (2003), including evaluations of different values of the restitution coefficient and internal angle of friction. 3-D simulations are required for getting quantitative and qualitative agreement with experimental data. They observed that the results from the Princeton model are in better agreement with the experimental data than those from the Schaeffer model. They also observed that both free slip and Johnson-Jackson boundary conditions gave nearly identical results. An increase in the coefficient of restitution (e) from 0.8 to 1 leads to larger bed expansions and lower heights of fluctuations in the bubbling regime, whereas it leads to unchanged bed expansion and to a massive reduction in the height of fluctuations in the slugging regime. The angle of internal friction (Φ) in the range 10-40° does not affect the bed expansion, but its reduction significantly reduces the height of fluctuations.

Yan et al. (1999) developed a previous numerical model of fluidized bed coal gasifiers to incorporate an overall energy balance. They used the improved model to simulate the performance of bubbling fluidized bed coal gasifiers of different scales. Their simulations showed that the predicted overall carbon conversion efficiency (or alternatively, "percentage" or "fraction"), operating bed temperature, and concentrations of individual gas species compared well with the experimental data from four individual fluidized bed coal gasifiers, including one full-scale gasifier. The full-scale gasifier is oxygen-blown, while the three pilot-scale ones are air-blown. The water-gas shift reaction, either driven by kinetics or in equilibrium in the dilute phase, has significant effects on the predictions for the pilot-scale, air-blown gasifiers but has little effect on a commercial-scale oxygen-blown gasifier. This is attributed to the much faster oxidation rate of H_2 and CO near the distributor in the oxygen-blown, commercialized gasifier than in the air-blown gasifiers. Their results also indicated that about 26-41% of feed oxygen is consumed in the homogeneous combustion reactions in the simulation. The percentage of oxygen consumption in the homogeneous reaction increases with a decrease in coal rank and with an increase in operating pressure and temperature. Carbon conversions due to char gasification are significant when compared to those due to char combustion in the simulated gasifier.

Chejne and Hernandez (2002) developed a one-dimensional steady-state mathematical model and a numerical algorithm to simulate the coal gasification process in a fluidized bed. The model contains two phases: the solid and the gas. The solid phase is composed of carbonaceous material, limestone, and inert bed material. The gaseous phase refers to the emulsion with the solid phase and

forms the bubbles. Their model could predict temperature, converted carbon fraction, and particle size distribution for the solid phase. For the gaseous phase, in both emulsion and bubble, their model could predict profiles of temperature, velocities, gas composition, and other fluid-dynamic parameters. In the feed zone, they considered a Gaussian distribution for the solid particle size. This distribution changes due to elutriation, attrition, consumption, and drag inside the reactor. They solved a system of 29 linear and 10 non-linear differential equations, derived from mass, momentum, and energy balances for each phase and at any point along the bed height, by the Gear and Adams Method (1971). They used experimental data from the Universidad de Antioquia and Universidad Nacional-Medellin to verify their model. Eventually, the model was used to optimize the gasification process by switching several parameters, such as excess of air, coal type, particle size distribution, and geometry of the reactor.

Yu et al. (2007) developed a numerical model based on the two-fluid model (TFM) including the kinetic theory of granular flow (KTGF) and complicated reactions to simulate coal gasification in a bubbling fluidized bed gasifier (BFBG). They determined the coal gasification rates by combining the Arrhenius rate and diffusion rate for heterogeneous reactions and using the turbulent mixing rate for homogeneous reactions. They predicted the flow behaviors of gas and solid phases in the bed and freeboard which are not easy to be measured through the experiments. They talked about the relationship between gas compositions profiles with the height of the gasifier and the distributions of temperature, gas and solid velocities, and solid volume fraction. The calculated exit values of gas composition agreed well with the experimental data.

Wang, Jin, and Zhong (2009) developed a comprehensive three-dimensional numerical model to simulate coal gasification in a fluidized bed gasifier. They considered both gas-solid flow and chemical reactions. They determined the reaction rates of homogeneous reaction and heterogeneous reaction by using the Arrhenius-Eddy dissipation reaction rate and Arrhenius-diffusion reaction rate, respectively. They considered the coal pyrolysis, homogeneous reactions, and heterogeneous reactions. They modeled the gas phase with the k-ε turbulent model and the particle phase with the kinetic theory of granular flow. They carried out the simulations in a fluidized bed coal gasifier with a height of 2.0 m and a diameter of 0.22 m. They obtained the flow patterns, gas velocities, particle velocities, composition profiles of the gaseous products, and distributions of reaction rates. They compared some numerical values with experimental data. The results showed that the predicted exit gas compositions were in a

good agreement with the experiments. This indicated that their proposed three-dimensional models and simulations were successful, which provided a promising way to simulate coal gasification in fluidized beds.

1.2.5.5 Entrained Bed Gasifier (EBG)

For an entrained bed gasifier, the gasification reactions take place in a dense cloud of very fine particles. This means the fuel must be pulverized, which requires somewhat more energy than for the other types of gasifiers. Most coals are suitable for this type of gasifier because of the high operating temperatures and because the coal particles are well separated from one another. The high temperatures and pressures also mean that a higher throughput can be achieved. However, thermal efficiency is somewhat lower as the gas must be cooled before it can be cleaned with existing technology. The high temperatures also mean that tar is not present in the product gas; however the oxygen requirement is higher than for the other types of gasifiers. All entrained flow gasifiers remove the major part of the ash as a slag since the operating temperature is well above the ash fusion temperature. Some entrained bed gasifiers do not possess a ceramic inner wall but have an inner water- or steam-cooled wall covered with partially solidified slag. These types of gasifiers do not suffer from the formation of corrosive slags. Some fuels have ashes with very high ash fusion temperatures. By far, the most energy consumption related to entrained bed gasification is not the milling of the fuel but the production of oxygen used for the gasification.

Figure 1.8 presents a simplified schematic the entrained bed gasifier. In an entrained bed gasifier, very fine fuel particles (< 100 μm) are suspended in a stream of oxygen/air and steam. Coal particles mix thoroughly with steam and oxygen, and the syngas produced exits through the outlet. Entrained bed gasifiers operate at very high temperature 1370-1650 °C (2500-3000 °F). Ash in the coal melts and is discharged as molten slag from the bottom of the gasifier. Entrained bed gasifiers are available in larger capacities compared to other types. The flow moves fast in the gasifier with a residence time typically around 3~5 seconds. The fast flow rate and better mixing of fuel and oxidant in the entrained bed gasifier when compared to moving-bed and fluidized bed gasifiers results in a higher carbon conversion efficiency and a higher yield. However, an entrained bed gasifier does have disadvantages as it requires the highest amount of oxygen and produces the lowest heating value gas.

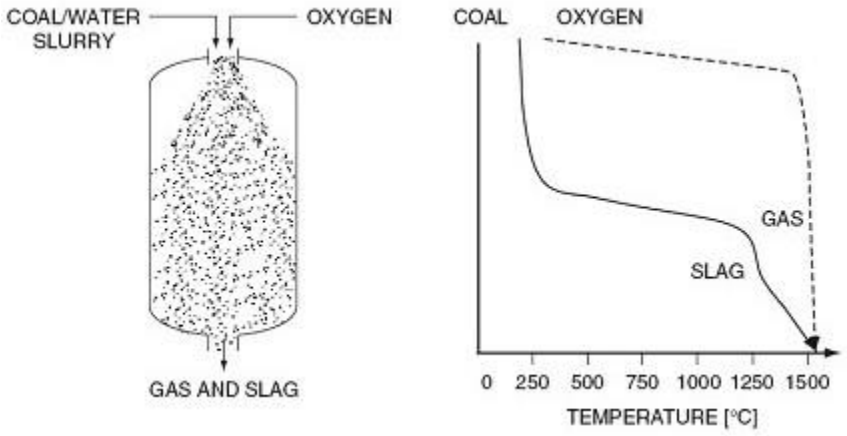

Figure 1.8 Schematic of a downdraft an entrained bed gasifier

(Source: Enggcyclopedia, http://www.enggcyclopedia.com/2011/12/gasification-process-types/)

Examples of commercial entrained bed gasifiers are given below:

(i) Shell Coal Gasification Process (SCGP)

The Shell gasifier is a high-pressure, dry-fed, oxygen-blown, entrained bed gasifier. Dry pulverized coal is fed into the high-pressure vessel with transport gas, which is usually nitrogen, through a lock hopper system. The Shell gasifier does not use refractory bricks for its wall, but instead uses membrane walls. Steam and oxygen enter into the gasifier together with dry coal particles. The gas temperature can reach 1370 °C (2500 °F). Because of the high temperature, no hydrocarbon volatiles or moisture will be left inside the feedstock. At the high operating temperature, ash in the coal melts and flows down the membrane wall. When the raw syngas at the temperature of 1370-1650 °C (2500-3000 °F) leaves the vessel, it contains a small amount of unburned carbon as well as about half of the molten ash. To prevent the molten ash from sticking to the wall, the raw syngas is partially cooled down to around 870 °C (1600 °F) by quenching it with cooled, recycled product gas. The raw syngas goes through a further cooling process in the syngas cooler unit for further clean up. The first commercial IGCC plant using the Shell gasifier is the one in Buggenum, the Netherlands, which was built in 1993. The plant is able to achieve an overall efficiency of 43%. It can process up to 2000 tons of coal per day.

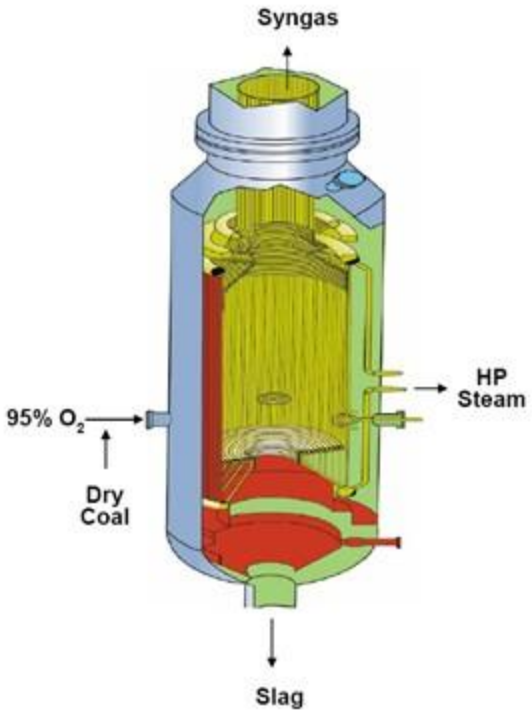

Figure 1.9 Schematic of the Shell gasifier

(ii) General Electric Gasifier (Previously Texaco gasifier)

The General Electric (GE) gasifier (Fig. 1.10) operates in the temperature range of 1250-1450 °C (2280-2650 °F) and uses a pressure of 3 MPa for power generation and 6-8 MPa for H_2 and chemical synthesis. A coal slurry and the oxidant are introduced from the top of the gasifier. The water in the slurry mixture replaces the steam that is normally injected into the system. The hot raw gas produced during the gasification process flow toward the bottom of the gasifier. The molten ash flows down the refractory-lined walls. The hot raw gas temperature is around 1400 °C (2550 °F). Two methods of raw syngas cooling are available: (a) cooling by water quenching, or (b) cooling in a radiant cooler. When a water quench is used, molten ash/slag is also removed from the syngas.

The first true IGCC demonstration technology was at the Southern California Edison Cool Water Station in 1984 and used a GE (Texaco) gasifier. The Cool Water gasifier was moved to a commercial installation at the Coffeyville refinery in Kansas after the completion of the demonstration program in

1989. The gasifier is still in operation at the refinery, converting petroleum coke into ammonia. There are currently 64 plants with GE gasifiers operating worldwide with 10 more plants in the planning phase.

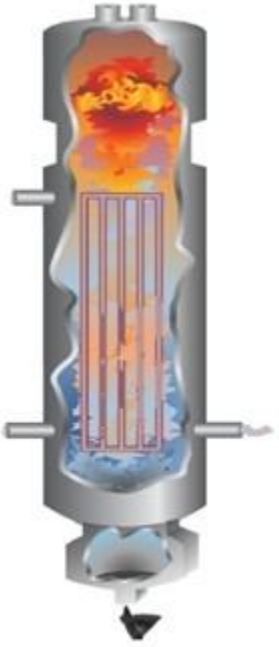

Figure 1.10 Schematic of the General Electric gasifier

(iii) Conoco-Phillips (E-Gas) Gasifier

The E-Gas gasifier is a two-stage, high-pressure, oxygen-blown, slurry-fed, slagging gasifier. Coal is mixed with water to make the coal slurry. About 80% of the coal slurry and 100% of the oxidant are injected into the first stage, while the remaining coal slurry is injected into the second stage. The first stage, a horizontal cylinder with one burner at each end, is located at the bottom part of the gasifier. One burner is used for the fresh coal slurry, and the other is for recycled, unburned char. Oxidation is dominant in the first stage, increasing the temperature to about 1316-1427 °C (2400-2600 °F). The ash melts and forms molten slag, which flows down and out of the vessel through a tap hole. The molten ash is quenched in a water bath and is then removed.

The hot gas from the first stage flows up to the second stage where the remaining 20% of the coal slurry is injected. The slow endothermic gasification reactions are dominant in the second stage,

whereas the more exothermic reactions were dominant in the first stage. The gas temperature decreases to around 1035 °C (1900 °F). Finally, the syngas and the unburned char leave the gasifier from the top, and all unburned char is removed from the syngas in the gas clean-up system and recycled back to the gasifier's first stage.

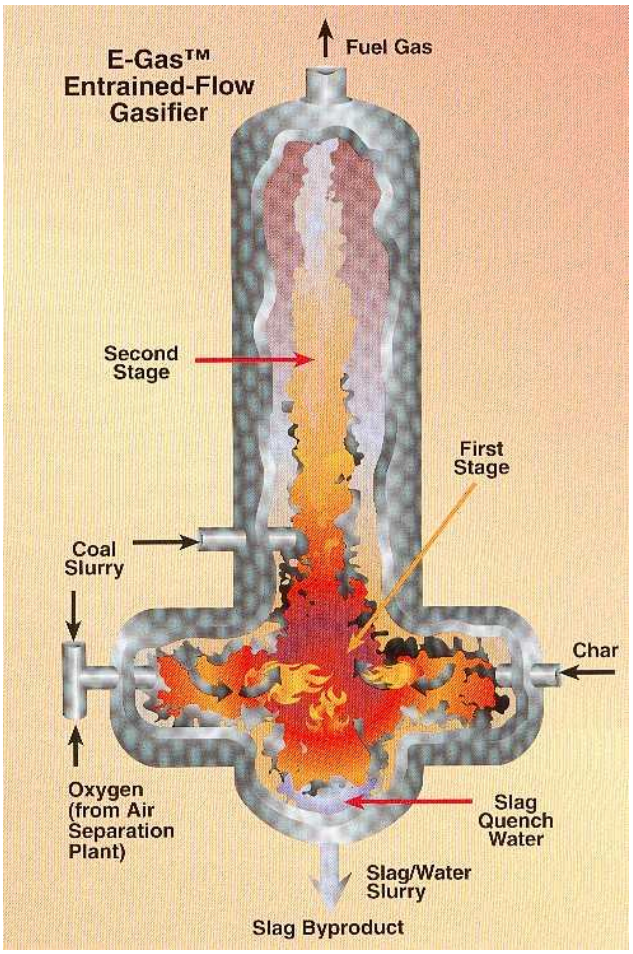

Figure 1.11 Schematic of the Conoco-Phillips (E-Gas) gasifier (Source: DOE).

(iv) PRENFLO (PREssurized ENtrained-FLOw) Gasifier

PRENFLO is a further development of the Kopper-Totzek process developed in the 1940s, which operates at atmospheric pressure. PRENFLO was developed by Uhde, which later merged with Krupp Koppers. PRENFLO is a one-stage, high pressure, dry-fed, oxygen-blown, slagging gasifier. The gas temperature inside a PRENFLO gasifier can exceed 2000 °C (3630 °F) and uses a membrane wall.

PRENFLO gasifiers are used in the world's largest solid-feedstock-based IGCC power plant in Puertollano, Spain.

Figure 1.12a shows an illustration of a PSG (PRENFLO with Steam Generation) gasifier. Coal is injected together with oxygen and steam through several injectors in the lower part of the gasifier. Raw syngas is then cooled down through the waste heat boiler in order to produce steam. The exit gas temperature is 1350-1600 °C (2460-3910 °F). In a PDQ (PRENFLOW with Direct Quench), illustrated in Fig. 1.12b, coal and oxygen/steam are injected in the upper part of the gasifier, while the raw syngas is directly quenched by water in the lower part of the gasifier. The cooled syngas finally leaves the system at around 200-250 °C (390-480 °F).

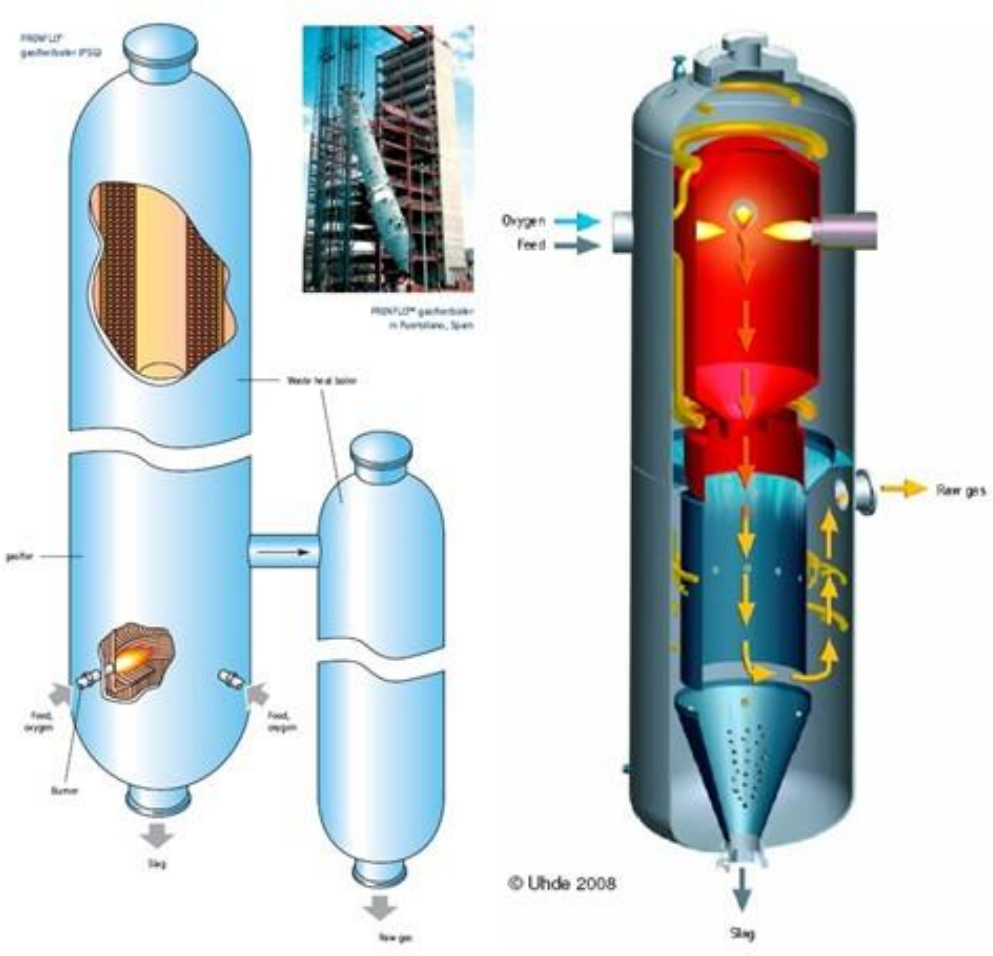

(a) PSG (b) PDQ

Figure 1.12 (a) PRENFLO with Steam Generation (PSG) and (b) PRENFLO with Direct Quench (PDQ)

1.2.5.6 EBG Design Considerations

The design of entrained bed gasifiers could start from selecting existing mathematical models which express the conservation of mass, momentum, and energy equations. The balance of mass and energy are coupled and give an estimation of multiphase variables, for example, the velocity field in terms of mixtures. The gasifier pressure profile and total pressure drop can be found by solving the momentum balance equations. All of these parameters refer to each other and need be taken care of while designing an entrained bed gasifier. Generally, the aim of designing this gasifier is to achieve the highest gasification rates, since it has short residence time and can withstand high pressures and temperatures. Also, entrained bed gasifiers generate product gases at high temperatures and lower heating values with high oxygen consumption.

Transport Gasifier

The Kellogg Brown & Root (KBR) transport gasifier, whose schematic is shown in Fig. 1.13, is a circulating-bed reactor that uses fine pulverized coal and limestone. The reactor consists of a mixing zone, a riser, cyclone filters, and a standpipe. Oxidant and steam are fed at the bottom of the gasifier in the mixing zone. The amount of oxidant fed is carefully controlled to limit char combustion inside the gasifier. The steam added to the gasifier functions as a reactant and a moderator to control the gas temperature. The oxidant reacts with the recycled unburned char. To avoid premature combustion with oxygen, coal (and lime) is injected in the upper section of the mixing zone. The endothermic char gasification primarily occurs in the riser. The gas and particles flow up through the riser and into the cyclones, where the syngas and solids are separated by gravity and/or centrifugal forces. The syngas exits the reactor and passes through the gas cooler, while the solids are discharged back into the mixing zone through the standpipe. The entrained solids circulate the reactor through the riser, the cyclone, and the standpipe. The KBR transport gasifier is a non-slagging gasifier. The operating temperature is fairly moderate (but sufficiently high to thermally crack the heavier volatiles and tars) and the use of dry coal means that the syngas has low tar and oil contents. The exit syngas temperature is around 1000 °C (1830 °F). One of the advantages of the transport gasifier is that coal is injected into the relatively low-temperature region (gasification region), so a typical problem related to fuel-injector's reliability is not present.

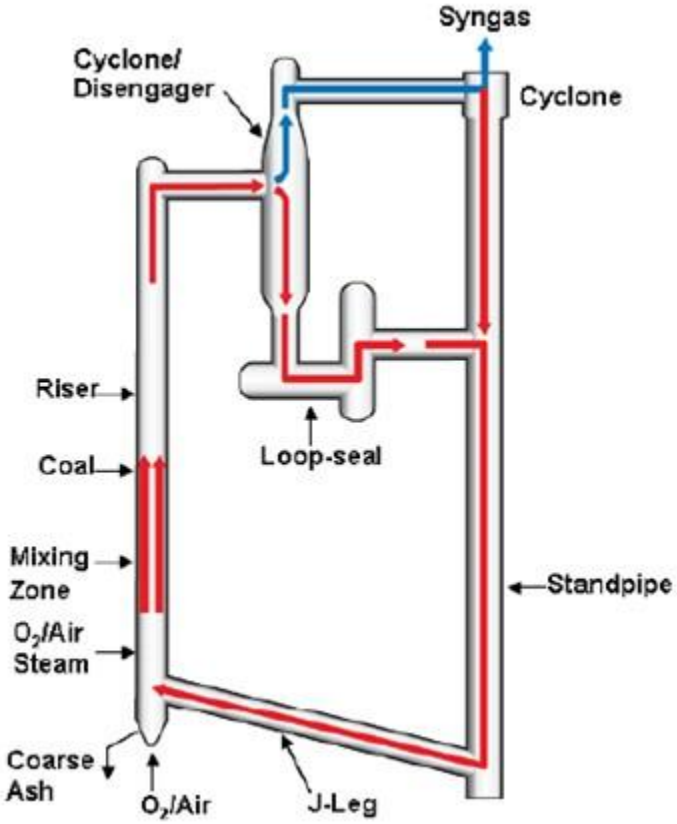

Figure 1.13 Kellogg Brown & Root (KBR) transport gasifier

Moving Bed Gasifier

In a moving-bed gasifier, steam and air/oxygen flow through a bed of solid fuel particles, as shown in Fig. 1.14. Fresh coal is fed from the top, while air or oxygen is injected from the bottom. This configuration, in which the steam and oxygen/air feed is counter-current to the coal feed, is referred to as an **"updraft"** or counter-current, moving-bed gasifier. The coal moves downward slowly: its residence time can reach up to 1 hour. The syngas exits from the upper part of the gasifier, while ash and unconverted char are removed from the bottom. The depth of the coal bed is kept constant by adding fresh coal from the top. Another configuration is the **"downdraft"** or co-current, moving-bed gasifier, where steam and air/oxygen are fed from the top, co-current to the coal feed.

A counter-current moving-bed gasifier can be divided into four zones (from top to bottom): (i) the drying/preheating zone, (ii) the devolatilization zone, (iii) the gasification zone, and (iv) the combustion zone. The coal in the top zone is dried/preheated by the hot gas that is flowing from the bottom. The coal then moves down to the devolatilization zone, where heat from the hot gas drives volatiles out of coal particles. Any remaining char is then reacted in the next zone: the gasification zone. Syngas produced by an updraft, moving-bed gasifier has high tar content because the tar released during the devolatilization process is carried away by the hot gas which is flowing up from gasification zone.

Ash can be removed from the bottom in the form of dry ash or slag. If dry ash is desired, the gasifier temperature is usually kept below ash fusion temperature (1300 °C or 2370 °F). Moving-bed gasifiers have the advantages of high carbon conversion efficiency, high thermal efficiency, and low exit gas temperature (450-600 °C or 840-1110 °F). However, a disadvantage is that they have low throughput (or gas yield).

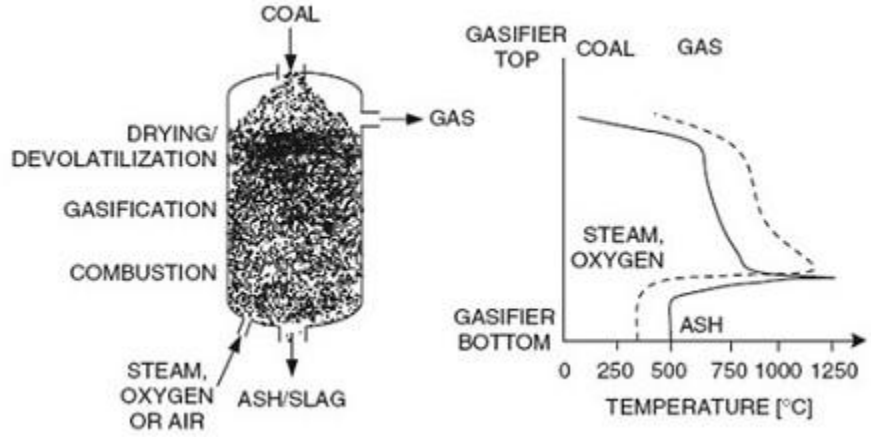

Figure 1.14 Schematic of a counter-current moving-bed gasifier

(Source: Enggcyclopedia, http://www.enggcyclopedia.com/2011/12/gasification-process-types/)

(i) Lurgi Gasifier

The Lurgi gasifier utilizes a bed of crushed coal moving downward through the reactor with a countercurrent flow of gas and operates at pressures of up to 450 PSI gauge (3100 kilopascals). Crushed coal, screened to remove fines, is fed to the top of the gasifier through a coal lock hopper and passes downward through the drying, pyrolysis, gasification, and combustion zones. Steam and oxygen are

admitted through a revolving grate at the bottom of the gasifier which also removes the ash produced. After a portion of the coal is burned to provide the heat required, the hot combustion gas passes upward through the zones of the coal bed. Steam is used as a reactant to gasify the coal and is also added to keep the temperature below the ash melting point. Although the predominant source of methane (CH_4) is devolatilization, some methane comes from coal hydrogenation. As the coal moves down through the gasifier, the temperature initially rises slowly. Further down in the gasifier, it rises dramatically as the coal approaches the combustion zone where the temperature exceeds 2200°F (1200°C). The Lurgi reactors commonly used are of the general type shown in Fig. 1.15. Because of the countercurrent flow in the gasifier, high carbon utilization and good heat recovery are obtained.

Figure 1.15 Schematic of the Lurgi pressure moving-bed gasifier (Source: DOE)

Table 1.3 Summary of coal gasifier comparisons

Gasifier Type	Fluidized-bed	Entrained-flow	Transport	Moving-bed
Process Description	Solid particle bed is fluidized by air and steam.	Solid particles are mixed thoroughly with air and steam and are entrained by the flow.	Circulating-bed reactor consist of mixing zone, riser, cyclones, and stand pipe	Coal is fed from top and moves down by gravity. Air and steam are injected from bottom.
Technology Providers	HTW, KRW	Shell,GE,Conoco-Phillips (E-Gas), Future Energy, sSiemens	Kellogg-Brown Root (KBR)	Lurgi
Fuel feed:				
Size	5-10mm	<100mm	< 400mm	5-50mm
Caking coal	Yes	No	Yes	Yes
Coal rank	Any	Dry feed -- any Slurry feed -- high rank	Any	Any
Operating issues:				
Syngas temperature	Moderate (1000 ºC)	High (1300-1600 ºC)	Moderate (1000 ºC)	Low (around 600 ºC)
Oxidant demand	Moderate	High	Moderate	Low
Steam demand	Moderate	Low	Moderate	High
Throughput	Low	High (residence time is 3-5 seconds)	High	Low (residence time is 30 minutes to 1 hour)
Feed rate	Low	High	High	Low

1.2.6 Mild Gasification

There are many terminologies to define the gasification rate: complete and partial gasification, and full and mild gasification. The definitions of completed gasification, partial gasification, and full gasification, mild gasification are as follows:

Complete gasification implies that all of the char is completely gasified, while a portion of the char remains unconverted for **partial gasification**. Again, these two approaches of gasification can be achieved by reacting the material at high temperature (>700^{o} C), without combustion, with a controlled amount of oxygen and/ or stream that thermally crack feedstock into lighter gases like CO, H_2, and CH_4.

The carbon conversion rate (CCR), also called carbon conversion efficiency, indicates the fraction of carbon reacted to describe the degree of gasification. CCR is defined as:

$$\mathrm{CCR} = \frac{\text{Amount of Carbon Reacted}}{\text{Amount of Total Carbon}} \tag{1.31}$$

Full and mild gasification represent the level (i.e., the products' molecular weight or average length of the molecular hydrocarbon chains) of the thermal cracking, which is typically affected by the temperature level and residence time of the reactions. Full gasification indicates that the feedstock goes though complete devolatilization, gasification, and thermal cracking into a composition of light species as the major combustible components of the syngas, such as: CO, H_2, and CH_4. Mild gasification preserves the heavier volatiles without further thermally cracking them into lighter components. To be specific, the operation of "**Mild Gasification**" refers to controlling the temperature and residence time to achieve varying levels of gasification between pyrolysis-only (0% gasification, volatiles left in original form) and full gasification (100% gasification, volatiles fully cracked).

There are two conceptual designs of Mild gasifier available: (a) the Wormser Mild gasifier and (b) the ECCC Mild gasifier. Explanations of each type are presented below.

1.2.6.1 Wormser Mild Gasifier

Figure 1.14 illustrates the Wormser mild gasifier that was designed by Alex Wormser (2008), Wormser Energy Solutions, Marblehead, MA, USA. Different from the full gasification process, mild gasification is a process of devolatilizing a heavily carbonaceous fuel (biomass, coal, petroleum bottoms, etc.) in an oxygen-deficient environment to create a fuel gas out of the volatile hydrocarbon components of the feedstock without thermally cracking further. The exit gas can be cleaned and used in a gas turbine to generate electricity, while the char is combusted in a conventional boiler to provide steam for power generation as well. The volatiles have an energy density about six times higher than fully-gasified syngas, so the required flow volume is much lower, resulting in smaller piping and a smaller clean-up system. Since no additional energy is needed to fully gasify the volatiles, the mild-gasification process requires less energy and thus less air for combustion than full gasification. This means that the Wormser mild gasifier is about $1/3^{rd}$ the size of a full gasifier with a corresponding decrease in capital cost. By retaining the largest hydrocarbon molecules possible without risking condensation of the tars on the clean-up equipment, the heating value of the syngas is higher than that of an air-blown full gasification cycle. Along with allowing the size of all the clean-up equipment to be smaller, the higher heating value also makes it easier for the plant operator to select a gas turbine capable of using this fuel.

Fig. 1.16 is one conceptual design of a mild gasifier that contains the following: an inlet tube, burners, draft tube, deflector, distributor, char exit, syngas cooler, syngas exit, and fluidized bed. Feedstock, such as coal, is injected from the bottom of the draft tube via the inlet tube. As soon as the coal is introduced into the draft tube, it will be instantly heated and pyrolyzed by the char circulating in the draft tube. The char leaving the draft tube is diverted into the fluidized bed by the deflector. In this particular design, steam and air are introduced into the bed to fluidize it and to provide reactants for some limited gasification reactions. While the feedstock is not fully gasified, some of the carbon is converted to CO and CO_2 to provide the heat necessary for devolatilization. A burner is located blow the draft tube, and recycled syngas is the primary source of heat for the draft tube. The syngas exits from the top of the gasifier, while the excess char is removed from the bottom to maintain a controlled bed level of char. While this example uses gasification reactions to generate some of the heat necessary, it is important to remember that no chemical reactions need to take place to achieve purely mild gasification (0% cracking/pyrolysis-only). As long as a heat source is present, the coal volatiles will boil off and generate the syngas.

The concept of mild gasification can enable existing coal power plants nearing the end of their service life to be retrofitted with a mild gasifier and gas turbine to increase their efficiency by up to 18 percentage points (50% more) while decreasing emissions. By retrofitting old plants we can increase power on the grid and decrease harmful emissions [Wormser, 2008].

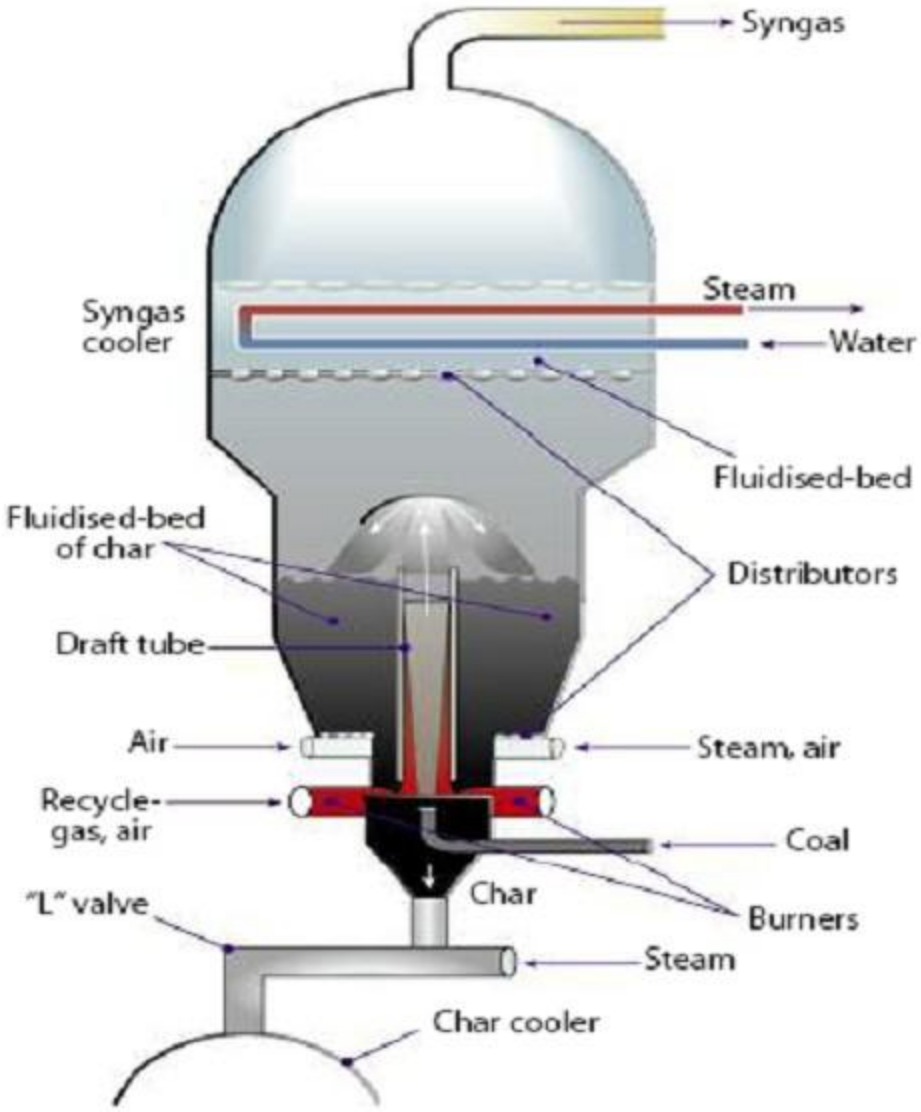

Figure 1.16 Schematic diagram of a Mild Gasifier [Wormser (2008)]

1.2.6.2 Introduction of IMGCC System

Following the similar concept introduced by Wormser's MaGIC, Khan and Wang (2011) introduced the concept of the Integrated Mild Gasification Combined Cycle (IMGCC). In a MaGIC system, the gasifier is operated air-blown without using an air separation unit (ASU). The advantages of not using an ASU are significantly reduced capital and O&M (operation and maintenance) costs, as well as energy savings related to work input. The disadvantages are lower syngas HHV and the requirement of relatively bigger gas clean-up system and gasifier. The concept of IMGCC actually expands MaGIC's

concept to including usage of an ASU. It is necessary to note that IMGCC is not similar to conventional partial gasification systems, which usually employ a carbonator to produce char, but require an extra amount of energy to thermally crack the volatiles into lighter gases. Rather it keeps the higher energy density volatiles in order to use them in gas turbines. Besides saving energy, there are several advantages for employing syngas produced from an IMGCC system. First, the syngas produced by the mild gasification process contains approximately 6 times more energy per unit mass than fully-gasified syngas. The sizes of mild gasifiers and their cleaning systems can be shrunk down by around 80% compared to ordinary gasifiers. Eventually, unconverted char from the mild gasifier can be used in the boiler of a conventional pulverized coal (PC) power plant with negligible sulfur or pollutant content (Fig.1.17). All of these advantages hint at the reasonable possibility of using IMGCC technology to retrofit existing coal-fired power plants by replacing the coal feedstock with char produced by a mild gasifier.

On the other hand, syngas goes though the gas cleaning system before it is burned in the gas turbine combustor. In a traditional IGCC or other combined cycle, the exhaust of the gas turbine is used to produce high temperature steam via an HRSG, and the steam is then routed to steam turbines to generate more electricity. In an IMGCC system, however, the steam produced by the HRSG is mixed with the steam produced by the boiler of the existing PC plant. Such a retrofit can significantly increase the plant efficiency from about 30% to 50% on a Higher Heating Value (HHV) basis as well as drastically reduce the emissions per kW output. In an IMGCC system, the syngas can be cleaned before combustion more economically than is possible for a traditional PC plant, which cleans the flue gases after combustion, due to the lower volume flow rate of the mildly-gasified syngas. In addition, the scrubber of the original PC plant could be removed to reduce the existing PC plant’s operating and maintenance (O&M) costs.

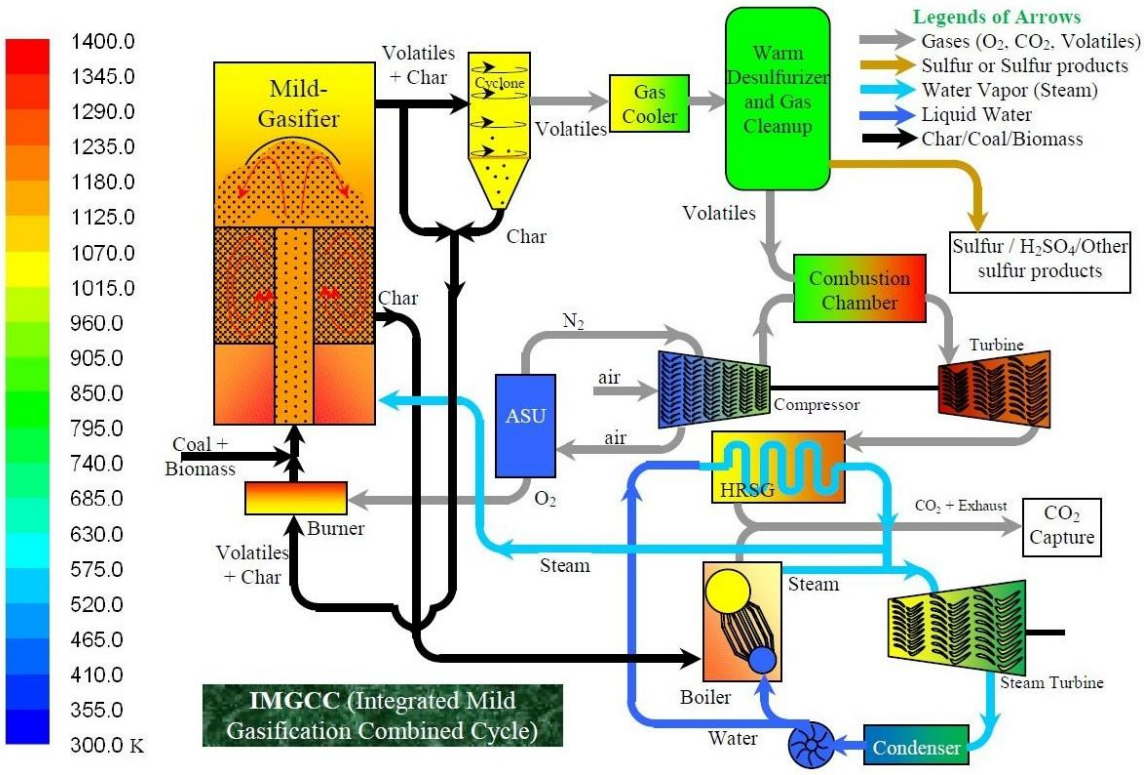

Figure 1.17 Schematic Diagram of an Integrated Mild Gasification Combine Cycle (IMGCC) System

1.2.6.3 ECCC Mild Gasifier

Figure 1.18 presents an illustration of the Energy Conversion and Conversion Center (ECCC) mild gasifier, designed by the ECCC team (2009), University of New Orleans, LA, USA. ECCC's mild gasifier is a conceptual design of mild gasifier based on the principle of Wormser's mild gasifier (2008).

The conceptual design of the ECCC mild gasifier contains the following components: a coal inlet tube, fluidization air inlet, combustion inlet, draft tube, deflector, char outlet, heat exchanger, syngas exit, recycled syngas exit, fluidized bed for char, and T-handle. Coal is introduced into the base of the draft tube via the coal inlet hose that is threaded into the coal inlet tube. Here it mixes with the combustion products and undergoes devolatilization. Once it leaves the draft tube, the flow rides along the deflector, depositing the char into the fluidized bed. Fluidization gases are blown into a plenum via two rectangular flanged ducts. The top of the plenum is screened, allowing the fluidization air to enter the bed. Note that the grate has two distinct geometries: the planar region closest to the outer wall of the

gasifier that fluidizes the outer portion of the bed and the conical region resembling a sump that will fluidize the innermost part of the bed. Once in the bed, char will be agitated with fluidization action until it is entrained out of the bed by one of the char outlet ducts on either side of the gasifier outer wall.

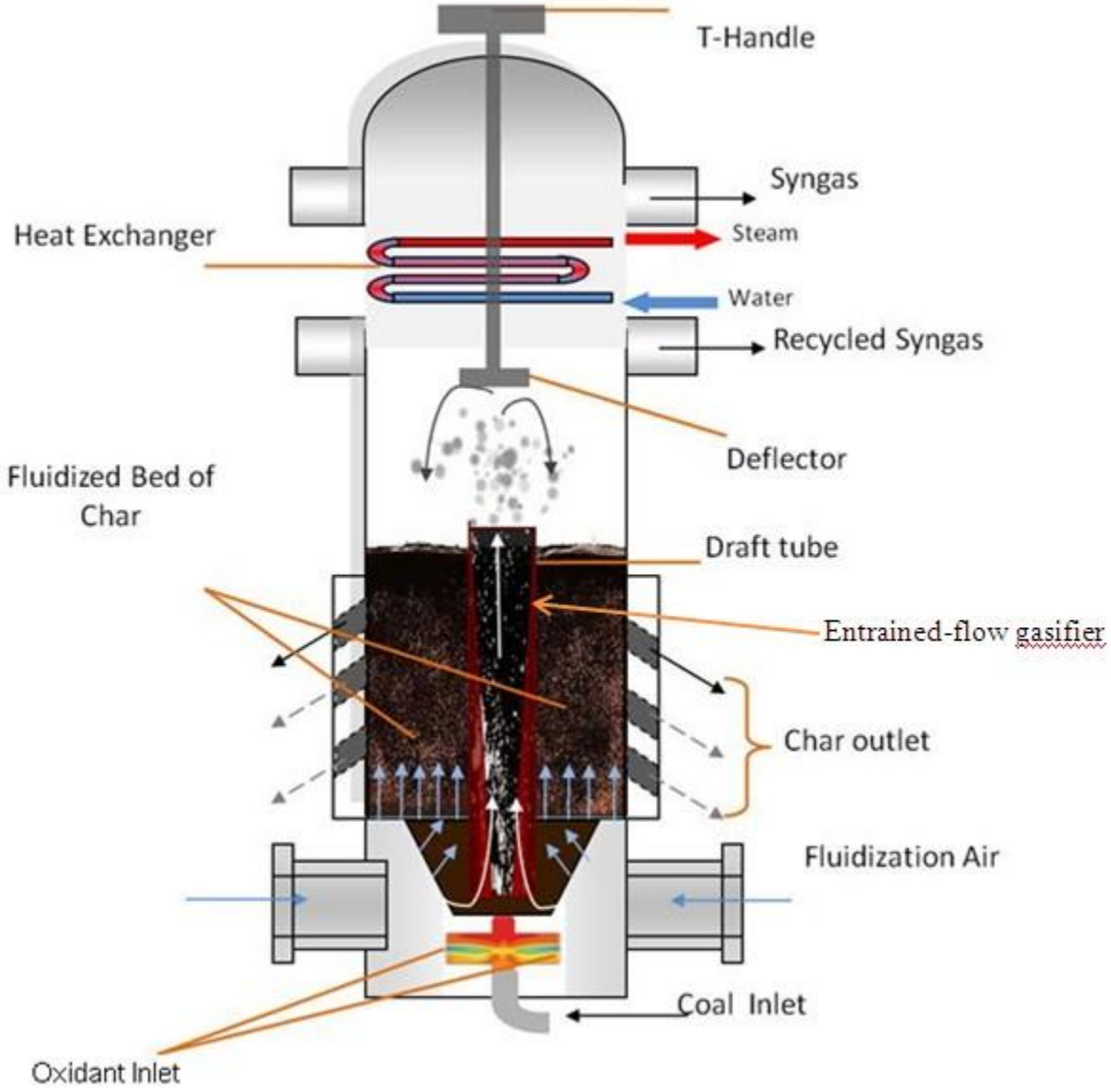

Figure 1.18 Schematic diagram of the cold-flow model of the ECCC Mild Gasifier

1.3 Motivation and Objectives

From the literature review, it is clear that there are many factors that affect the performance, efficiency, and reliability of the exiting coal-fired power plants. The Integrated Mild Gasification Combined Cycle (IMGCC) technology seems technically, financially, and politically attractive to retrofitting old, inefficient, and dirty Pulverized Coal (PC) plants with fewer issues than building a full-blown IGCC plant. Since the IMGCC technology is still at the conceptual level, both Wormser's mild and the ECCC's hybrid gasifiers are not proven technologies. The ECCC team is currently using both experimentation and computer modeling to optimize its mild gasifier design. The ECCC team has designed a cold flow apparatus for observing the flow behavior under different conditions to validate the CFD results. Mazumder and Wang (2011) introduced a numerical model to simulate the coal gasification process inside a 2-D ECCC mild gasifier. They carried out heterogeneous and homogeneous reactions throughout the coal gasification process. Their results gave an overall view of how coal gasification works in a mild gasifier, but the devolatilization process was not incorporated. Later, Khan and Wang (2011) improved this model by incorporating a multiphase devolatilization process, which was and is still not available in the commercial multiphase Eulerian-Eulerian method. In their simulations, the fluidized bed couldn’t be sustained and was blown away quickly. Considering the above development status, hereby, the objective of this study is to extend the current computational domain from 2-D to 3-D and perform a comprehensive parametric investigation to further improve the ongoing design of the ECCC mild gasifier and help determine the appropriate operation conditions through the following tasks:

1. Incorporate the coal devolatilization model into the multiphase Eulerian-Eulerian method.

2. Investigate the effects of fluidization velocity on the mixing pattern in the fluidized bed as well as on the sustainability of the fluidized bed depth.

3. Investigate the thermo-flow behavior and gasification process under different designs of the coal feeding port, char chute, and deflector geometry.

4. Use CFD to design the size of the draft tube by investigating the effect of injection speeds of coal and entrained hot gases on the devolatilization process in the draft tube.

5. Investigate the operating conditions for achieving mild gasification.

6. Expand the 2-D multiphase model to 3-D and compare the differences in operating conditions between the 2-D and 3-D models.

CHAPTER TWO
CFD FORMULATION AND THEORY

2.1 Problem Statement

A Computational Fluid Dynamics (CFD) simulation is an economical and effective tool to study coal gasification. A 2-D, multiphase, reactive model was established by Mazumder and Wang (2010) to simulate the ECCC mild gasifier. In that model, the volatiles were provided as a part of the coal but were injected to the gasifier as independent components by assuming that the volatiles are outside the coal, i.e. no devolatilization process was modeled. In this study, the devolatilization process is to be implemented and the model is to be expanded to 3-D. Coal gasification is a multiphase, reactive flow phenomenon. It is a multiphase problem between gases and coal particles and is also a reactive flow, which involves homogeneous reactions among gases and heterogeneous reactions between coal particles and gases. The Eulerian-Eulerian method is adopted in this study because the concentrations of coal particles are dense in the fluidized bed, and tracing each particle with the Lagrangian method is not realistic. Although, inside the draft tube, the conditions are similar to an entrained bed gasifier, so the Lagrangian-Eulerian method could be used here. However, since the Lagrangian-Eulerian method can't be used to obtain a solution within the fluidized bed, while Eulerian-Eulerian can be used in both the entrained bed and fluidized bed portions of the gasifier, the Eulerian-Eulearian method is adopted in this study. This means that both the gas phase (primary phase) and the coal phase (secondary phase) are solved by using the Eulerian method.

In the fluidized bed portion, all of the solid particles are placed side by side inside the gasifier like a bed of granular material, and the gas mixture is passed up through this bed, converting this granular material from a static, solid-like state to a dynamic, fluid-like state. This process is known as "fluidization." In the draft tube, on the other hand, the coal phase is transported by hot gases (either air or carbon-dioxide and water vapor), absorbing heat from the hot gases and releasing the volatiles and water vapor into gas phases. This is how the devolatilization and demoisturization processes are to be modeled in this study. The gasification process involves both homogeneous (gas-gas) reactions and heterogeneous (gas-solid) reactions.

2.1.1 ECCC Mild Gasifier Design Consideration

One of the objectives of this study is to use CFD to guide the modification of the existing design of the ECCC mild gasifier. In the previous study (Mazumdar and Wang, 2011), only full gasification was simulated. In this study, the focus is placed on meticulously controlling the particle residence time to achieve various degrees of mild gasification. The CFD simulation can be very helpful in monitoring the syngas composition information at each incremental time step at any location in the gasifier. By using the existing design, the height of the mild gasifier is fixed at 33.75 inches (86cm); however, the particle velocity and gasifier power (i.e. the total energy of the coal fed into the gasifier per unit time, MW) could vary with different geometric designs of the inlets for fuel and combusted gas injections. The exact power generation of this mild gasifier is not fixed in this study, since the mass flow rate could vary by changing fuel injection velocity and injection area as expressed in Eq. 2a:

$$\dot{m}_{coal} = \rho_{coal} \times V_{coal} \times A \times \varepsilon \qquad (2a)$$

where: ρ_{coal} = 916 kg/m^3, A= π (D/2)^2,
the bulk coal velocity V_{coal} = (height of mild gasifier / particle residence time), and
ε = volume fraction of the coal particles.

The rated power of the mild gasifier is defined as the energy contained in the coal fed into the gasifier per unit time, which can be calculated by Eq. 2b:

$$\text{Rated Power} = \dot{m}_{coal} \times HV_{coal} \qquad (2b)$$

The coal heating value could be obtained from the coal supplier: 23.8 MJ/kg is used here. The initial residence time is set as 3 seconds. This residence time will be revised by examining the syngas composition at the gasifier exit. With the initial particle residence time being selected as 3 seconds, many parameters could be then selected accordingly for a preliminary design of the mild gasifier.

The ECCC mild gasifier is designed to remove accumulated char from the gasifier to the boiler for the steam cycle through the char chutes; however, the 2-D study from Khan and Wang (2011)

shows that the char is removed too fast through the char chute, so the height of fluidized bed can't be maintained. This problem is caused by simulating a 3-D gasifier with a simplified, 2-D geometry. In a 2-D model, the geometry does not represent all of the characteristics of the actual 3-D gasifier unless all of the inlets and outlets are axisymmetrically placed. For example, if a circular pipe in a 3-D configuration is represented as an opening with a width having the same dimension as the pipe diameter in 2-D, then this opening actually represents a rectangular slot which occupies a larger percentage of area than the circular cross-section does in the 3-D configuration. Under this circumstance, the 2-D computation will over-predict the char removal rate through the char chute. In order to solve this problem, the pressure at the char chutes is intentionally increased to reduce the char removal rate. But, the next question is "What is the appropriate pressure that should be assigned at the char chute exit?" To answer this question, the physics of char removal mechanisms need to be examined. Since the char is removed through gravity, the reference char chute exit pressure is then calculated as:

$$P_{coal} = \frac{F_{coal\ gravity\ force}}{A_{contact\ area}} \tag{2c}$$

This equation yields the equivalent hydraulic pressure of a single coal particle as: $P_{coal} = 3.27$ Pascals. The total number of coal particles stacked up in the char outlets is calculated to be 152.4 based on the following Eq. (2d):

$$N = \frac{vertical\ lenght\ of\ char\ chute\ exit}{diameter\ of\ single\ coal\ particle} = \frac{L \times \sin\theta}{D_{coal\ particle}} \tag{2d}$$

where L is the length of the char chute, and θ is the angle between gasifier outside wall and the char chute pipe.

Thus, the total pressure that should be assigned to each char outlet is equal to 3.27 Pascals times 152.4, which is equal to 498.3 Pascals.

2.1.2 Description of Modified 2-D Gasifier Geometry

This study modifies the preliminary mild gasifier configuration used in the previous study of Mazumder and Wang (2011) with the following changes:

1. Change the shape of the deflector from a flat plate to an arc.
2. Adjust the diameters of the coal inlet and syngas outlets.

Due to the complexity of this simulation, this study is conducted progressively following the sequence below:

1. Two-dimensional multiphase flow with thermal-flow behavior only (without reactions)
2. Two-dimensional multiphase flow with reactive thermal-flow behavior (complete simulation)
3. Three-dimensional multiphase flow with thermal-flow behavior only (without reactions)
4. Three- dimensional multiphase flow with reactive thermal-flow behavior (complete simulation.)

To save computational time, the modified 2-D geometry (Fig. 2.1) is employed first. The reasons to make such a modification are:

1. In the previous 2-D design, coal particles unrealistically fell through the perforated openings with a diameter less than the coal particle diameter due to the adoption of the volume fraction method, which does not actually simulate the true particles. In order to resolve this problem, the bottom boundary of the computational domain is moved from the actual gasifier's outer casing to the perforated plate surface. By doing this, two fluidization air inlet zones are outside the computational domain. Since this study is focused on reaction areas inside the gasifier, rather than on studying the fluidization air flow before it enters the fluidized bed, this modification is justified.
2. The previous 2-D design had a flat deflector. This study shows that the char accumulates on top of it. Making the deflector as an arc resolves the problem.

3. The entraining openings between the draft tube and the fluidized bed are closed because it was found by Khan and Wang (2011) that the fluidized bed is blown away by the strong flow coming from the draft tube through these entraining openings.
4. The majority of the char has been shown being blown away from the fluidization zone due to the high fluidization velocity. To resolve this issue, the diameter of the syngas outlet duct is reduced from 5 inches to 2.5 inches, and the draft tube diameter is also reduced from 2 inches to 1 inch.

2.1.3 Description of the Simulated 2-D Mild Gasifier Geometry

The central-plane geometry of the 2-D Mild Gasifier used in the simulation is shown in Fig. 2.1. The height and width of the bench-top mild gasifier is 33.75 inches (86 cm) and 18 inches (45.75 cm), respectively. In total, there are three velocity inlets: one for coal at the bottom of the draft tube and two for the hot combusted gases. At each side of fluidization zone, four holes are arranged at the horizontal perforated plate inlet, 0.15 inches in diameter (0.38 cm) each, and ten holes are arranged on the inclined perforated surface with an inlet width of 0.15 inches (0.38 cm) each. There are four outlets: two for the char and two for the produced syngas. The width of the left and right horizontal syngas outlets are 2.5 inches (6.35 cm), and the width of the char outlets are 1.75 inches (0.15 cm), which are all inclined 45 degrees. A draft tube is designated with a 4-inch (10.15 cm) width to provide a passage for the entrained coal, and to separate it from the devolatilized coal (char). The heat in the hot air or combusted gases in the draft tube is transferred to the fluidized bed through the draft tube wall. Above the draft tube, an arched deflector with an 8-inch horizontal width is installed to block the particles from being entrained out of the gasifier with the gases. Coal and combusted gases enter the draft tube through the draft tube's bottom inlet. They mix and drive out the volatiles during the journey upward through the draft tube. Fluidization air goes through the 28 holes in the perforated plates.

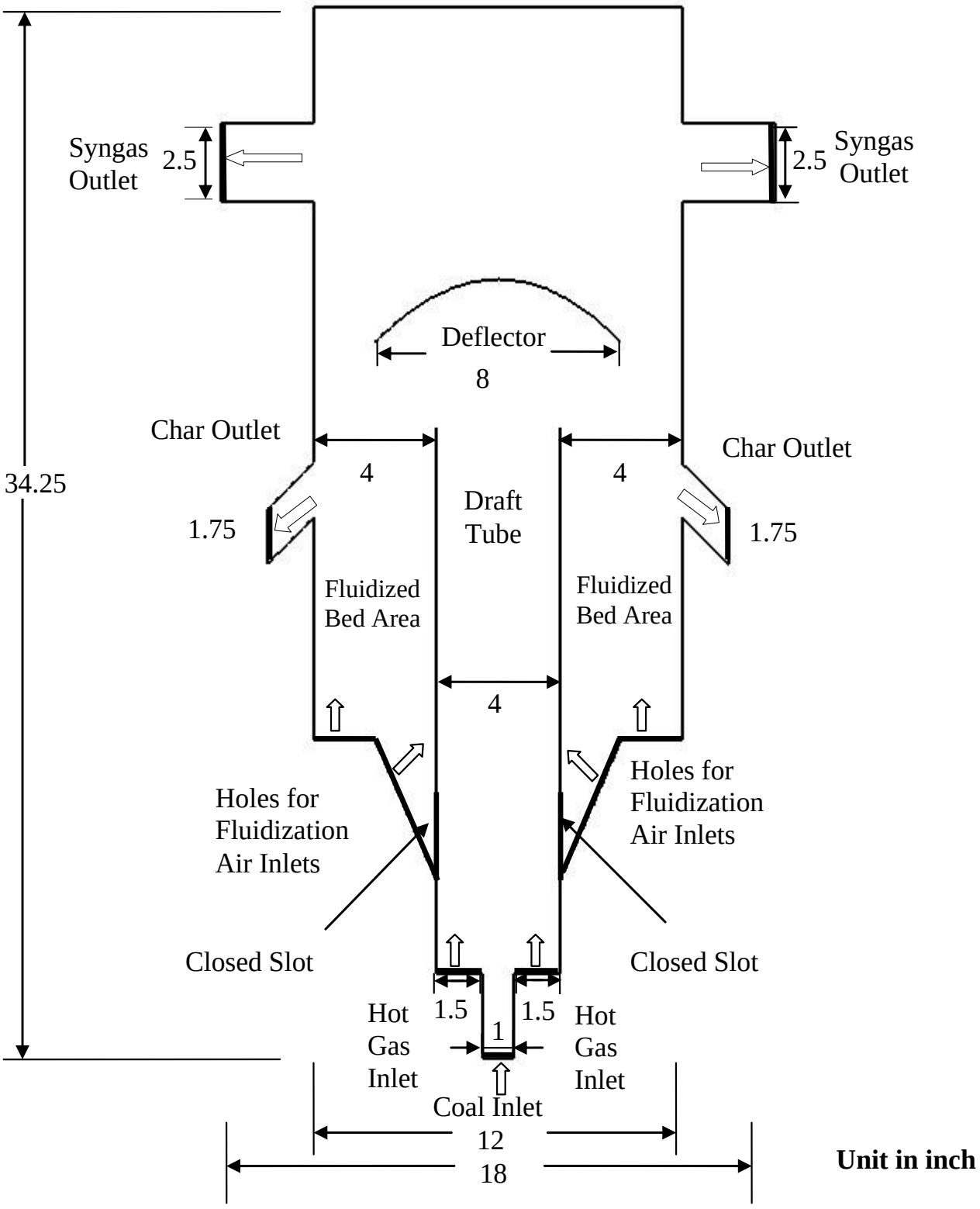

Figure 2.1 Schematic of the 2-D Mild Gasifier

2.1.4 Description of the Simulated 3-D Mild Gasifier Geometry

The design for the 3-D mild gasifier is shown in Fig. 2.2. The height of the gasifier is 33.75 inches (85.73cm). There are four outlets, two for the char and two for the syngas. The area of char outlet is 2.4 in^2(15.48 cm^2) and is inclined 45 degrees, and the syngas outlet is 12.56 $inch^2$ (81.03 cm^2). Also, there are three types of velocity inlets. The first type has a diameter of 2 inches (5.08 cm), is located on the bottom of the draft tube, and is used for coal injection. The second type of inlet is designed for the hot (or combusted) gases with an annular passage surrounding the central pipe. These hot gases provide the energy needed for driving devolatilization and mild gasification. The outside diameter of the annular passage is 4 inches (10.16 cm). Coal is transported by warm gases at 500K to the center pipe and is entrained by hot gases from the annular passage with a temperature 1600K into the mild gasifier. The third type of inlet, consisting of horizontal and inclined perforated plates, is used for providing fluidization gas. The horizontal perforated plate is simplified as eight opening slots shaped as echelons, with an area of 4.28 square inches each (the outer side is 3.09 inches wide, the inner side is 2.08 inches wide, and the radial distance is 1.63 inches). On the inclined perforated surface, there are eighty-four holes with an area of 0.0175 in^2 (0.1129 cm^2 or 0.15 inches in diameter) each.

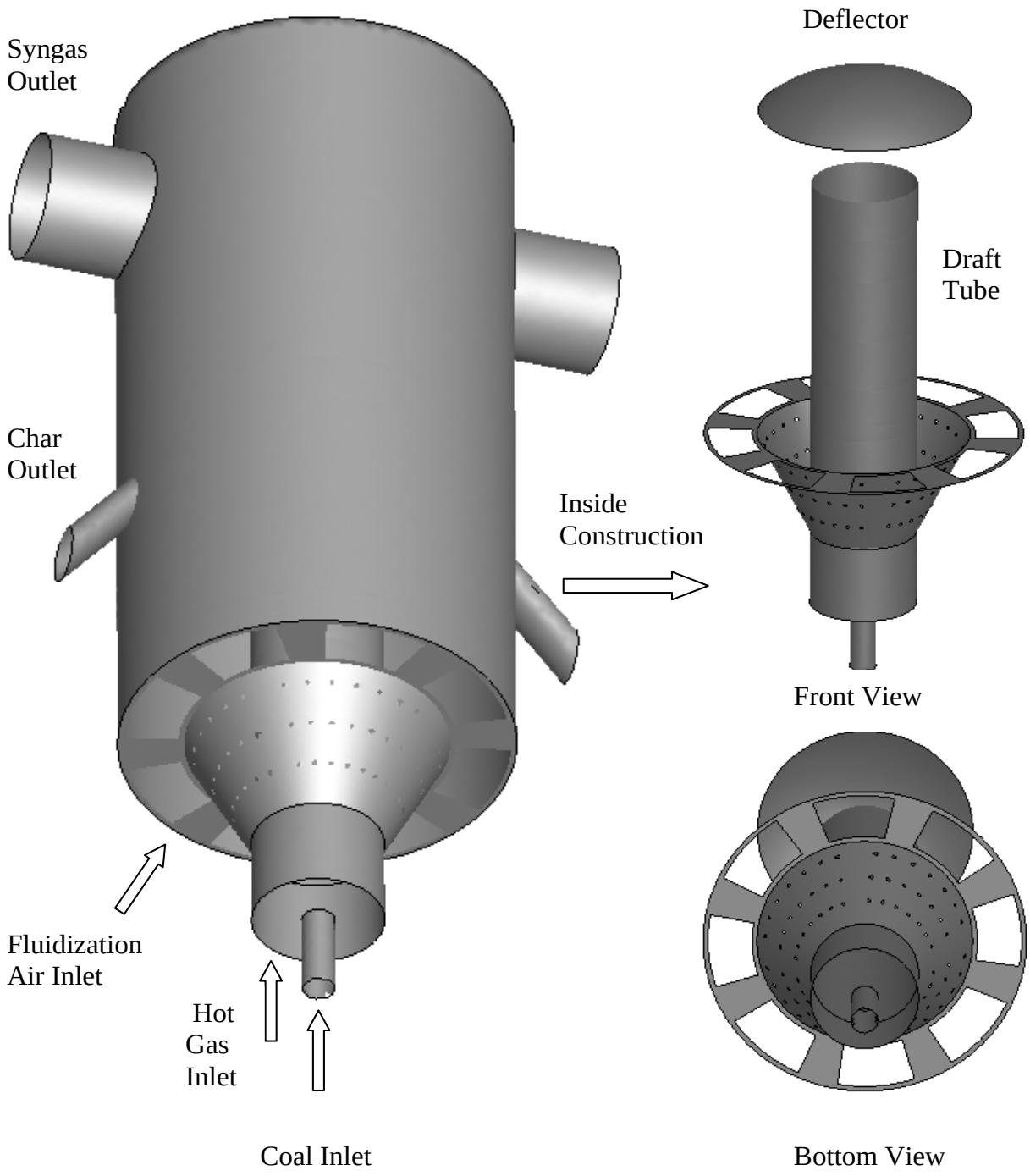

Figure 2.2 Schematic of the 3-D simulated mild gasifier

2.2 Computational Model

2.2.1 Physical Characteristics of the Problem

The physical characteristics of the problem are modeled as follows:

1. The flow inside the 2-D domain is incompressible and turbulent.
2. The flow inside the 3-D domain is incompressible and turbulent.
3. The gravitational force is considered.
4. All gas species involved in this study are Newtonian fluids with variable properties as functions of temperature. These variable properties are calculated by using a piecewise-polynomial method.
5. A mass-weighted mixing law for specific heat and a User Define Function for density are used for the coal and gas mixture phase species.
6. The walls are impermeable and adiabatic.
7. The flow is unsteady for both 2-D and 3-D multiphase cases.
8. The no-slip condition (zero velocity) is imposed on all wall surfaces.

2.2.2 General Governing Equations

As mentioned earlier, the Eulerian-Eulerian method is adopted for both 2-D and 3-D cases. In the Eulerian method for the gas phase (primary phase), mass conservation, energy conservation, and Navier-Stokes equations are solved in 2-D and 3-D cases. The governing equations for the conservations of mass, momentum, and energy based on Reynolds Averaged N-S equations with turbulent stress and heat flux terms are given as:

$$\frac{\partial \rho}{\partial t} + \frac{\partial}{\partial x_i}(\rho u_{ij}) = 0 \qquad (2.1)$$

$$\frac{\partial}{\partial t}(\rho u_i) + \frac{\partial}{\partial x_i}(\rho u_i u_j) = -\frac{\partial p}{\partial x_j} + \frac{\partial}{\partial x_i}(\tau - \rho\overline{u_i' u_j'}) + \rho \vec{g}_j + \vec{F}_j \qquad (2.2)$$

$$\frac{\partial}{\partial t}(\rho E)+\nabla\bullet\left(\vec{V}(\rho E+p)\right)=\nabla\bullet\left(k_{eff}\nabla T-\sum_j h_j\vec{J}_j+\left(\overline{\overline{\tau}}_{eff}\bullet\vec{v}\right)\right)+S_h \tag{2.3}$$

As the momentum equations are solved with the complete Navier-Stokes equations, so, $\overline{\overline{\tau}}$, the stress tensor is given by,

$$\overline{\overline{\tau}}=\mu\left[\left(\nabla\vec{v}+\nabla\vec{v}^T\right)-\frac{2}{3}\nabla\bullet\vec{v}\bullet I\right] \tag{2.4}$$

Where μ is the molecular dynamic viscosity, I is the unit tensor, and the second term on the right-hand side is the effect of volume dilatation.

The first three terms on the right-hand side of equation (2.3) represent heat transfer due to conduction, species transport, and viscous dissipation. S_h is a source term including the enthalpy formation from the chemical reaction of the species. The energy E is defined as

$$E=h-\frac{p}{\rho}+\frac{v^2}{2} \tag{2.5}$$

Where h is the sensible enthalpy and for incompressible flow and is given as

$$h=\sum_j Y_j h_j+\frac{p}{\rho} \tag{2.6}$$

Y_j is the mass fraction of species j and

$$h_j=\int_{T_{ref}}^{T} c_{p,j}dT \tag{2.7}$$

T_{ref} is the reference temperature, taken as 298.15 K

$\vec{J}_j$ is the diffusion flux of species j.

k_{eff} in Eq. (2.3) is the effective conductivity, consisting of molecular conductivity and turbulent conductivity. For the standard k-ε models, the effective thermal conductivity is given as bellow as,

$$k_{\text{eff}} = k + \frac{c_p \, \mu_t}{\text{Pr}_t}$$

Where k is molecular thermal conductivity, Pr_t is turbulent Prandtl number as 0.85, μ_t is turbulent viscosity.

The term $(\tau_{ij})_{eff}$ in Eq. (2.3) is deviatoric stress tensor and defined as:

$$(\tau_{ij})_{eff} = \mu_{eff} \left(\frac{\partial u_j}{\partial x_i} + \frac{\partial u_i}{\partial x_j} \right) - \frac{2}{3} \mu_{eff} \frac{\partial u_k}{\partial x_k} \delta_{ij}$$

2.2.3 Turbulence Model

The velocity field in turbulent flows keeps fluctuating. Therefore, the transported quantities such as momentum, energy, and species concentration are fluctuating too. The fluctuations can be small scale and high frequency, and it is unrealistic and expensive to capture such variances by direct computational simulation. The way to handle this problem is to set up a group of modified equations that take less computational time to solve and can be achieved by replacing the instantaneous governing equations with their time-averaged, ensemble-averaged, or otherwise manipulated counterparts to remove the small time scales. Such modifications of the instantaneous governing equations, however, bring in new unknown variables. Many turbulence models have been developed to determine these new unknown variables (such as Reynolds stresses or higher order terms) in terms of known variables or low order terms. Namely, this is the "closure" problem of the turbulence models.

General turbulence models widely available are:

a. Spalart-Allmaras (one equation)

b. k-ε models (two equation)
    i. Standard k-ε model
    ii. RNG k-ε model
    iii. Realizable k-ε model
c. k-ω models (two equation)
    i. Standard k-ω model
    ii. Shear-stress transport (SST) k-ω model
d. Reynolds Stress model (five equation)

2.2.3.1 Standard k-ε Model

The standard k-ε model is employed in this study to simulate the turbulent flow due to its suitability and robustness for a wide range of wall-bounded and free-shear flows. The standard k-ε model is the simplest of the turbulence two-equation models in which the solution of two separate transport equations allows the turbulent velocity and length scales, which are to be independently determined, to be found. The k-ε model is a semi-empirical model with several constants, which were obtained from experiments.

All three of the k-ε models have similar forms with major differences in the method of calculating the turbulent viscosity, the turbulent Prandtl numbers, and the generation and destruction terms in the k-ε equations.

The standard k-ε model is based on the model transport equations for the turbulence kinetic energy (k) and its dissipation rate (ε). The model transport equation for (k) is derived from the exact equation, while the model transport equation for (ε) is obtained using physical reasoning and bears little resemblance to its mathematically exact counterpart.

The turbulence kinetic energy (k), and its rate of dissipation (ε), are obtained from the following transport equations,

$$\frac{\partial}{\partial t}(\rho k)+\frac{\partial}{\partial x_i}(\rho k u_i)=\frac{\partial}{\partial x_j}\left[\left(\mu+\frac{\mu_t}{\sigma_k}\right)\frac{\partial k}{\partial x_j}\right]+G_k+G_b-\rho\varepsilon-Y_M+S_k \tag{2.8}$$

$$\frac{\partial}{\partial t}(\rho \varepsilon)+\frac{\partial}{\partial x_i}(\rho \varepsilon u_i)=\frac{\partial}{\partial x_j}\left[\left(\mu+\frac{\mu_t}{\sigma_\varepsilon}\right)\frac{\partial \varepsilon}{\partial x_j}\right]+C_{1\varepsilon}\frac{\varepsilon}{k}(G_k+C_{3\varepsilon}G_b)-C_{2\varepsilon}\rho\frac{\varepsilon^2}{k}+S_\varepsilon \tag{2.9}$$

In equations (2.8) and (2.9), G_k represents the generation of turbulence kinetic energy due to the mean velocity gradients and the Reynolds stress, calculated as

$$G_k=-\rho\overline{u_i' u_j'}\frac{\partial u_j}{\partial x_i} \tag{2.10}$$

G_b represents the generation of turbulence kinetic energy due to buoyancy, calculated as following,

$$G_b=\beta g_i\frac{\mu_t}{Pr_t}\frac{\partial T}{\partial x_i} \tag{2.11}$$

Pr_t is the turbulent Prandtl number and g_i is the component of the gravitational vector in the i-th direction. For standard k-ε model the value for Pr_t is set 0.85 in this study.
β is the coefficient of thermal expansion and is given as

$$\beta=-\frac{1}{\rho}\left(\frac{\partial \rho}{\partial T}\right)_P \tag{2.12}$$

Y_M represents the contribution of the fluctuating dilatation in compressible turbulence to the overall dissipation rate, and is defined as

$$Y_M=2\rho\varepsilon M_t^2 \tag{2.13}$$

Where M_t is the turbulent Mach number which is defined as

$$M = \sqrt{\frac{k}{a^2}} \tag{2.14}$$

Where a $\left(\equiv \sqrt{\gamma RT}\right)$ is the speed of sound.

The turbulent (or eddy) viscosity, μ_t, is computed by combining k and ε as

$$\mu_t = \rho C_\mu \frac{k^2}{\varepsilon} \tag{2.15}$$

$C_{1\varepsilon}$, $C_{2\varepsilon}$, C_μ, σ_k and σ_ε are constants and have the following values
$C_{1\varepsilon} = 1.44$, $C_{2\varepsilon} = 1.92$, $C_\mu = 0.09$, $\sigma_k = 1.0$, and $\sigma_\varepsilon = 1.3$

These constant values have been determined from experiments using air and water for fundamental turbulent shear flows including homogeneous shear flows and decaying isotropic grid turbulence. They have been found to work fairly well for a wide range of wall-bounded and free-shear flows. The initial value for k and ε at the inlets and outlets are set as 1 m^2/s^2 and 1 m^2/s^3 respectively.

In general, turbulent flows are significantly affected by the presence of walls. Very close to the wall, viscous damping reduces the tangential velocity fluctuations. Usually, kinematic blocking reduces the normal fluctuations. Away from the wall, however, the turbulence is increased by the production of turbulence kinetic energy. In the near-wall region, the solution variables have large gradients, and the momentum and other scalar transports strongly occur. Therefore, accurate representation of the flow in the near-wall region is required for successful predictions of wall-bounded turbulent flows.

The k-ε turbulence model used in this study is primarily valid for turbulent core flows (i.e., the flow in the regions somewhat far from walls). Wall functions are used to make this turbulence model suitable for wall-bounded flows. Wall functions are a collection of semi-empirical formulas and functions that link the solution variables at the near-wall cells to the corresponding quantities on the wall. The wall functions consist of the following:

- ✓ Laws of the wall for mean velocity and temperature (or other scalars)
- ✓ Equations for near-wall turbulent quantities

2.2.3.1.1 Standard Wall Function

The law-of-the-wall for mean velocity gives

$$U^{+} = \frac{1}{\kappa}\ln\left(Ey^{+}\right) \tag{2.16}$$

Where,

$$U^{+} \equiv \frac{U_P C_\mu^{0.25} k_P^{0.5}}{\frac{\tau_w}{\rho}} \tag{2.17}$$

$$y^{+} \equiv \frac{\rho C_\mu^{0.25} k_P^{0.5} y_P}{\mu} \tag{2.18}$$

And

κ = von Karman constant (= 0.42)

E = empirical constant (= 9.793)

U_P = mean velocity of the fluid at point P

k_P = turbulence kinetic energy at point P

y_P = distance from point P to the wall

μ= dynamic viscosity of the fluid

The logarithmic law for mean velocity is valid for y^{+} > about 30 to 60

The wall function for the temperature is given as,

$$T^{+} \equiv \frac{\left(T_w - T_P\right)\rho c_p C_\mu^{0.25} k_P^{0.5}}{q''} = Pry^{+} + 0.5\rho.5\,\frac{C_\mu^{0.25} k_P^{0.5}}{q''} U_P^2 \qquad \left(y^{+} < y_T^{+}\right) \tag{2.19}$$

Or,

$$T^+ = Pr_t\left[\frac{1}{\kappa}\ln\left(Ey^+\right)+P\right]+0.5\rho\frac{C_\mu^{0.25}k_P^{0.5}}{q''}\left[Pr_t\,U_P^2+\left(Pr-Pr_t\right)U_c^2\right] \qquad \left(y^+ > y_T^+\right) \tag{2.20}$$

Where, P is given as

$$P = 9.24\left[\left(\frac{Pr}{Pr_t}\right)^{3/4}-1\right]\cdot\left[1+0.28e^{-0.007Pr/Pr_t}\right] \tag{2.21}$$

k_f = thermal conductivity of the fluid

ρ = density of fluid

cP = specific heat of fluid

q" = wall heat flux

T_P = temperature at the cell adjacent to the wall

T_w = temperature at the wall

Pr = molecular Prandtl number ($\mu c_P / k_f$)

Pr_t = turbulent Prandtl number (= 0.85 at the wall)

A = 26 (van Driest constant)

κ = 0.4187 (von Karman constant)

E = 9.793 (wall function constant)

U_c = mean velocity magnitude at $y^+ = y^+_T$

y^+_T= non-dimensional thermal sublayer thickness.

The species transport is assumed to behave analogously to the heat transfer. The equation is expressed as

$$Y^+ \equiv \frac{\left(Y_{i,w}-Y_i\right)\rho c_p C_\mu^{0.25}k_P^{0.5}}{J_{i,w}} = \begin{cases} Scy^+, y^+ < y_c^+ \\ Sc_t\left[\frac{1}{\kappa}\ln\left(Ey^+\right)+P_c\right], y^+ > y_c^+ \end{cases} \tag{2.22}$$

Where Y_i is the local mass fraction of species i, Sc and Sc_t are the molecular and turbulence Schmidt numbers, and $J_{i,w}$ is the diffusion flux of species i at the wall. The molecular Schmidt number, Sc, is

given as $\frac{\mu}{\rho D}$, where μ is the viscosity and D is the diffusivity. The P_c and y^+_c are calculated in a similar way as P and y^+_T, with the difference being that the Prandtl numbers are replaced by the corresponding Schmidt numbers.

For the k - ε turbulence model, the k-equation is solved in the whole domain, including the wall-adjacent cells. The boundary condition for k imposed at the wall is

$$\frac{\partial k}{\partial n} = 0 \tag{2.23}$$

Where n is the local coordinate normal to the wall. The production of kinetic energy, G_k, and its dissipation rate, ε, at the wall-adjacent cells, which are the source terms in k equation, are computed on the basis of equilibrium hypothesis with the assumption that the production of k and its dissipation rate assumed to be equal in the wall-adjacent control volume. The production of k and ε is computed as

$$G_k \approx \tau_w \frac{\partial U}{\partial y} = \tau_w \frac{\tau_w}{\kappa \rho C_\mu^{0.25} k_P^{0.5} y_P} \tag{2.24}$$

And

$$\varepsilon_P = \frac{C_\mu^{0.75} k_P^{1.5}}{\kappa y_P} \tag{2.25}$$

2.2.3.1.2 Enhanced Wall Function

The k-ε model is mainly valid for fully turbulent flows with high Reynolds numbers. Special treatment is needed in the region close to the wall. The enhanced wall function is one of several methods that model the near-wall flow. In the enhanced wall treatment, the two-layer model is combined with the wall functions. The whole domain is separated into a viscosity-affected region and a fully-turbulent region by defining a turbulent Reynolds number, Re_y, as:

$$Re_y = yk^{1/2} / \nu \tag{2.26}$$

where k is the turbulence kinetic energy and y is the distance from the wall. The standard k-ε model is used in the fully turbulent region where $Re_y > 200$, and the one-equation model of Wolfstein (1969) is used in the viscosity-affected region where $Re_y < 200$. The turbulent viscosities calculated from these two regions are blended with a blending function (θ) to smoothen the transition. This function is defined as:

$$\mu_{t,enhanced} = \theta\mu_t + (1-\theta)\mu_{t,l} \tag{2.27}$$

where μ_t is the viscosity obtained from the k-ε equations, and $\mu_{t,l}$ is the viscosity from the near-wall one-equation model. The blending function is defined so it is equal to 0 at the wall and 1 in the fully turbulent region. The linear (laminar) and logarithmic (turbulent) laws of the wall are also blended to make the wall functions applicable throughout the entire near-wall region. A similar thermal wall function equation is employed for temperature calculation.

2.2.3.2 Other Models

Many turbulence models have been developed, such as the RNG k-ε model, standard k-ω model, the shear-stress transport (SST) k-ω model, Reynolds stress model (RSM), etc. Choudhury (1993) derived the RNG k-ε model by using renormalization group theory. It has an additional term in the ε-equation to improve the accuracy for rapidly strained flows. It uses the effective viscosity to account for low-Reynolds-number effects. Theoretically, this model is more accurate and reliable than the standard k-ε model. Wilcox (1998) indicated that the standard k-ω model is an empirical model based on the transport equations for the turbulence kinetic energy (k) and the specific dissipation rate (ω), which can also be considered as the ratio of ε to k. Low-Reynolds-number effects are accounted for in the k-ω model. Menter (1993) developed the SST model, which is a mixture of the k-ω model and the k-ε model. It uses the k-ω model close to the wall, while the k-ε model is applied in the far-field.

2.2.4 Radiation Models

In the coal mild gasification process investigated in this study, the mild gasification temperature is 1600 K at the inlet, so the radiative heat flux $Q_{rad} = \sigma(T_{max}^4 - T_{min}^4)$ is large compared to the heat transfer rates due to convection or conduction. This, generally, will occur at high temperatures where the fourth-order dependence of the radiative heat flux on temperature indicates that radiation will be dominant.

Basically, there are five radiation models that have been examined: the discrete transfer radiation model, P-1 radiation model, Rosseland radiation model, Discrete Ordinates (DO) radiation model, and Surface-to-Surface (S2S) radiation model. In this study, the P-1 model is used.

2.2.4.1 P-1 Radiation Model

The P-1 radiation model is the simplest case of the more general P-N model, which is based on the expansion of the radiation intensity *I* into an orthogonal series of spherical harmonics. If only four terms in the series are used, the following equation is obtained for radiation flux q_r:

$$q_r = -\frac{1}{3(a+\sigma_s) - C\sigma_s}\nabla G \tag{2.31}$$

where, G = linear-anisotropic phase function coefficient.
After introducing the parameter

$$\Gamma = -\frac{1}{(3(a+\sigma_s) - C\sigma_s)} \tag{2.32}$$

Equation 2.31 is simplified to

$$q_r = -\Gamma\nabla G \tag{2.33}$$

where the transport equation for G is

$$\nabla \cdot (\Gamma \nabla G) - aG + 4an^2 \sigma T^4 = S_G \tag{2.34}$$

where S_G = user-defined radiation source

Combing equation 2.33, 2.34, yields,

$$-\nabla \cdot q_r = aG - 4an^2 \sigma T^4 \tag{2.35}$$

The expression for $-\nabla \cdot q_r$ can be directly substituted into energy equation to account for heat sources/sinks due to radiation. Cheng (1964) first presented this model, Siegel and Howell (1992) further developed this model and for more complicated application.

2.2.4.2 Advantages and Limitations of the P-1 Radiation Model

P-1 has several advantages: Eq. (2.28) for the P-1 model is a diffusion equation, which is easy to solve with little CPU demand. The model includes the effect of scattering. For coal gasification, which involves coal particles and participating gases such as CO, H_2, and H_2O, the optical thickness is large, so the P-1 model works reasonably well. In addition, the P-1 model can easily be applied to complicated geometries with curvilinear coordinates.

Although the P-1 model was chosen for modeling radiation in this study, it is necessary to understand its limitations:

- The P-1 model assumes that all surfaces engage in diffuse reflection. This means that the reflection of incident radiation at the surface is isotropic with respect to the solid angle.
- The implementation is restricted to either gray radiation or non-gray radiation using a gray-band model. The non-gray implementation is used to specify the absorption coefficient in each band. The non-gray implementation also assumes the spectral emissivity at the walls to be constant within each band.

- There may be a loss of accuracy, depending on the complexity of the geometry, if the optical thickness is small.
- The P-1 model tends to over-predict radiative fluxes from localized heat sources or sinks.

2.2.5 Chemical Reaction Model R

Two different chemical reaction models have been used in this study: homogeneous (gas-gas) reactions and heterogeneous (particle-gas) reactions. The major difference between these two models depends on how the carbon species is modeled. The homogeneous gas reaction assumes that the carbon species gasifies instantaneously, and the carbon is treated as a gas, while the heterogeneous particle-gas reactions treat carbon as solid particles, and they go through a typical, finite-rate reaction at the particle surface. These two models focus on different aspects of the reaction processes, and each has their own advantages.

2.2.5.1 Instantaneous Gasification Model

The assumptions, theory, and limit of the instantaneous gasification are detailed below.

Instantaneous Gasification Model – The mass, momentum, and energy exchange rates between multiple phases are assumed to be infinitely fast. Carbon particles are made to gasify instantaneously. Thus, the solid-gas reaction process can be modeled as a series of homogeneous combustion reactions. Faeth (1987) proposed this approach based on the locally-homogeneous flow (LHF) model, which implies infinitely-fast interphase transport rates. The instantaneous gasification model can effectively reveal the whole picture of the combustion process without dealing with the details of the otherwise complicated heterogeneous particle surface reactions, heat transfer, species transport, and particle tracking in turbulent reacting flow. The eddy-dissipation model is used to model the chemical reactions. The eddy-dissipation model assumes that the chemical reactions are faster than the turbulence eddy transport, so the reaction rate is controlled by the flow motions.

The instantaneous gasification model can significantly reduce computational time but can only provide a qualitative trend of the gasification process. Although the instantaneous gasification model is

crude, it catches the effect of thermal-fluid fields (including turbulence structures) on chemical reactions, which are not readily available from the equilibrium method or non-reacting method.

On the other hand, the particle combustion model provides a more accurate modeling of heterogeneous reactions by modeling the heat transfer and species transport. Due to its complex dealing of the heterogeneous combustion process, intensive computational power is required.

The global instantaneous gasification mechanism is modeled to involve the following gaseous species: C, O_2, N_2, CO, CO_2, H_2O, C_6H_6, H_2, and volatiles ($CH_{2.121}O_{0.585}$, see Eq. 2.44 to Eq. 2.50). All of the species are assumed to mix at the molecular level. In this approach, carbon is modeled as a gas species based on the instantaneous gasification model described above, and the complete combustion of carbon is modeled by a two-step reaction (Eq. 2.44 and Eq. 2.47). The mixing and transport of chemical species is modeled by solving the conservation equations describing convection, diffusion, and reaction sources for each component species. The species transport equations are solved by predicting the local mass fraction of each species, Y_i, through the solution of a convection-diffusion equation for the i-th species. The general form of the species transport equation is given as:

$$\frac{\partial}{\partial t}\left(\rho Y_i\right)+\nabla\bullet\left(\rho\vec{v}Y_i\right)=-\nabla\bullet\vec{J}_i+R_i+S_i \tag{2.40}$$

where R_i is the net rate of production of species i by chemical reaction. S_i is the rate of creation (a source term) from the dispersed phase. $\vec{J}_i$ is the diffusion flux of species i, which arises due to concentration gradients. Mass diffusion for laminar flows is given as

$$\vec{J}_i=-\rho D_{i,m}\nabla Y_i \tag{2.41}$$

For turbulent flows, mass diffusion flux is given as

$$\vec{J}_i=-\left(\rho D_{i,m}+\frac{\mu_t}{Sc_t}\right)\nabla Y_i \tag{2.42}$$

where Sc_t is the turbulent Schmidt number given as $\mu_t/\rho D_t$, where μ_t is the turbulent viscosity and D_t is the turbulent diffusivity.

The transport equations for each chemical species are

$$\frac{\partial}{\partial t}\left(\rho Y_C\right)+\nabla\cdot\left(\rho\vec{v}Y_C\right)=-\nabla\cdot\vec{J}_C+R_C \tag{2.43a}$$

$$\frac{\partial}{\partial t}\left(\rho Y_{O_2}\right)+\nabla\cdot\left(\rho\vec{v}Y_{O_2}\right)=-\nabla\cdot\vec{J}_{O_2}+R_{O_2} \tag{2.43b}$$

$$\frac{\partial}{\partial t}\left(\rho Y_{N_2}\right)+\nabla\cdot\left(\rho\vec{v}Y_{N_2}\right)=-\nabla\cdot\vec{J}_{N_2}+R_{N_2} \tag{2.43}$$

$$\frac{\partial}{\partial t}\left(\rho Y_{CO}\right)+\nabla\cdot\left(\rho\vec{v}Y_{CO}\right)=-\nabla\cdot\vec{J}_{CO}+R_{CO} \tag{2.43d}$$

$$\frac{\partial}{\partial t}\left(\rho Y_{CO_2}\right)+\nabla\cdot\left(\rho\vec{v}Y_{CO_2}\right)=-\nabla\cdot\vec{J}_{CO_2}+R_{CO_2} \tag{2.43e}$$

$$\frac{\partial}{\partial t}\left(\rho Y_{H_2O}\right)+\nabla\cdot\left(\rho\vec{v}Y_{H_2O}\right)=-\nabla\cdot\vec{J}_{H_2O}+R_{H_2O} \tag{2.43f}$$

$$\frac{\partial}{\partial t}\left(\rho Y_{H_2}\right)+\nabla\cdot\left(\rho\vec{v}Y_{H_2}\right)=-\nabla\cdot\vec{J}_{H_2}+R_{H_2}. \tag{2.43g}$$

The reaction equations that need to be solved are given below.

$$C + \tfrac{1}{2} O_2 \rightarrow CO \tag{2.44}$$

$$C + CO_2 \rightarrow 2CO \tag{2.45}$$

$$C + H_2O\ (g) \rightarrow CO + H_2 \quad (2.46)$$

$$CO + \tfrac{1}{2}\ O_2 \rightarrow CO_2 \quad (2.47)$$

$$CO + H_2O\ (g) \rightarrow CO_2 + H_2 \quad (2.48)$$

(Two-step volatiles cracking and gasification process)

$$CH_{2.121}O_{0.585} \rightarrow 0.585CO+0.853H_2+0.069C_6H_6 \quad (2.49)$$

$$C_6H_6+3O_2 \rightarrow 6CO+3H_2 \quad (2.50)$$

There are three approaches to solve these reactions.

(a) Eddy-dissipation model: The assumption in this model is that the chemical reactions are faster than the time scale of the turbulence eddies. Thus, the reaction rate is determined by the turbulent mixing of the species. The reaction is assumed to occur instantaneously when the reactants meet.

(b) Equilibrium model: The rate of chemical reaction is governed by the rate of mixing of the gaseous oxidant and reactant. The reactions are fast compared to the time scale of turbulence. The gaseous properties become functions of the turbulent mixing rate and can be calculated using equilibrium considerations [Fletcher, 1983].

(c) Finite-rate reaction model: The rate of chemical reaction is computed using an expression that takes into account temperature and pressure and ignores the effects of the turbulent eddies.

In the homogeneous reaction simulation in this study, the reaction rate that appears as a source term, "R_i" in Eq. 2.40 is given by the eddy-dissipation model. The overall rate of reaction for the fastest burning fuels is controlled by turbulent mixing. The net rate of production of species i due to reaction r, $R_{i,r}$, is given by the smaller of the two given expressions below,

$$R_{i.r} = \nu'_{i,r} M_{w,i} A \rho \frac{\varepsilon}{\kappa} \min_R \left(\frac{Y_R}{\nu'_{R,r} M_{w,R}} \right) \quad (2.51)$$

$$R_{i.r} = \nu'_{i,r} M_{w,i} AB \rho \frac{\varepsilon}{\kappa} \frac{\sum_P Y_P}{\sum_j^N \nu''_{j,r} M_{w,j}} \quad (2.52)$$

Where,

Y_P is the mass fraction of any product species, P

Y_R is the mass fraction of a particular reactant, R

A is an empirical constant equal to 4.0

B is an empirical constant equal to 0.5

$\nu'_{i,r}$ is the stoichiometric coefficient for reactant i in reaction r

$\nu''_{j,r}$ is the stoichiometric coefficient for product j in reaction r

In the above Eqs. 2.51 and 2.52, the chemical reaction rate is governed by the large-eddy mixing time scale, κ/ε, and an ignition source is not required. This is based on the assumption that the chemical reaction is much faster than the turbulence mixing time scale, so the actual chemical reaction is not important.

The procedure to solve the reactions is as follows.

1. The net local production or destruction of species "i″ in each reaction is calculated by solving Eqs. 2.51 and 2.52.
2. The smaller of these values is substituted into the corresponding species transport Eq. 2.40 to calculate the local species mass fraction, Y_i.
3. Y_i is then used in Eq. 2.6 to calculate the net enthalpy production of each reaction equation.
4. The net enthalpy production becomes the source term in energy Eq. 2.3 that affects the temperature distribution. In an endothermic process, the net enthalpy production is negative, which becomes a sink term in the energy Eq. 2.3.

2.2.5.2 Finite Rate Model

In the finite-rate model, the reactions involve both homogeneous and heterogeneous reactions. The details of the two types of reactions are explained below.

Homogeneous Reactions

The Finite-Rate/Eddy-Dissipation model is used to simulate the homogeneous reactions. Reaction rates based on the Laminar Finite-Rate Model and Eddy-Dissipation Model are calculated and compared. The minimum of the two results is used as the homogeneous reaction rate. The reason for taking the minimum reaction rate calculated from the eddy-dissipation model and finite rate model is that, in practice, the Arrhenius rate acts as a kinetic "switch," preventing reaction before the flame holder. Once the flame is ignited, the eddy-dissipation rate is generally smaller than the Arrhenius rate, and reactions are mixing-limited.

In this study, the homogeneous reactions are:

$$CO + 0.5O_2 \rightarrow CO_2 \quad (2.53)$$

$$CO + H_2O\ (g) \leftrightarrow CO_2 + H_2 \quad (2.54)$$

Where in equation (2.55) and (2.57), CO comes from the following carbon particle reactions:

$$C + 0.5O_2 \rightarrow CO \quad (2.55)$$

$$C + CO_2 \rightarrow 2CO \quad (2.56)$$

$$C + H_2O \rightarrow CO + H_2 \quad (2.57)$$

Which are modeled as the heterogeneous reactions described below.

Laminar Finite-Rate Model

The laminar finite-rate model computes the chemical source terms using Arrhenius expressions and ignores the effects of turbulent fluctuations. The net source of chemical species i due to reaction R_i (kg/m^3-s) is computed as the sum of the Arrhenius reaction sources over the N_R reactions that the species participate in, and is given as

$$R_i = M_{w,i} \sum_{r=1}^{N_R} \hat{R}_{i,r} \tag{2.58}$$

Where $M_{w,i}$ is the molecular weight of species i and $R_{i,r}$ is the Arrhenius molar rate of creation/destruction of species i in reaction r.

The r-th reaction can be written in a general form as

$$\sum_{i=1}^{N_R} \upsilon'_{i,r} M_i \underset{k_{b,r}}{\overset{k_{f,r}}{\Leftrightarrow}} \sum_{i=1}^{N} \upsilon''_{i,r} M_i \tag{2.59}$$

Where

N = number of chemical species in the system

$\upsilon'_{i,r}$ = stoichiometric coefficient for reactant i in reaction r

$\upsilon''_{i,r}$ = stoichiometric coefficient for product i in reaction r

M_i = symbol denoting species i

$k_{f,r}$ = forward rate constant for reaction r

$k_{b,r}$ = backward rate constant for reaction r.

The molar reaction of creation/destruction of species i in reaction r, which is $\hat{R}_{i,r}$ (kgmol/m^3-s) in equation (2.58), is given as

$$\hat{R}_{i,r} = \Gamma\left(\upsilon''_{i,r} - \upsilon'_{i,r}\right)\left(k_{f,r} \prod_{j=1}^{N_r} \left[C_{j,r}\right]^{\eta'_{j,r}} - k_{b,r} \prod_{j=1}^{N_r} \left[C_{j,r}\right]^{\eta''_{j,r}} \right) \tag{2.60}$$

Where,

N_r = number of chemical species in reaction r

$C_{j,r}$ = molar concentration of each reactant and product species j in reaction r (kgmol/m^3)

$\eta'_{j,r}$ = forward rate exponent for each reactant and product species j in reaction r

$\eta''_{j,r}$ = backward rate exponent for each reactant and product species j in reaction r.

Γ represents the net effect of third bodies on the reaction rate and is given by

$$\Gamma = \sum_{j}^{N_r} \gamma_{j,r} C_j \tag{2.61}$$

Where $\gamma_{j,r}$ is the third body efficiency of the j-th species in the r-th reaction.

The forward rate constant for reaction r, $k_{f,r}$, is computed using the Arrhenius expression

$$k_{f,r} = A_r T^{\beta_r} e^{-E_r/RT} \tag{2.62}$$

Where

A_r = pre-exponential factor (consistent unit)

β_r = temperature exponent (dimensionless)

E_r = activation energy for the reaction (J/kgmol)

R = universal gas constant (J/kgmol-K).

If the reaction is reversible, the backward rate constant, $k_{b,r}$, is computed from the forward rate constant using relation below

$$k_{b,r} = \frac{k_{f,r}}{K_r} \tag{2.63}$$

Where K_r is the equilibrium constant for the r-th computed from

$$K_r = \exp\left(\frac{\Delta S_r^0}{R} - \frac{\Delta H_r^0}{RT}\right)\left(\frac{p_{atm}}{RT}\right)^{\sum_{r=1}^{N_R}\left(\upsilon''_{j,r} - \upsilon'_{j,r}\right)} \tag{2.64}$$

Where, p_{atm} is the atmospheric pressure (101,325 Pa). The term within the exponential function represents the change in Gibbs free energy, and its components are computed as following,

$$\frac{\Delta S_r^0}{R} = \sum_{i=1}^{N} \left(\upsilon_{i,r}^{''} - \upsilon_{i,r}^{'}\right) \frac{S_i^0}{R} \tag{2.65}$$

$$\frac{\Delta H_r^0}{RT} = \sum_{i=1}^{N} \left(\upsilon_{i,r}^{''} - \upsilon_{i,r}^{'}\right) \frac{h_i^0}{R} \tag{2.66}$$

Where S_i^0 and h_i^0 are the standard-state entropy and standard-state enthalpy (heat of formation), respectively.

Heterogeneous Reaction

The particle reaction, R (kg/m^2-s), is expressed as

$$R = D_0 (C_g - C_s) = R_c (C_s)^N \tag{2.67}$$

Where

D_0 = bulk diffusion coefficient (m/s)

C_g = mean reacting gas species concentration in the bulk (kg/m^3)

C_s = mean reacting gas species concentration at the particle surface (kg/m^2)

R_c = chemical reaction rate coefficient (units vary)

N = apparent reaction order (dimensionless).

The concentration at the particle surface, C_s, is not known, so it is eliminated and the expression is recast as follows,

$$R = R_c \left[C_g - \frac{R}{D_0} \right]^N \tag{2.68}$$

This equation has to be solved by an iterative procedure, with the exception of the cases when N = 1 or N = 0. When N = 1, equation (2.68) can be written as

$$R = \frac{C_g R_c D_0}{D_0 + R_c} \tag{2.69}$$

In the cases of N = 0, if there is a finite concentration of reactant at the particle surface, the solid depletion rate is equal to the chemical reaction rate. If there is no reactant at the surface, the solid depletion rate changes abruptly to the diffusion-controlled rate.

The reaction stoichiometry of a particle undergoing an exothermic reaction in a gas phase is given as:

Particle Species j (s) + Gas Phase Species n $\rightarrow$ Products.

Its reaction rate is given as

$$\overline{R}_{j,r} = A_p \eta_r Y_j R_{j,r} \tag{2.70}$$

$$R_{j,r} = R_{kin,r}\left(p_n - \frac{R_{j,r}}{D_{0,r}}\right)^{N_r} \tag{2.71}$$

where

$\overline{R}_{j,r}$ = rate of particle surface species depletion (kg/s)

A_p = particle surface area (m^2)

Y_j = mass fraction of surface species j in the particle

η_r = effectiveness factor (dimensionless)

$R_{j,r}$ = rate of particle surface species reaction per unit area (kg/m^2-s)

p_n = bulk concentration of gas phase species (kg/m^3)

$D_{0,r}$ = diffusion rate coefficient for reaction r

$R_{kin,r}$ = kinetic rate of reaction r (units vary)

N_r = apparent order of reaction r.

The effectiveness factor, r, is related to the surface area, and can be used in each reaction in the case of multiple reactions.

$D_{0,r}$ is given by

$$D_{0,r} = C_{1,r} \frac{\left[\left(T_p + T_\infty\right)/2\right]^{0.75}}{d_p} \tag{2.72}$$

Equation (2.72) is modification of relationship given by [Smith, 1982] by assuming negligible change in gas density.

The kinetic rate of reaction r is defined as

$$R_{kin,\,r} = A_p T^{\beta} e^{-(E_r/RT)} \tag{2.73}$$

The rate of particle surface species depletion for reaction order $N_r = 1$ is given by

$$\overline{R}_{j,r} = A_p \eta_r Y_j p_n \frac{R_{kin,\,r} D_{0,r}}{D_{0,r} + R_{kin,\,r}} \tag{2.74}$$

For reaction order $N_r = 0$,

$$\overline{R}_{j,r} = A_p \eta_r Y_j R_{kin,\,r} \tag{2.75}$$

2.2.5.3 Carbon Combustion Reaction Rates

The investigations of coal char combustion kinetics for ten U.S. coals of various ranks have been conducted by Hurt and Mitchell (1992). They found that char reactivity decreased with increasing coal rank, which implies that char reactivity decreases with increasing carbon content. The reactivity differences are more pronounced at low temperatures than at high temperatures. Based on coal rank

under conditions relevant to pulverized coal-fired combustors, Hurt and Mitchell provided a char reactivity correlation.

Field (1968) conducted an experiment to measure the rate of reaction for $C(s) + \frac{1}{2} O_2 \rightarrow CO$. The gas temperature used by Field ranged from 1200K to 1720K at atmospheric pressure. Oxygen concentrations used ranged from 1% to 20%, and particle size ranged from 20 μm to 100 μm. The measured particle temperatures ranged from 1200K to 2000K.

It was assumed that the product formed inside and on the surface of the char was carbon monoxide and that, on average, CO was transported some distance away from the particle before it could combine with oxygen to form carbon dioxide. The reaction rate was calculated from the weight loss of a char sample in a given transit time at a given oxygen concentration. An overall reaction rate coefficient is defined as the rate of removal of carbon per unit external surface area per unit atmospheric partial pressure of oxygen in the gas. Field found that the variation of the diffusional reaction rate coefficient was not strong. The experiment did not detect any effect of particle size on the reaction rate. The kinetic reaction rate was found to be $k = T (A+BT)$ where $A = -0.067$ m/(s-K) and $B = 5.26 \times 10^{-5}$ m/s-K^2.

Investigation of the rate of reaction for $C(s) + CO_2 \rightarrow 2CO$, where graphite was used as the C, has been carried out by Mayers (1934(a)) through his experiment. This experiment was conducted at atmospheric pressure. He measured the reduction rate of CO_2. The effects of diffusion as the rate determining factor were eliminated by increasing the gas velocity across the particle surface, thus removing the concentration gradients.

The rate of reduction of CO_2 throughout the reaction appeared in two temperature ranges: (a) between 1125K and 1225K and (b) between 1225K and 1575K. Mayers found that CO was formed at the same rate as that at which CO_2 disappeared, while CO_2 reacted with carbon at low temperatures ($T <$ 1250K). This is proved by the retention of half of the oxygen from the carbon dioxide by the graphite ($C + CO_2 \rightarrow CO + C\text{-}O_{solid}$). Mayers pointed out that the CO_2 reduction rate at the high temperature range could be represented by two reactions: $C + CO_2 \rightarrow CO + C\text{-}O_{solid}$ and $C\text{-}O_{solid} \rightarrow CO$, where the second reaction follows so rapidly after the first that there is no accumulation of $C\text{-}O_{solid}$. Thus, the product of

the CO_2 reduction is CO only. The CO_2 reduction rate is expressed in Arrhenius form: $k = AT^n \exp(-E/RT)$, where n = 1.0, A = 4.4 m/s-k, and $E = 1.62 \times 10^{+8}$ J/kmol.

Another experiment had been conducted by Mayers (1934(b)) to measure the rate for $C(s) + H_2O(g) \rightarrow CO + H_2$, where graphite was used as the source of C, at atmospheric pressure in the temperature range of 1123-1433K under conditions which eliminated the effects of diffusion as the rate determining process. He found that the appearance CO and of CO_2 varied rather widely within the same temperature group, but their sum was found to be constant. The ratio CO/CO_2 of the products of reaction depends on the speed of the secondary reaction ($CO + H_2O \rightarrow CO_2 + H_2$) and the time during which the mixture of gases remains in the heated zone. The rate of oxidation of carbon by steam appeared within the temperature ranges 1133-1233K and 1273-1433K. Mayers documented that the rate of oxidation of C was of the same order of magnitude as the rate of appearance of C as CO when graphite was oxidized by CO_2. The kinetic reaction rate was found to be $k = AT^n \exp(-E/RT)$, where n = 1.0, A = 1.33 m/s-K, and $E = 1.47 \times 10^{+8}$ J/kmol.

In this study, three heterogeneous and two homogeneous reactions are modeled and their reaction rates are:

1. $C + 0.5O_2 \rightarrow CO$

   Rate coefficient: $R = A\,T^n \exp(-E/RT)$

   Where n = 0

   $A = 92.32$ kg/m^2-s

   $E = 8.4 \times 10^{+7}$ J/kmol.

The reaction rate is based on the work of Mann, A. P. and Kent, J. H. [1994]

2. $C + CO_2 \rightarrow 2CO$

   Rate coefficient: $R = A\,T^n \exp(-E/RT)$

   Where n = 0

   $A = 23.3$ kg/m^2-s

   $E = 1.15 \times 10^{+8}$ J/kmol.

The reaction rate is based on the work of Mann, A. P. and Kent, J. H. [1994]

3. $C + H_2O\ (g) \rightarrow CO + H_2$

Rate coefficient: $R = A\ T^n \exp(-E/RT)$

Where $n = 0$

$A = 24.9\ kg/m^2\text{-}s$

$E = 1.125x10^{+8}\ J/kmol.$

The reaction rate is based on the work of Mann, A. P. and Kent, J. H. [1994]

4. $CO + ½\ O_2 \rightarrow CO_2$

Rate coefficient: $R = A\ T^n \exp(-E/RT)$

Where $n = 0$

$A = 2.2x10^{+12}$

$E = 1.67x10^{+8}\ J/kmol.$

The reaction rate is based on the work of Watanabe, H., and Otaka, M. [2006]

5. $CO + H_2O\ (g) \rightarrow CO_2 + H_2$

Rate coefficient: $R = A\ T^n \exp(-E/RT)$

Where $n = 0$

$A = 2.75x10^{+10}$

$E = 8.38x10^{+7}\ J/kmol.$

The reaction rate is based on the work of Watanabe, H., and Otaka, M. [2006]

2.2.5.4 Coal Devolatilization Model

Coal Devolatilization is an important step for the mild gasification process in this study. It is modeled with two stages. The first stage occurs in the draft tube with a portion (estimated to be about 70%) of the volatiles being driven out. The rest of the coal is deflected by the deflector and falls down to the fluidized bed, where it continues to absorb energy and release volatile matters. Many operational parameters should be considered while setting up a devolatilization model, such as particle size, oxygen ratio of the fluidizing gas, particle residence time, and fluidization velocity. Basically, the devolatilization models can be categorized into two groups: structural and empirical approaches. Some of the devolatilization models are introduced in the following section.

2.2.5.4.1 Structural Models

Fletcher, etc (1990) developed the Chemical Percolation Model (CPD) for the coal devolatilization process. They described coal conversion behavior based on the chemical structure of the parent coal. During coal pyrolysis, the labile bonds between the aromatic clusters in the coal structure lattice are cleaved, resulting in two general classes of fragments. One set of fragments has a low molecular weight (and correspondingly high vapor pressure), which escapes from the coal particle as a light gas. The other set of fragments consists of tar gas precursors that have relatively high molecular weight (and correspondingly low vapor pressures) and tend to remain in the coal for a long period of time during typical devolatilization conditions. During this time, reattachment with the coal lattice (which is referred to as cross-linking) can occur. The high molecular weight compounds plus the residual lattice are referred to as the metaplast. The softening behavior of a coal particle is determined by the quantity and nature of the metaplast generated during devolatilization. The portion of the lattice structure that remains after devolatilization is comprised of char and mineral-compound-based ash.

The Functional-Group & Devolatilization-Vaporization-Cross-linking (FG-DVC) model has been derived by Solomon, etc (1988). FG-DVC model have the same starting point as the CPD model. However, it treats tar formation and the behavior of the char produced during devolatilization more extensively. In the FG-DVC model, linear oligomers of a certain number of aromatic ring clusters having a molecular weight distribution are linked by a certain number of cross-links per monomer. During the thermal decomposition, bridges are broken, and the cross-links are formed.

These two typical structural models are useful in predicting the production of tar and char, and the evolution of light gases during the coal devolatilization process. Both of these models utilize the data generated by instrumental analysis. The quality of the data should be high, but this model is only applicable to certain types of coal.

2.2.5.4.2 Empirical Models

Empirical models take a less physical approach than structural models do. Instead of paying attention to local variables, they adopt a global method to model the coal devolatilization. These empirical models come from modeling the devolatilization process of pulverized bituminous coals.

Chen and Hayhurst (2004) presented the shrinking–core model that assumes that the core of the coal particle continues to shrink throughout the devolatilization process, but the particle size is assumed to be held constant. They also gave an equation for the devolatilization time, t_v, based on their bituminous and lignite coals in a fluidized bed in a nitrogen-rich atmosphere:

$$t_v = \left(\frac{\rho \Delta H}{k_t \Delta T}\right)\left(\frac{k_t}{3ah} + \frac{1}{6}\right)a^2$$

where k_t is the thermal conductivity of coal, a is the radius of the coal particle, h is the convective heat transfer coefficient, ρ is the density of original coal, ΔT is the difference of temperature between the fluidized bed and the surface of the shrinking reaction core, and ΔH is the enthalpy required to devolatilize a unit mass of coal.

Because the series of complex chemical reactions and species transports processed during the coal devolatilization is still not fully understood, a set of simple, first-order Arrhenius-type models have been studied. Rather than consider the breakup of bonds between various coal macromolecules, if the assumption that the overall devolatilization process can be presented by a simplified global reaction rate is made, it follows that empirical models are more straightforward than structural models. Furthermore, such models do not need extensive data to clarify the structure of the coal used, and, hence, the amount of data input is reduced. However, empirical models cannot reflect the real picture of the structure of coal and are limited to model less complex processes. Again, empirical models are prone to larger uncertainties in predicting the yields of tar, char, and volatiles. In this study, a single rate model is employed as described below.

The devolatilization process can be modeled by defining a devolatilization rate (DR) as:

$$\mathrm{DR} = \frac{\text{Amount of Volatiles in Gas Phase}}{\text{Total Amount of Volatiles in Coal Phase Initially}}$$

Kobayashi (1976) indicated that two competing devolatilization rates can be expressed as a weighted function of two competing rates, k_1 and k_2, as:

$$\frac{m_v(t)}{(1-f_{w,0})m_{p,0}-m_a} = \int_0^t (\alpha_1 k_1 + \alpha_2 k_2) \exp\left[-\int_0^t (k_1+k_2)\,dt\right] dt$$

Where, α_1 and α_2 are yield factors, f_w is the mass fraction of moisture, m_p is the mass of a particle, m_a is the mass of ash, and k_1 and k_2 are given as:

$$k_1 = A_1 e^{-(E_1/RT_P)}$$

And

$$k_2 = A_2 e^{-(E_2/RT_P)}$$

The value of the constants are $A_1 = 2 \times 10^5$, $A_2 = 1.3 \times 10^7$, $E_1 = 1.046 \times 10^8$J/kg-mol, $E_2 = 1.67 \times 10^8$J/kg-mol.

Badzioch and Hawsley (1970) also introduced a similar single rate model by modifyingthe devolatilization rate, depending on the amount of volatiles remaining in coal following the Arrhenius form:

$$k = Ae^{(-E/RT)}$$

Where the pre-exponential factor, $A = 4.92 \times 10^5$ and the activation energy, $E = 7.4 \times 10^7$J/kg-mol

Baum and Street (1971) also assumed a constant devolatilization rate in their model. Compared to them, Pillai (1981) chose 12/s in his model. Khan & Wang (2011) simulated the coal devolatilization process inside a mild gasifier with a constant reaction rate. Silaen & Wang (2010) simulated the gasification process in a two-stage, entrained bed coal gasifier by using the Eulerian–Lagrangian

approach. They concluded that the Kobayashi model produces a slower devolatilization rate than the other models, while the constant rate model produces the fastest devolatilization rate. The single rate model and the CPD model produce moderate and consistent devolatilization rates. Typically, the CPD model requires much more computational time than the single rate model. Following Silaen and Wang's conclusion, the single rate model is adopted in this study.

Since there is no built-in devolatilization model in Ansys/Fluent for Eulerian-Eulerian multiphase flow (although it has devolatilization models for the Eulerian-Langrangian method), a devolatilization process must be developed and added as a User Defined Function to the computational process. To this need, a two-step devolatilization model was specifically developed by Khan and Wang (2011) of the same research group for the mild gasification process. Khan's and Wang's multiphase devolatilization model is structured in two steps. Firstly, the coal releases moisture and volatile matters as long as they absorb heat from the ambient gases. Based on the coal composition, the volatiles are chemically formulated as $CH_{2.12}O_{0.585}$. Two pseudo-heterogeneous reactions modeled with a single reaction rate in the Arrhenius form are introduced here to model these two steps. The two Eulerian-Eulerian phases assigned in this study are the primary gases phase and the secondary solid coal phase. The primary phase contains all gases includingO_2, N_2, H_2O(gas), CO, CO_2, H_2, C_6H_6, and volatiles, and the secondary phase contains Char (solid carbon), H_2O (liquid), and condensed volatiles. Initially, the primary phase does not contain any water vapor H_2O or volatiles, and the secondary phase contains liquid water and condensed volatiles according to the coal composition. As devolatilization (along with demoisturization) continues, the secondary phase starts to lose moisture and volatiles, and, in the meantime, the primary phase starts to gather more water vapor and volatiles. These two pseudo-chemical reactions are formulated as:

$$\text{Moistures}(H_2O)_{\text{coal phase}} \Leftrightarrow \text{Moistures}(H_2O)_{\text{gases phase}}$$

$$\text{Volatiles}(CH_{2.121}O_{0.585})_{\text{coal phase}} \Leftrightarrow \text{Volatiles}(CH_{2.121}O_{0.585})_{\text{gases phase}}$$

2.2.6 Boundary Conditions

Figures 2.3a and 2.3b show the boundary conditions of the 2-D mild gasifier geometry (Case 3 in Ch. 5) and 3-D mild gasifier geometry (Case 4 in Ch. 5), respectively. The detailed inlet conditions for

the coal devolatilization reactions (Case 3 in Ch. 5) are given in Table 2.1 for 2-D, and the 3-D inlet conditions for the carbon solid fluidization simulation are given in Table 2.2 for 3-D.

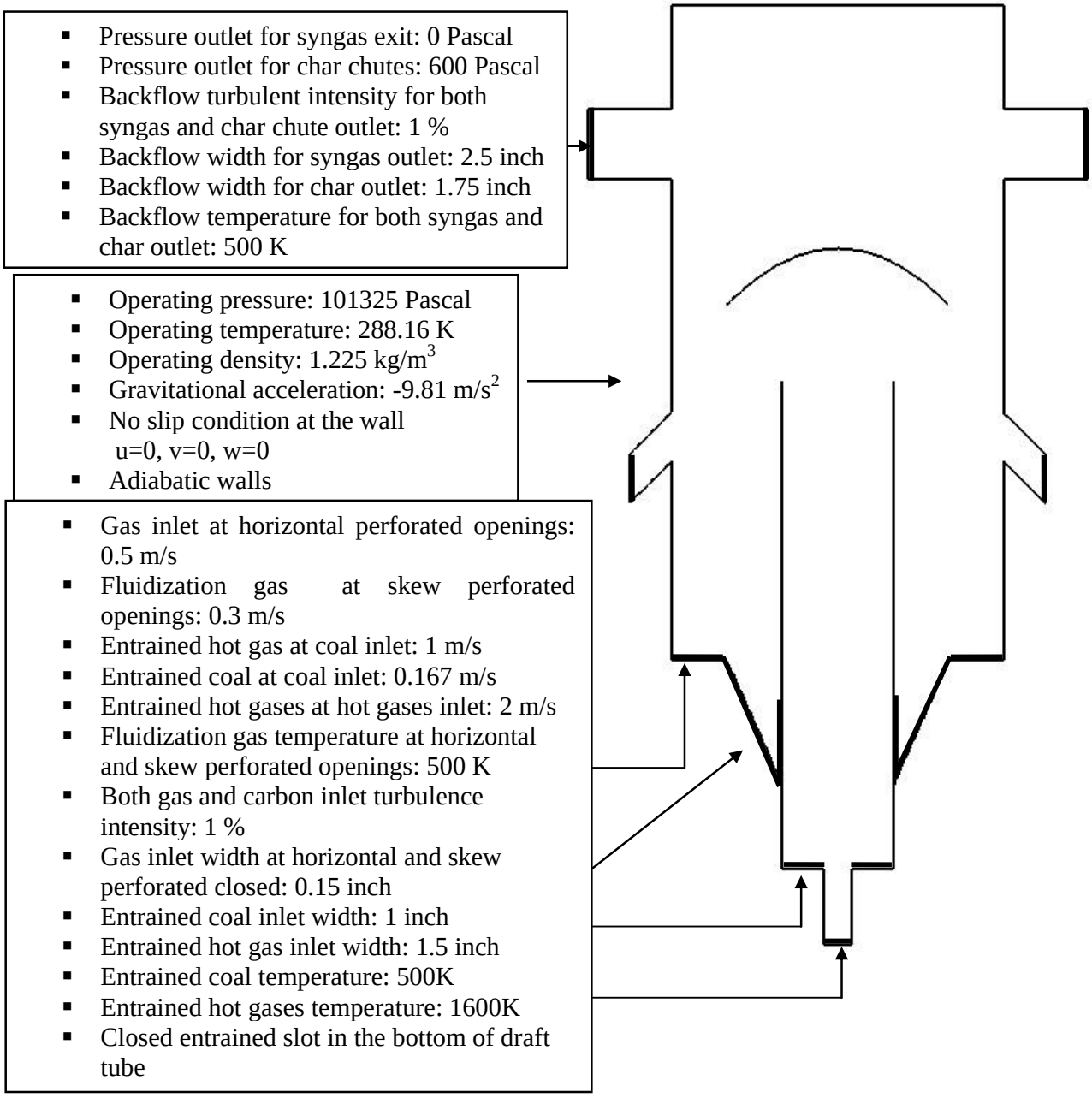

Figure 2.3a Boundary conditions for the 2-D Mild Gasifier

Table 2.1 Parameters: inlet and operating conditions for coal devolatilization reactions (Case 3 in Ch. 5)

Parameters	**Cases 3**	
Inlet position	Fluidized bed inlet	Draft tube inlet
Feedstock & transport agenct	air	carbon solid, water vapor, volatiles
Air inlet velocity at horizontal perforated openings, m/s	0.5	
Air inlet velocity at skew perforated openings, m/s	0.3	
Entrained air inlet velocity at draft tube, m/s		1.0
Entrained coal velocity at draft tube, m/s		0.2
Entrained hot air velocity at draft tube. m/s		2.0
Inlet temperature, coal, K		500
Inlet temperature, hot gas, K	500	1600
Mass fraction at inlet		
O_2	0.23	0.4533
N_2	0.77	0.0976
$CH_{2.121}O_{0.585}$	0	0.4491
Operating pressure (pascal)	101325	101325
Operating temperature (K)	288.16	288.16
Operating density (kg/m^3)	1.225	1.225
Gravitational acceleration (m/s^2)	9.81	9.81
Wall temperature, K	Adiabatic	Adiabatic

It can be seen from Table 2.1 that coal inlet velocity inside the draft tube is 0.167m/s. The mass flow rate (kg/s) per unit depth (1 m) of coal is calculated below:

Mass flow rate of carbon of per unit depth = $\varepsilon_v \rho$ w V_{in} (w is the width of the inlet),

where: ε_v = volume fraction of carbon = 0.1,

ρ = density of coal = 916 kg/m^3,

w = 1 inch/unit depth = 0.0254 m/ m (The unit depth is chosen to be 1 meter),

and,

V_{in} = coal inlet velocity = 0.167 m/s.

The mass flow rate of coal = 0.1 × 916 × 0.0.0254 × 0.167 = 0.3908 kg/s-m.

The output power of the 2-D mild gasifier: = 0.3908 kg/s-m × 23.8 MJ/kg = 9.4724 MW-m

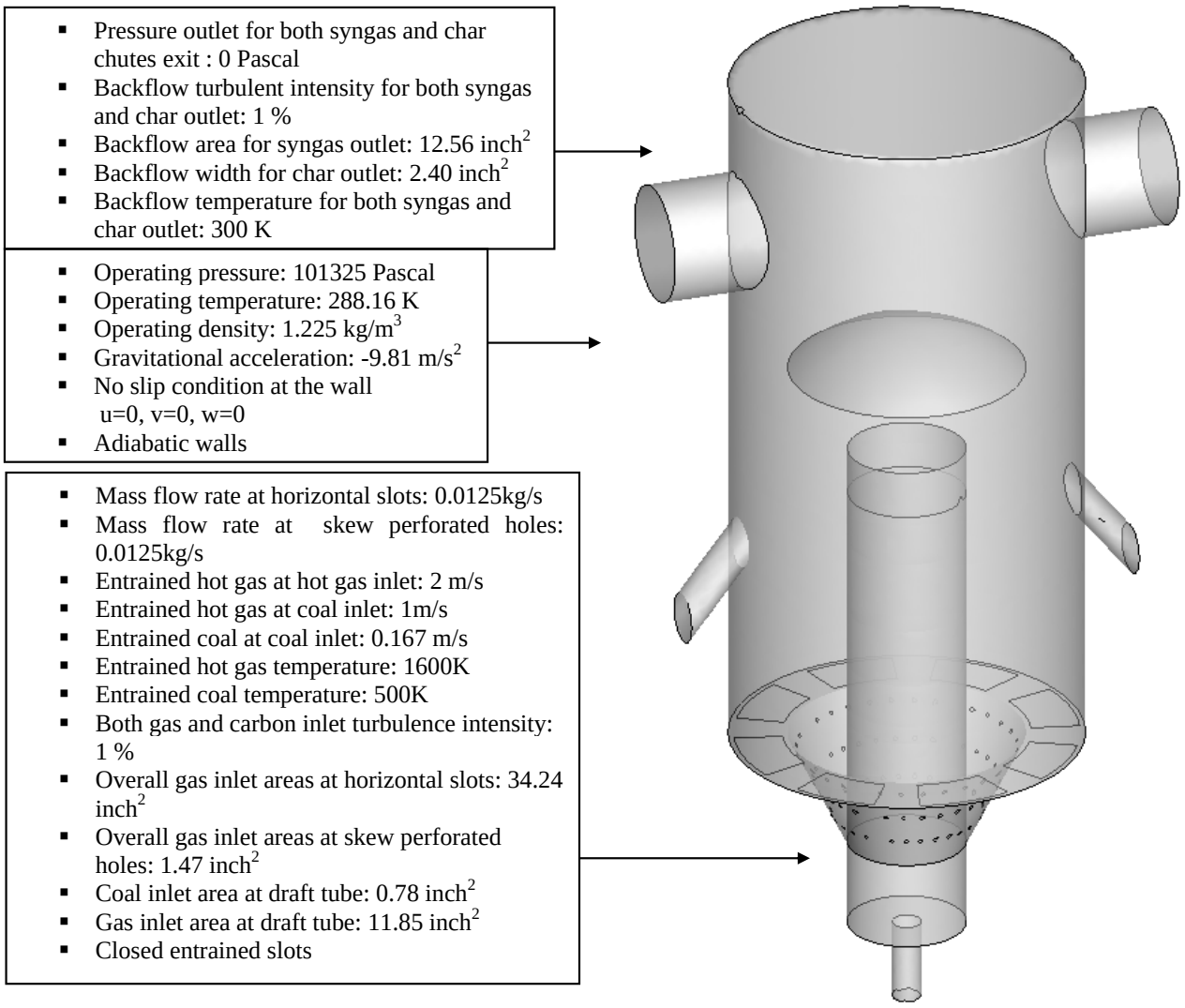

Figure 2.3b Boundary conditions of the 3-D Mild Gasifier

Table 2.2 Parameters: inlet and operating conditions for coal devolatilization reactions (Case 4 in Ch. 5)

Parameters	**Cases 4**	
Inlet position	Fluidized bed inlet	Draft tube inlet
Feedstock & transport agenct	air	carbon solid, air
Entrained air velocitiy at coal inlet, m/s		1
Entrained coal velocity at coal inlet, m/s		0.167
Entrained hot gas velocity at hot gas inlet, m/s		2
Air inlet velocity at inlcined perforated openings, m/s	12 (0.01049 kg/s)	
Air inlet velocity at horizontal perforated openings, m/s	0.5 (0.01105 kg/s)	1
Entrained air temperature, K	1600	1
Entrained coal temperature, K	500	
		300
Mass fraction at inlet		
O_2	0.23	N/A
N_2	0.77	N/A
$CH_{2.121}O_{0.585}$	0	N/A
Carbon solid	0	1
Operating pressure (pascal)	101325	101325
Operating temperature (K)	288.16	288.16
Operating density (kg/m^3)	1.225	916
Gravitational acceleration (m/s^2)	9.81	9.81
Wall temperature, K	Adiabatic	Adiabatic

By using Eq. (2.a), the carbon solid mass flow rate for 3-D mild gasifer is given bellow:

$$\dot{m}_{\text{carbon solid}} = \rho_{\text{carbon solid}} \times V_{\text{carbon solid}} \times A \times \varepsilon$$

Plug in values and yields:

$$\dot{m}_{\text{carbon solid}} = 0.02926 \text{ kg/s}$$

The output power of the 3-D mild gasifier based on this mass flow rate of carbon solid is rated as:

$$\text{Power}_{\text{gasifier}} = 0.02926 \text{ kg/s} \times 23.8 \text{ MJ/kg} = 696.38 \text{ kW}$$

2.3 Computational Scheme

2.3.1 Solution Methodology

The major steps in the CFD simulation are divided into three areas: (a) preprocessing, (b) processing, and (c) post processing.

2.3.1.1 Preprocessing

Preprocessing refers to the geometry generation, geometry mesh, model specifications, and boundary specifications. Before any calculation can be done, the computational domain has to be created. The commercial preprocessing software ANSYS ICEM CFD is used to generate mesh geometries (computational domains). Once the computational domain geometry has been meshed in ANSYS ICEM CFD, it is imported into the commercial CFD code ANSYS FLUENT R14.0 from ANSYS, Inc. Then, the appropriate models and boundary conditions are set.

2.3.1.2 Processing

In the processing step, calculations are performed to obtain the solution for the governing equations. ANSYS FLUENT is a finite-volume based CFD solver written in the computer language "C" and has the ability to solve fluid flow, heat transfer, and chemical reaction problems in complex geometries and supports both structured and unstructured meshes. The solution is obtained through iteration until the convergence criteria, which are set by the user, are satisfied. Residuals are used as a means to determine when convergence has been achieved. Residuals are the imbalanced errors in the governing equations over all of the cells in the computational domain.

2.3.1.3 Post-processing

Post-processing involves analyzing and interpreting the solution obtained. Charts and various visualization schemes can be employed to aid in understanding the physics of the solution. The results are presented in the form of x-y plots, contour plots (e.g. temperature and mass fraction contours),

velocity vector plots, streamline plots, and animations via the built-in plotting software in ANSYS FLUENT or the third party software, Tecplot 360.

2.3.2 Computational Grid

The geometry is generated and meshed in 64-bit ANSYS ICEM CFD 14.0. Quadrilateral and triangular surface meshes are used in the revised 2-D domain. Hybrid meshes, such as hexahedral, tetrahedral, and pyramidal meshes, are employed in the 3-D domain. An unstructured mesh is used for meshing the 2-D geometry as well as the 3-D mild gasifier (Fig. 3.4a-c and Fig. 3.5, respectively). In this study, a total of 10,115 cells are employed for the 2-D geometry and followed by denser grids of 21,582 cells (Fig. 2.4b) and 46,917 cells (Fig. 2.4c) for the final case (Case 2). An initial 815,666 cells are used for the 3-D mild gasifier. After the model has been meshed, it is exported to ANSYS/FLUENT R14.0.

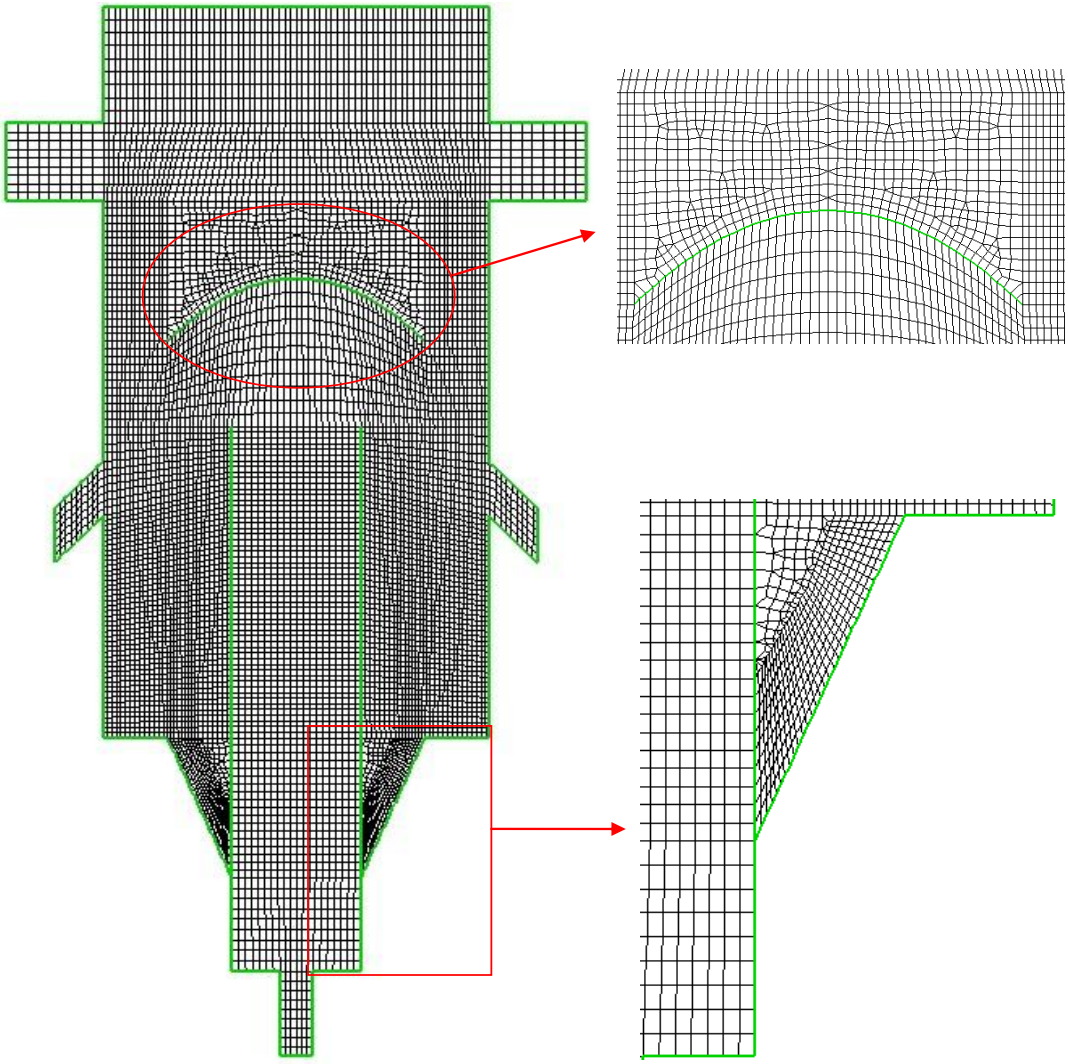

Figure 2.4a 2-D unstructured mesh (10,115 cells) of the 2-D mild gasifier

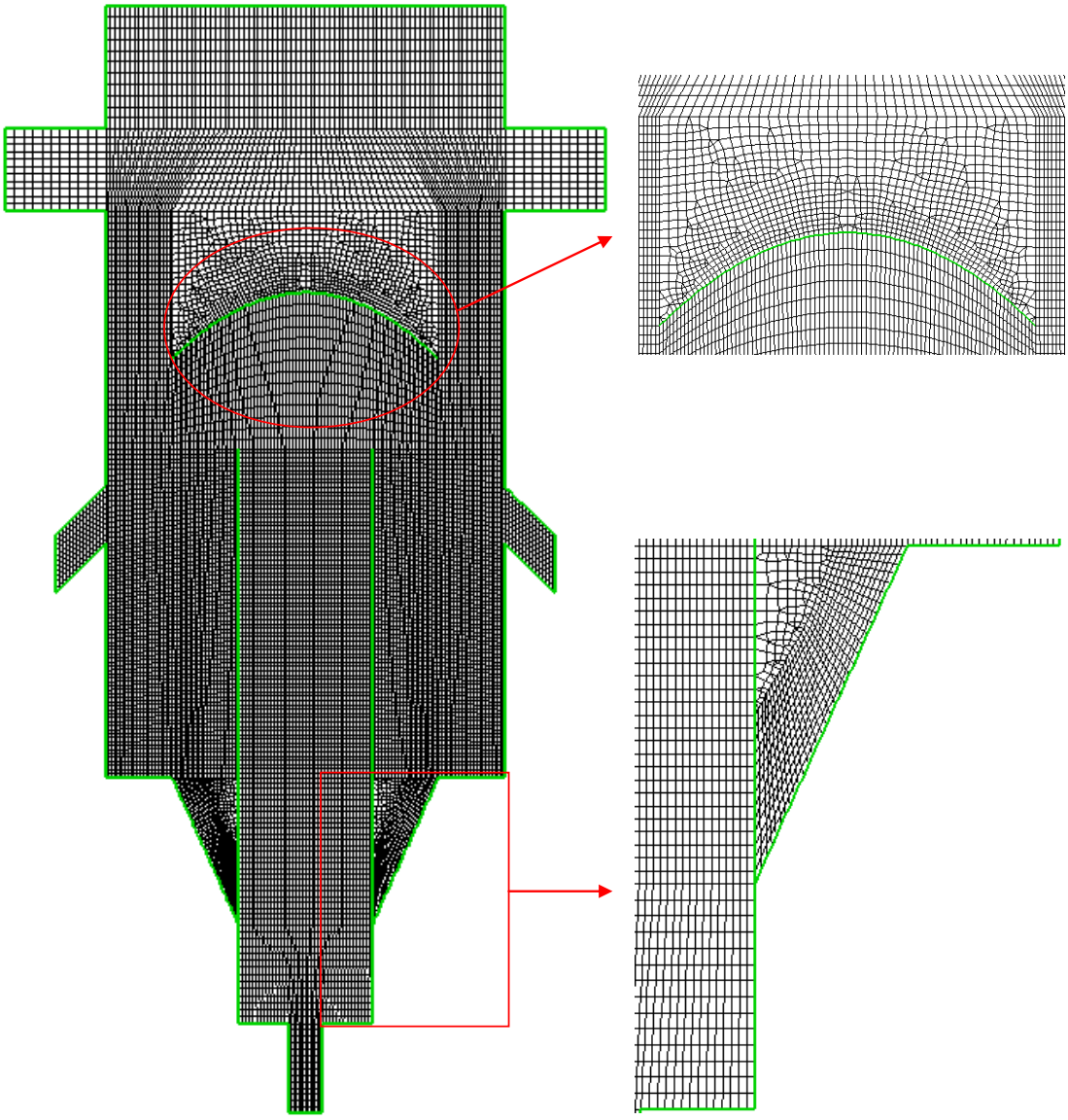

Figure 2.4b 2-D unstructured mesh (21,582 cells) of the 2-D mild gasifier

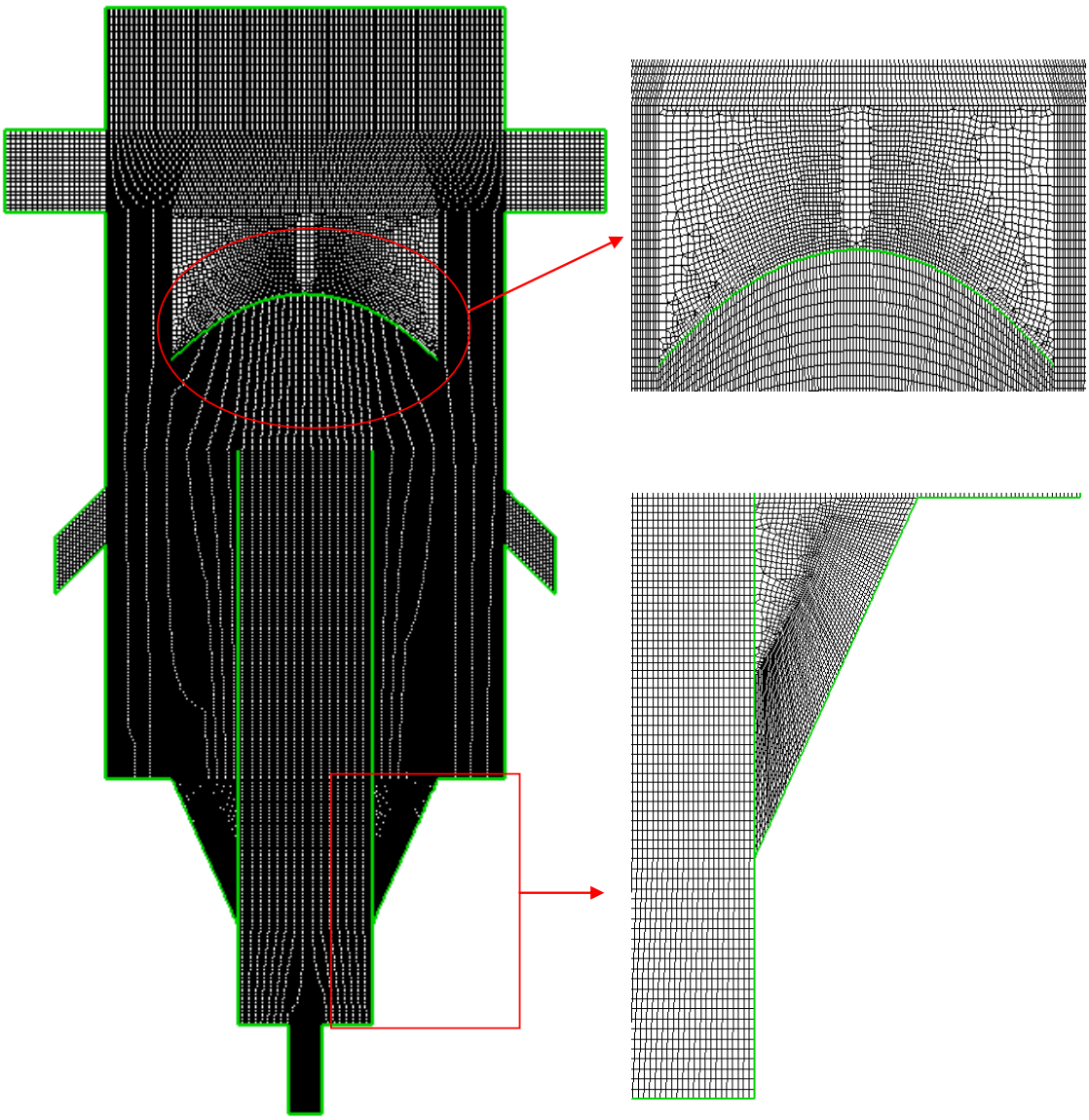

Figure 2.4c 2-D unstructured mesh (46,917 cells) of the 2-D mild gasifier

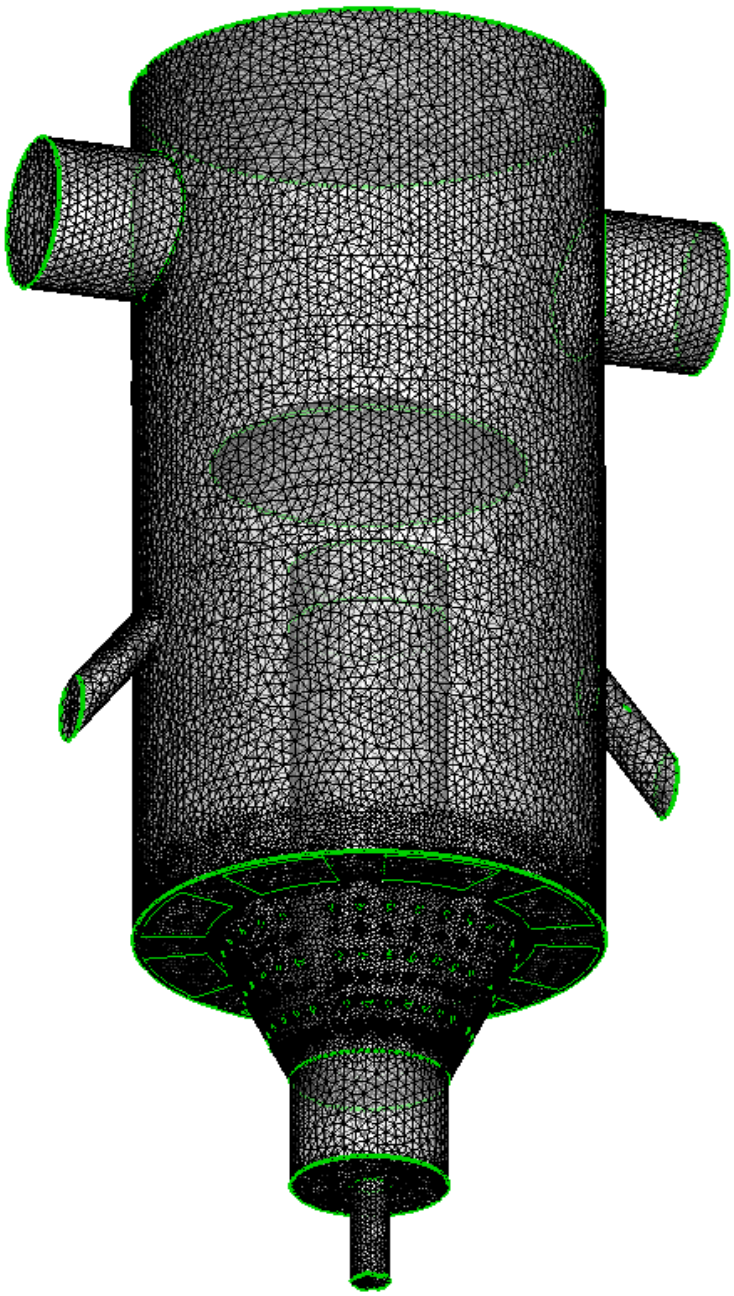

Figure 2.5 3-D Unstructured mesh (816,731 cells) of the 3-D mild gasifier

2.3.2.1 Grid Sensitivity Study for Case 3a

A grid sensitivity study has been conducted for 2-D mild gasifier case using three different grids: coarse grid, medium grid, and fine grid. Parameters and operating conditions for Case 3a given in Table 5.5 are used in this grid sensitivity study. Table 2.3 shows, after 4.4 seconds, the mass-weighted average temperature and species mass fractions , although all have achieve convergence, they have not reached grid-independence. Due to the limitation of the current computer capability, further refinements of the solution will be left for future study when more computational resources are available.

Table 2.3 Grid sensitivity study of Case 3a

Parameters	**Coarse Grid (10,115 cells)**	**Medium Grid (21,582 cells)**	**Fine Grid (46,917 cells)**	**Percentage Change Between Medium and Fine Grids**
Exit gas temperature (K)	524.39	413.74	406.22	1.85%
Exit carbon solid temperature (K)	719.54	512.85	428.85	19.58%
Exit mass fraction of CO	0.0893	0.0645	0.0408	58.08%
Exit mass fraction of CO_2	0.1067	0.0864	0.0798	8.27%
Exit mass fraction of H_2	0.0135	0.0103	0.0079	30.37%
Exit mass fraction of Volatiles	0.0218	0.0395	0.0340	16.17%
Exit mass fraction of C_6H_6	0.0273	0.0204	0.0132	54.54%

2.3.3 Numerical Procedure

The procedure for performing the simulation in ANSYS FLUENT 14.0 is outlined below:

1. Create and mesh the geometry model using ANSYS ICEM CFD
2. Import geometry into ANSYS FLUENT 14.0
3. Define the solver model
4. Define the turbulence model
5. Define the species model

6. Define the materials and the chemical reactions
7. Define phases: primary and secondary phase
8. Define phase interactions, such as drag force, heterogeneous reactions, etc.
9. Define the boundary conditions
10. Define region adaptation and patching
11. Initialize the calculations
12. Iterate/calculate until convergence is achieved
13. Post processes the results.

ANSYS FLUENT 14.0 offers two solution methods: (a) Pressure-based solution method and (b) density-based solution method. The pressure-based solution method solves the governing equations of continuity, momentum, energy, and species transport sequentially. In the pressure-based solution, the non-linear governing equations are **implicitly** linearized, which means that each unknown value is computed using a relation that includes both existing and unknown values from neighboring cells. As a result, each unknown will appear in more than one equation in the linear system produced. Thus, these equations must be solved simultaneously in order to obtain the unknown quantities.

The non-linear governing equations can also be linearized **explicitly** with respect to the dependent variables. If the equations are linearized explicitly, the unknown value in each cell is computed using a relation that includes only existing values.

The governing equations are discretized spatially to yield discrete algebraic equations for each control volume. There are several discretization schemes available in ANSYS FLUENT:

(a) First Order
(b) Second Order
(c) Power Law
(d) QUICK

The second order scheme is used as the discretization scheme for the momentum, turbulence kinetic energy "k" and dissipation rate "ε," energy, and species equations. The volume fraction of the

solid phase uses the QUICK scheme. ANSYS FLUENT also provides three algorithms for pressure-velocity coupling in the pressure-based solver:

(a) SIMPLE
(b) SIMPLEC
(c) PISO

The SIMPLE algorithm (Patankar et. al, 1980) is used in this study to couple the pressure and velocity. The built-in standard k-ε turbulence model is used, and the model constants $C_{1\varepsilon}$, $C_{2\varepsilon}$, C_{μ}, σ_k, and σ_t have the following values:

$C_{1\varepsilon} = 1.44$, $C_{2\varepsilon} = 1.92$, $C_{\mu} = 0.09$, $\sigma_k = 1.0$, and $\sigma_{\varepsilon} = 1.3$.

The following boundary conditions on the surface geometry have been assigned in ANSYS ICEM CFD:

a. **Velocity inlet:** All of the inlet surfaces are defined as velocity inlets. The velocity, temperature, and the mass fractions of all species of the gas mixture are specified.
b. **Pressure outlet**: The outlet surface is assigned a known pressure value. Pressure, temperature, and species mass fractions of the gas mixture just downstream of the outlet (outside the domain) are specified. This information does not affect the calculations inside the computational domain, but will be used if backflow occurs at the outlet.
c. **Walls**: The outside surfaces are defined as a wall boundary, which means that the no-slip condition (zero velocity) is imposed on the stationary surface. For an adiabatic case, the heat flux on the wall is set to zero.

The primary phase enters the computational domain through the inlets. The iterations are conducted alternatively between the primary and the secondary phases. The primary phase is updated in the next iteration based on the secondary phase calculation results, and the process is repeated.

The detailed steps of the calculation process are given below. Figure 2.6 depicts the flow chart of these steps.

(i) Fluid properties are updated based on the current solution or the initialized solution.

(ii) The momentum equations are solved using the current values of pressure and face mass fluxes to get the updated velocity field.

(iii) The equation for the pressure correction is calculated from the continuity equation and the linearized momentum equations since the velocity field obtained in step (ii) may not satisfy the continuity equation.

(iv) The pressure correction equations obtained from step (iii) are solved to correct the pressure and velocity fields and face mass such that the continuity equation is satisfied.

(v) The equations for turbulence are solved using the updated values of the other variables.

(vi) The homogeneous gas phase reactions are solved. Production and consumption of each species are calculated.

(vii) Enthalpy changes due to reaction are calculated.

(viii) The species transport equations are solved. Changes in the species mass fraction due to the reactions in steps (vi) and (xii) appear as source or sink terms in the species transport equations.

(ix) The energy equation is solved. This includes source or sink terms due to reactions in steps (vi) and (vii).

----- Start Secondary Phase----------

(x) The forces on the particles (secondary phase), such as the drag force, lift force, and virtual mass force, are calculated.

(xi) The particles' (secondary phase) heat transfer rate is calculated.

(xii) Heterogeneous reactions (gas-solid) are calculated. Production and consumption of each species are calculated.

(xiii) Enthalpy changes due to reaction are calculated.

(xiv) The species transport equations are solved. Changes in the species mass fraction due to the reactions in step (xii) appear as source or sink terms in the species transport equation.

(xv) The energy equation is solved. This includes source or sink terms due to reactions in steps (xiii) and (xiv).

(xvi) Primary phase properties are updated based on the secondary phase.

(xvii) The equation is checked for convergence.

(xviii) If convergence criteria are met, the process is stopped. Otherwise, the process is repeated from step (i).

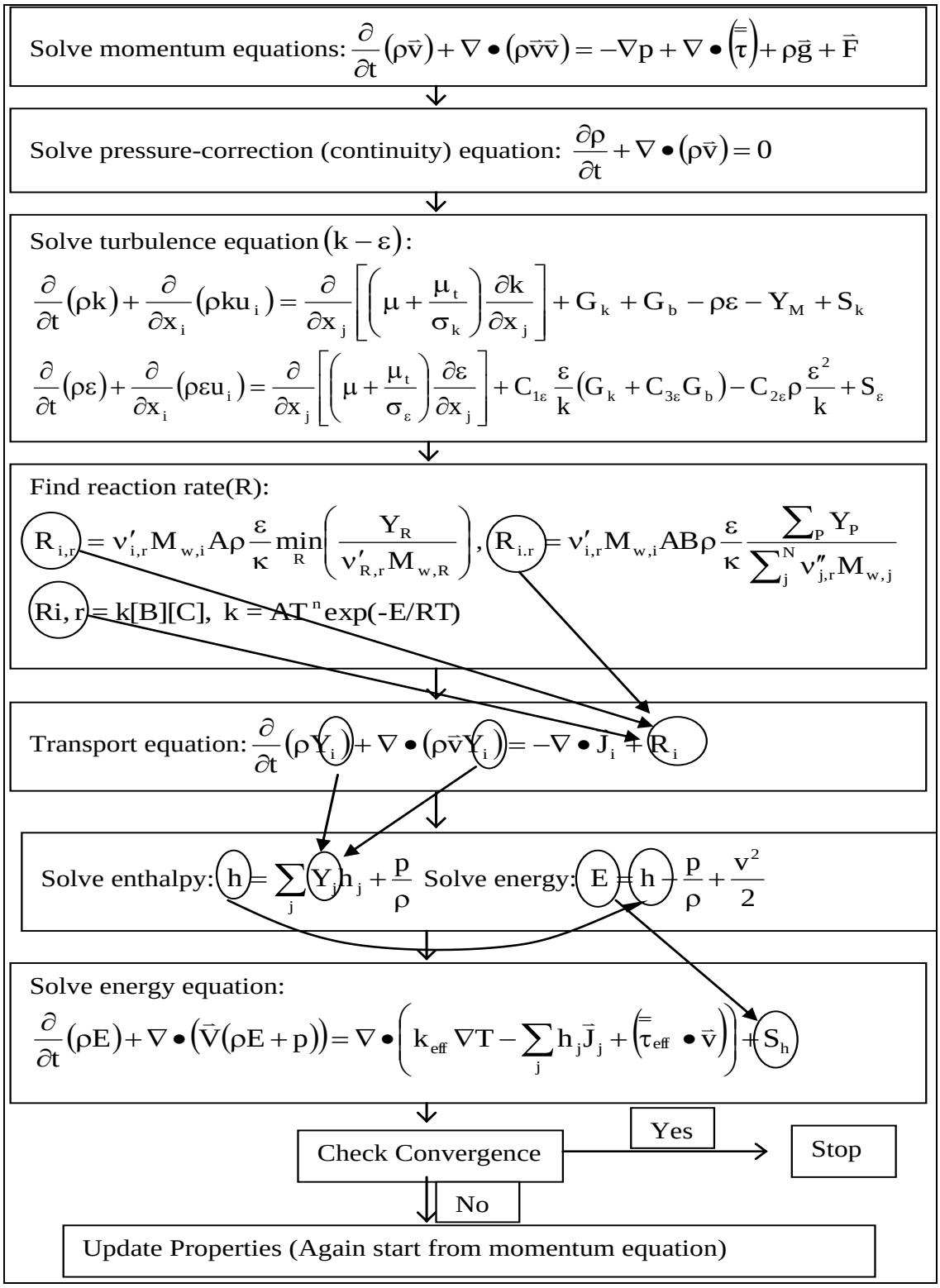

Figure 2.6 Outline of the numerical procedures for the gaseous (primary) phase. The heterogeneous reaction (secondary) follows the similar process. Iterations proceed alternately between the primary and secondary phases.

2.3.4 Convergence Criterion

There are no universal metrics for judging convergence. Convergence can be hindered by a number of factors, including: number of computational cells, underestimated relaxation factors, and complex flow physics. In this study, the convergence criterion of 10^{-3} for the residuals of the continuity, momentum, and energy equations for both gas and solid phases; the turbulence kinetic energy "k" and dissipation rate "ε;" species equations; and volume fraction of coal phase are chosen for the transient case.

For the baseline case (Case 2: coal mild gasification), the solution convergence is obtained by monitoring the residuals of the continuity, momentum, and energy equations for both gas and coal phases; turbulence; species equations; and volume fraction of the coal phase separately as follows:

- ✓ Continuity (mass conservation) < 8×10^{-1}
- ✓ X-velocity of gas phase < 6×10^{-3}
- ✓ X-velocity of coal phase < 3×10^{-6}
- ✓ Y-velocity of gas phase < 6×10^{-3}
- ✓ Y-velocity of coal phase < 2×10^{-6}
- ✓ Energy of gas phase < 5×10^{-4}
- ✓ Energy of coal phase < 5×10^{-7}
- ✓ k (turbulence energy) < 6×10^{-4}
- ✓ ε (turbulence dissipation) < 6×10^{-4}
- ✓ O_2 < 3×10^{-5}
- ✓ CO < 7×10^{-4}
- ✓ CO_2 < 7×10^{-4}
- ✓ H_2 < 7×10^{-4}
- ✓ H_2O < 5×10^{-5}
- ✓ Volume fraction of solid phase < 1×10^{-4}

Figure 2.7 shows the residuals for the transient template case (Case 2: coal mild gasification). The fluctuations in the residuals' history is not caused by instability of computation oscillations, rather it is a typical feature caused by alternating iterations between the coal and gas phases.

The physical iteration time step size is 2×10^{-4} seconds. Typically, 10,000 time steps are required to achieve convergence with 200 iterations in each time step. Computation is conducted in an 8-node, 64-bit computer with 16GB of RAM. A typical converged run of a 2-D case takes approximately 48 hours (2 days).

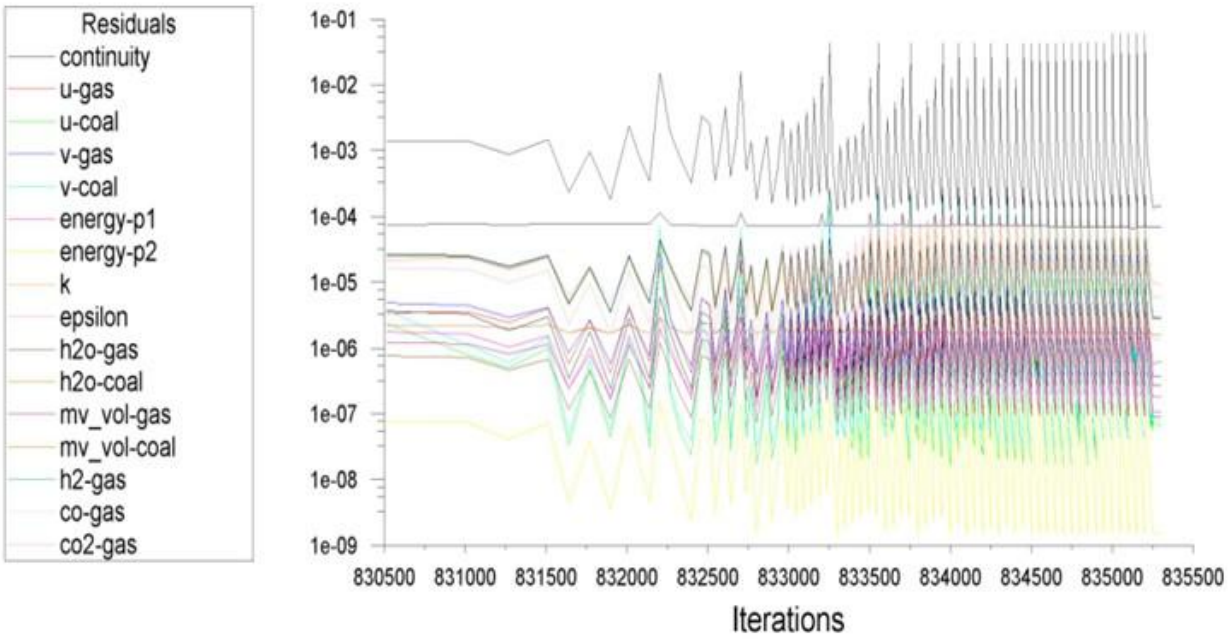

Figure 2.7 Residuals for the transient ultimate case (Case 2: coal mild gasification). The fluctuations in the residuals' history is not caused by instability of computation oscillations, rather it is a typical feature caused by alternating iterations between the coal and gas phases. (Note: Iterations before 830,500 steps are not shown for clarity.)

2.3.5 Material Properties

Variable properties for enthalpy, specific heat, and conductivity are used for each species. The specific heat is calculated using a piecewise-polynomial relation as a function of temperature, which is defined as:

$$\text{For } T_{min1} < T < T_{max1},\ F(T) = A_1T + A_2T^2 + A_3T^3 + \ldots$$
$$\text{For } T_{min2} < T < T_{max2},\ F(T) = B_1T + B_2T^2 + B_3T^3 + \ldots \quad (2.76)$$

The specific heat of the primary phase, which is a mixture of species, is also variable and is calculated as a mass fraction average of the individual species heat capacities, defined as:

$$F = \sum_i Y_i F_i \quad (2.77)$$

where F is the property (enthalpy, specific heat, or conductivity), Y_i is the mass fraction of species i, and F_i is the property of species i.

The density of mixture phases were defined by a User Defined Function.

2.3.6 Patching Temperature

The initial gas temperature in the gasifier is specified to be the same as the gas temperature at the inlets, which is 300 K in this study. Gasification will not occur at this temperature becausethe energy available at this temperature is below the activation energy of the reactions. Thus, the reactions will not occur. High temperature is needed to start the reactions. Thus, the domain needs to be patched with a higher temperature. This process is akin to using a lighter to ignite combustion inside a combustor. This temperature patching is done by setting the temperature of the cells near the injections to 1600K, which is high enough to start the devolatilization reactions.

2.3.7 Under-relaxation Factor

The under-relaxation factor for variables can slow down the convergence behavior of the variables. Equation 2.78 defines how the under-relaxation factor, α, affects the value of the variable.

$$\phi = \phi_{old} + \alpha \, \Delta\phi \tag{2.78}$$

ϕ is the variable and $\Delta\phi$ is the change in the variable. The value of the under-relaxation factor, α, ranges from 0 to 1. Therefore, the smaller the under-relaxation factor, the smaller the change in the variable during the iteration. It can help stabilize the convergence, but makes the simulation require more iteration steps to reach convergence. In this study, the under-relaxation factors are set to 0.3 for pressure, 0.7 for momentum, 0.2 for volume fraction of the secondary phase, and 0.8 for species, k, and ε.

CHAPTER THREE
MODELING MULTIPHASE FLOWS

3.1 Introduction

In multiphase flow modeling, each of the phases is considered to have a separately defined volume fraction and velocity field. Conservation equations for the flow of each species can be written down straightforwardly; however, the momentum equation for each phase is less straightforward. It can be shown that a common pressure field can be defined, and that each phase is subject to the gradient of this field, weighted by the volume fractions. There are various forms of multiphase flow; four different groups are categorized and elaborated in this chapter.

3.2 Multiphase Flow Regimes

Multiphase flow regimes can be separated into four categories:

a. Gas-liquid flows
b. Gas-solid flows
c. Liquid-solid flows
d. Three-phase flows

a. Gas-liquid flows

The following regimes are known as gas-liquid or liquid-liquid flows:

- Bubble flows: This is a kind of flow where small bubbles are dispersed or suspended as discrete substances in a liquid continuum. Typical features of this flow are moving and deformable interfaces of bubbles in the time and space domains and complex interactions between the interfaces and also between the bubbles and the liquid flow. According to the magnitude of these interactions, bubble flow is classified into four different flow regimes: i.e. ideally-separated bubble flow, interacting bubble flow, churn turbulent bubble flow, and clustered bubble flow.

- Slug flows: The word slug normally refers to a heavier, slower moving fluid, but sometimes to the bubbles of a lighter fluid. There are also small bubbles within the liquid, but many of these have coalesced to form larger bubbles that eventually span across the entire pipe. In gas-liquid flow mixtures, a slug flow is similar to a plug flow, but the bubbles are generally larger and move faster. As flow rates increase, slug flow becomes churn flow.
- Stratified/free-surface flow: This is the flow of immiscible fluids separated by an interface. Example: sloshing in offshore separator devices and boiling and condensation in nuclear reactors.

b. Gas-solid flows

The following regimes are known as gas-solid flows:

- Gas-particle flows: This type of flow is characterized by the flow of gases with suspended solids. This type of flow is fundamental to many industrial processes such as pneumatic transport, particulate pollution control, combustion of pulverized coal, drying of food products, sand blasting, plasma-arc coating, and fluidized bed mixing. The dynamics and thermal history of particles in gases also affect the performance of rocket motors using metalized fuels, the quality of some pharmaceutical products and the design of advanced techniques for materials processing. This is the flow of discrete particles in a continuous gas.

c. Liquid-solid flows

The following regimes are known as liquid-solid flows:

- Slurry flows: This flow is a mixture in which fine particles are suspended in a fluid where they are supported by buoyancy. Example: slurry transport and mineral processing.
- Hydro-transport: This is the flow that describes densely-distributed solid particles in a continuous liquid. Example: mineral processing and biomedical and physiochemical fluid systems.

- Sediment transport: This is the movement of solid particles (sediment), typically due to a combination of the force of gravity acting on the sediment, and/or the movement of the fluid in which the sediment is entrained. Sediment transport due to fluid motion occurs in rivers, the ocean, lakes, seas, and other bodies of water due to currents and tides; in glaciers; and on terrestrial surfaces under the influence of wind.

d. Three-phase flows

Three-phase flows are combinations of the other flow regimes listed above.

- Bubbles in a slurry flow
- Droplets/particles in gaseous flows

3.3 Approaches of Multiphase Modeling

Two approaches are generally considered for simulating multiphase flows:

1. The Eulerian-Lagrangian approach and
2. The Eulerian-Eulerian approach

3.3.1 Eulerian-Lagrangian Approach

In the Eulerian-Lagrangian approach, the fluid phase is treated as a continuum by solving the time-averaged Navier-Stokes equations, while the dispersed phase is solved by tracking a large number of particles, bubbles, or droplets through the calculated flow field. The dispersed phase exchanges momentum, mass, and energy with the fluid phase. In this model, the fundamental assumption is that, even though high mass loading is acceptable, the dispersed phase occupies a low volume fraction. During the fluid phase calculation, the particle or droplet trajectories are computed individually at particular intervals. This makes the model appropriate for the modeling of spray dryers, coal and liquid fuel combustion, and some gas-particle flows. This model is inappropriate for the modeling of fluidized

beds, liquid-liquid mixtures, or any application where the volume fraction of the second phase is not negligible.

3.3.2 Eulerian-Eulerian Approach

In the Eulerian-Eulerian approach, the different phases are treated mathematically as interpenetrating continua. The concept of phasic volume fraction is introduced in this approach. These volume fractions are assumed to be continuous functions of space and time and their sum is equal to one. For each phase, conservation equations are derived to obtain a set of equations which have similar structure for all phases. These equations are closed by providing constitutive relations that are obtained from empirical information, or, in the case of granular (solid) flows, by the application of kinetic theory. There are three different Eulerian-Eulerian multiphase models:

1. The volume of fluid (VOF) model
2. The mixture model
3. The Eulerian model

The Eulerian model of the Eulerian-Eulerian approach is used in this study. The detailed description of this model is presented later section in this chapter.

3.3.2.1 The Volume of Fluid (VOF) Model

The VOF model is a surface-tracking technique applied to a fixed Eulerian mesh. It is designed for two or more immiscible fluids. In the VOF model, a single set of momentum equations is shared by the fluids, and the volume fraction of each of the fluids in each computational cell is tracked throughout the domain. The applications of the VOF model are stratified flows, free-surface flows, the motion of large bubbles in a liquid, the prediction of jet breakup (surface tension), the steady or transient tracking of any liquid-gas interface, etc.

3.3.2.2 The Mixture Model

The applications of the mixture model are gas-particle flows with low loading, bubbly flows, sediment transport, cyclone separators, etc. This model is suitable for flows in which the dispersed-phase volume fractions are less than or equal to 10%. The mixture model is a simplified multiphase model that can be used to model multiphase flows where there are existing velocity gradients between the phases. However, it still assumes that equilibrium happens locally though a short spatial length scale. The mixture model is a good substitute for the full Eulerian multiphase model sometimes, if the interphase laws are unable to be acquired or are not trustful, or there is a wide distribution of the particulate phase. A simplified model such as mixture model can replace the role of Eulerain multiphase model with solving a smaller number of variables. The mixture model allows the phases to be interpenetrating. The interphase slip velocity is assigned to be zero (i.e., no drag law is applied between the phases) or solved by an algebraic equation. The volume fractions for different phases for a defined volume can therefore be equal to any value between 0 and 1, relying on the space occupied by individual phases. Also, the mixture model allows the phases to move at different velocities by using the definition of slip velocity.

3.3.2.3 The Eulerian Model

The Eulerian model is the most complex multiphase model. This model allows for the modeling of multiple separate, yet interacting phases. The phases can be liquids, gases, or solids in nearly any combination. Any number of secondary phases can be modeled by this multiphase model if sufficient memory is available. It solves a set of "n" momentum and continuity equations for each phase. There is a coupling between the pressure and interphase exchange coefficients in this model. The applications of the Eulerian multiphase model are bubble columns, risers, particle suspension, and fluidized beds. Three extensions of the Eulerian Model can help deal with specific conditions including a dense discrete phase, wall boiling, and sharper interfacial contours of the VOF model.

3.3.2.3.1 The Dense Discrete Phase Model

The dense discrete phase model (DDPM) extends from the Eulerian multiphase model by allowing for phases to be represented by a Lagrangian description for all volume fractions up to the maximum packing. This model provides solutions to problems that involve the need to model particle tracks as well as those that involve a wide range of particle sizes.

The essential idea of this model is to assume that the volume fraction of the discrete phase is sufficiently low, and not taken into account when assembling the continuous phase equations. The momentum exchange term is considered only in the primary equations in this model. In the resulting set of equations (one continuity and one momentum conservation equation per phase) those corresponding to a discrete phase are not solved. The solution of the discrete phase parameters, such as volume fraction or velocity field, is taken from the Lagrangian tracking solution. Since the given approach makes use of the Eulerian multiphase model framework, it does have some limitations:

- The turbulence models: Large Eddy Simulation (LES) and Direct Eddy Simulation (DES) turbulence models are not applicable.
- The combustion models: Finite-rate kinetics in turbulent flames, Premixed, Non-premixed and partially premixed combustion models are not applicable.
- The solidification and melting models are not applicable.
- The Wet Steam model is not applicable.
- The real gas model (pressure-based and density-based) is not applicable.
- The density-based solver and models dependent on it are not applicable.
- The Parallel Discrete Particle Model (DPM) with the shared memory option is not available.

3.3.2.3.2 The Wall Boiling Model

The wall boiling phenomenon is modeled by the Rensselaer Polytechnic Institute (RPI) nucleate boiling model of Kurual and Podowski (1991) and an extended formulation for the departed nucleate boiling (DNB) regime by Lavieville et al (2005). The term "subcooling boiling" is used to describe the

physical situation where the wall temperature is high enough to cause boiling to occur at the wall even though the bulk volume averaged liquid temperature is less than the saturation value. Under this circumstance, the energy is transferred directly from the wall to the liquid. Part of this energy will cause the temperature of the liquid to increase and part will generate vapor. Interphase heat transfer will also increase the average liquid temperature. Nevertheless, the saturated vapor will condense. Additionally, some of the energy may be transferred directly from the wall to the vapor. These basic mechanisms are the foundations of the so called RPI models. The wall boiling models are compatible with three different wall boundaries: isothermal wall, specified heat flux, and specified heat transfer coefficient (coupled wall boundary).

3.3.2.3.3 The Multi-Fluid VOF Model

The multi-fluid VOF model for the Eulerian multiphase model can do both the geo-reconstruct and the Compressive Interface Capturing Scheme for Arbitrary Meshes (CICSAM) sharpening schemes with the explicit VOF algorithm. This model is only applicable for a problem which requires sharp interface treatment between phases. This model might help in overcoming some limitations of the VOF model because of the shared velocity and temperature formulation. This multi-fluid VOF model in the context of the Eulerian multiphase model offers the anisotropic drag law, which can be used for free surface flow modeling, and also can be used while there is higher drag in the normal direction of the interface and lower drag in the tangential direction of the interface.

To compare the above three models of the Eulerian-Eulerian approach, the volume of fluid (VOF) model is suitable for stratified or free-surface flows, and the mixture and Eulerian models are appropriate for flows in which the phases mix or separate and/or the dispersed-phase volume fractions exceed 10%.

Consider the following guidelines to choose between the mixture model and the Eulerian model:

- If there is a wide distribution of the dispersed phases, the mixture model is more preferable than Eulerian model as it is less computationally expensive.

- If inter-phase drag laws are applicable to the system, the Eulerian model gives more accurate results than the mixture model. If the inter-phase drag laws are unknown or their applicability to the system is open to discussion, the mixture model is a better choice.
- To solve a simpler problem, the mixture model is a better choice, since it solves a smaller number of equations which requires less computational effort than the Eulerian model. If accuracy is more important than computational effort, the Eulerian model is a better choice.

3.4 Eulerian Multiphase Model Theory

Detailed descriptions of the Eulerian multiphase model are presented here because this model is used in this study. A single set of conservation equations for momentum, continuity, and energy is solved in a single-phase model. To change from a single-phase model to a multiphase model, additional sets of conservation equations have to be introduced. The modifications involve the introduction of the volume fraction, ε, for the multiple phases and the exchange mechanisms of momentum, heat, and mass between the phases.

3.4.1 Conservation Equations using the Eulerian Multiphase Model

The equations for conservation of mass, momentum, and energy used in the Eulerian multiphase model are presented below:

Conservation of Mass

The continuity equation for phase "q" is:

$$\frac{\partial}{\partial t}\left(\varepsilon_q \rho_q\right) + \nabla \bullet \left(\varepsilon_q \rho_q \vec{v}_q\right) = \sum_{p=1}^{n}\left(\dot{m}_{pq} - \dot{m}_{qp}\right) + S_q \qquad (3.1)$$

where $\vec{v}_q$ = the velocity of phase "q,"

$\dot{m}_{pq}$ = the mass transfer from phase "p" to "q,"

$\dot{m}_{qp}$ = the mass transfer from phase "q" to "p,"

ε_q = the volume fraction of phase "q," and

S_q = the source term of phase "q"

Conservation of Momentum

The momentum balance for phase "q" is:

$$\frac{\partial}{\partial t}\left(\varepsilon_q \rho_q \vec{v}_q\right)+\nabla\bullet\left(\varepsilon_q \rho_q \vec{v}_q \vec{v}_q\right)=-\varepsilon_q \nabla p+\nabla\bullet\left(\overline{\overline{\tau}}_q\right)+$$
$$\varepsilon_q \rho_q \vec{g}+\sum_{p=1}^{n}\left(\vec{R}_{pq}+\dot{m}_{pq}\vec{v}_{pq}-\dot{m}_{qp}\vec{v}_{qp}\right)+\vec{F}_q+\vec{F}_{lift,q}+\vec{F}_{vm,q} \qquad (3.2)$$

where $\overline{\overline{\tau}}_q$, is the stress-strain tensor of phase "q" given by:

$$\overline{\overline{\tau}}_q=\varepsilon_q \mu_q\left(\nabla\vec{v}_q+\nabla\vec{v}_q^{T}\right)+\varepsilon_q\left(\lambda_q-\frac{2}{3}\mu_q\right)\nabla\bullet\vec{v}_q\bullet\overline{\overline{I}} \qquad (3.3)$$

The inter-phase force, $\vec{R}_{pq}$, depends on the friction, pressure, cohesion, and other effects and is subject to the conditions that $\vec{R}_{pq}=-\vec{R}_{qp}$ and $\vec{R}_{qq}=0$ is given by:

$$\sum_{p=1}^{n}\vec{R}_{pq}=\sum_{p=1}^{n}K_{pq}\left(\vec{v}_p-\vec{v}_q\right) \qquad (3.4)$$

where μ_q = the shear viscosity of phase "q,"

λ_q = the bulk viscosity of phase "q,"

$\vec{F}_q$ = an external body force of phase "q,"

$\vec{F}_{lift,q}$ = a lift force of phase "q,"

$\vec{F}_{vm,q}$ = a virtual mass force of phase "q,"

$\vec{R}_{pq}$ = an interaction force between phase "p" and "q,"

∇p = the pressure gradient shared by all phases,

$\vec{v}_{pq}$ = the inter-phase velocity,

$\vec{g}$ = acceleration due to gravity, and

K_{pq} = the inter-phase momentum exchange coefficient.

Conservation of Energy

To describe the conservation of energy in the Eulerian multiphase model, a separate enthalpy equation is written for each phase, and is of the form:

$$\frac{\partial}{\partial t}\left(\varepsilon_q \rho_q h_q\right) + \nabla \bullet \left(\varepsilon_q \rho_q \vec{v}_q h_q\right) = -\varepsilon_q \frac{\partial p_q}{\partial t} + \overline{\overline{\tau}}_q : \nabla \vec{v}_q - \nabla \bullet \vec{q}_q + S_q + \sum_{p=1}^{n}\left(Q_{pq} + \dot{m}_{pq} h_{pq} - \dot{m}_{qp} h_{qp}\right) \quad (3.5)$$

where h_q= the specific enthalpy of the phase "q,"

$\vec{q}_q$ = the heat flux of the phase "q,"

S_q = a source term that includes sources of enthalpy,

Q_{pq}= the intensity of heat exchange between the phase "p" and "q," and

h_{pq}= the inter-phase enthalpy.

3.4.2 Description of Momentum Equations

To describe the conservation of momentum equations in the Eulerian model, several equations need to be written for each phase, such as: lift forces, virtual mass forces, inter-phase momentum exchange coefficients, solid pressures, solid shear stresses, and granular temperatures.

3.4.2.1 Lift Forces

The effect of lift forces on the particles, droplets, or bubbles are included in the multiphase flow calculations. These lift forces act on a particle mainly due to velocity gradients in the primary-phase flow field. It is more significant for larger particles. If the particle diameter is much smaller than the inter-particle spacing and closely packed particles, the inclusion of lift forces is not appropriate.

The lift force acting on a secondary phase "p" in a primary phase "q" is computed from following equation:

$$\vec{F}_{lift} = -0.5\,\rho_q\,\varepsilon_p\left(\vec{v}_q - \vec{v}_p\right)\times\left(\nabla\times\vec{v}_q\right) \tag{3.6}$$

The lift force is insignificant in most cases compared to the drag force, so there is no reason to include this extra term. It is important to note that if the lift force is included in the calculation, this term needs not be included everywhere in the computational domain since it makes achieving convergence more computationally expensive. The lift force, $\vec{F}_{lift}$, needs be added to the right-hand side of the momentum equation (Eq. 3.2) for both phases, i.e. $(\vec{F}_{lift}, q = -\vec{F}_{lift}, p)$.

3.4.2.2 Virtual Mass Force

In multiphase flows, the effect of "virtual mass force" exists when a secondary phase "p" accelerates relative to the primary phase "q". The inertia of the primary phase mass encountered by the accelerating particles, droplets, or bubbles exerts a "virtual mass force" on the particles, as in Eq. 3.7:

$$\vec{F}_{vm} = 0.5\,\rho_q\,\varepsilon_p\left(\frac{d_q\,\vec{v}_q}{dt} - \frac{d_p\,\vec{v}_p}{dt}\right) \tag{3.7}$$

The term $\left(\frac{d_q}{dt}\right)$ denotes the phase material time derivative, which has the following form:

$$\frac{d_q(\phi)}{dt} = \frac{\partial(\phi)}{\partial t} + \left(\vec{v}_q\cdot\nabla\right)\phi \tag{3.8}$$

The virtual mass effect is significant when the secondary phase density is much smaller than the primary phase density. The virtual mass force is neglected in this study as the secondary phase density (the density of carbon solid is 2000 kg/m^3) is much larger than the primary phase density (the density of air is 1.225 kg/m^3.)

3.4.2.3 Inter-phase Momentum Exchange Coefficient

One of the major differences between the single phase momentum equation and the Eulerian multiphase momentum equation is the interphase momentum exchange coefficient. This term is needed if the Eulerian multiphase momentum equation needs to be solved. Three kinds of interphase momentum exchange coefficients are available: One for the fluid-fluid momentum equations known as the fluid-fluid exchange coefficient, the second one for the fluid-solid momentum equation (granular flows) known as the fluid-solid exchange coefficient, and the third one for the solid-solid exchange coefficient.

3.4.2.3.1 Fluid-Fluid Momentum Equations

For a fluid phase "q" the conservation of momentum equation is:

$$\frac{\partial}{\partial t}\left(\varepsilon_q \rho_q \vec{v}_q\right) + \nabla \bullet \left(\varepsilon_q \rho_q \vec{v}_q \vec{v}_q\right) = -\varepsilon_q \nabla p + \nabla \bullet \left(\overline{\overline{\tau}}_q\right) + \varepsilon_q \rho_q \vec{g} + \sum_{p=1}^{n}\left(K_{pq}\left(\vec{v}_p - \vec{v}_q\right) + \dot{m}_{pq}\vec{v}_{pq} - \dot{m}_{qp}\vec{v}_{qp}\right) + \vec{F}_q + \vec{F}_{lift,q} + \vec{F}_{vm,q} \tag{3.9}$$

The exchange coefficient for these types of liquid-liquid or gas-liquid mixtures is known as the **fluid-fluid exchange coefficient,** K_{pq}, which can be written as:

$$K_{pq} = \frac{\varepsilon_q \varepsilon_p \rho_p f}{\tau_p} \tag{3.10}$$

where f = the drag function is defined differently for the different exchange coefficient models. τ_p = the "particulate relaxation time" is defined as:

$$\tau_p = \frac{\rho_p d_p^2}{18\mu_q} \tag{3.11}$$

where d_p = the diameter of the droplets or bubbles of phase "p".

The definition of the drag function "f" includes a drag coefficient, C_D, that is based on the relative Reynolds number, Re, which is calculated by the relative velocity between the two phases. The drag function "f" is always multiplied by the volume fraction of the primary phase "q", as the fluid-fluid exchange coefficient K_{pq} should become zero whenever the primary phase is not present within the domain. The drag function "f" differs among the exchange coefficient models. From the model of Schiller and Naumann (1935):

$$f = \frac{C_D \, Re}{24} \tag{3.12}$$

where the drag coefficient, C_D, is defined as:

$$C_D = \frac{24\left(1 + 0.15\,Re^{0.687}\right)}{Re} \qquad \text{when } Re \le 1000 \tag{3.13a}$$

$$C_D = 0.44 \qquad \textit{when } Re > 1000 \tag{3.13b}$$

and Re is the relative Reynolds number. The relative Reynolds number for the primary phase "q" and secondary phase "p" is obtained based on the relative velocity between the two phases as:

$$Re = \frac{\rho_q \left| \vec{v}_p - \vec{v}_q \right| d_p}{\mu_q} \tag{3.14}$$

The Schiller and Naumann (1935) model is acceptable for all fluid-fluid pairs of phases.

3.4.2.3.2 Fluid-Solid Momentum Equations

For a solid phase "s" the conservation of momentum equation is:

$$\frac{\partial}{\partial t}\left(\varepsilon_s \rho_s \vec{v}_s\right)+\nabla\bullet\left(\varepsilon_s \rho_s \vec{v}_s \vec{v}_s\right)=-\varepsilon_s \nabla p-\nabla p_s+\nabla\bullet\left(\overline{\overline{\tau}}_s\right)$$
$$+\varepsilon_s \rho_s \vec{g}+\sum_{l=1}^{n}\left(K_{ls}\left(\vec{v}_l-\vec{v}_s\right)+\dot{m}_{ls}\vec{v}_{ls}-\dot{m}_{sl}\vec{v}_{sl}\right)+\vec{F}_s+\vec{F}_{lift,s}+\vec{F}_{vm,s} \qquad (3.15)$$

where p_s = the solid pressure of the solid phase "s" and

$K_{ls} = K_{sl}$ = the momentum exchange coefficient between fluid phase "l" and solid phase "s".

The solid-phase stresses are derived by making an analogy between the random particle motion arising from particle-particle collisions and the thermal motion of molecules in a gas, taking into account the inelasticity of the granular phase. Similar to a gas, the intensity of the particle velocity fluctuations determines the stresses, viscosity, and pressure of the solid phase. The kinetic energy associated with the particle velocity fluctuations is represented by a "pseudo-thermal" or granular temperature which is proportional to the mean square of the random motion of particles. The interphase momentum exchange coefficients in the fluid-solid momentum equation are evaluated by a fluid-solid exchange coefficient and a solid-solid exchange coefficient.

(a) The fluid-solid exchange coefficient, K_{sl}, can be written in the following general form:

$$K_{sl}=\frac{\varepsilon_s \rho_s f}{\tau_s} \qquad (3.16)$$

where f = the drag function, is defined differently for the different exchange-coefficient models τ_s = the "particulate relaxation time," is defined as

$$\tau_s=\frac{\rho_s d_s^2}{18\mu_l} \qquad (3.17)$$

where d_s = the diameter of particles of phase "s."

The definition of the drag function "f" includes a drag coefficient, C_D, that is based on the relative Reynolds number, Re_s. The drag function "f" differs among the exchange coefficient models. For the model of Syamlal and O'Brien (1989):

$$f = \frac{C_D \, Re_s \, \varepsilon_l}{24 \, v_{r,s}^2} \tag{3.18}$$

where $v_{r,s}$ = the terminal velocity for the solid phase "s" and C_D = the drag coefficient with the following form derived by Valle (1948):

$$C_D = \left(0.63 + \frac{4.8}{\sqrt{Re_s / v_{r,s}}} \right)^2 \tag{3.19}$$

The Syamlal and O'Brien model is based on measurements of the terminal velocities of particles in fluidized or settling beds, with correlations that are a function of the volume fraction and relative Reynolds number, which is defined as:

$$Re_s = \frac{\rho_l \left| \vec{v}_s - \vec{v}_l \right| d_s}{\mu_l} \tag{3.20}$$

where the subscript "l" is for the fluid phase "l," the subscript "s" is for the solid phase "s," and d_s is the diameter of the particles in the solid phase "s".
The terminal velocity correlation for the solid phase "s" has the following form:

$$v_{r,s} = 0.5 \left(A - 0.06 \, Re_s + \sqrt{(0.06 \, Re_s)^2 + 0.12 \, Re_s \left(2B - A \right) + \left(A \right)^2} \right) \tag{3.21}$$

with $A = \varepsilon_l^{4.14}$

and $B = 0.8 \, \varepsilon_l^{1.28}$ for $\varepsilon_l \leq 0.85$

or $B = \varepsilon_l^{2.65}$ for $\varepsilon_l > 0.85$

This model is appropriate when the solid shear stresses are defined according to M. Syamlal and T. J. O'Brien (1989).

(b) The solid-solid exchange coefficient, K_{sl}, can be written in the following general form:

$$K_{sl} = \frac{3\left(1+e_{sl}\right)\left(\frac{\pi}{2}+C_{fr,sl}\frac{\pi^2}{8}\right)\varepsilon_s\,\rho_s\,\varepsilon_l\,\rho_l\left(d_l+d_s\right)^2 g_{o,sl}\left|\bar{v}_s-\bar{v}_l\right|}{2\,\pi\left(\rho_s\,d_s^3+\rho_l\,d_l^3\right)} \qquad (3.22)$$

where e_{sl} = the coefficient of restitution,

$C_{fr,sl}$ = the coefficient of friction between the solid phase "s" and "l" particles,

d_l = the diameter of the particles of solid phase "l,"

and $g_{o,sl}$ = the radial distribution coefficient.

The description of coefficient of restitution, the solid pressure, the radial distribution coefficient, the solid shear stresses, and the granular temperature are given below.

3.4.2.3.2.1 Solids Pressure

For granular (solid) flows in the compressible regime, i.e. where the solid volume fraction is less than its maximum allowed value, a solid pressure is calculated independently. This solid pressure is used for the pressure gradient term, ∇p_s, in the granular-phase fluid-solid momentum equation. A granular temperature is introduced into the model and appears in the expression for the solid pressure because a Maxwellian velocity distribution is used for the particles. The solid pressure is composed of a kinetic term and a second term due to particle collisions:

$$p_s = \varepsilon_s\,\rho_s\,\theta_s + 2\,\rho_s\left(1+e_{ss}\right)\varepsilon_s^2\,g_{o,ss}\,\theta_s \qquad (3.23)$$

where e_{ss} = the coefficient of restitution for particle collisions,

$g_{o,ss}$ = the radial distribution function, and

θ_s = the granular temperature.

3.4.2.3.2.2 Radial Distribution Function

The radial distribution function, g_o, is a correction factor that modifies the probability of collisions between grains when the solid granular phase becomes dense. This is also a distribution function that governs the transition from the "compressible" condition where the spacing between the solid particles can continue to decrease to the "incompressible" condition where no further decrease in the spacing can occur. This function may also be interpreted as the non-dimensional distance between sphere centers:

$$g_o = \frac{s + d_p}{s} \tag{3.24}$$

where s = the distance between grains and d_p = the diameter of a particle.

The radial distribution function is closely connected to the factor "χ" of Chapman and Cowling's theory (1990) of non-uniform gases. "χ" is equal to 1 for a rarified gas, and increases and tends to infinity when the molecules are so close together that motion is not possible.
There is no unique formulation for the radial distribution function in the literature but the following empirical functions can be used with discretion,

- ✓ For one solid phase:

$$g_o = \left[1 - \left(\frac{\varepsilon_s}{\varepsilon_{s,max}} \right)^{1/3} \right]^{-1} \tag{3.25}$$

- ✓ For "n" solid phases:

$$g_{o,kl} = \frac{1}{\left(1-\varepsilon_s\right)} + \frac{3\left(\sum_{k=1}^{n} \frac{\varepsilon_k}{d_k}\right) d_k\, d_l}{\left(1-\varepsilon_s\right)^2 \left(d_k + d_l\right)} \qquad (3.26)$$

Syamlal (1993) used this formula that was derived by Lebowitz (1964) for a mixture of hard spheres.

3.4.2.3.2.3 Solid Shear Stresses

Due to translation and collision, the solid stress tensor contains bulk and shear viscosities arising from particle momentum exchange.

Bulk Viscosity

The solid bulk viscosity accounts for the resistance of the granular particles to compression and expansion. It has the following form from Lun et al. (1984):

$$\lambda_s = \frac{4}{3}\varepsilon_s\, \rho_s\, d_s\, g_{o,ss} \left(1+e_{ss}\right)\left(\frac{\theta_s}{\pi}\right)^{1/2} \qquad (3.27)$$

Solid Shear Viscosity

The collisional and kinetic parts and the optional frictional part are added to give the solid shear viscosity:

$$\mu_s = \mu_{s,col} + \mu_{s,kin} + \mu_{s,fr} \qquad (3.28)$$

- ✓ **Collisional Viscosity**

  The collisional part of the shear viscosity is modeled from Gidaspow et al. (1992) and Syamlal et al. (1993):

$$\mu_{s,col} = \frac{4}{5}\varepsilon_s\,\rho_s\,d_s\,g_{o,ss}\left(1+e_{ss}\right)\left(\frac{\theta_s}{\pi}\right)^{1/2} \tag{3.29}$$

- ✓ **Kinetic Viscosity**

  The kinetic part of the shear viscosity is modeled from Syamlal et al. (1993):

$$\mu_{s,kin} = \frac{\varepsilon_s\,\rho_s\,d_s\,\sqrt{\theta_s\pi}}{6\left(3-e_{ss}\right)}\left[1+\frac{2}{5}\left(1+e_{ss}\right)\left(3e_{ss}-1\right)\varepsilon_s\,g_{o,ss}\right] \tag{3.30}$$

- ✓ **Frictional Viscosity**

  In dense flow at low shear, where the secondary volume fraction for a solid phase nears the packing limit, the generation of stress is mainly due to friction between particles. Schaeffer's expression can be used if the frictional viscosity is included in the calculation:

$$\mu_{s,fr} = \frac{p_s\,\sin\phi}{2\sqrt{I_{2D}}} \tag{3.31}$$

Where p_s = the solids pressure,

ϕ = the angle of internal friction, and

$I_{2\text{-}D}$ = the second invariant of the deviatoric stress tensor.

The frictional stresses are usually written in Newtonian form:

$$\tau_{friction} = -P_{friction}\,\vec{I} + \mu_{friction}\left(\nabla\vec{u}_s + \left(\nabla\vec{u}_s\right)^T\right) \tag{3.32}$$

The frictional stress is added to the stress predicted by the kinetic theory when the solid volume fraction exceeds a critical value, as in the following:

$$P_s = P_{kinetic} + P_{friction} \tag{3.33}$$

$$\mu_s = \mu_{kinetic} + \mu_{friction} \tag{3.34}$$

The derivation of the frictional pressure is mainly semi-empirical, while the frictional viscosity can be derived from first principles. The application of the modified Coulomb law leads to an expression of the form:

$$\mu_{friction} = \frac{P_{friction} \sin\phi}{2\sqrt{I_{2D}}} \tag{3.35}$$

3.4.2.3.2.4 Granular Temperature

The granular temperature, θ_s, for the solid phase "s" is proportional to the kinetic energy of the fluctuating particle motion. The transport equation derived from kinetic theory takes the following form derived by J. Ding & D. Gidaspow (1990):

$$\frac{3}{2}\left[\frac{\partial}{\partial t}\left(\varepsilon_s \rho_s \theta_s\right) + \nabla \bullet \left(\varepsilon_s \rho_s \vec{v}_s \theta_s\right)\right] = \left(-p_s \bar{\bar{I}} + \bar{\bar{\tau}}_s\right) : \nabla \vec{v}_s + \nabla \bullet \left(k_{\theta_s} \nabla \theta_s\right) - \gamma_{\theta_s} + \phi_{ls} \tag{3.36}$$

where

$\left(-p_s \bar{\bar{I}} + \bar{\bar{\tau}}_s\right) : \nabla \vec{v}_s$ = the generation of energy by the solid stress tensor,

$\left(k_{\theta_s} \nabla \theta_s\right)$ = the diffusion of energy (k_{θ_s} is the diffusion coefficient),

γ_{θ_s} = the collisional dissipation of energy, and

ϕ_{ls} = the energy exchange between the fluid or solid phase "l" and the solid phase "s."

The above equation describing the diffusive flux of granular energy contains the term $\left(k_{\theta_s} \nabla \theta_s\right)$. The diffusion coefficient for the granular energy, k_{θ_s}, is given by the model of Syamlal et al. (1993):

$$k_{\theta_s} = \frac{15 \varepsilon_s \rho_s d_s \sqrt{\theta_s \pi}}{4\left(41 - 33\eta\right)}\left[1 + \frac{12}{5}\eta^2\left(4\eta - 3\right)\varepsilon_s g_{o,ss} + \frac{16}{15\pi}\left(41 - 33\eta\right)\eta \varepsilon_s g_{o,ss}\right] \tag{3.37}$$

where $\eta = \frac{1}{2}\left(1+e_{ss}\right)$.

The rate of energy dissipation within the solid phase "s" due to collisions between particles is represented by the collisional dissipation of energy, γ_{θ_s}. This term is represented by the expression derived by Lun et al. (1984):

$$\gamma_{\theta_s} = \frac{12\left(1-e_{ss}^2\right)g_{o,ss}\,\rho_s\,\varepsilon_s^2\,\theta_s^{3/2}}{d_s\,\sqrt{\pi}} \tag{3.38}$$

The transfer of the kinetic energy of random fluctuations in particle velocity from the fluid or solid phase "l" to solid phase "s" is represented by:

$$\phi_{ls} = -3\,K_{ls}\,\theta_s \tag{3.39}$$

3.4.3 Description of Energy Equations

To describe the conservation of energy in terms of the Eulerian multiphase model, a separate enthalpy equation is written for each phase:

$$\frac{\partial}{\partial t}\left(\varepsilon_q\,\rho_q\,h_q\right)+\nabla\bullet\left(\varepsilon_q\,\rho_q\,\vec{v}_q\,h_q\right)=$$
$$-\varepsilon_q\frac{\partial p_q}{\partial t}+\overline{\overline{\tau}}_q:\nabla\vec{v}_q-\nabla\bullet\vec{q}_q+S_q+\sum_{p=1}^{n}\left(Q_{pq}+\dot{m}_{pq}\,h_{pq}-\dot{m}_{qp}\,h_{qp}\right) \tag{3.40}$$

where h_q= the specific enthalpy of the phase "q,"
Q_{pq} = the rate of energy transfer between the phase "p" and "q," and
h_{pq} = the inter-phase enthalpy.

The rate of energy transfer between the phases "p" and "q" is a function of the temperature difference, as in the following:

$$Q_{pq} = h_{pq} \left(T_p - T_q \right) \tag{3.41}$$

where $h_{pq} = h_{qp}$ = the heat transfer coefficient between the phases "p" and "q."

The heat transfer coefficient is related to the Nusselt number, Nu_p, of phase "p" and is given by:

$$h_{pq} = \frac{6\, k_q\, \varepsilon_q\, \varepsilon_p\, Nu_p}{d_p^2} \tag{3.42}$$

Here, k_q = the thermal conductivity of the phase "q."

The Nusselt number is determined from one of the many correlations reported in the literature. In the case of **fluid-fluid multiphase flows**, the correlation of Ranz and Marshall (1952) is given as:

$$Nu_p = 2.0 + 0.6\, Re_p^{1/2}\, Pr^{1/3} \tag{3.43}$$

where Re_p is the relative Reynolds number based on the diameter of the phase "p" and relative velocity. The relative Reynolds number for the primary phase "q" and secondary phase "p" is defined as:

$$Re = \frac{\rho_q \left| \vec{v}_p - \vec{v}_q \right| d_p}{\mu_q} \tag{3.44}$$

and Pr is the Prandtl number of the phase "q," which is defined as:

$$Pr = \frac{c_{p_q}\, \mu_q}{k_q} \tag{3.45}$$

In the **fluid-solid multiphase flows (or granular flows)**, the Nusselt number correlation given by Gunn (1978), applicable to a porosity range of 0.35 to 1.0 and a Reynolds number of up to 10^5, is given as:

$$Nu_s = \left(7 - 10\,\varepsilon_f + 5\,\varepsilon_f^2 \right)\left(1 + 0.7\, Re_s^{0.2}\, Pr^{1/3} \right) + \left(1.33 - 2.4\,\varepsilon_f + 1.2\,\varepsilon_f^2 \right) Re_s^{0.7}\, Pr^{1/3} \tag{3.46}$$

where the subscript "f" is for the primary fluid phase "f," the subscript "s" is for the secondary solid phase "s," and Pr is the Prandtl number of the primary phase "f," defined as:

$$\mathrm{Pr} = \frac{c_{p_f}\ \mu_f}{k_f} \tag{3.47}$$

From Eqs. 4.43 and 4.46, the heat transfer coefficient in Eq. 4.42 can be calculated. The heat transfer coefficient is always multiplied by the volume fraction (ε) of the primary phase as it should tend to zero whenever one of the phases is not present within the domain.

3.5 Multiphase Turbulence Models

The velocity field in turbulent flows always fluctuates. The fluctuations can be small scale and high frequency, which is computationally expensive to be directly simulated. In a single phase, various types of closure models can be used to describe the effects of turbulent fluctuations of velocities. In comparison to single-phase flows, the modeling of turbulence in multiphase simulations is extremely complex as the number of terms to be modeled in the momentum equations in multiphase flows is large. General turbulence models in multiphase flows widely available are:

e. k-ε turbulence model options
    i. Mixture turbulence model
    ii. Dispersed turbulence model
    iii. Turbulence model for each phase

f. Reynolds Stress turbulence model options (RSM)
    i. Dispersed turbulence model
    ii. Mixture turbulence model

The standard k-ε mixture turbulence model is employed in this study to simulate the turbulent flow. The detailed descriptions of the standard k-ε mixture turbulence model in multiphase flows are given below.

3.5.1 k-ε Mixture Turbulence Model

The standard k-ε model is the simplest and most robust of turbulence two-equation models in which the solution of two separate transport equations allows the turbulent velocity and length scales to be independently determined. The k-ε model is a semi-empirical model with several constants, which were obtained from experiments. The mixture turbulence model is the default multiphase turbulence model. The k-ε mixture turbulence model in multiphase flows is applicable when phases separate and when the density ratio between phases is close to one. The turbulence kinetic energy (k), and its rate of dissipation (ε), are obtained from the following transport equations:

$$\frac{\partial}{\partial t}\left(\rho_m\, k\right)+\nabla\bullet\left(\rho_m\,\vec{v}_m\, k\right)=\nabla\bullet\left(\frac{\mu_{t,m}}{\sigma_k}\nabla k\right)+G_{k,m}-\rho_m\,\varepsilon \tag{3.48}$$

$$\frac{\partial}{\partial t}\left(\rho_m\,\varepsilon\right)+\nabla\bullet\left(\rho_m\,\vec{v}_m\,\varepsilon\right)=\nabla\bullet\left(\frac{\mu_{t,m}}{\sigma_\varepsilon}\nabla\varepsilon\right)+\frac{\varepsilon}{k}\left(C_{1\varepsilon}\,G_{k,m}-C_{2\varepsilon}\,\rho_m\,\varepsilon\right) \tag{3.49}$$

where the mixture density, ρ_m, mixture velocity, $\vec{v}_m$, turbulent viscosity, $\mu_{t,m}$, and production of turbulence kinetic energy, $G_{k,m}$, are computed from the volume fraction of phase "i," α_i, and mass weighted equations as:

$$\rho_m=\sum_{i=1}^{N}\rho_i\,\alpha_i \tag{3.50}$$

$$\vec{v}_m=\frac{\sum_{i=1}^{N}\rho_i\,\alpha_i\,\vec{v}_i}{\sum_{i=1}^{N}\rho_i\,\alpha_i} \tag{3.51}$$

$$\mu_{t,m}=\rho_m\,C_\mu\,\frac{k^2}{\varepsilon} \tag{3.52}$$

$$G_{k,m} = \mu_{t,m} \left(\nabla \vec{v}_m + \left(\nabla \vec{v}_m \right)^T \right) : \nabla \vec{v}_m \qquad (3.53)$$

The constants in these equations are the same as those of standard k-ε model for the single phase. $C_{1\varepsilon}$, $C_{2\varepsilon}$, C_μ, σ_k, and σ_t are constants and have the following values:

$C_{1\varepsilon} = 1.44$, $C_{2\varepsilon} = 1.92$, $C_\mu = 0.09$, $\sigma_k = 1.0$, and $\sigma_t = 1.3$.

3.6 Modeling Species Transport in Multiphase Flows

For each phase "q", the conservation equations for chemical species in multiphase flows can be solved through Eq. 3.54:

$$\frac{\partial}{\partial t} \left(\varepsilon^q \rho^q Y_i^q \right) + \nabla \bullet \left(\varepsilon^q \rho^q \vec{v}^q Y_i^q \right) = -\nabla \bullet \varepsilon^q \vec{J}_i^q + \varepsilon^q R_i^q + \varepsilon^q S_i^q + \sum_{p=1}^{n} \left(\dot{m}_{p^i q^j} - \dot{m}_{q^j p^i} \right) + R \qquad (3.54)$$

where R_i^q = the net rate of production of homogeneous species "i" by chemical reaction for phase "q,"

$\dot{m}_{q^j p^i}$ = the mass transfer source between species "i" and "j" from phase "q" to "p,"

ε^q = the volume fraction for phase "q,"

S_i^q = the rate of creation of species "i" by addition from the dispersed phase plus any user-defined sources, and

R = the heterogeneous reaction rate.

The species model for multiphase species transport simulations allows inclusion of volumetric, wall surface, and particle surface reactions. The homogeneous gas phase chemical reactions in multiphase flows are the same as a single-phase chemical reaction. The reactants and the products belong to the same mixture material and, hence, the same phase. The reaction rate is scaled by the volume fraction of the particular phase in the cell. There is no implicit relationship between the species of different phases. Explicit relationships between species of different phases can be specified through mass transfer and heterogeneous reactions.

Mass and Momentum Transfer with Multiphase Species Transport

The multiphase mass transfer model accommodates mass transfer between species of different phases. Each mass transfer mechanism defines the mass transfer phenomenon from one entity to another entity. An entity is either a particular species in a phase or the bulk phase itself if the phase does not have a mixture material. The mass transfer mechanisms compute the net mass gain/loss of each species in each phase. The net mass gain/loss of a species is used to compute species and mass source terms.

Mass Transfer

Consider the following reaction:

$$a\,A + b\,B \rightarrow c\,C + d\,D \tag{3.55}$$

Assume that A and C belong to phase 1 and B and D to phase 2.

The values of the mass source terms for the phases are given by the following:

$$S_1 = R\left(c\,M_c - a\,M_a\right) \tag{3.56}$$

$$S_2 = R\left(d\,M_d - b\,M_b\right) \tag{3.57}$$

where "S" is the mass source term, "M" is the molecular weight, and "R" is the reaction rate.

The general expression for the mass source term for the phase "i" is as follows:

$$S_{r_i} = -R \sum_{r_i} \gamma_j^r\, M_j^r \tag{3.58}$$

$$S_{p_i} = R \sum_{p_i} \gamma_j^p\, M_j^p \tag{3.59}$$

$$S_i = S_{p_i} + S_{r_i} \tag{3.60}$$

where "γ" is the stoichiometric coefficient, subscript "p" represents the product, and subscript "r" represents the reactant.

Momentum Transfer

Momentum transfer is more complicated than mass transfer. The net velocity, $\vec{u}_{net}$, of the reactants is given by:

$$\vec{u}_{net} = \frac{a\, M_a\, \vec{u}_1 + b\, M_b\, \vec{u}_2}{a\, M_a + b\, M_b} \tag{3.61}$$

The general expression for the net velocity of the reactants is given by:

$$\vec{u}_{net} = \frac{\sum_r \gamma_j^r\, M_j^r\, \vec{u}_{r_j}}{\sum_r \gamma_j^r\, M_j^r} \tag{3.62}$$

where subscript "j" represents the j^{th} species (either a reactant or a product).

The momentum transfer for the phases is given by:

$$S_1^{\vec{u}} = R\left(c\, M_c\, \vec{u}_{net} - a\, M_a\, \vec{u}_1\right) \tag{3.63}$$

$$S_2^{\vec{u}} = R\left(d\, M_d\, \vec{u}_{net} - b\, M_b\, \vec{u}_2\right) \tag{3.64}$$

The general expression is given by:

$$S_i^{\vec{u}} = S_{p_i}\, \vec{u}_{net} - R\sum_{r_i} \gamma_j^r M_j^r \vec{u}_i \tag{3.65}$$

If there is no momentum transfer, then the above term will be zero.

The superscript "u" is to differentiate between the mass source terms and the momentum source terms.

Species Transfer

The general expressions for sources of species "k" in the phase "j" are given by:

$$S_{r_i^k} = -R \sum_{r_i^k} \gamma_j^{r^k}\, M_j^{r^k} \tag{3.66}$$

$$S_{p_i^k} = R \sum_{p_i^k} \gamma_j^{p^k} \; M_j^{p^k} \tag{3.67}$$

$$S_i^k = S_{p_i^k} + S_{r_i^k} \tag{3.68}$$

Heat Transfer

The net enthalpy of the reactants is given by:

$$H_{net} = \frac{a\, M_a \left(H_a + h_a^f \right) + b\, M_b \left(H_b + h_b^f \right)}{a\, M_a + b\, M_b} \tag{3.69}$$

where "h^f" represents the formation enthalpy, and "H" represents the enthalpy.
The general expression for "H_{net}" is given by:

$$H_{net} = \frac{\sum_r \gamma_j^r \, M_j^r \left(H_j^r + h^{f\,r}_j \right)}{\sum_r \gamma_j^r \, M_j^r} \tag{3.70}$$

If this enthalpy gets distributed to the products by way of the ratio of their mass production rates, heat transfer for the phases are given by:

$$S_1^H = R \left(c\, M_c \; H_{net} - a\, M_a \; H^a - c\, M_c \; h_f^c \right) \tag{3.71}$$

$$S_2^H = R \left(d\, M_d \; H_{net} - b\, M_b \; H^b - d\, M_d \; h_f^d \right) \tag{3.72}$$

The general expression for the heat source term is given by:

$$S_i^H = S_{p_i} \; H_{net} - R \left(\sum_{r_i} \gamma_j^r \, M_j^r \, H_j^r + \sum_{p_i} \gamma_j^p \, M_j^p \, h^{f\,p}_j \right) \tag{3.73}$$

If there is no heat transfer, then the different species only carry their formation enthalpies with them. Thus, the expression for "H_{net}" will be:

$$H_{net} = \frac{\sum_r \gamma_j^r M_j^r h^{f\,r}_j}{\sum_r \gamma_j^r M_j^r} \tag{3.74}$$

The expression for S_i^H will be:

$$S_i^H = S_{p_i} H_{net} - R\left(\sum_{p_i} \gamma_j^p M_j^p h^{f\,p}_j \right) \tag{3.75}$$

In summary, the Eulerian-Eulerian multiphase model has been selected in this study. All these conservation equations in the frame of Eulerian multiphase model have been evaluated by taking into account the interfacial coefficients, such as the fluid-fluid exchange coefficient, K_{pq}, fluid-solid exchange coefficient, K_{sl}, solid-solid exchange coefficient, K_{sl}, and so forth. This chapter mainly focuses on setting up multiphase flow model, while the equation for the continuous phase has been discussed in Ch. 2.

CHAPTER FOUR
RESULTS AND DISCUSSIONS

The primary objective of this study is to use the computational model previously developed by Mazumder and Wang (2010) to conduct parametric studies to help understand the thermal-flow and gasification behaviors in the mild gasifier and to further improve design of the ECCC mild gasifier. The simulation is formulated utilizing the transient Eulerian-Eulerian multi-phase model as described in Ch. 2. The simulation process is built up step-by-step, starting in the 2-D geometry with fluid mechanics and heat transfer without reactions or particles, then chemical reactions are added one by one, and, finally, the particles are added. After the 2-D results are established, a parametric study is conducted and analyses are performed to modify the mild-gasifier design. Eventually, the evolved 2-D geometry is transformed into a 3-D geometry and the parametric values selected from the 2-D study are incorporated into the 3-D simulation geometry, which is evolved from the 2-D parametric study. The simulated cases in this study are given below in Fig. 4.1. The first three cases are conducted in the 2-D geometry and the last case is in the 3-D geometry.

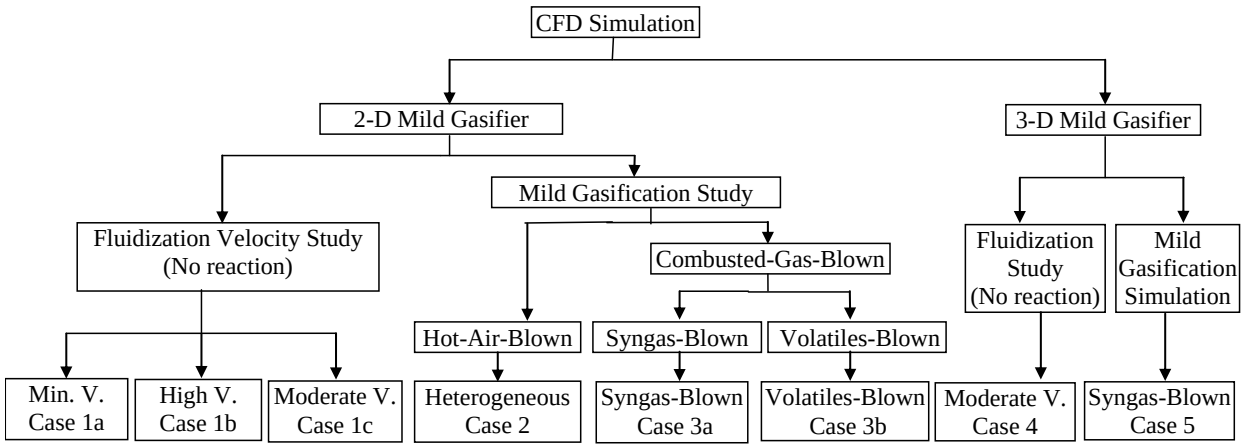

Figure 4.1 Organization of simulated cases

4.1 Case 1 Fluidization Flow Behavior Study with Solid Particles

This case investigates the fluidization flow behavior in the 2-D geometry. The process of converting the granular (solid) material from a static, solid-packed state to a dynamic, fluid-like state is known as "fluidization." For investigating the fluidization phenomena, all of the solid particles are in a bed of granular coal particles, and the air enters the fluidized bed through the bottom perforated plate.

The minimum fluidization velocity is an important milestone during simulation iterations because, below this velocity, the particles will not move or change their orientation. Fluidization will become more dynamic when the air blowing velocity progressively increases above this minimum velocity. If the air velocity is much larger than the minimum velocity, some portion of the particles could be driven out of the fluidized bed and exit the gasifier, resulting in a non-ideal condition for operating said gasifier. Table 4.1 summarizes and compares the minimum fluidization velocity calculated from different empirical correlations that have been explained in Ch. 1. In CFD, the minimum fluidization velocity is determined by gradually increase the velocity from a very low speed to higher speeds until the particles start to move. The result of CFD is 0.2 m/s, which falls between the results of Saxena and Vogel (1977, Eq.1.26) and the Ergun rule (1952, Eq.1.5).

Various fluidization velocities have been tested from 0.2 to 2.5 m/s. In the baseline study, the fluidization velocity 0.5 m/s at the horizontal inlets and 0.3 m/s at the inclined surface inlets are selected to provide a dynamic but sustained level of fluidization.

Table 4.1 Comparison of minimum fluidization velocity between those calculated from different correlations and that obtained from the CFD result for 0.25mm diameter and 0.6 volume fraction of carbon solid

Correlation	Minimum fluidization velocity (m/s)
Todes and Citovich (1981, Eq. 1.26)	0.075
Saxena and Vogel (1977, Eq.1.25)	0.1338
Ergun rule (1952, Eq.1.5)	0.3868
Kumar and Gupta (1980, Eq.1.27)	0.1138
CFD result of this study	0.2

4.1.1 Case 1a: Minimum Fluidization Velocity

In this case, the inlet gas velocity in the draft tube is assigned to be 1 m/s, and the fluidization gas velocity is 0.2 m/s for both the horizontal perforated holes and the inclined perforated holes. Figure 4.2 shows selected snapshots of the transient fluidization phenomena via an evolution of volume fraction of carbon solid (char) at different time steps.

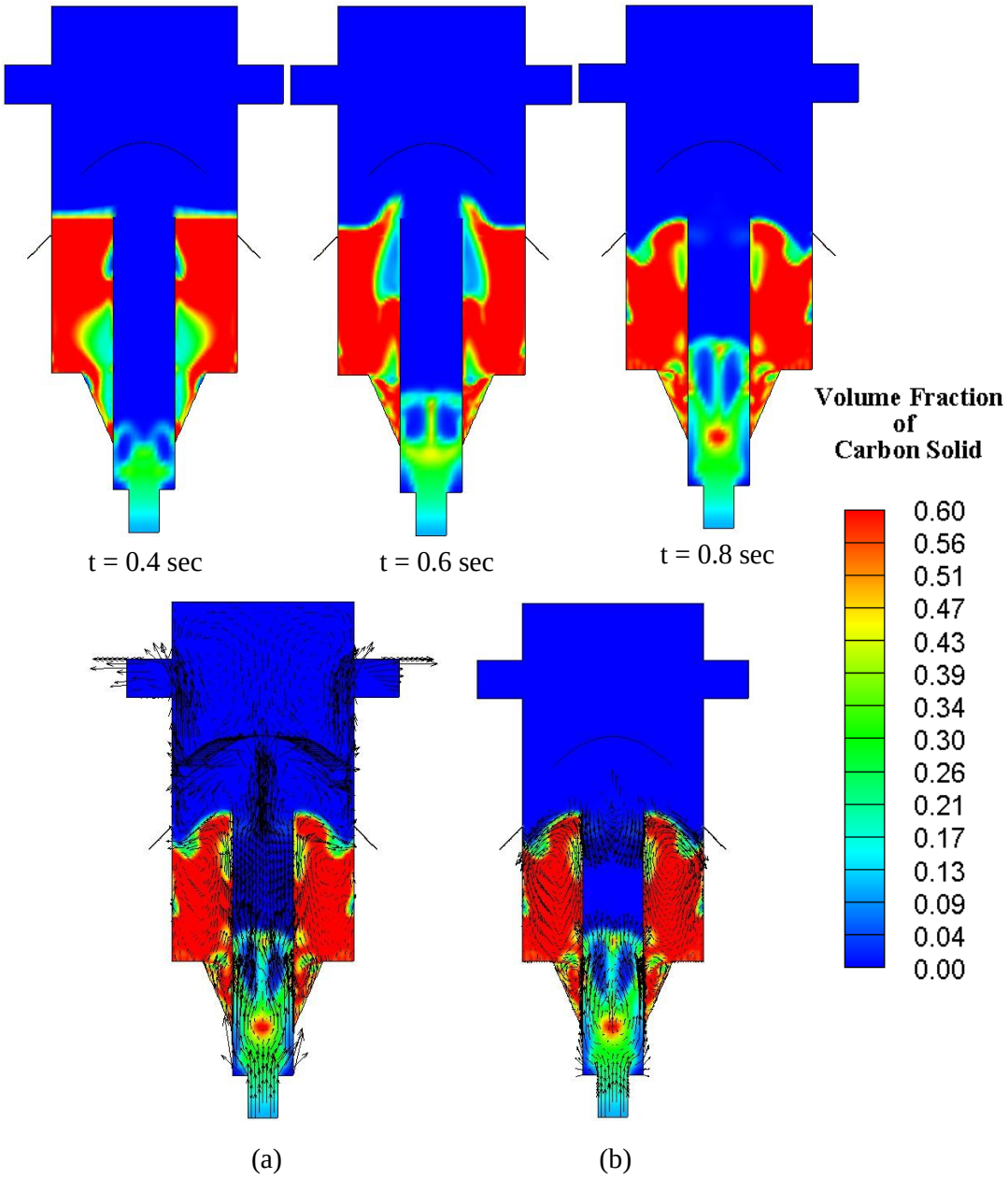

Figure 4.2 Case 1a: Top row – 2-D transient distribution of the volume fraction of carbon solid with 0.2 m/s fluidization air and 1 m/s inlet gas inside draft tube for time intervals between 0.2 and 0.8 seconds. Bottom row – (a) velocity profile of air (b) velocity profile of carbon at 0.8 seconds.

It can be easily observed from Fig. 4.2 that fluidization air bubbles continue coming out from the perforated holes at the bottom. In this 2-D case, the char chute's cross-sectional dimensional is reduced to provide an effective slot width that would reflect the cross-sectional area of a circular pipe in a 3-D case. If the char chute width is not reduced, the percentage of the mass flow rate exiting from the char chutes would be more than that in a 3-D geometry. Another approach is to assign the 2-D char chute's

width the same dimension of its diameter as in the 3-D geometry, but to impose an increased exit pressure boundary condition to reduce the overflow in the 2-D simulation. The second approach is used later in Case 3. It should be noticed that because the fluidization velocity of 0.2 m/s is just beyond the minimum theoretical fluidization velocity, small air bubbles can be seen emerging from the inclined wall more readily than from the horizontal portion of the perforated wall.

4.1.2 Case 1b: High Fluidization Velocity

In this case, the fluidization air velocity is arbitrarily increased to be 2.5 m/s to see what will happen in the gasifier. The results in Fig. 4.3 and Fig. 4.4 show that all the carbon solid particles (chars) in the fluidized bed are blown away to the exit within 0.5 seconds.

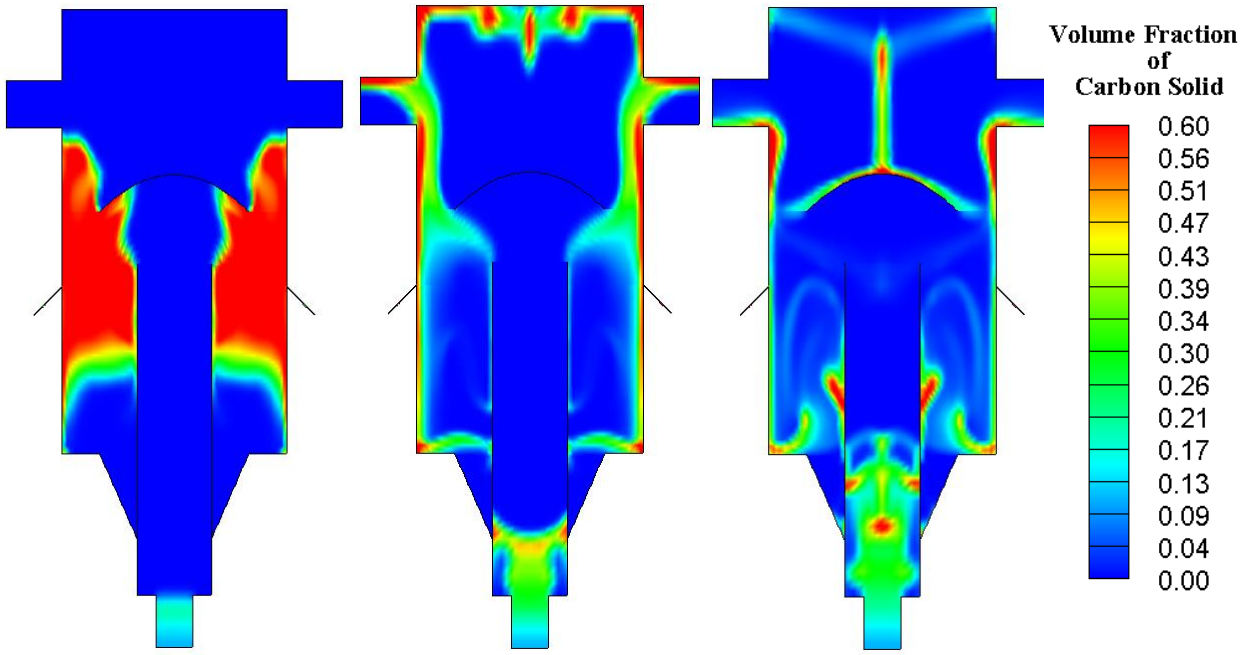

Figure 4.3 Case 1b: 2-D transient distribution of volume fraction of carbon solid using 2.5 m/s fluidization air and 1 m/s in the draft tube inlet for time interval between 0.1 and 0.5 seconds.

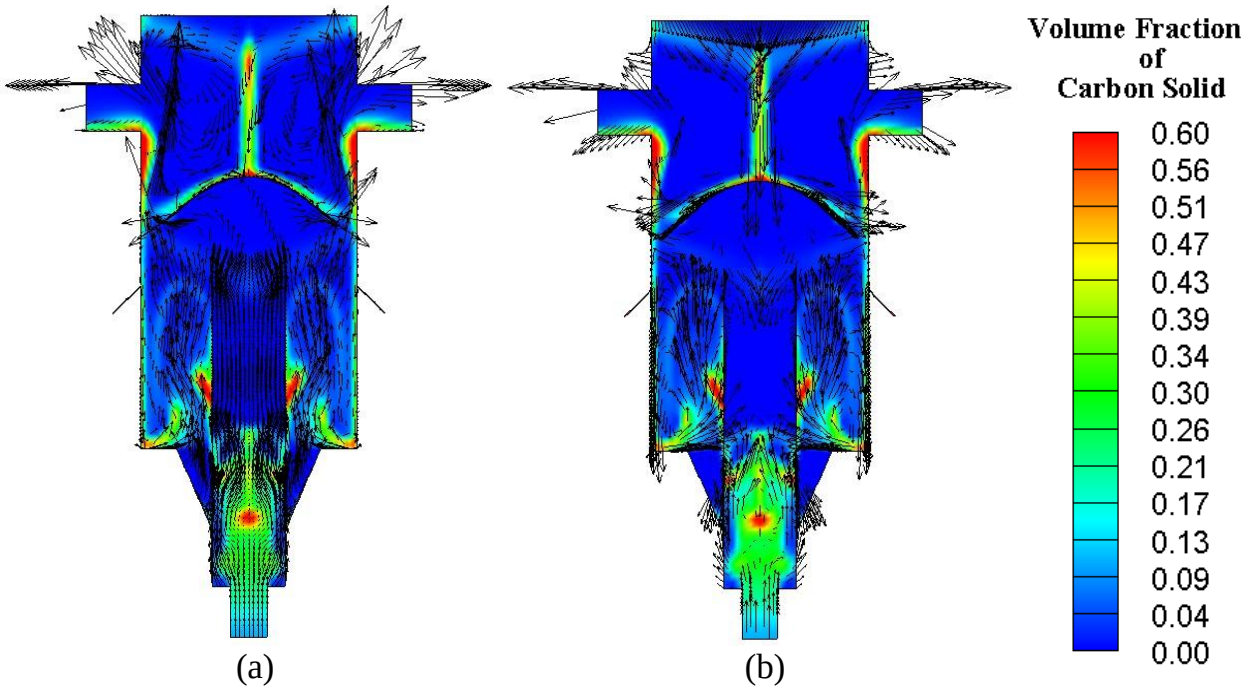

Figure 4.4 Case 1b: (a) velocity profile of air (b) velocity profile of carbon solid at 0.5 seconds.

4.1.3 Case 1c: A Moderate Fluidization Velocity

Case 1a and 1b represent the lower bound (minimum fluidization) and higher bound (blowing away all chars) of fluidization velocity, respectively. It will be interesting in examining the phenomenon of other fluidization velocities within these two limits. Hereby, 0.5 m/s and 0.3 m/s are selected for fluidization velocity at the horizontal and inclined surfaces, respectively. The result in terms of transient volume fraction of carbon particles are shown in Fig. 4.5. In this case, it can be clearly observed that air bubble formation is frequent, and mixing activity is very dynamic. At this velocity range, almost no particles escape from the gasifier upper exit.

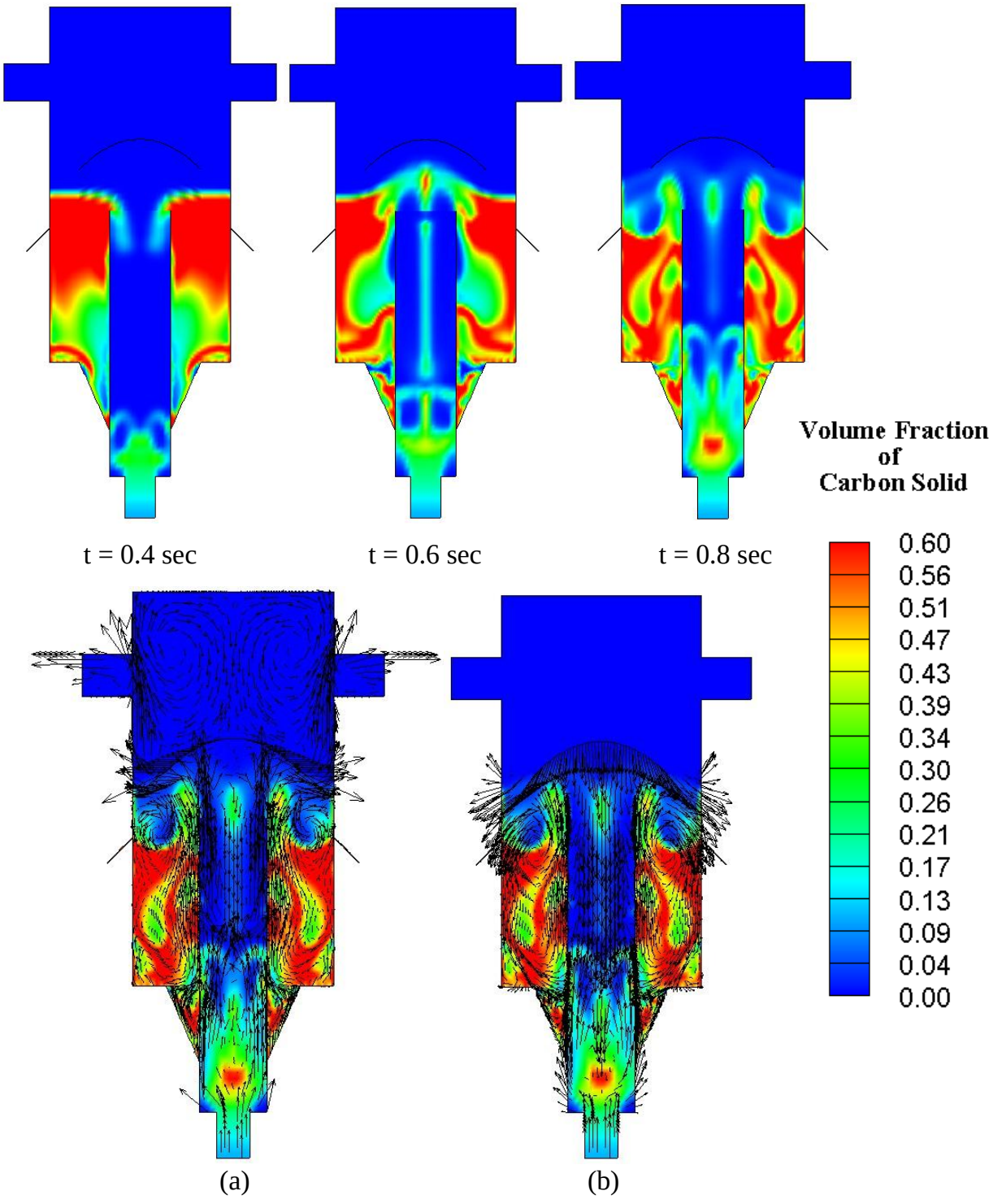

Figure 4.5 Case 1c: Top row – 2-D transient distribution of volume fraction of carbon solid with 0.5 m/s fluidization velocity at horizontal inlet and 0.3 m/s velocity at the inclined surface inlet; Bottom row – (a) velocity profile of air (b) velocity profile of carbon solid at 0.5 seconds.

4.2 Mild Gasification Simulation in ECCC Gasifier

In this study, two situations have been considered: (a) air blown in both the draft tube and fluidized bed and (b) combusted gases in the draft tube and syngas for fluidization.

4.2.1 ECCC Mild Gasifier Design Considerations

Many issues need to be considered in designing a mild gasifier. An initial design consideration is to find the appropriate fluidization velocity in order to provide dynamic mixing of the char in the fluidized bed. This will help sustain the bed depth. The next consideration is to keep the residence time of the particles in the draft tube and free board region below 1 second for mild gasification. The third consideration is to ensure that the temperature in the gasifier is maintained above 800K to avoid condensation of volatiles. To achieve this requirement, the relationship between the overall fuel energy input and the gas speed in the draft tube (and, therefore, the draft tube size) will need to be matched. This section is dedicated to discussing all these design considerations. For example, in order to make the particle residence time close to 3 seconds within the reaction chamber, the entrainment gas velocity was reduced from 2 m/s to 0.167 m/s.

Discussion of Operation Temperature

Depending on the structures of the volatiles, thermal cracking of heavy volatiles generally starts at around 600 K (620F). As the hydrocarbon bonds continue to break, more energy and higher temperatures beyond 800K (980^{o}F) are needed to continue to thermally crack volatiles into lighter products such as CO, CH_4, C_2H_2, etc. If the temperature decreases below 800K, some volatiles would condense to liquid form as tars. However, Fig. 4.6 shows that the temperature of the gas phase in the freeboard area drops below 350K, which is too low to keep all volatile components in the vapor phase. The coal velocity in this case was assigned to be 1 m/s through the coal inlet with a diameter of 2 inches, which leads to a coal mass flow rate of 4.67 kg/s-m. The low free-board temperature means that too much fuel has been injected into the mild gasifier and there is insufficient thermal energy provided to thermally crack the volatiles. The large amount of carbon and gases absorb a large amount of energy, leading to this low temperature (350K) in the freeboard region. To fix this problem, both the coal and

transporting gas velocities are reduced to 0.5 m/s, and, in the meantime, the temperature of the combusted gases is assigned to be 1600K to provide the needed energy for thermal cracking for later cases.

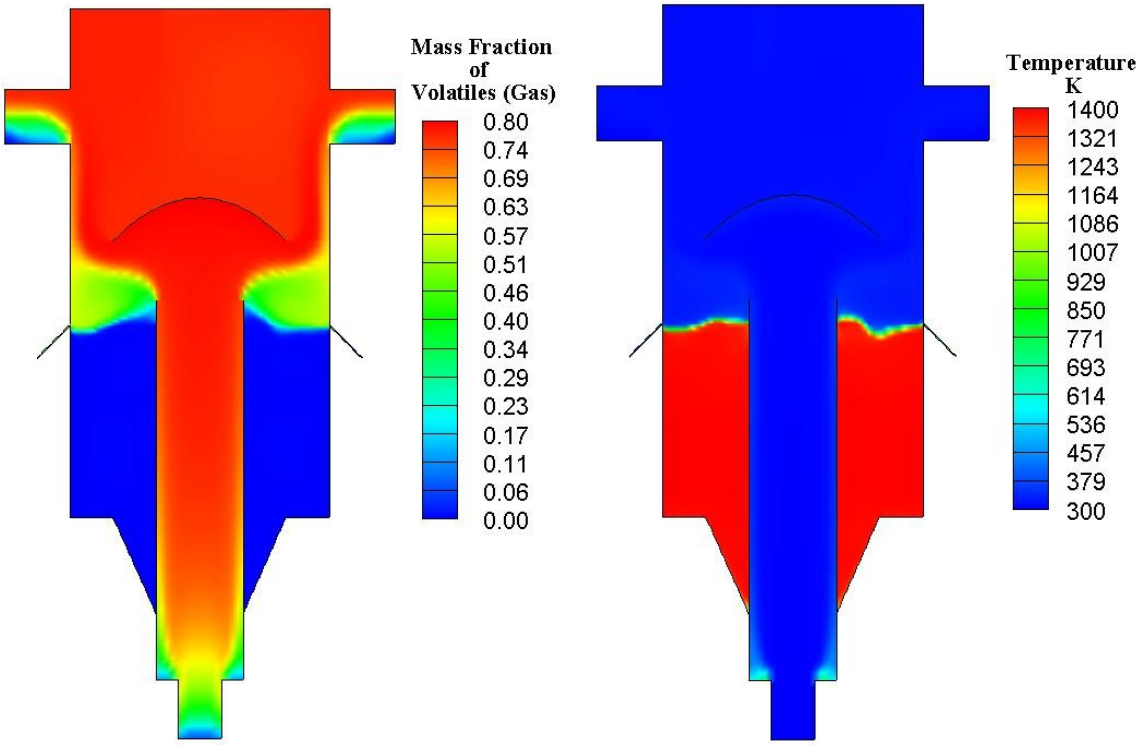

(a) (b)

Figure 4.6 2-D transient distribution of (a) mass fraction of volatiles in gas phase and (b) temperature of gas phase at t = 2.0 seconds with 1 m/s coal feed speed.

4.2.2 Case 2: Air-blown Mild Gasification (char chute exit pressure at 600 Pascal)

Coal mild gasification is a multiphase problem between gases and coal particles, and it is also a reactive flow that involves homogeneous reactions among gases and heterogeneous reactions between coal particles and gases. In this study, both the gas phase (primary phase) and coal phase (secondary phase) are solved by using the Eulerian-Eulerian multiphase model. Both homogeneous (gas-gas) reactions and heterogeneous (gas-solid) reactions are simulated in this case.

In this case, hot air preheated to 500K is blown into the fluidized bed and the coal transported by air is also preheated to 500K. The coal enters at 0.167 m/s and the transporting air enters at 1 m/s. (Note, it is understood that coal particles should not be transported by hot air at 500K because it can cause combustion during transportation. In this simulation, the coal/air mixture is assigned an inlet boundary

condition of 500K for the convenience of simulation.) The major portion of the air enters the draft tube from the outer annular passage at 2 m/s with a temperature of 1600K to simulate the hot gas that will be used to provide energy for devolatilization and mild gasification.

In the fluidized bed, 0.25 mm diameter carbon solid particles are packed at a volume fraction of 0.6. The air consisting of 23% O_2 and 77% N_2 by volume (O_2+3.76N_2) enters the horizontal perforated plates at 0.5 m/s and enters the inclined perforated plate at 0.3 m/s at 500K. There are total 28 perforated openings in the 2-D geometry.

The draft tube is designed to prevent the fluidized bed from contacting the oxygen in the draft tube air while still transferring heat to the fluidized bed through the draft tube wall. Above the draft tube, a deflector is installed to block the particles from being entrained out of the gasifier. There are four outlets, two for char at middle portion and two for the produced syngas at the top portion of the gasifier. The inlet conditions are summarized in Table 5.2.

Figure 4.7 shows the transient distribution of the solid carbon mass fraction. Due to the large difference in solid carbon's mass fraction between that in the draft tube and in the fluidized bed, two separated color maps are used in Fig. 4.7(a) and (b) respectively. Fig. 4.7 (a) emphasizes the information inside the draft tube and Fig. 4.7(b) emphasizes the same information inside the fluidized bed. With this composite presentation in Fig. 4.7 (a) and (b), it can be seen that the coal particles are successfully blocked by the deflector and most of the coal particles fall off to the fluidized bed. For those that escape from the deflector and rise to the freeboard, some of them fall off to the top of the deflector and accumulate there as time increases.

The transient distribution of various species mass fraction in the fluidized bed mild gasifier is shown in Fig. 4.8. The separate velocity vector plots of both the coal particle phase and the gas phase colored by corresponding phase temperature at time t = 0.58 seconds are shown in Fig. 4.11. The particle velocity field clearly shows the circulation in the fluidized bed. In Fig. 4.8, it looks like volatile matters having been partially thermally cracked and some minor mild gasification also occurs above the deflector (Fig. 4.8) with traces of benzene, carbon monoxide, and hydrogen. The existence of CO_2 in this case implies that some minor combustion occurs, since air (and hence oxygen) is blown in this case.

The presence of these species (C_6H_6, CO, and H_2) only in the upper part (i.e. freeboard region) of the gasifier implies that longer residence time is needed to allow the right amount of thermal cracking and mild gasification to happen. The notably reduced temperature also provides further evidence that endothermic reactions such as thermal cracking and gasification occur in the freeboard region.

The mass weighted averages of volatiles $CH_{2.121}O_{0.5855}$ (gas phase), H_2O (gas phase), O_2, CO, CO_2, H_2, C_6H_6 (Benzene), and N_2 (as an inert gas) at the syngas exit of the domain are shown in Table 5.3. The mass weighted average temperature of the solid phase (815K) is about 200 K higher than that of the gas phase (606.77 K) at the outlet. The complete profile information of the syngas at the outlet is given in Table 4.3.

Table 4.2 Parameters, boundary and operating conditions for Case 2

Parameters	**Case 2**	
Inlet position	Fluidized bed inlet	Draft tube inlet
Feedstock & transport agent	air	coal & air
Air inlet velocity at horizontal holes, m/s	0.5	
Air inlet velocity at inclined surface holes,	0.3	
Transport gas inlet velocity at coal inlet, m/s		1.0
Coal velocity at coal inlet, m/s		0.167
Velocity at hot gas inlet, m/s		2.0
Temperature for fluidization gas, K	500	
Inlet temperature for transporting gas, K		1600
Coal inlet temperature, K		500
Mass fraction at inlet (%)		
O_2	0.2331	
N_2	0.7669	
Volatiles	0	0.4491
Char		0.4533
Water Vapor		0.0976
Operating pressure (pascal)	101325	101325
Operating temperature (K)	288.16	288.16
Operating density (kg/m^3)	1.175	911.30&1.175
Gravitational acceleration (m/s^2)	9.81	9.81
Wall temperature, K	Adiabatic	Adiabatic

Table 4.3 Species composition at syngas exit at t = 1.94 seconds for Case 2

	Temp(K)	Components	Mass (%)	Vol. (%)
Gas phase 99.8% volume)	606.77	O2	16.00	13.21
		N2	64.76	60.31
		Volatiles	0.26	0.02
		Moisture	2.78	3.93
		CO	6.95	6.31
		CO2	5.97	3.51
		H2	0.95	11.88
		C6H6	2.33	0.87
Coal phase (0.2% volume)	815.55	Char	49.33	
		Volatiles	0	
		Moisture	0	
Mass flow rate (kg/s-m)			-1.132477	

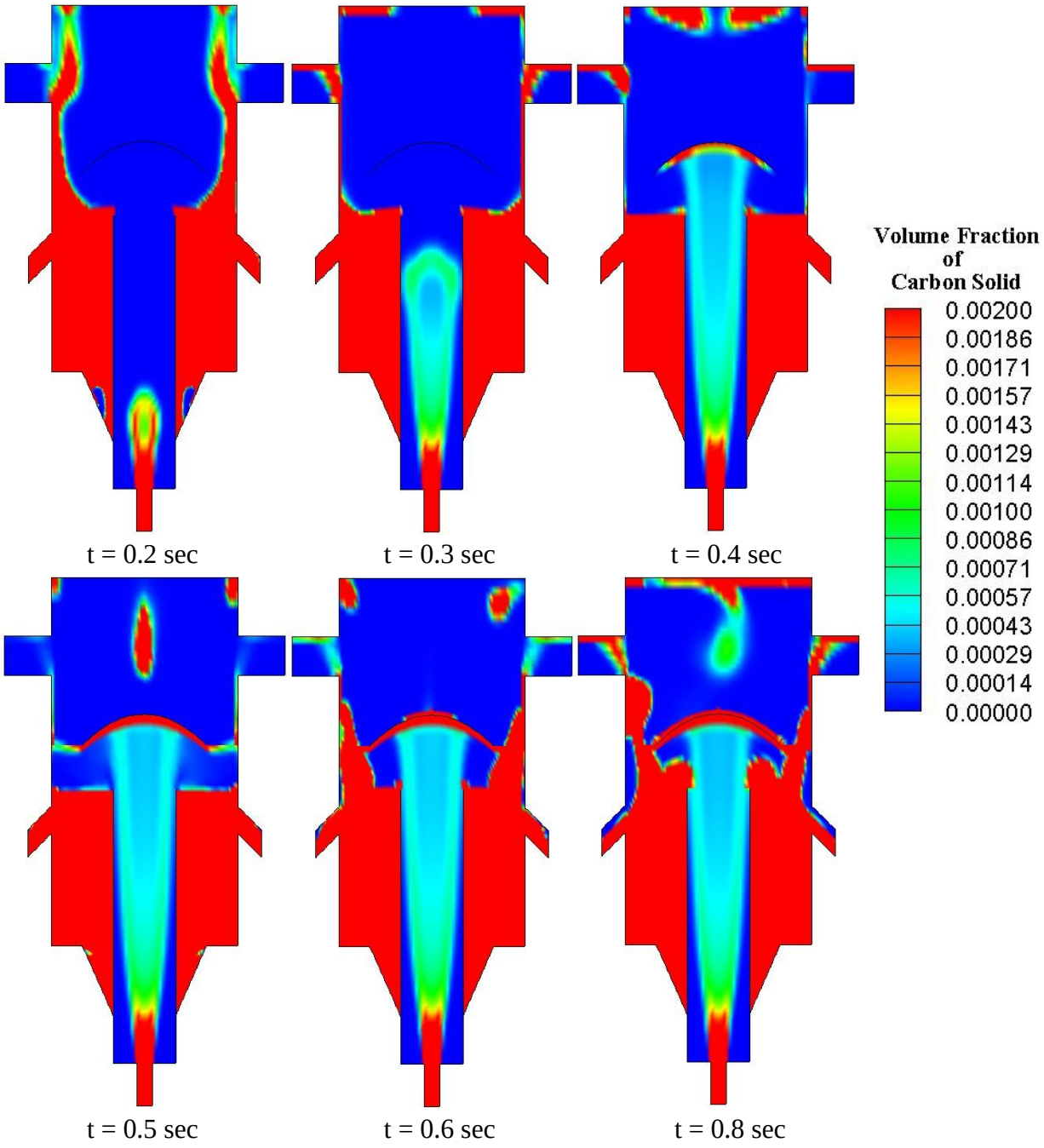

Figure 4.7 (a) 2-D transient distribution of volume fraction of carbon solid with an emphasis within the draft tube for Case 2.

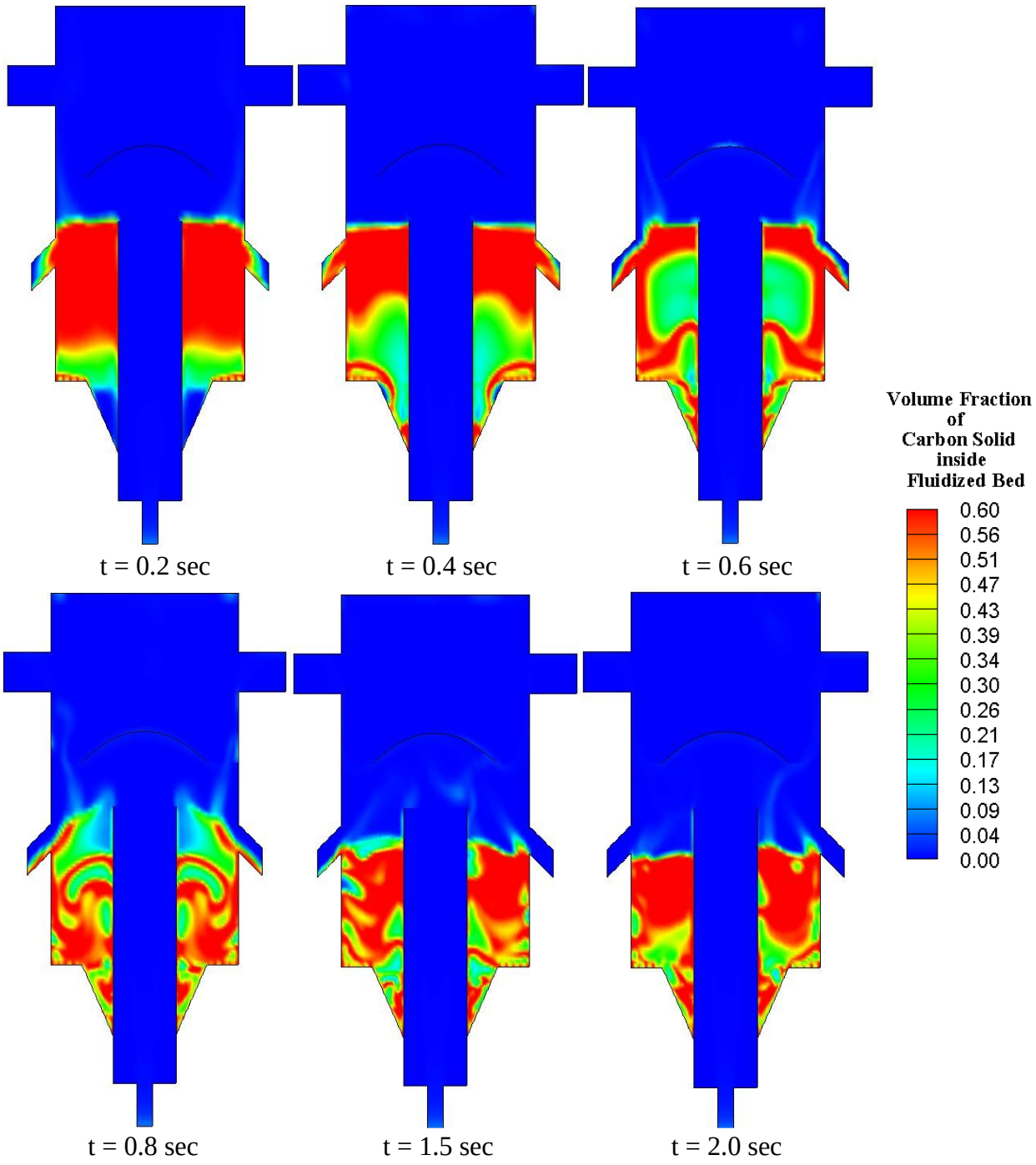

Figure 4.7(b) 2-D transient distribution of volume fraction of carbon solid with an emphasis on the fluidized bed for Case 2.

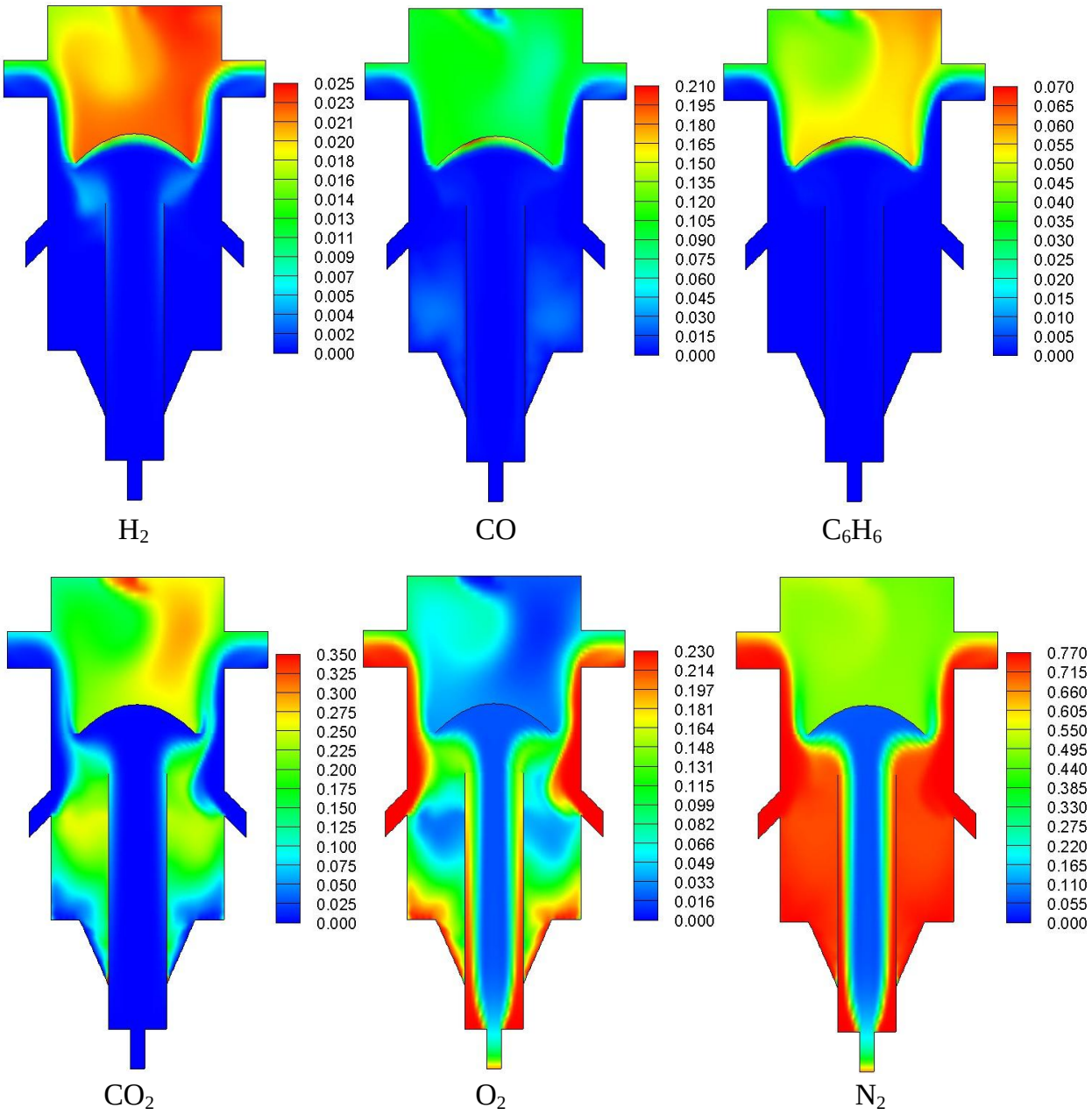

Figure 4.8 2-D transient distribution of mass fractions of various species at time t = 1.94 seconds for Case 2

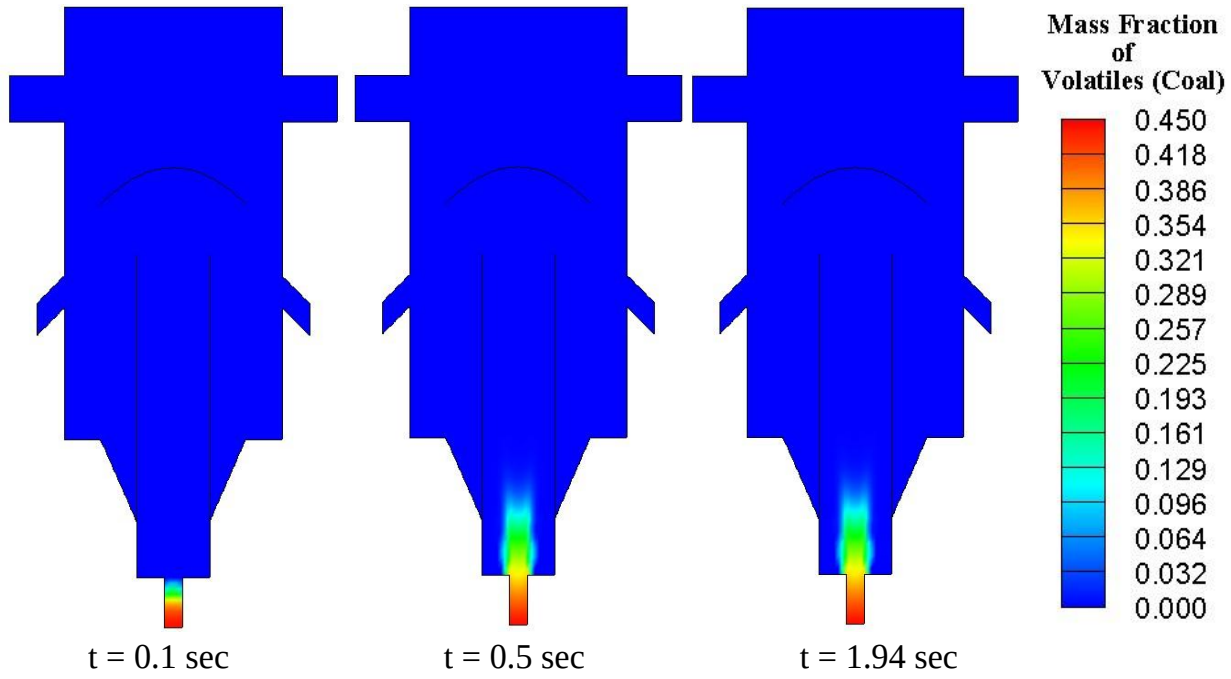

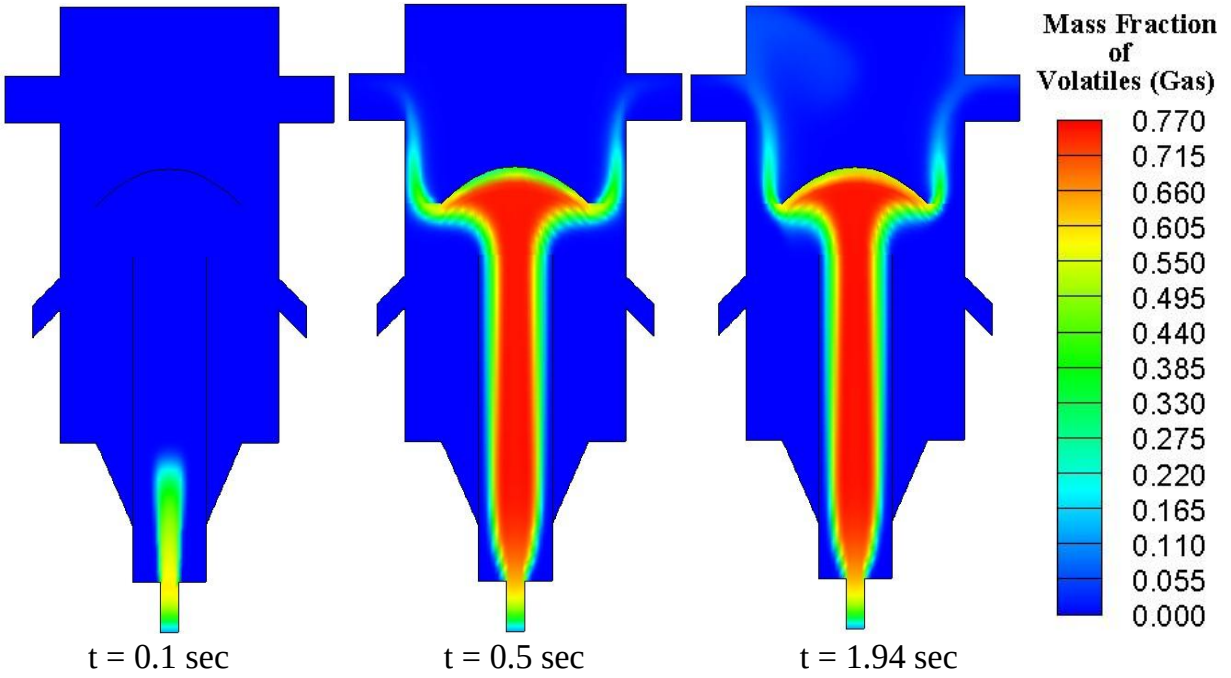

Figure 4.9 2-D transient distribution of mass fractions of volatiles (inside the coal) versus volatiles (gas phase outside the coal) from 0.1 seconds to 1.94 seconds for Case 2.

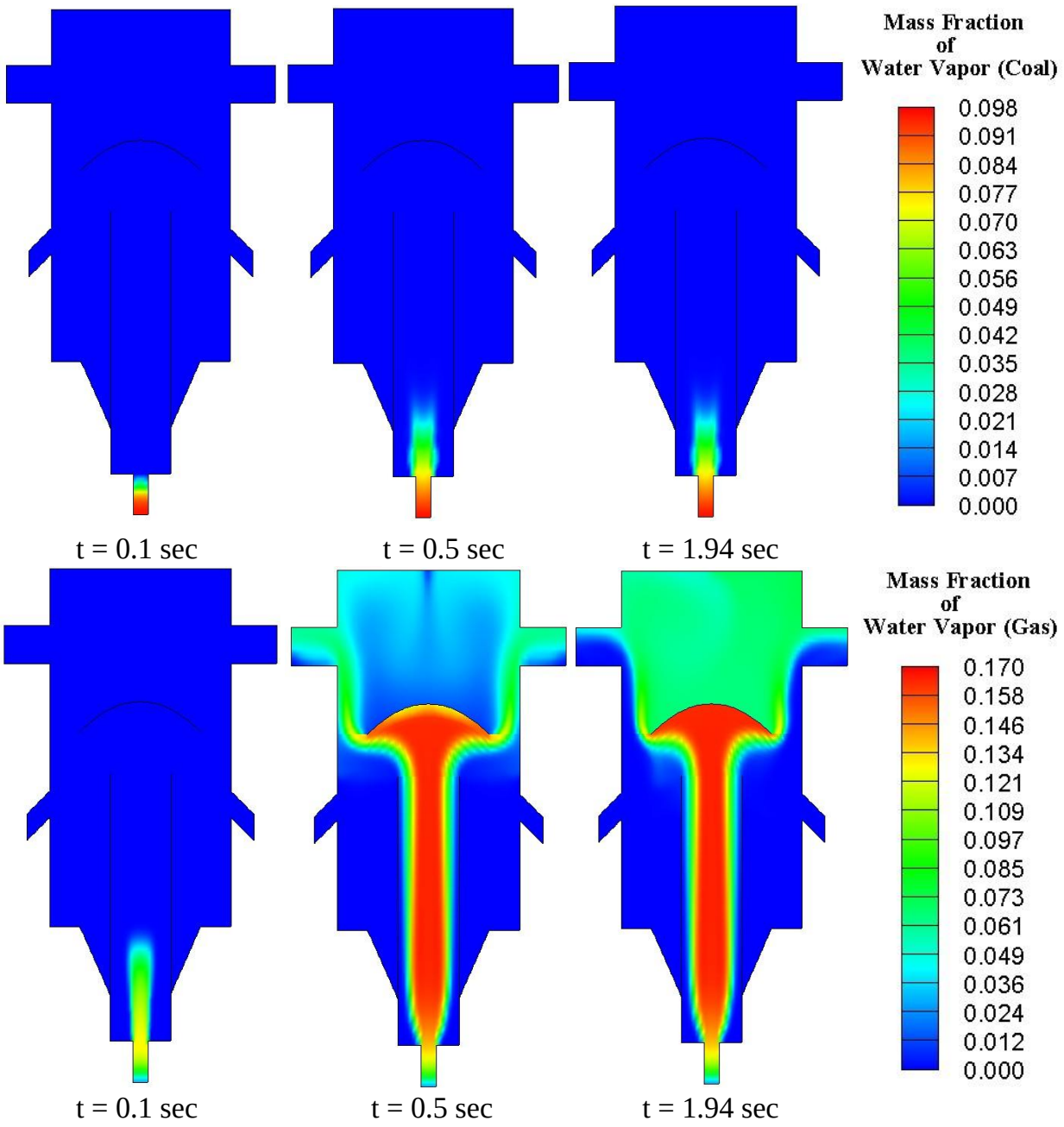

Figure 4.10 2-D transient distribution of mass fractions of water vapor (inside coal) vs. water vapor (gas phase) from 0.1 seconds to 1.94 seconds for Case 2

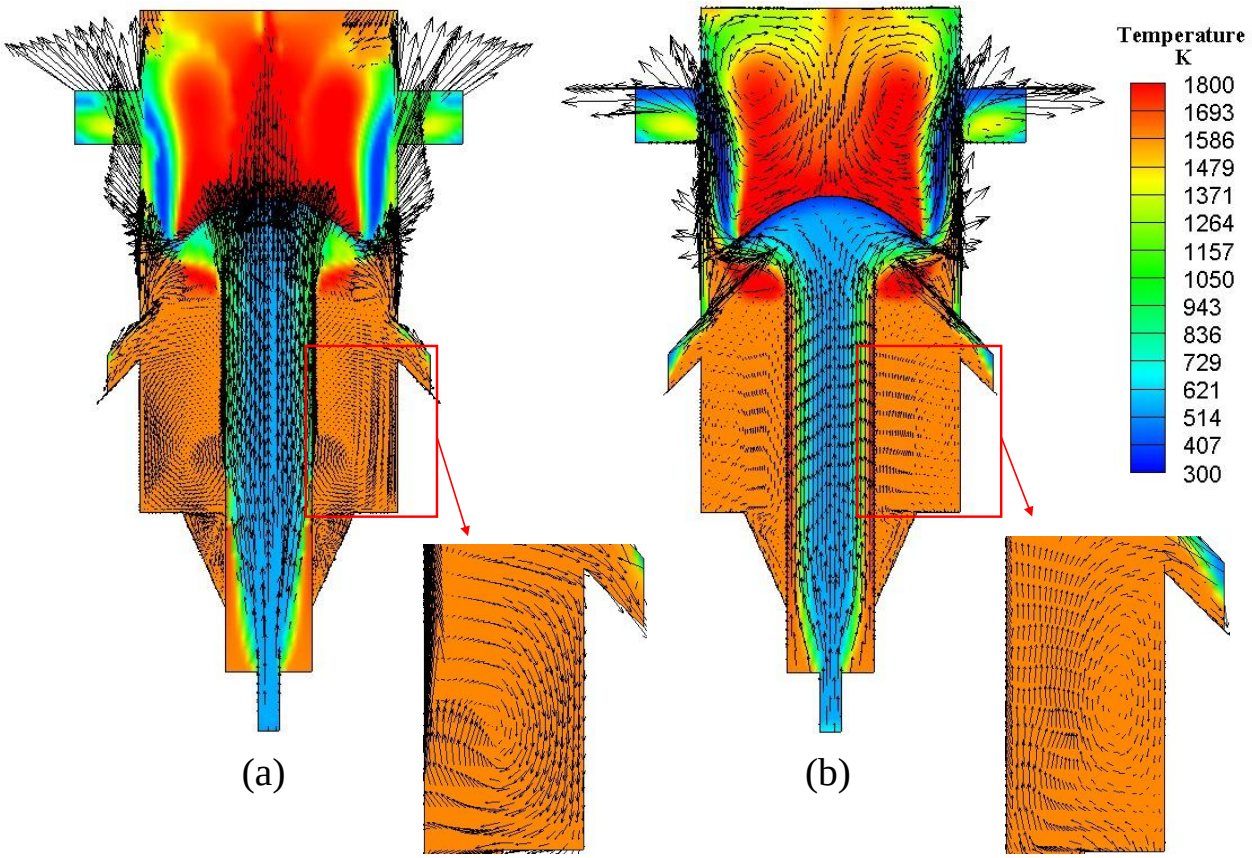

Figure 4.11 Velocity vector plots for (a) particles and (b) air with corresponding particle and air temperature contours (K) at 0.58 seconds for Case 2.

4.2.3.1 Case 3a: Combusted Gas Blown in the Draft Tube and Syngas Blown in the Fluidized Bed

In Case 2, the hot air at 1600K was blown into the draft tube to simulate the hot gases, whereas, in this case, the hot air is replaced with more realistic combusted gases in the draft tube inlet, and a small portion of the raw syngas exiting the gasifier is extracted to fluidize the fluidized bed. The combusted gases consist of carbon dioxide, water vapor, and nitrogen, which are produced from an external combustor. The oxygen is assumed to be completely consumed in combustion, so no oxygen is included in the combusted gases. By doing this change, an oxygen-free situation is created for mild gasification. The mild gasification processes ($C + CO_2 \rightarrow 2CO$ and $C + H_2O \rightarrow CO + H_2$) could occur with CO_2 from the combusted gases and H_2O (water vapor) from the coal and combusted gases.

The combusted gases can come from burning the raw syngas or chars extracted from the syngas exits or char chutes of this gasifier. Burning char is more involved than burning raw syngas in the

current system arrangement. Therefore, in this case, a portion of the raw syngas is extracted and combusted outside the gasifier. In consideration of mild gasification, the raw syngas consists mainly of volatiles, so the combusted gases are assumed to be the products of complete combustion of the volatiles following reactions under stoichiometric conditions:

$$CH_{2.121}O_{0.5855} + 1.2378O_2 + 4.714288N_2 \rightarrow CO_2 + 1.061H_2O\ (g) + 4.714288N_2$$

A portion of the combusted gases is used to transport the coal. It enters the inner tube of the draft tube with coal at 0.167 m/s and 500K. The remaining portion of the combusted gases is used to entrain the coal from the annular duct surrounding the inner coal-fed tube. It enters at 1 m/s and 1600K.

Regarding the fluidization fluid in Case 2, air was used. However, in Case 3, the raw syngas consisting of 88% carbon monoxide and 12% hydrogen by weight is used instead. The raw syngas is assigned a temperature of 500K with an inlet velocity of 0.5 m/s at the horizontal perforated plate and 0.3 m/s at the inclined perforated openings into the fluidized bed. The inlet conditions of case 3(a) are listed in Table. 4.4.

The distributions of the mass fractions of various species in the mild gasifier are shown in Fig. 4.12. The mass weighted average temperatures for the gas phase and solid phase are 849.92K and 818.47K, respectively, at the outlet. The syngas composition at the exit is given in Table 4.5.

Table 4.4 Parameters, boundary and operating conditions for Case 3a

Parameters	**Case 3a**	
Inlet position	Fluidized bed inlet	Draft tube inlet
Feedstock & transporting agent	syngas	coal & combusted gas
Syngas inlet velocity at horizontal holes, m/s	0.5	
Snygas inlet velocity at skew holes, m/s	0.3	
Combusted gas velocity at coal inlet, m/s		1.0
Entrained coal velocity at coal inlet, m/s		0.167
Combusted gas velocity at hot gas inlet, m/s		2.0
Temperature for fluidization gas, K	500	
Temperature for entrained combusted gas, K		1600
Temperature for entrained coal, K		500
Mass fraction at inlet (%)		
CO_2		0.2274(combusted gas)
N_2		0.6738(combusted gas)
Water Vapor		0.0976(coal) 0.0987(combusted gas)
CO	0.882	
H_2	0.118	
Char		0.4533(coal)
Volatiles		0.4491(coal)
Operating pressure (pascal)	101325	101325
Operating temperature (K)	288.16	288.16
Operating density (kg/m^3)	1.177	919.56/1.18
Gravitational acceleration (m/s^2)	9.81	9.81
Wall temperature, K	Adiabatic	Adiabatic

Table 4.5 Species composition at syngas exit at t = 2.0 seconds for Case 3a

	Temp(K)	Components	Mass (%)	Vol (%)
Gas phase 99.4% volume)	849.92	O2	8.62	6.89
		N2	58.58	51.82
		Volatiles	0.77	0.04
		Moisture	5.12	6.82
		CO	8.44	7.27
		CO2	14.68	8.76
		H2	1.48	17.69
		C6H6	2.31	0.71
Coal phase (0.6% volume)	818.47	Char	51.03	
		Volatiles	0	
		Moisture	0	
Mass flow rate (kg/s-m)			-2.4683299	

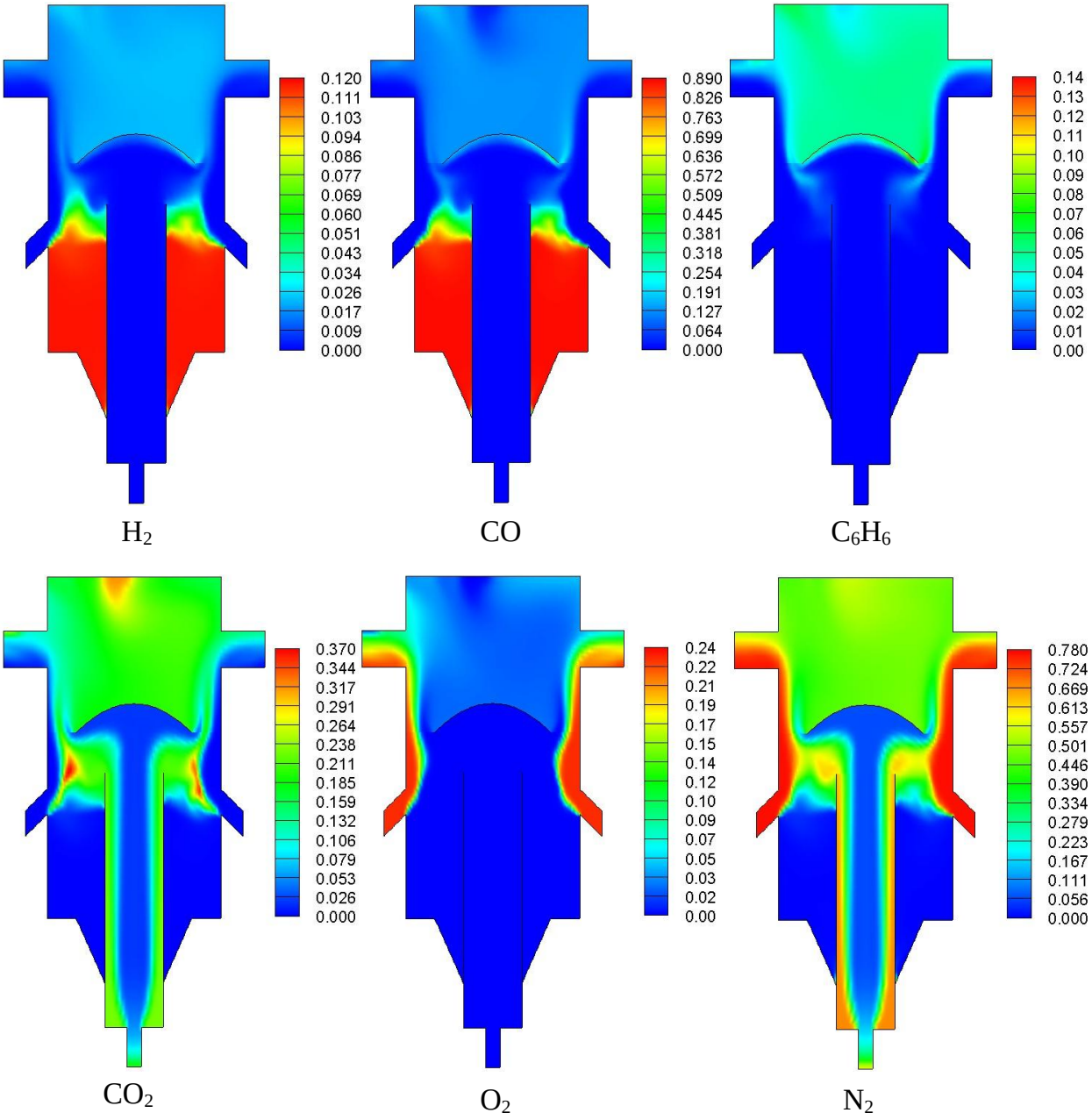

Figure 4.12 2-D transient distribution of mass fractions of various species at time t = 2 seconds for Case 3a

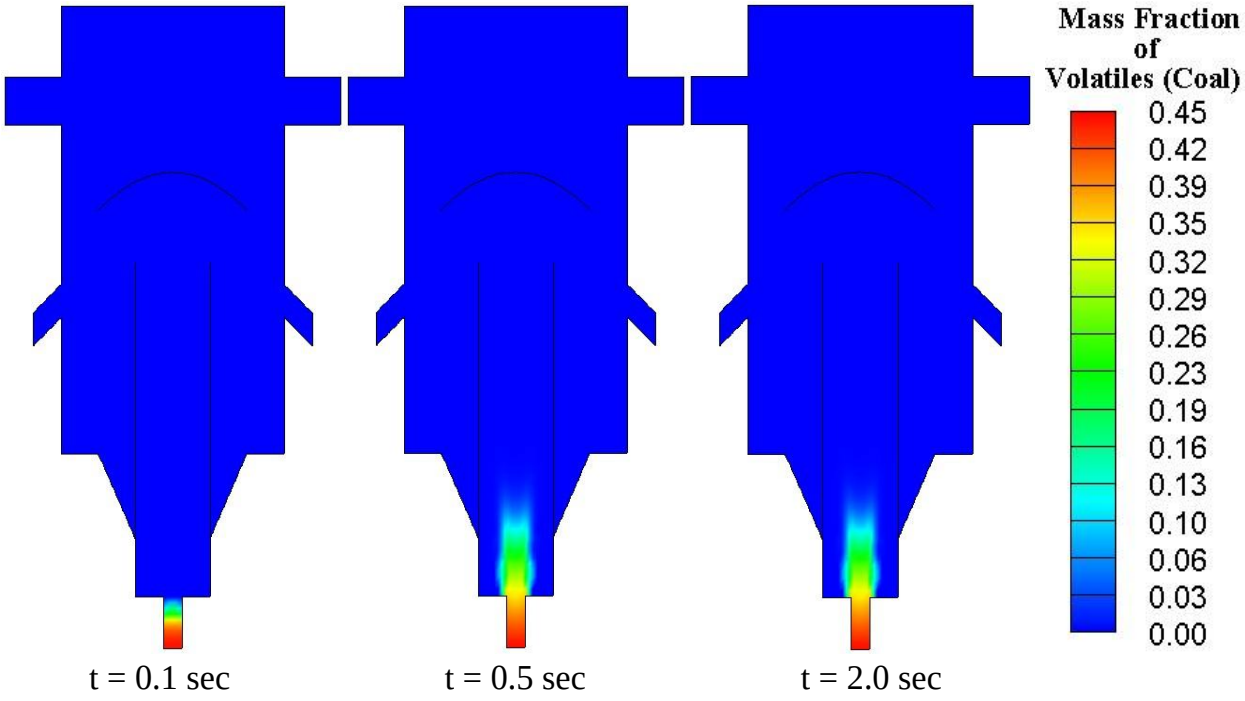

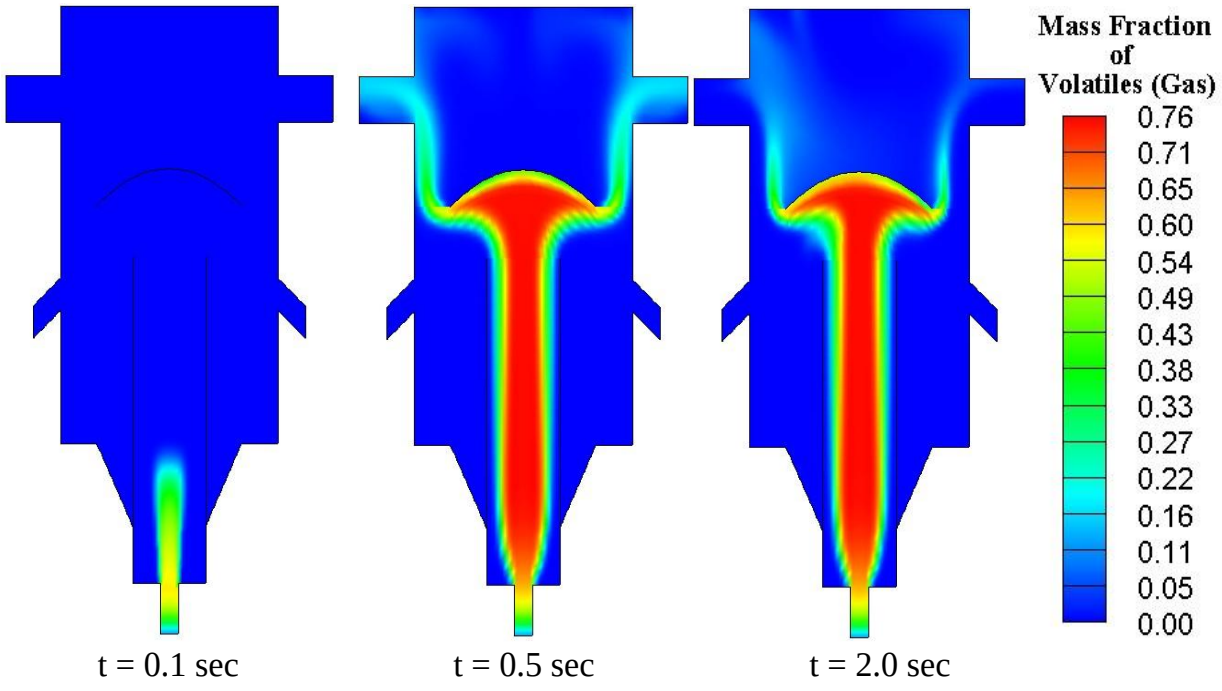

Figure 4.13 2-D transient distributions of mass fractions of volatiles (in coal phase) vs. volatiles (in gas phase) from 0.1 seconds to 2.0 seconds for Case 3a

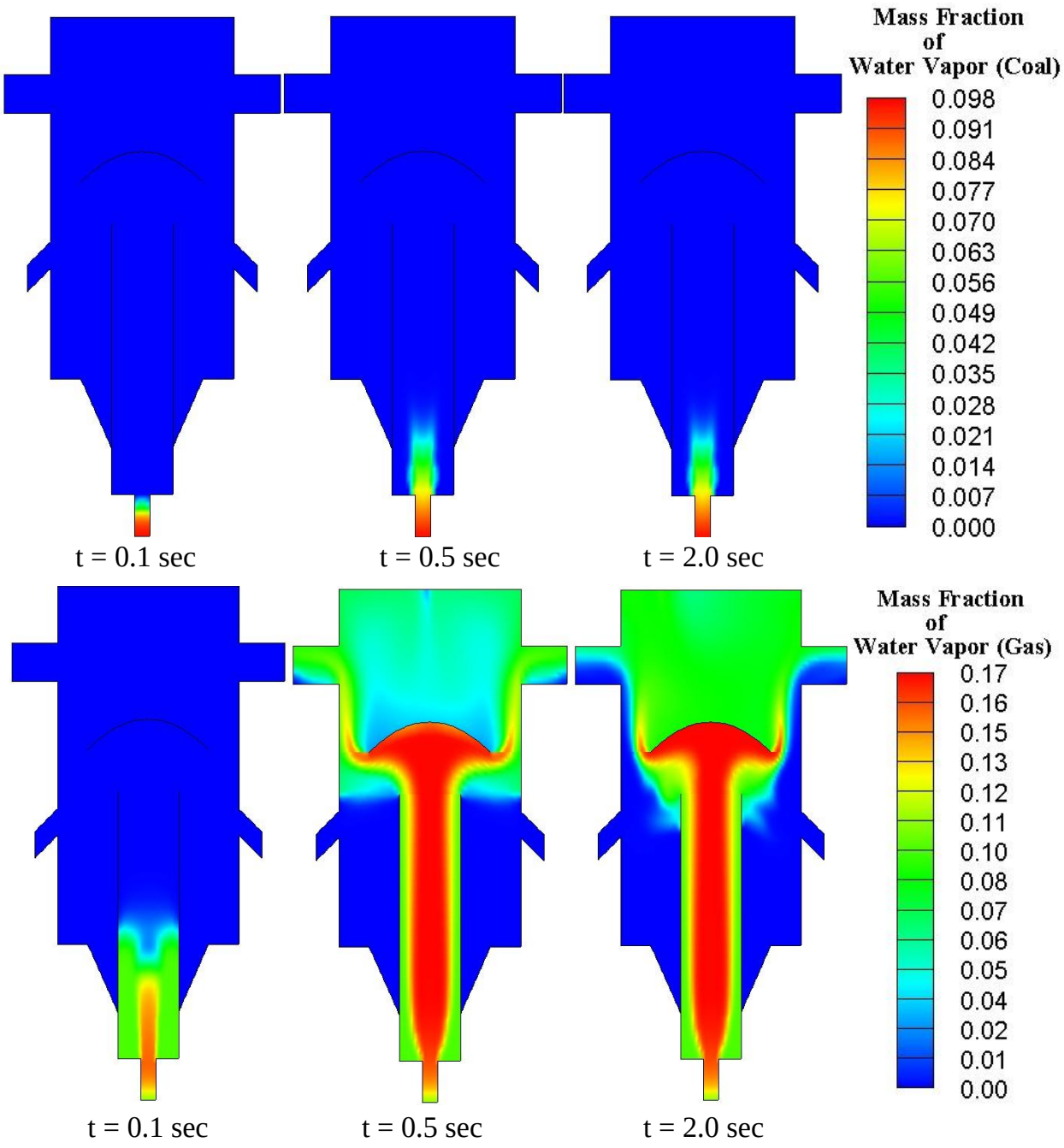

Figure 4.14 2-D transient distributions of mass fractions of water vapor (in coal phase) vs. water vapor (gas phase) from 0.1 seconds to 2.0 seconds (Case 3a)

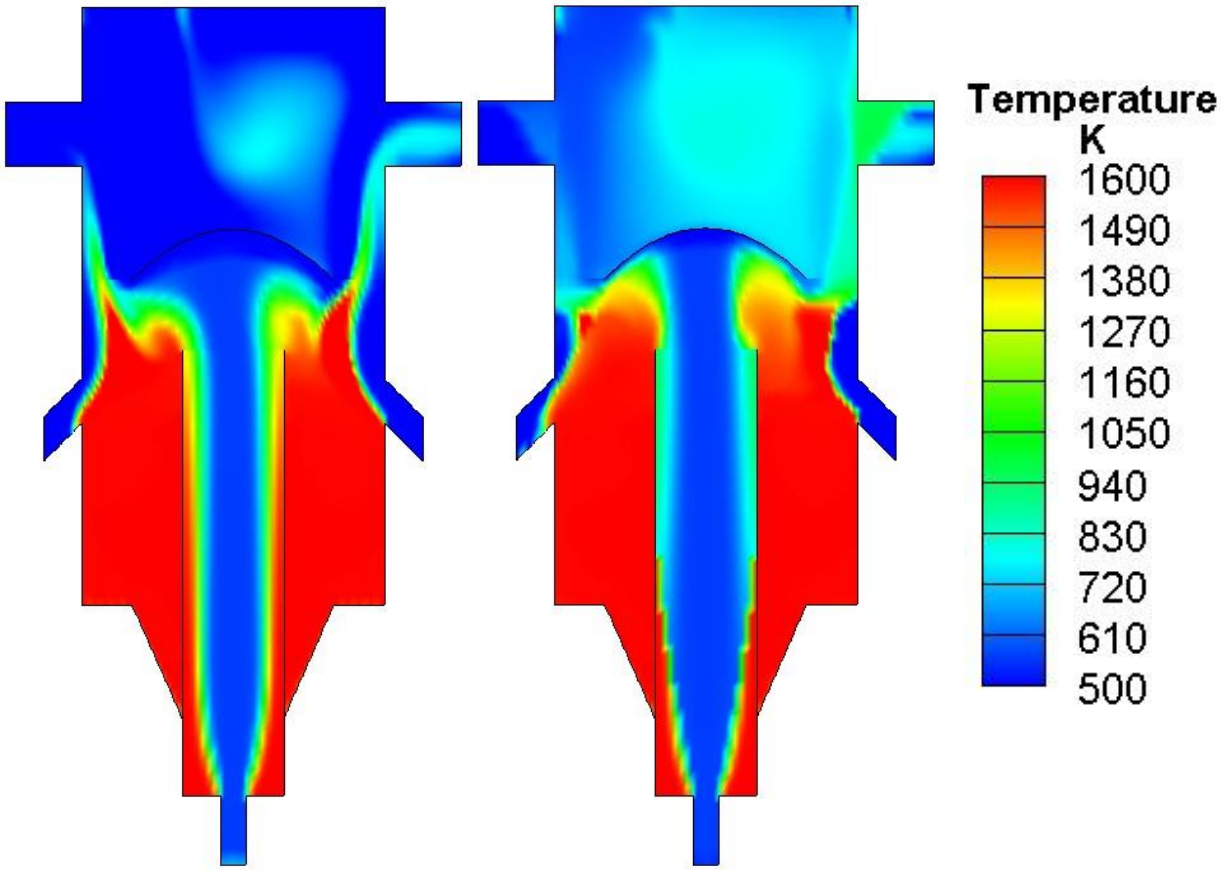

Figure 4.15 2-D temperature distribution of (a) gas phase and (b) coal phase at t = 0.9 second. (Case 3a)

4.2.2.2 Case 3b: Combusted Gas Blown at the Draft Tube and Volatiles Blown at the Fluidized Bed

In this case, volatiles have been treated as the fluidization gas. This is based on the assumption that if the mild gasifier were to successfully produce volatiles, a small amount of volatiles can be conveniently used as the fluidization fluid. This case will show how the volatiles would react by going through the chars in the fluidized bed. Meanwhile, the inlet conditions in the draft tube are the same as those in Case 3a. The inlet conditions are summarized in Table 4.6.

The distributions of various species mass fractions in the mild gasifier are shown in Fig. 4.16. The mass weighted average temperatures for the gas phase and solid phase are 416.06K and 528.73K, respectively, at the outlet. The syngas composition at the outlet is given in Table 4.7.

Table 4.6 Parameters, boundary and operating conditions for Case 3b

Parameters	Case 3b	
Inlet position	Fluidized bed inlet	Draft tube inlet
Feedstock & transporting agent	volatiles	coal & combusted gas
Syngas inlet velocity at horizontal holes, m/s	0.5	
Snygas inlet velocity at skew holes, m/s	0.3	
Combusted gas velocity at coal inlet, m/s		1.0
Entrained coal velocity at coal inlet, m/s		0.167
Combusted gas velocity at hot gas inlet, m/s		2.0
Temperature for fluidization gas, K	500	
Temperature for entrained combusted gas, K		1600
Temperature for entrained coal, K		500
Mass fraction at inlet (%)		
CO_2		0.2274(combusted gas)
N_2		0.6738(combusted gas)
Water Vapor		0.0976(coal) 0.0987(combusted gas)
CO		
H_2		
Char		0.4533(coal)
Volatiles	1	0.4491(coal)
Operating pressure (pascal)	101325	101325
Operating temperature (K)	288.16	288.16
Operating density (kg/m^3)	1.177	919.56/1.18
Gravitational acceleration (m/s^2)	9.81	9.81
Wall temperature, K	Adiabatic	Adiabatic

Table 4.7 Species composition at syngas exit at t=2.0 seconds for case 3b

	Temp(K)	Components	Mass (%)	Vol (%)
Gas phase 99.6% volume)	416.06	O2	9.90	8.01
		N2	56.76	51.57
		Volatiles	7.22	7.50
		Moisture	5.54	7.57
		CO	6.74	5.94
		CO2	10.62	6.01
		H2	1.03	12.69
		C6H6	2.17	0.69
Coal phase (0.4% volume)	528.73	Char	55.47	
		Volatiles	0	
		Moisture	0	
Mass flow rate (kg/s-m)			-2.4856045	

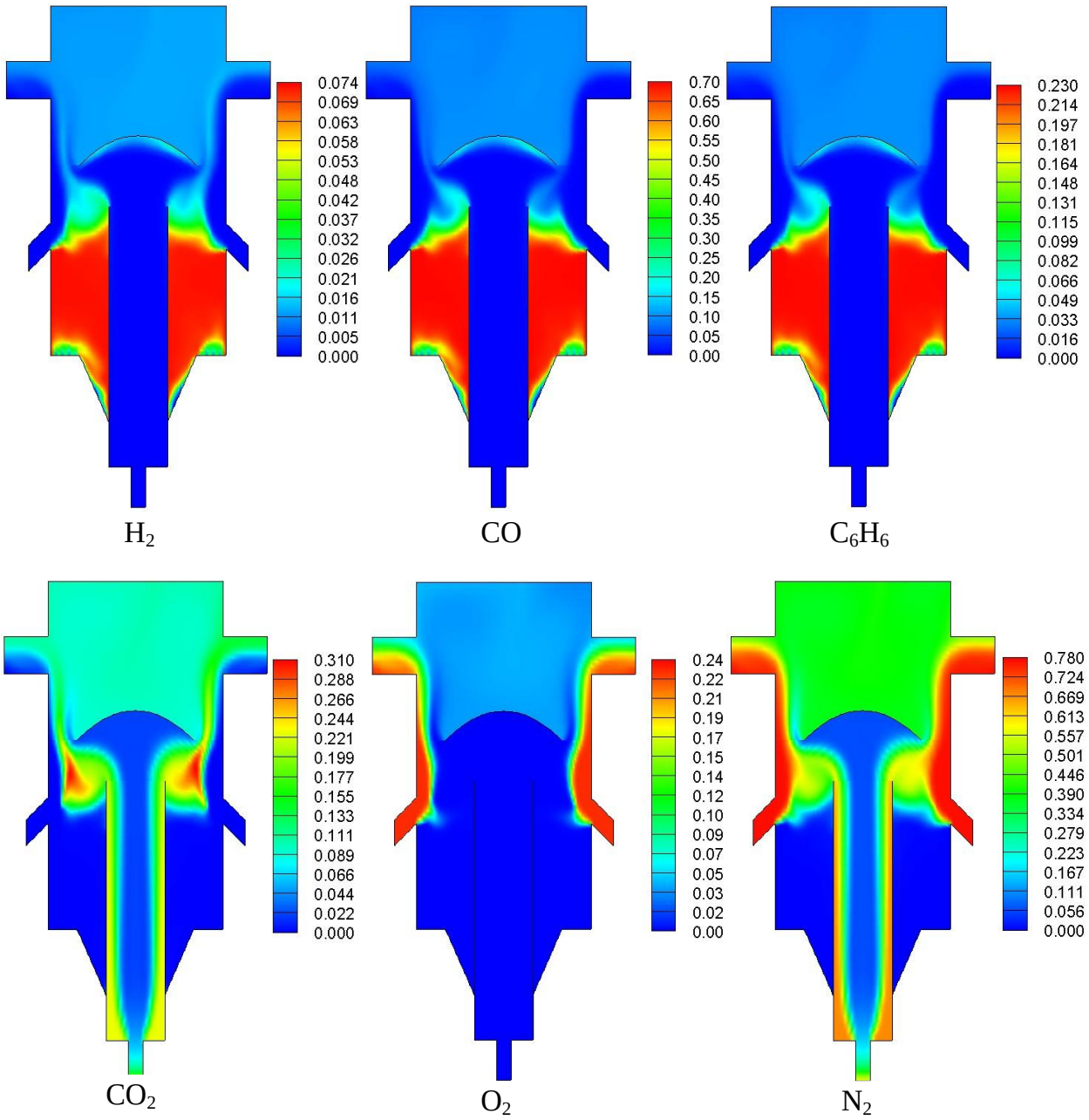

Figure 4.16 2-D transient distribution of mass fractions of various species at time t = 2 seconds for Case 3b

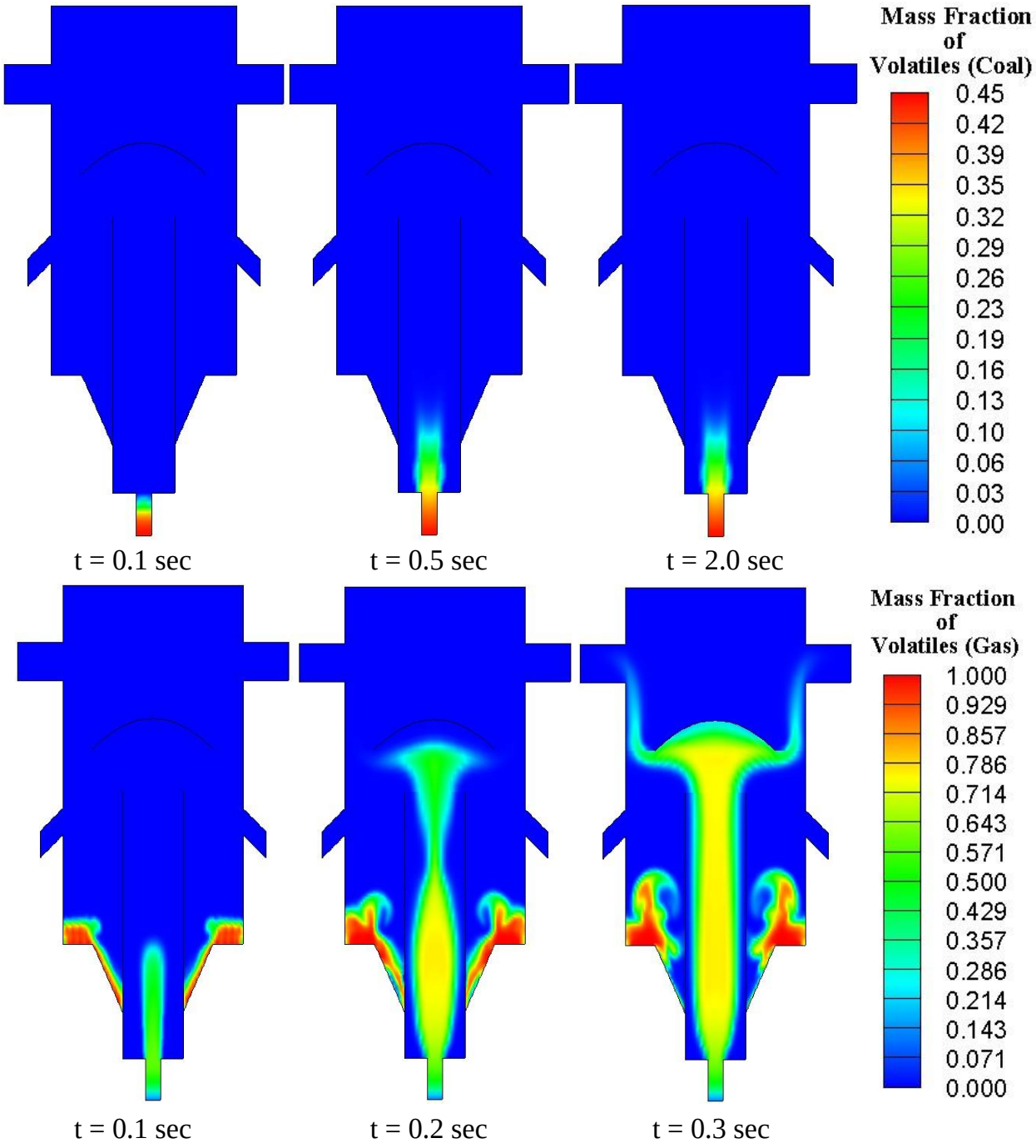

Figure 4.17 2-D transient distributions of mass fractions of volatiles (coal phase) vs. volatiles (gas phase) from 0.1 seconds to 2.0 seconds for Case 3b

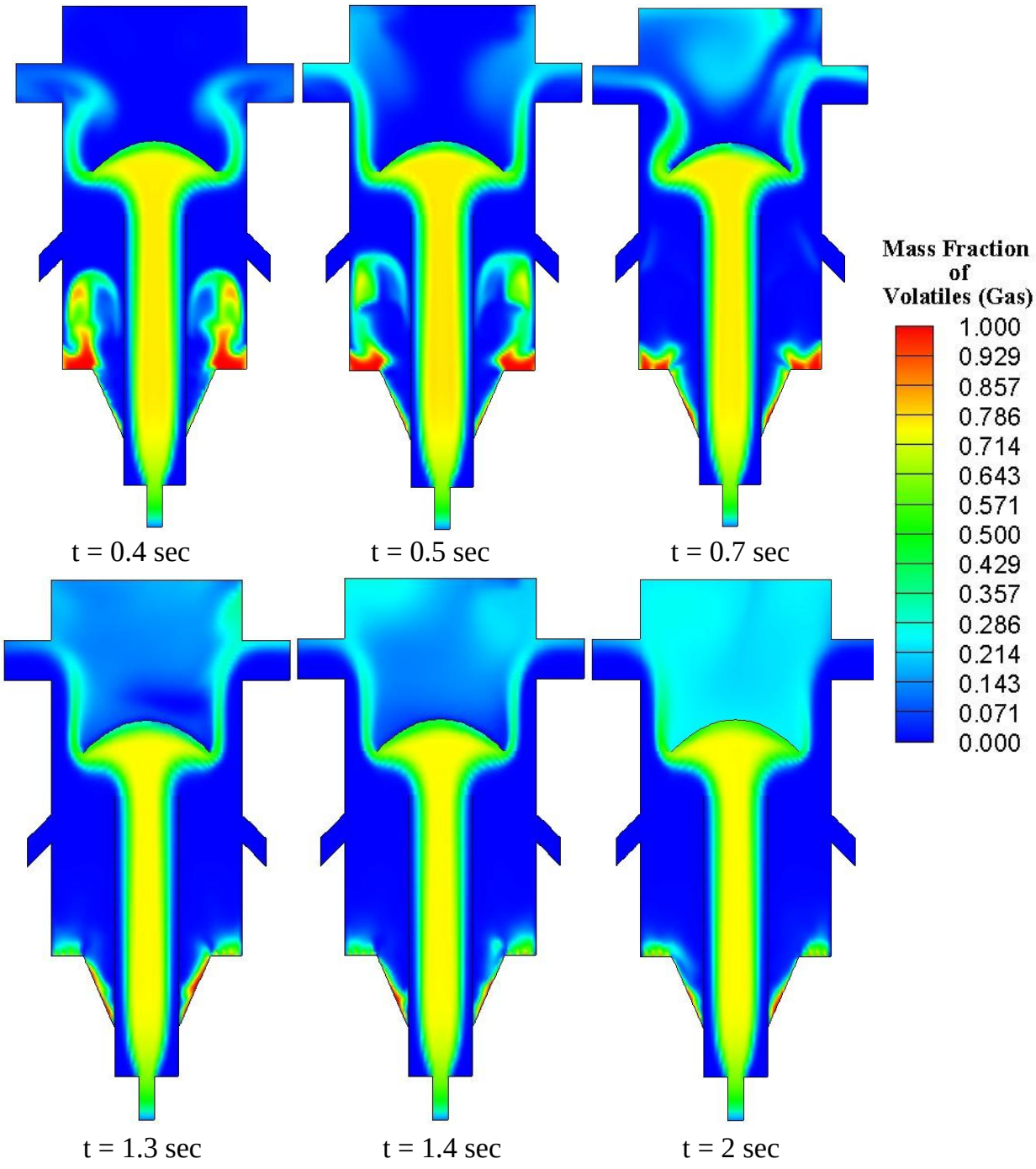

Figure 4.18 Transient distributions of mass fractions of volatiles (coal phase) vs. volatiles (gas phase) from 0.1 seconds to 2.0 seconds (Case 3b)

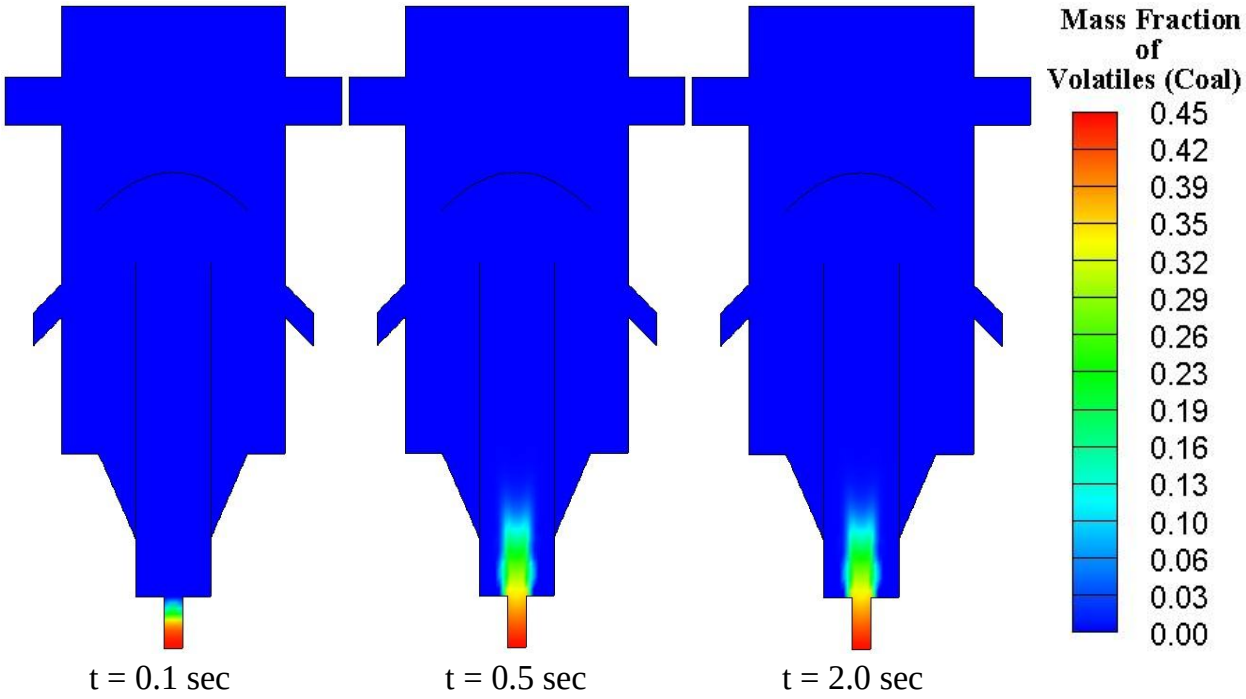

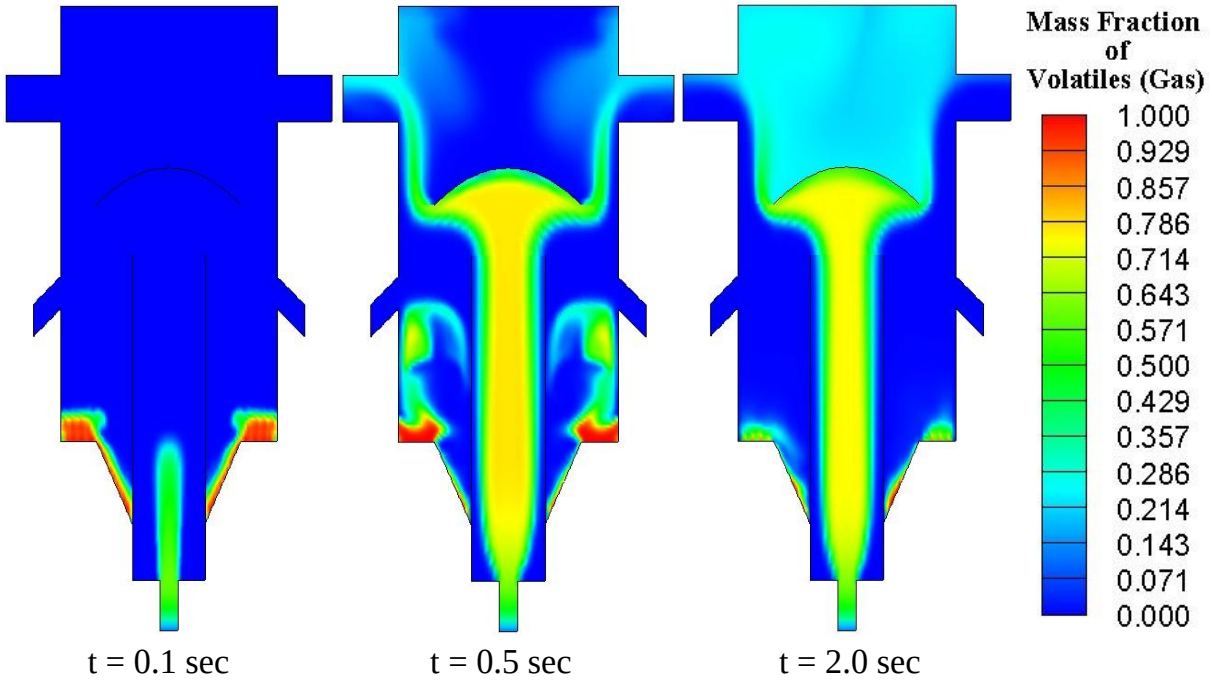

Figure 4.19 Distribution of mass fractions of volatiles (coal phase) vs. volatiles (gas phase) from 0.1 seconds to 2.0 seconds (Case 3b)

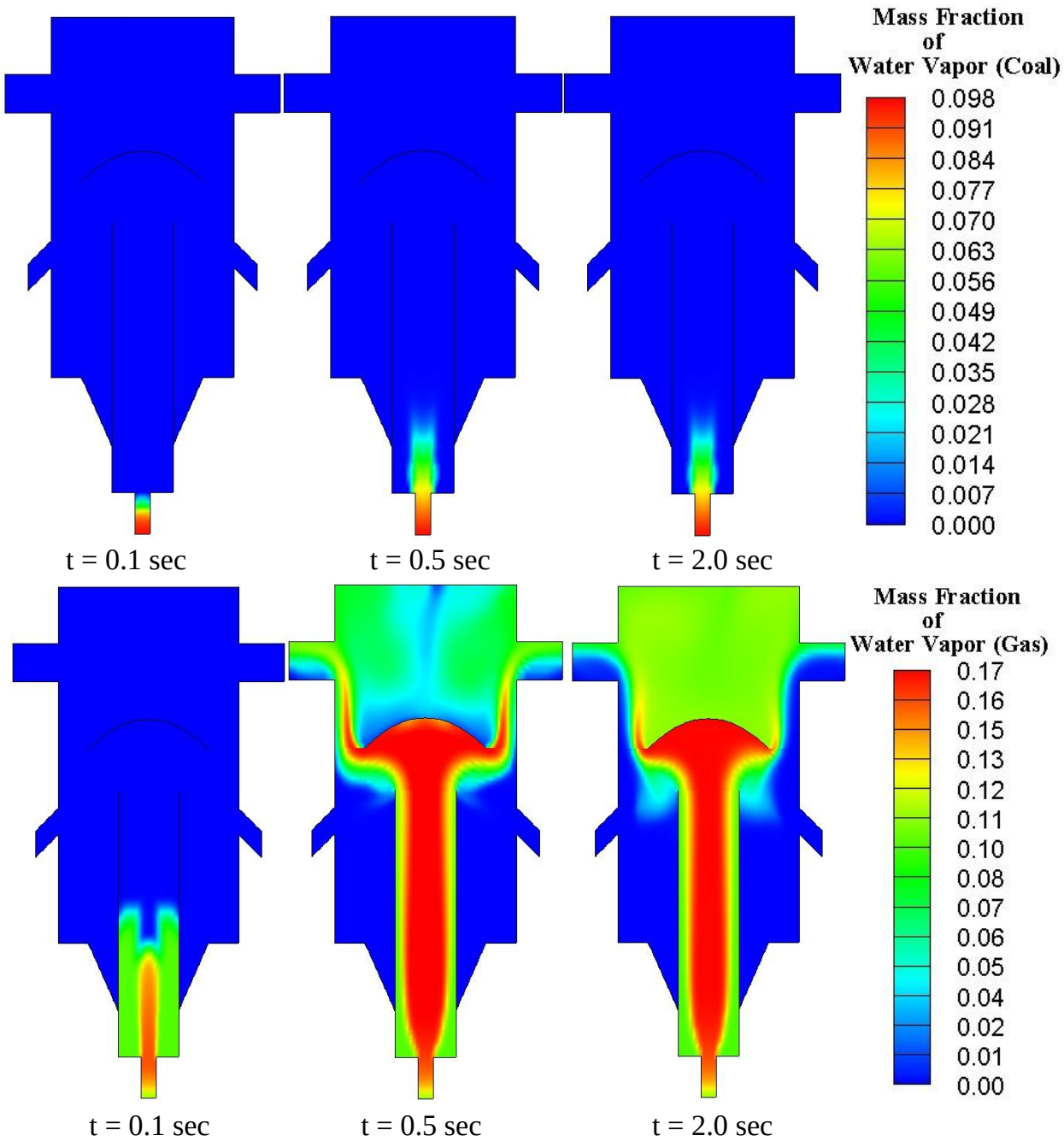

Figure 4.20 Distribution of mass fractions of water vapor (coal phase) vs. water vapor (gas phase) from 0.1 seconds to 2.0 seconds (Case 3b)

4.2.3 Case 4: 3-D Thermal-flow Behavior with Solids (no reaction)

Due to the complex reactions in multiphase flow computations, a 2-D simulation takes about four days to obtain a converged result. Based on this computation speed, a full simulation of a 3-D case will take about one month to complete. Therefore, in the case of this 3-D study, only the thermal-flow behavior of the multiphase flow is conducted without including chemical reactions.

The whole domain is filled up with 0.25 mm diameter carbon particles. One portion of the air serving as the coal transport gas enters through the coal inlet with a velocity of 1 m/s at 1600K. The other portion of the air goes through the hot gas inlet with a velocity of 2 m/s at 1600K. Carbon solid is fed into the domain with a velocity 0.167 m/s at 500K through the coal inlet at the bottom of the draft tube. The horizontal holes in the 2-D geometry are replaced by slots to reduce the requirements of very fine meshing near the small holes, whereas the holes in the inclined perforated plate are maintained at their original geometry with a diameter of 0.15 inches (0.381 cm, see Fig. 2.2). The inlet velocity at the horizontal slot and at the inlet of the inclined holes is assigned to be 0.5 m/sand 12 m/s, respectively, while the temperature in both places is taken to be 500K.. The inlet conditions of Case 4 are summarized in Table 4.8.

Table 4.8 Parameters, boundary and operating conditions for Case 4

Parameters	**Cases 4**	
Inlet position	Fluidized bed inlet	Draft tube inlet
Feedstock & transporting agenct	air	carbon solid & air
Air inlet velocity at horizontal slots, m/s	0.5	
Air inlet velocity at skew holes, m/s	12.0	
Air inlet velocity at coal inlet, m/s		1.0
Entrained coal velocity at coal inlet, m/s		0.167
Entrained air velocity at hot gas inlet, m/s		2.0
Temperature for fluidization gas, K	500	
Temperature for entrained air, K		1600
Temperature for entrained coal, K		500
Operating pressure (pascal)	101325	101325
Operating temperature (K)	288.16	288.16
Operating density (kg/m^3)	1.225	2000/1.225
Gravitational acceleration (m/s^2)	9.81	9.81
Wall temperature, K	Adiabatic	Adiabatic

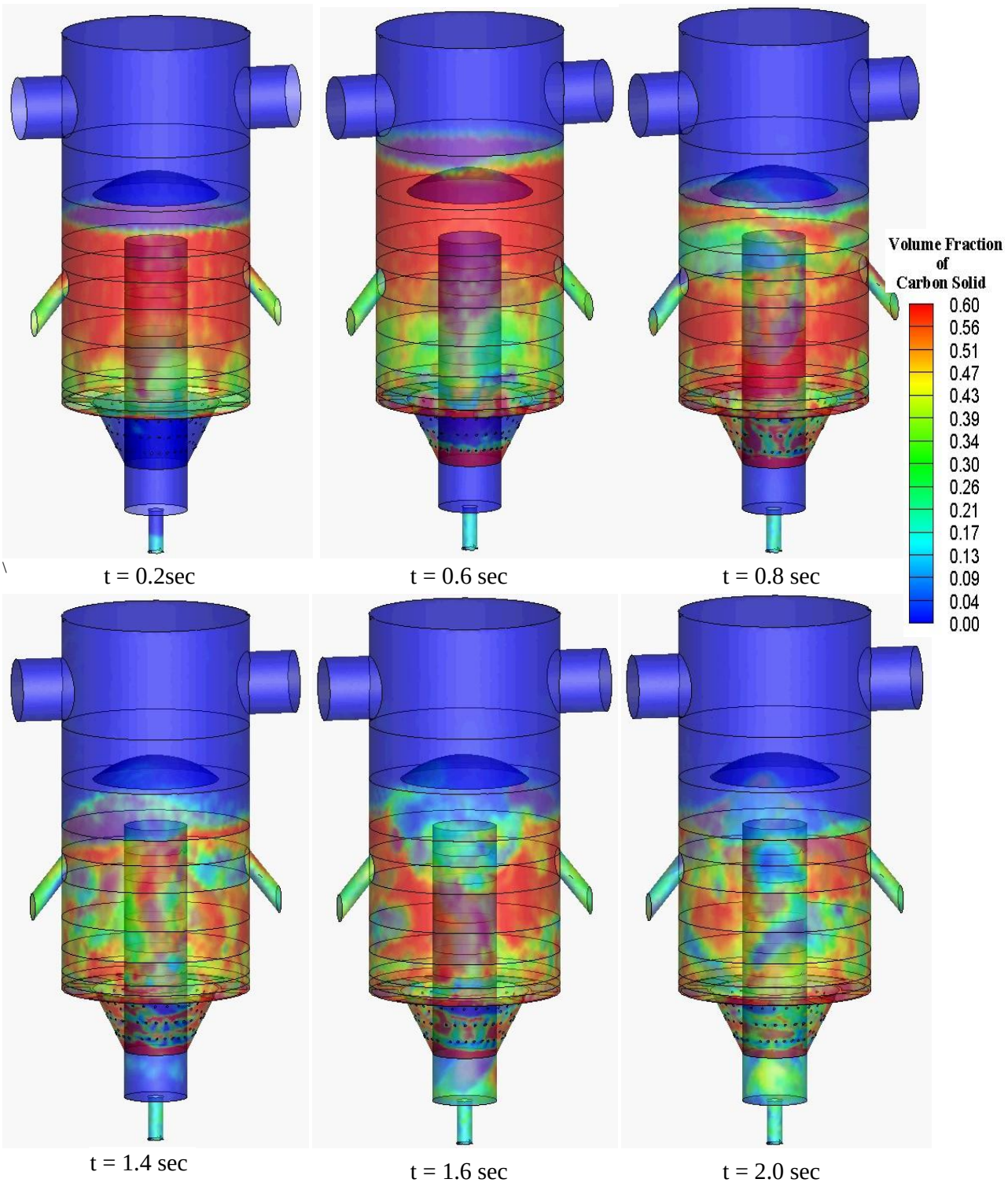

Figure 4.21 3-D transient distribution of the volume fraction of carbon solid from t = 0.2-2.0 seconds (Case 4)

In Case 2 and Case 3a, the height of the fluidized bed is sustained for a while, but eventually drops below the char chute entrance after the initially "patched" char was extracted from the char chute or entrained out by the gases exiting the gasifier through the syngas outlets. But, in Case 4, the fluidized bed height is always maintained at the same height as the char chute exit. Figure 4.21 shows the 3-D transient distribution of the volume fraction of carbon solid in the whole domain up to 2 seconds into the simulation. Figure 4.21 also shows that the arched deflector successfully removes char accumulation on its roof, which was previously shown on a flat-top deflector.

4.2.4 Case 5: 3-D Mild Gasification Simulation (Syngas blown at fluidized bed)

In this case, coal is transported by nitrogen with a pre-heated temperature of 500K through the draft tube feedstock inlet entering the mild gasifier. Meanwhile, the combusted gases with a temperature of 1600K go through the draft tube to provide devolatilization energy. These combusted gases contain mainly carbon dioxide, water vapor, and nitrogen. For convenience, no oxygen is assumed in the combusted gases. Since there is no oxygen, combustion will not happen within the draft tube. On the other side, the fluidization gas is supplied with the raw syngas that is assumed to contain CO and H_2 only, which are directly drawn from the exit of the mild gasifier. The inlet conditions of Case 5 are listed in Table 4.9. The complete information of syngas outlet is given in Table 4.10.

Table 4.9 Parameters, boundary and operating conditions for Case 5

Parameters	**Case 5**	
Inlet position	Fluidized bed inlet	Draft tube inlet
Feedstock & transporting agent	syngas	coal & combusted gas
Syngas inlet velocity at horizontal holes, m/s	0.5	
Snygas inlet velocity at skew holes, m/s	12	
Combusted gas velocity at coal inlet, m/s		1.0
Entrained coal velocity at coal inlet, m/s		0.167
Combusted gas velocity at hot gas inlet, m/s		2.0
Temperature for fluidization gas, K	500	
Temperature for entrained combusted gas, K		1600
Temperature for entrained coal, K		500
Mass fraction at inlet (%)		
CO_2		0.2274(combusted gas)
N_2		0.6738(combusted gas)
Water Vapor		0.0976(coal) 0.0987(combusted gas)
CO	0.882	
H_2	0.118	
Char		0.4533(coal)
Volatiles		0.4491(coal)
Operating pressure (pascal)	101325	101325
Operating temperature (K)	288.16	288.16
Operating density (kg/m^3)	1.177	919.56/1.18
Gravitational acceleration (m/s^2)	9.81	9.81
Wall temperature, K	Adiabatic	Adiabatic

Table 4.10 Species composition at syngas exit at t = 1.56 seconds for Case 5

	Temp(K)	Components	Mass (%)	Vol (%)
Gas phase 99.9% volume)	1587	O2	0.03	0
		N2	43	27.03
		Volatiles	0	0
		Moisture	4.93	4.62
		CO	37.74	23.19
		CO2	7.64	2.98
		H2	4.89	41.79
		C6H6	1.76	0.39
Coal phase (0.1% volume)	1587	Char	10.58	
		Volatiles	0	
		Moisture	0	
Mass flow rate (kg/s)			-0.0421157	

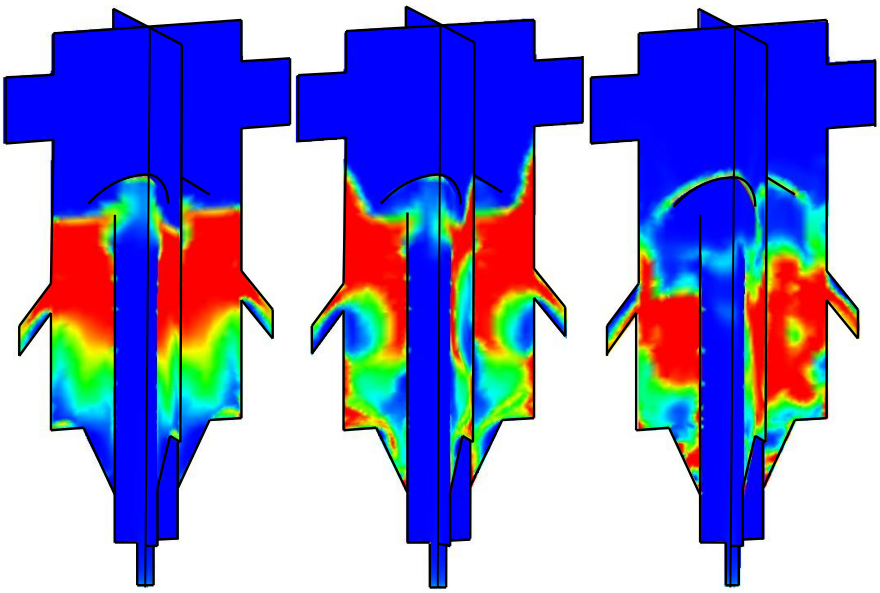

Figure 4.22 Transient distribution of the volume fraction of carbon solid at the mid-plane of the 3-D mild gasifier (Case 5)

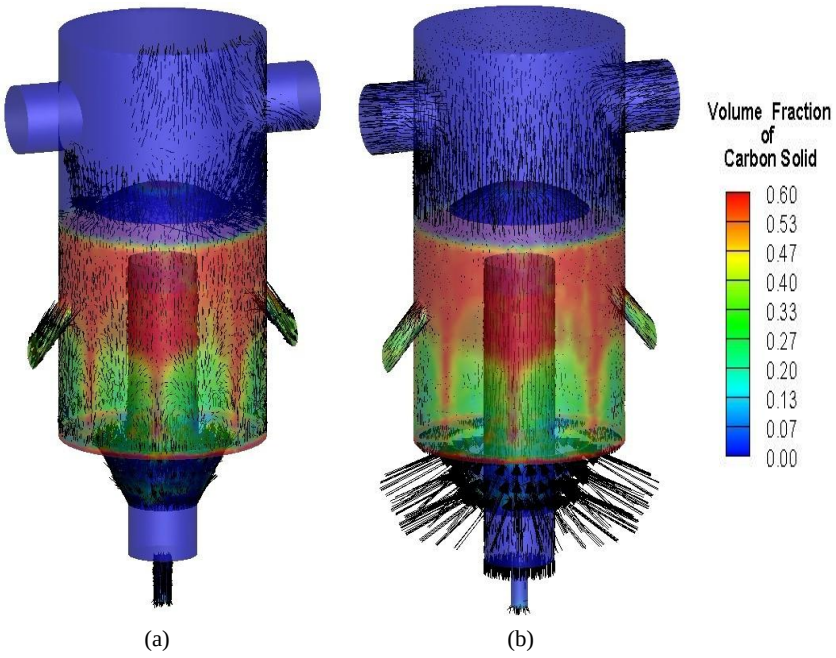

Figure 4.23 A snapshot of the 3-D (a) velocity profile of the coal phase and (b) velocity profile of the gas phase at 0.3 seconds with the volume fraction of carbon solid being displaced in color (Case 5)

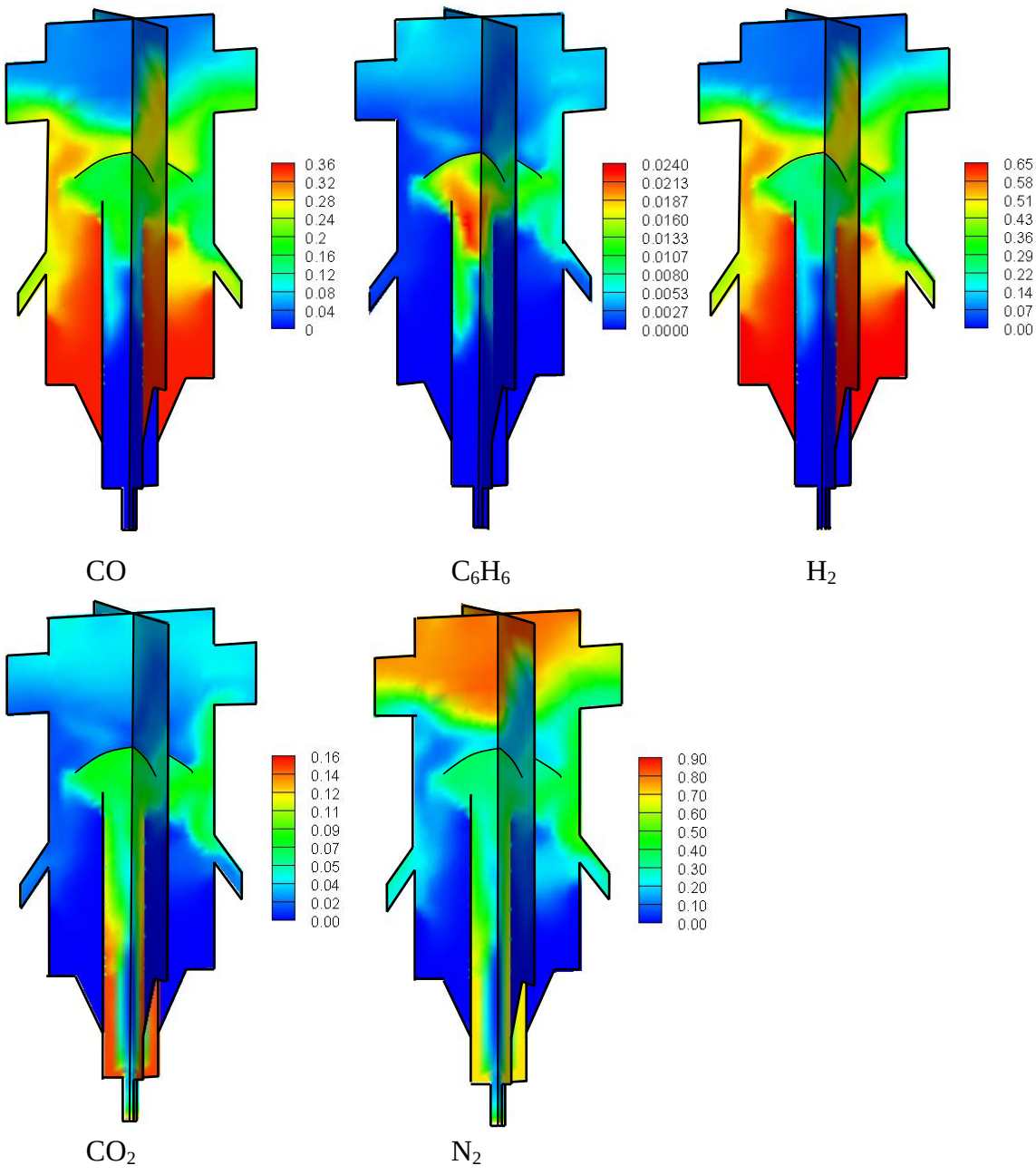

Figure 4.24 A snapshot of the transient distribution of the volume fraction of various gas species at the mid-plane of the 3-D mild gasifier at 0.9 seconds (Case 5)

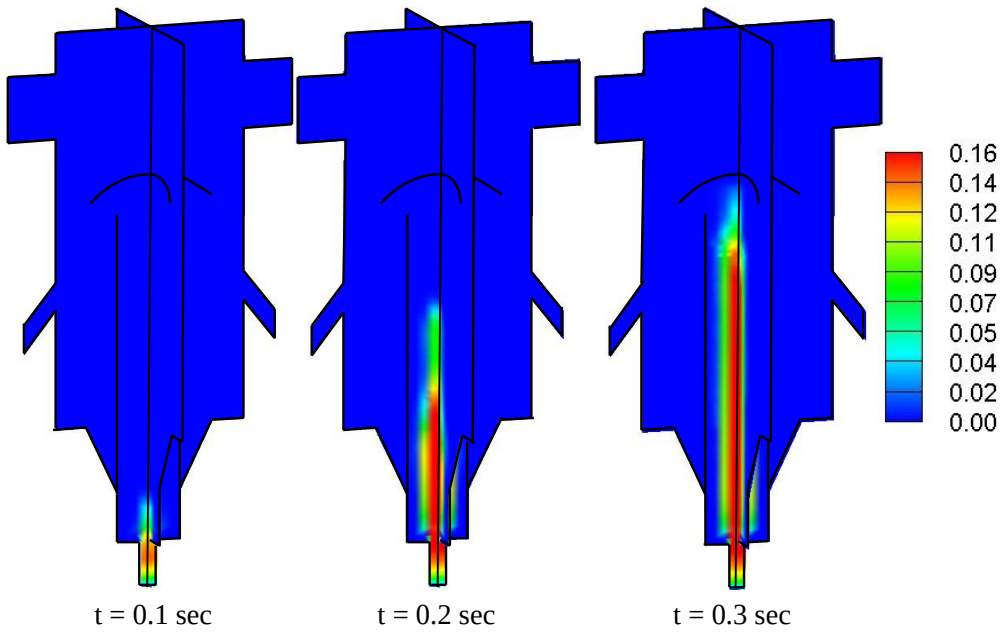

Figure 4.25 Transient distribution of the mass fraction of volatiles within the gas phase in the mid-plane of the 3-D mild gasifier (Case 5)

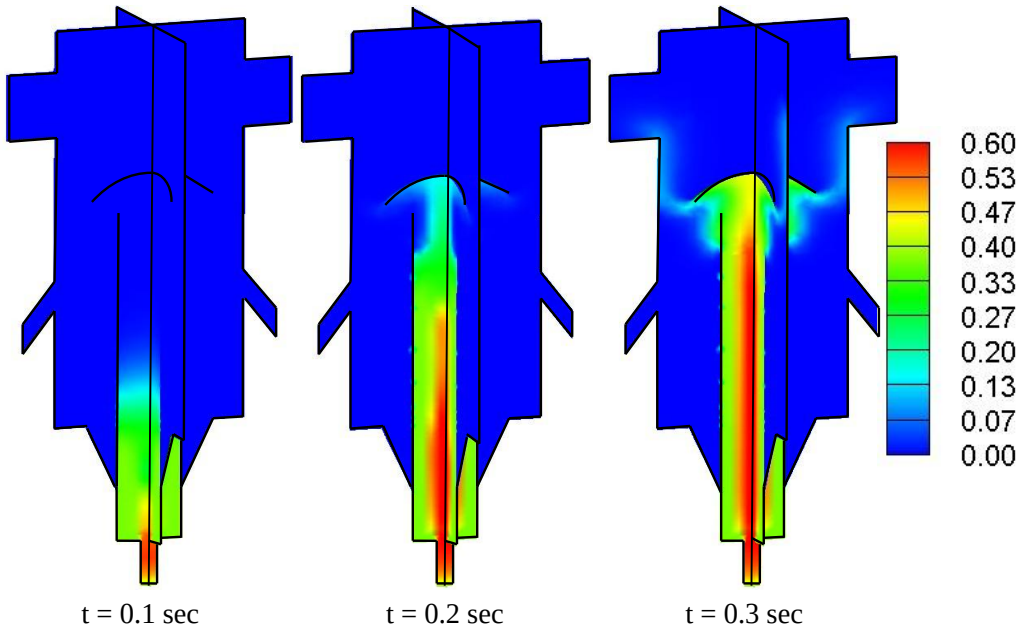

Figure 4.26 Transient distribution of the mass fraction of water vapor within the gas phase in the mid-plane of the 3-D mild gasifier (Case 5)

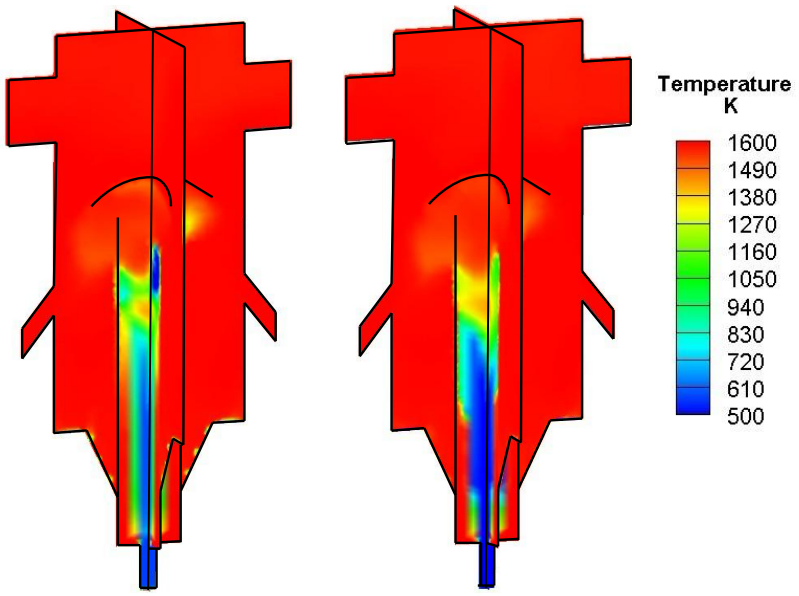

Figure 4.27 3-D temperature distribution of the (a) gas phase and (b) coal phase at t = 0.9 seconds (Case5)

In Case 5, the entire 3-D mild gasification process has been simulated. The fluidization gas velocity was selected to be 0.167 m/s in the previous 2-D cases. However, in order to keep the same percentage ratio of the fluidization mass flow rate versus the volume of fluidized medium as in the 2D cases, the fluidization gas inlet velocity of the 3-D case has to be increased to 12 m/s for the perforated holes, located on the inclined plate, but the other portion of the fluidization velocity through the horizontal slots must remain unchanged. Figure 4.22 shows that carbon solid undergoes a vivid fluidization movement in the fluidized bed, as displayed on the two perpendicular planes. Also, Fig. 4.23 gives the velocity profiles for both the gas phase and the solid phase. In the previous 2-D cases, recall that the pressure at the char chutes was purposely assigned a higher value in order to simulate the control valve action as well as to adjust the ratio between the char chute cross-sectional area and the gasifier cross-sectional area. In addition, this slows down the extraction speed of the carbon solid and sustains the height of the fluidized bed. In this 3-D case, no such manipulation is needed. The fluidized bed is sustained well with the given input fluidization velocities.

Figure 4.24 presents the volume fraction of various species in the gas phase. Figures 4.25 and 4.26 indicate that the devolatilization process that has been developed in the 2-D model has been successfully incorporated into the 3-D model. Figure 4.27 gives the global picture of temperature

distribution for the two phases. It seems there is decent thermal energy remaining in the syngas in the freeboard region. This is in contrast to the conditions in the 2-D simulation shown in Fig. 4.15. Volatiles and water vapor, which are inherent in the coal, have been driven out by the combusted hot gases. Since not too much volatile matters have been detected at the syngas exits in the 3-D case (see Fig. 4.25), it appears that the volatiles have been all thermally cracked in the 3-D case, which is in contrast to the 2-D result that shows only a fair amount of volatiles surviving at the exit (Case 3b in Fig. 4.18). It will be just a matter of trial-and-error to obtain the different degrees of mild gasification for practical applications. Based on these results, the objectives have been successfully achieved in this project.

CHAPTER FIVE
CONCLUSIONS

In this study, a mild gasification process has been developed to provide an innovative form of clean coal technology called the Integrated Mild Gasification Combined Cycle (IMGCC), which could help build a power plant with high thermal efficiency and highly economical operation or to refurbish an existing coal-fired power plant with more economical means to raise efficiency and reduce emissions. The essential technology of a mild gasification power plant relies on the successful design and operation of mild gasifiers that can generate synthesis gas consisting primarily of high energy-density volatiles. A preliminary concept of a hybrid mild-gasifier has been designed by combing the features from both entrained bed and fluidized bed gasifiers at the Energy Conversion and Conservation Center (ECCC). This study has successfully incorporated a fixed-rate devolatilization model to the existing 2-D reactive multiphase model, and then expanded it to a complex 3D model. The expanded and improved model has been used to gain understanding and insight of the thermal-flow and mild gasification process inside this mild gasifier. The knowledge obtained from this simulation has been applied to guide the modification of the existing design as well as to obtain the appropriate operating conditions for fluidization speeds and control of residence time for devolatilization and reactions. The commercial Computational Fluid Dynamics solver ANSYS/FLUENT 14.0 is used.

The Eulerian-Eulerian multiphase model is employed to simulate both the primary phase (air) and the secondary phase (coal particles). The transient multiphase Navier-Stokes equations and species transport equations are solved with heterogeneous (gas-solid) and homogeneous (gas-gas) global gasification reactions and a two-step volatile cracking reaction. In addition, a fixed-rate devolatilization model and a demoisturization (liquid-gas) reaction are implemented to simulate the mild gasification process. For each homogeneous reaction, both the finite rate and the eddy-dissipation reaction models are solved. The lower of the two obtained rates is then selected and used. Multiphase constitutive equations derived from kinetic theory are used to calculate the effective shear viscosities, bulk viscosities, and other interaction coefficients between the primary and secondary phases.

The study begins with simulations of fluid dynamics and heat transfer phenomena under different design and operating considerations. After confirming that the airborne particle residence time within the gasifier is close to 3 seconds, and the fluidization velocity of 0.5 m/s is workable, a full, reactive multiphase model is employed to investigate the effects of coal particle size, fluidization velocity, coal feed speed, and residence time on the flow pattern and gasification process. The impact of selecting different coal transportation agents (air vs. combusted gases) is also considered. To sustain the fluidized bed depth to reach steady state, efforts have been spent to investigate the entrainment control between the fluidized bed and the entrained-flow regime in the draft tube, the effect of draft tube size, and the char chute exit pressure control.

The results are summarized below:

- ✓ A series of mild gasifier design modifications have been considered to achieve effective mild gasification by controlling the particle's residence time in the draft tube within one second and keeping the gases and air-borne particles in the mild-gasifier for about 3 seconds.

- ✓ In 2-D cases, the minimum fluidization velocity is found to be 0.2 m/s seconds, which is close to the 0.38 m/s calculated from the Ergun equation.

- ✓ In 2-D cases, the appropriate velocity needed to sustain fluidization with effective and vigorous mixing but without depleting the fluidized bed contents has been identified to be in the range of 0.2 – 0.5 m/s.

- ✓ A narrow slot was originally designed at the bottom of the draft tube to allow the flow in the draft tube to entrain the particles from the fluidized bed. It is discovered that the high pressure difference between the coal inlet and syngas exit has adversely pushed the flow from the draft tube to move through the entrainment slot to the fluidized bed. This stream of high-velocity flow inadvertently blows the fluidized particles away, destroying the fluidized bed. Due to this result, the entrainment slot is closed for all subsequent studies.

- ✓ The goal of sustaining the fluidized bed in the 2-D configuration has been achieved by closing the entrainment slot and pressurizing the char chute at the exit or by reducing the char chute's cross-sectional area so that the ratio of char chute diameter over the gasifier perimeter remains the same as that of the 3-D geometry.

- ✓ The capacity for power generation from the ECCC mild gasifier is evaluated and the overall energy balance is calculated. Based on these values, the size and coal feeding rates are determined during the design process. The 2-D gasifier has a total power of 9.92 MW/-m, while the 3-D gasifier has a power around 0.275 MW.

- ✓ The devolatilization and demoisturization processes have been successfully implemented in the 3-D case. Using the results obtained in the 2-D cases, the fluidized bed can be successfully operated and sustained in the 3-D case.

- ✓ The volatiles have been shown to be fully cracked in the freeboard region in the 3-D case. This means that full gasification, rather than mild gasification, has been achieved. The high temperature distribution of the gas phase in the freeboard regions of the 3-D case indicates that there appears to have been more thermal energy input from the coal feed mass than that is needed to achieve mild gasification. Continuously fine-tuning the fluidization velocity and the coal mass flow rate will most likely allow the achievement of mild gasification in future studies.

Recommended Future Studies

Many assumptions have been made in the mild gasification model developed in this study. The following studies are recommended to improve the existing mild gasification model and optimize the design of the ECCC's Fluidized Bed Mild Gasifier:

1. Fine-tune the devolatilization energy or devolatilization rate with published data to allow more accurate modeling of the devolatilization process. This is important to slow down or stop the devolatilization process when the temperature drops below the threshold devolatilization temperature.

2. Continue to fine-tune the fluidization velocity and input coal mass flow rate to achieve different levels of mild gasification.

3. Conduct a simulation on the effect of the entrainment slot on the bottom of the draft tube so that a more effective transporting mechanism from the fluidized bed to the entrained bed (draft tube) can be realized.

4. Implement a condensation sub-model in the current mild gasification model to truly reflect the potential tar-formation phenomenon in the mild gasification process.

5. Check the input thermal energy amount for mild gasification based on the 3-D model, and then find out the most reasonable amount for mild gasification in 3-D. Meanwhile, revise pivotal parameters to help manipulate the gasification rate.

6. Conduct experiments to verify the CFD results.

REFERENCES

Ahmadi, G., and Shahinpoor, M., 1983, "A Note on Collision Operators in Rapid Granular Flows of Rough Inelastic Particles," Journal of Powder Technology, Vol. 35, 1983, pp 119-122.

ANSYS/FLUENT 14.0 User's Guide, November 2011.

Arastoopour, H., Lin, D., and Gidaspow, D., 1980, "Hydrodynamic Analysis of Pneumatic Transport of a Mixture of Two Particle Sizes," Multiphase Transport, Hemisphere Publishing Corp., Washington, 1980, pp 1853-1871.

Arastoopour, H., Wang, C. H., and Weil, S., A., 1982, "Particle-Particle Interaction Force in a Dilute Gas-Solid System," Journal of Chemical Engineering Science, Vol. 37, No. 9, 1982, pp 1379-1386.

Arastoopour, H., and Cutchin III, Joseph, H., 1985, "Measurement and Analysis of Particle-Particle Interaction in a Cocurrent Flow of Particles in a Dilute Gas-Solid System," Journal of Chemical Engineering Science, Vol. 40, No. 7, 1985, pp 1135-1143.

Badzioch, S., and Hawsley, P. G. W., 1970, "Kinetics of Thermal Decomposition of Pulverized Coal Particles," Ind. Eng. Chem. Process Des. Dev. Vol.9, No.4, 1970, pp. 521–530.

Baum, M. M., and Street, P. J., "Predicting the combustion behavior of coal particles," Combust. Sci. Technol. 1971, Vol.3, pp 231–243.

Benyahia, Sofiane., Syamlal, Madhava, and O'Brien, Thomas, J., 2004, "The Effect of Model Parameters on the Predictions of Core-Annular flow behavior in a fast Fluidized Gas/Solids Bed," Annual Meeting Conference Proceedings, 2004, pp 3283-3297.

Boerner, A., Renz, H., Qi, U., Vasquez, S., and Boysan, F., 1995, "Eulerian Computation of Fluidized Bed Hydrodynamics-A Comparison of Physical Models," Fluidized Bed Combustion, Vol. 2, ASME 1995, pp 775-787.

Borah, Ramesh, C., Ghosh, P., and Rao, Paruchuri, G., "A review on devolatilization of coal in fluidized bed," International Journal of Energy Research, Vol.35, 2011, pp.929-963.

Chapman, S., and Cowling, T. G., 1990, "The Mathematical Theory of Non-Uniform Gases," Cambridge University Press, Cambridge, England, 3rd edition.

Chen, J. S., Hayhurst, AN., 2004, "Does a large coal particle in a hot fluidized bed lose its volatile content according to the shrinking core model?", Combustion and Flame, 2004, Vol.139, pp.208-221.

Chejne, F., and Hernandez, J. P., 2002, "Modeling and Simulation of Coal Gasification process in Fluidized Bed," Fuel, Vol. 81, 2002, pp 1687-1702.

Comelissen, Jack, T., Taghipour, F. E. R., Ellis, N., Grace, John, R., 2007, "CFD Modeling of a Liquid-Solid Fluidized Bed," Chemical Engineering Science, Vol. 62, 2007, pp 6334-6348.

Dalla, Valle, J. M., 1948, Micromeritics, Pitman, London.

Ding, Jianmin., and Gidaspow, D., 1990, "A Bubbling Fluidization Model Using Kinetic Theory of Granular Flow," AlChE Journal, Vol. 36, No. 4, 1990, pp 523-538.

Elgobashi, S. E., and Abou-Arab, T. W., 1983, "A Two-Equation Turbulence Model for Two-Phase Flows," Phys. Fluids, Vol. 26, No. 4, pp 931–938.

Enwald, H., and Almstedt, A. E., 1999, "Fluid Dynamics of a Pressurized Fluidized Bed: Comparison between Numerical Solutions from Two-Fluid Models and Experimental Results," Journal of Chemical Engineering Science, Vol. 54, 1999, pp 329-342.

Enwald, H., Peirano, E., Almstedt, A.E., and Leckner, B., 1999, "Simulation of the Fluid Dynamics of a Bubbling Fluidized Bed. Experimental Validation of the Two-Fluid Model and Evaluation of a Parallel Multiblock Solver," Chemical Engineering Science, Vol. 54, 1999, pp 311-328.

Ergun, S., 1952, "Fluid Flow through Packed Columns," Journal of Chemical Engineering Progress, Vol. 48, No. 2, 1952, pp 89-94.

Faeth, G. M., 1987, "Mixing, Transport and Combustion in Sprays," Progress in Energy Combustion Science, Vol. 13, pp 293-345.

Fedors, R. F., and Landel, R. F., 1979, "An Empirical Method of Estimating the Void Fraction in Mixtures of Uniform Particles of Different Size," Journal of Powder Technology, Vol. 23, 1979, pp 225-231.

Fletcher, T. H., Kerstein, A. R., Pugmire, R. J., and Grant, D. M., 1990, "Chemical Percolation Model for Devolatilization: 2. Temperature and Heating Rate Effects on Product Yields," Energy Fuels, No. 4 (1990) 54.

Fletcher, T. H., and Kerstein, A. R., "Chemical Percolation Model for Devolatilization: 3. Direct use of CNMR Date to Predict Effects of Coal Type," Energy Fuels No. 6 (1992) 414.

Geldart, D., 1972, "The Effect of Particle Size and Size Distribution on the Behavior of Gas-fluidized Beds," Powder Technology, Vol. 6, pp 201–205.

Gidaspow, D., and Ettehadleh, B., 1983, "Fluidization in Two-Dimensional Beds with a Jet. 2. Hydrodynamic Modeling," Journal of Industry Engineering Chemical Fundamentals, Vol. 22, No. 2, 1983, pp 193-201.

Gidaspow, D., Lin, C. L., and Seo, Y. C., 1983, "Fluidization in Two-Dimensional Beds with a Jet. 1. Porosity Distributions," Journal of Industry Engineering Chemical Fundamentals, Vol. 22, No. 2, 1983, pp 187-193.

Gidaspow, D., Bezburuah, R., and Ding, J., 1992, "Hydrodynamics of Circulating Fluidized Beds, Kinetic Theory Approach," Fluidization VII, Proceedings of the 7th Engineering Foundation Conference on Fluidization, pp 75–82.

Grant, D. M., Pugmire, R. J., Fletcher, T. H., and Kerstein, A. R., 1989, "Chemical Percolation of Coal Devolatilization using Percolation Lattice Statistics," Energy Fuels 3 (2), pp 175-186.

Grewal, W. S., and Saxena, S. C., 1980, "Comparison of Commonly Used Relations for Minimum Fluidization Velocity of Small Solid Particles," Powder Technology, Vol. 26, No. 2, pp 229–238.

Gunn, D. J., 1978, "Transfer of Heat or Mass to Particles in Fixed and Fluidized Beds," Journal of Heat Mass Transfer, Vol. 21, 1978, pp 467-476.

Hinze, J. O., 1975, Turbulence, McGraw-Hill Publishing Co., New York.

Hong, R. Y., Guo, Q. J., Luo, G. H., Zhang, J. Y., and Ding, J., 2003, "On the Jet Penetration Height in Fluidized Beds with Two Vertical Jets," Powder Technology, Vol. 133, 2003, pp 216-227.

Huilin, Lu., Gidaspow, D., Bouillard, J., and Wentie, Liu., 2003, "Hydrodynamic Simulation of Gas-Solid Flow in a Riser Using Kinetic Theory of Granular flow," Journal of Chemical Engineering, Vol. 95, 2003, pp 1-13.

Lavieville, J., Quemerais, E., Mimouni, S., Boucker, M., and Mechitoua, N., "NEPTUNE CFD V1.0 Theory Manual". EDF. 2005

Jiradilok, V., Gidaspow, D., Damronglerd, S., Koves, W.J., and Mostofi, R., 2006, "Kinetic Theory Based CFD Simulation of Turbulent Fluidization of FCC Particles in a Riser," Chemical Engineering Science, Vol. 61, 2006, pp 5544-5559.

Keairns, D. L., Archer, D. H., Hamm, J. R., Lancaster, B. W., O'Neill, E. P., Newby, R. A., Peterson, C. H., Sun, C. C., Sverdrup, E. F., Vidt, E. J., and Yang, W. C., "Systems Implications of Desulfurization by Limestone in Pressurized Fluidized Bed Combustion," Westinghouse Research Laboratories, pp 493-523.

Khan, J. R., and Wang, T., "Development of a Devolatilization Model in Multi-Phase Simulation for a Hybrid Entrained-Flow and Fluidized Bed Mild Gasifier," Paper 32-3, Proceedings of the 28th International Pittsburgh Coal Conference, Pittsburgh, Pennsylvania, Sept. 12-15, 2011

Kobayashi, H., Howard, J. B., and Sarofim, A. F., "Coal Devolatilization at High Temperatures," 16th Symp. (Int'l.) on Combustion, The Combustion Institute, 1976.

Kuipers, J. A. M., Prins, W., and Van, Swaaij, W.P.M., 1992, "Numerical Calculation of Wall-to-Bed Heat-Transfer Coefficients in Gas-Fluidized Beds," AlChE Journal, Vol. 38, No. 7, July 1992, pp 1079-1091.

Lebowitz, J. L., 1964, "Exact Solution of Generalized Percus-Yevick Equation for a Mixture of Hard Spheres," Journal of Experimental and Theoretical Physical Review, Vol. 133, No. 4A, 1964, pp A895-A899.

Lun, C. K. K., Savage, S.B., Jeffrey, D.J., and Chepurniy, N., 1984, "Kinetic Theories for Granular Flow: Inelastic Particles in Couette Flow and Slightly Inelastic Particles in a General Flowfield," Journal of Fluid Mechanics, Vol. 140, 1984, pp 223-256.

Mathiesen, V. S. T., and Hjertager, B. H., 2000, "Predictions of Gas/Particle Flow with an Eulerian Model Including a Realistic Particle Size Distribution," Powder Technology, Vol. 112, 2000, pp 34-45.

Mazumder, A. K. M., Wang, T., and Khan, J. R., "Design and Simulation of a Mild Gasifier, Part 1– Development of a Multiphase Computational Model," ASME paper IMECE 2011-64473, Proceedings of the ASME International Mechanical Engineering Congress & Exposition, Nov. 11-17, 2011, Denver, Colorado.

Mazumder, A. K. M., Wang, T., "Development of a Simulation Model for Fluidized Bed Mild Gasifier." ECCC Report 2010-05. Energy Conversion and Conservation Center. University of New Orleans. November 2010.

Mazumder, A.K.M., Wang, T., and Khan, J. R., "Design and Simulation of a Mild Gasifier, Part 2 – Case Study and Analysis," ASME paper IMECE 2011-64485, Proceedings of the ASME International Mechanical Engineering Congress & Exposition, Nov. 11-17, 2011, Denver, Colorado.

Nakamura, K., and Capes, C. E., 1976, "Vertical Pneumatic Conveying of Binary Particle Mixtures," Fluidization Technology, Editors Keairns, D.L., Hemisphere Publishing Corp., Washington, 1976, pp 159-184.

Nakamura, M., Hamada, Yoichi, Toyama, Shigeki, Fouda, A.K., and Capes, C.E., 1983, "An Experimental Investigation of Minimum Fluidization Velocity at Elevated Temperature and Pressures," Proceedings: 33rd Canadian Chemical Engineering Conference, Vol. 2, 1983, pp 515-520.

N. Kurul, and M. Z. Podowski., "On the modeling of multidimensional effects in boiling channels". In Proceedings of the 27th National Heat Transfer Conference, Minneapolis, Minnesota, USA. 1991.

O'Brien, T.J., and Syamlal, M., 1990, "NIMPF: A Non-isothermal Multi particle Fluidized Bed Hydrodynamic Model," Journal of ASME, Vol. 91, 1982, pp 65-72.

Ocampo, A., Areanas, E., Chejne, F., Espinel, J., Londono, C., Aguirre, J., and Perez, J. D., 2003, "An Experimental Study on Gasification of Colombian Coal in Fluidized Bed," Journal of Fuel, Vol. 82, 2003, pp 161-164.

Pain, C. C., Mansoorzadeh, S., and Oliveira, C. R. E. de., 2001, "A Study of Bubbling and Slugging Fluidized Beds Using the Two-Fluid Granular Temperature Model," International Journal of Multiphase Flow, Vol. 27, 2001, pp 527-551.

Panneerselvam, R., Savithri, S., and Surneder, G. D., 2007, "CFD Based Investigation on Hydrodynamics and Energy Dissipation Due to Solid Motion in Liquid Fluidized Bed," Journal of Chemical Engineering, Vol. 132, 2007, pp 159-171.

Pillai, K. K., 1981, "The Influence of Coal Type on Devolatilization and Combustion in Fluidized Beds," J. Inst. Energy, 1981.

Ranz, W. E., and Marshall, W. R., March 1952, Jr. Evaporation from Drops, Part I. Chemical Engineering Progress, Vol. 48, No. 3, pp 141–146.

Ranz, W. E., and Marshall, W. R., April 1952, Jr. Evaporation from Drops, Part II. Chemical Engineering Progress, Vol. 48, No. 4, pp 173–180.

Patanker, S. V., Numerical Heat Transfer and Fluid Flow, McGraw Hill, 1980.

Reuge, N., Cadoret, L., Saudejaud, Coufort, C., Pannala, S., Syamlal, M., and Caussat, B., 2008, "Multifluid Eulerian Modeling of Dense Gas-Solid Fluidized bed Hydrodynamics: Influence of the Dissipation Parameters," Journal of Chemical Engineering Science, Vol. 63, 2008, pp 5540-5551.

Savage, S. B., and Jeffrey, D. J., 1981, "The Stress in a Granular Flow at High Shear Rates," Journal of Fluid Mechanics, Vol. 110, 1981, pp 255-272.

Saxena, S. C., Vogel, G. S., 1977, "The Measurements of Incipient Fluidization Velocities in a Bed of Coarse Dolomite at Temperature and Pressure," Trans. Inst. Chem. Eng., Vol. 3, pp 184–195.

Schiller, L., and Naumann, Z., 1935, Z. Ver. Deutsch. Ing., Vol. 77, pp 318.

Schmidt, A., Renz, U., 1999, "Eulerian Computation of Heat Transfer in Fluidized Beds," Chemical Engineering Science, Vol. 54, 1999, pp 5515-5522.

Simonin, C., and Viollet, P. L., 1990, "Predictions of an Oxygen Droplet Pulverization in a Compressible Subsonic Co-flowing Hydrogen Flow," Numerical Methods for Multiphase Flows, FED, Vol. 91, pp 65–82.

Syamlal, M., and Gidaspow, D., 1985, "Hydrodynamic of Fluidization: Prediction of Wall to Bed Heat Transfer Coefficients," AIChE Journal , Vol. 31, No. 1, 1985, pp 127-135.

Syamlal, M., and O'Brien, T.J., 1989, "Computer Simulation of Bubbles in a Fluidized Bed," AlChE Symposium series, Vol. 85, No. 270, pp 22-31.

Syamlal, M., Rogers, W., and O'Brien, T. J., 1993, MFIX Documentation: Volume 1, Theory Guide. National Technical Information Service, Springfield, VA, DOE/METC-9411004, NTIS/DE9400087.

Syamlal, M., 1987, "The Particle-Particle Drag Term in a Multi-particle Model of Fluidization," Topical Report, Work Performed under Contract No.: DE-AC21-85MC21353, May 1987.

Silaen, A., and Wang, T., 2004, "Simulation of Coal Gasification inside a Two stage Gasifier," Energy Conversion & Conservation Center Report, November 2004.

Silaen, A., and Wang, T., 2010, "Effect of Turbulence and Devolatilization Models on Coal Gasification Simulation in an Entrained-Flow Gasifier," International Journal of Heat and Mass Transfer, No. 53, 2010, pp. 2074-2091.

Subramanian, Shankar, R., "Flow Through Packed Beds and Fluidized Beds."

Todes, O. M., Citovich, O. B., 1981, "Reactors with Coarse Particle Fluidized Beds (in Russian)," Leningrad, Khimiya.

Turns, Stephen, R., 2000, An Introduction to Combustion, Concepts and Application, 2nd Edition, McGraw-Hill, 2000.

Vuthaluru, Rupa, Tade, Moses, Vuthaluru, Hari, Tsvetnenko, Yuri, Evans, Louis, Milne, Jason, 2009, "Application of CFD Modeling to Investigate Fluidized Limestone Reactors for the Remediation of Acidic Drainage Waters," Journal of Chemical Engineering, Vol. 149, 2009, pp 162-172.

Wachem, B. G. M., van, Schouten, J. C., Bleek, C. M. van, den, Krishna, R., and Sinclair, J. L., 2001, "Comparative Analysis of CFD Models of Dense Gas-Solid Systems," AIChE Journal, Vol. 47, No. 5, 2001, pp 1035-1051.

Wang, Shuyan., Lu, Huilin., Li, Xiang., Yu, Long., Ding, Jianmin., Zhao, Yunhua., 2008, "CFD Simulation of Bubbling Beds of Rough Spheres," Chemical Engineering Science, Vol. 63, 2008, pp 5653-5662.

Wang, X. F., Jin, B. S., Zhong, W. Q., 2009, "Three-Dimensional Simulation of Fluidized Bed Coal Gasification," Chemical Engineering and Processing: Process Intensification, Vol. 48, 2009, pp 695-705.

Yang, W. C., and Keairns, D. L., 1978a, "Design of Re-circulating Fluidized Beds for Commercial Applications," Fluidization, Cambridge University Press, Vol. 74(176), 1978, pp 218-228.

Yang, W. C., and Keairns, D. L., 1978b, "Design and Operating Parameters for a Fluidized Bed Agglomerating Combustor/Gasifier," Fluidization, Cambridge University Press, 1978, pp 208-214.

Yang, W. C., and Keairns, D.L., 1982, "Rate of Particle Separation in a Gas Fluidized Bed," Journal of Industrial Engineering Chemical Fundamentals, Vol. 21, 1982, pp 228-235.

Yang, Wen Ching, 2003, Handbook of Fluidization and Fluid-Particle Systems, Siemens Westinghouse Power Corporation, Pittsburgh, Pennsylvania, USA, Taylor & Francis Group LLC.

Yang, W. C., 1998, "Comparison of Jetting Phenomena in 30-cm and 3-m Diameter Semicircular Fluidized Beds," Powder Technology, Vol. 100, 1998, pp 147-160.

Yang, W. C., and Keairns, D. L., "Momentum Dissipation of and Gas Entrainment into a Gas-Solid Two-Phase Jet in Fluidized Bed," Research and Development Center Report, Westinghouse Electric Corporation, Pittsburg, Pennsylvania 15235.

Yang, W. C., and Keairns, D. L., 2000, "Operational Analysis of Ash-Agglomerating Fluidized Bed Gasifiers," Powder Technology, Vol. 111, 2000, pp 168-174.

Yang, W. C., and Keairns, D. L., 1975, "Tow-Dimensional Recirculating Bed Data with Simulated Heat Transfer Surface in the Downcomers," Industrial Engineering Chemical, Process Des. Dev., Vol. 14, No. 3, 1975, pp 259-264.

Yang, W. C., and Keairns, D. L., 1979, "Estimating the Jet Penetration Depth of Multiple Vertical Grid Jets," Industrial Engineering Chemical Fundamentals, Vol. 18, No. 4, 1979, pp 317-320.

Yang, W. C., and Keairns, D. L., 1983, "Studies on the Solid Circulation Rate and Gas Bypassing in Spouted Fluid-Bed with a Draft Tube," The Canadian Journal of Chemical Engineering, Vol. 61, 1983, pp 349-355.

Yan, H. M., Heidenreich, C., and Zhang, D. K., 1999, "Modeling of Bubbling Fluidized Bed Coal Gasifiers," Fuel, Vol. 78, 1999, pp 1027-1047.

Yu, Liang., Lu, J., Zhang, X. P., Zhang, S. J., 2007, "Numerical Simulation of the Bubbling Fluidized Bed Coal Gasification by the Kinetic Theory of Granular Flow (KTGF)," Fuel, Vol. 86, 2007, pp 722-734.

Zhong, W. Q., Zhang, M. Y., Jin, B. S., Yuan, Z. L., 2007, "Flow Behaviors of a Large Spout-Fluid Bed at High Pressure and Temperature by 3D Simulation with Kinetic Theory of Granular Flow," Power Technology, Vol. 175, 2007, pp 90-103.

APPENDIX A

Calculation of Inlet Gas Mass Fraction at the Draft Tube Inlet

In the draft tube inlet, the air-carbon mixture is fed with a velocity of 1 m/s with the carbon volume fraction of 0.1 as the secondary phase. The density of carbon solid is 2000 kg/m^3. The mass flow rate of carbon = 0.1 x 2000 x 0.0508 x 4 = 40.64 kg/s-m. The total mass flow rate at the draft tube inlet is calculated as below:

$C+ (O_2+3.76N2) = CO_2+3.76N_2$
L.H.S= [12+32+105.28] ==R.H.S= [44+105.28]
Air=32+105.28 =137.28

Mass fraction of oxygen (O_2) in air = 32/137.28=0.2331
Mass fraction of nitrogen (N_2) in air = 105.28/137.28=0.7669

The theoretical amount of air needed for the complete combustion of carbon solid particles is calculated below. For this reaction, the product contains only the carbon dioxide and nitrogen (as inert gas).

$C+ (O_2+3.76N_2) = CO_2+3.76N_2$

Ratio of air and carbon (mass basis) = [air / carbon (C)] = [(32+3.76 x 28)/12] = [137.28/12] = 11.44 kg of air/kg of carbon (based on the theoretical amount of air).

Only 10% of the theoretical amount of air is needed for mild gasification.

10% of the theoretical air = 10% of 137.28 = 13.728
Ratio of 10% of the theoretical air and carbon (mass basis) = [10% of air / carbon (C)] = [(137.28 x 0.1)/12] =1.144 kg of air/kg of carbon (based on 10% of the theoretical amount of air).

Ratio of mass flow rate [air/ carbon (C)] = [air /40.64] ==1.144 kg of air/kg of carbon (based on 10% of the theoretical amount of air).

Mass flow rate of air = 46.4921 kg/s-m

For Indonesian coal (according to Appendix "B"),
Ratio of fixed carbon and volatiles = [Fixed carbon/volatiles] = [47.54/51.29]
Ratio of mass flow rate [carbon (C)/volatiles] = [40.64/volatiles] == [47.54/51.29]

Mass flow rate of volatiles = 43.8457 kg/s-m

Total gas mass flow rate of (volatiles +air) = (43.8457+46.4921) =90.3378 kg/s-m.

Gas mass fraction of volatiles = 43.8457/90.3378 =**0.4854**
Gas mass fraction of oxygen (O_2) = (46.4921 /90.3378) x 0.2332 =**0.1200**
Gas mass fraction of nitrogen (N_2) = (46.4921 /90.3378) x 0.7668 =**0.3946**

Total gas mass fraction =0.4854+0.1200+0.3946 =1.0000

APPENDIX B

Calculations of Molecular Compositions and Enthalpy of Formation of Volatiles

Table 1 Moisture-free (MF) composition of Indonesian coal

Proximate Analysis (MF), wt%		***Ultimate Analysis (MF), wt%***	
Volatile	51.29	C	73.32
Fixed Carbon (FC)	47.54	H	4.56
Ash	1.17	O	20.12
	100.00	N	0.72
		S	0.11
		Ash	1.17
			100.00

Devolatilization Model

After all the moisture contained in the coal particle has evaporated, the particle undergoes devolatilization. The Chemical Percolation Devolatilization (CPD) model is used. The CPD model considers the chemical transformation of the coal structure during devolatilization. It models the coal structure transformation as a transformation of chemical bridge network, which results in release of light gas, char, and tar [Fletcher and Kerstein (1992), Fletcher et. Al (1990), and Grant et. Al (1989)]. In this study, the volatile contained is calculated to be $CH_{2.121}O_{0.5855}$. The detailed calculation process will be shown later. The initial fraction of the bridges in the coal lattice is 1, and the initial fraction of char is 0. The lattice coordination number is 5. The cluster molecular weight is 400, and the side chain molecular weight is 50.

The devolatilization model used in this study adopts a two-step process:

(i) Release of a volatile gas modeled using the CPD.

(ii) Thermally cracking the volatile gas into lighter gases CO, H_2 via an intermediate gas, C_6H_6.

Volatile's Chemical Composition

To model part (i), the chemical formula of volatile matters has to be known. However, coal composition given in Table 1 does not provide the volatiles' chemical composition. Thus, the chemical composition needs to be found out indirectly. Based on the proximate and ultimate analyses listed in Table 1, the elemental composition of the volatiles is determined below.

$$\text{wt\%}_{\text{C, volatiles}} = \frac{\text{wt\%}_{\text{C}}}{\text{wt\%}_{\text{volatiles}}} = \frac{\text{wt\%}_{\text{C, ultimate}} - \text{wt\%}_{\text{FC, proximate}}}{\text{wt\%}_{\text{volatiles}}} = \frac{73.32\% - 47.54\%}{51.29\%} = 50.26\%$$

$$\text{wt\%}_{\text{H, volatiles}} = \frac{\text{wt\%}_{\text{H}}}{\text{wt\%}_{\text{volatiles}}} = \frac{4.56\%}{51.29\%} = 8.89\%$$

$$\text{wt\%}_{\text{O, volatiles}} = \frac{\text{wt\%}_{\text{O}}}{\text{wt\%}_{\text{volatiles}}} = \frac{20.12\%}{51.29\%} = 39.23\%$$

$$\text{wt\%}_{\text{N, volatiles}} = \frac{\text{wt\%}_{\text{N}}}{\text{wt\%}_{\text{volatiles}}} = \frac{0.72\%}{51.29\%} = 1.40\%$$

$$\text{wt\%}_{\text{S, volatiles}} = \frac{\text{wt\%}_{\text{S}}}{\text{wt\%}_{\text{volatiles}}} = \frac{0.11\%}{51.29\%} = 0.22\%$$

The chemical formula of the volatiles is assumed to be in the form of $C_xH_yO_z$. The other elements, N and S, will be injected as gas, together with the oxidant through the inlet injections.

Weight percentages of C, H, and O in the volatiles after N and S have been removed are,

$$\text{wt\%}_{\text{C in } C_xH_yO_z} = \frac{\text{wt\%}_{\text{C, volatiles}}}{\text{wt\%}_{\text{volatiles}} - \text{wt\%}_{\text{N, volatiles}} - \text{wt\%}_{\text{S,volatiles}}} = \frac{50.26\%}{100\% - 1.40\% - 0.22\%} = 51.09\%$$

$$\text{wt\%}_{\text{H in } C_xH_yO_z} = \frac{\text{wt\%}_{\text{H, volatiles}}}{\text{wt\%}_{\text{volatiles}} - \text{wt\%}_{\text{N, volatiles}} - \text{wt\%}_{\text{S,volatiles}}} = \frac{8.89\%}{100\% - 1.40\% - 0.22\%} = 9.03\%$$

$$\text{wt\%}_{\text{O in } C_xH_yO_z} = \frac{\text{wt\%}_{\text{O, volatiles}}}{\text{wt\%}_{\text{volatiles}} - \text{wt\%}_{\text{N, volatiles}} - \text{wt\%}_{\text{S,volatiles}}} = \frac{39.23\%}{100\% - 1.40\% - 0.22\%} = 39.88\%$$

For part (ii), the volatile matters, $C_xH_yO_z$, are assumed to be thermally cracked into CO, H_2 and C_6H_6 according to the equation below,

$$C_xH_yO_z \rightarrow a\ CO + b\ H_2 + c\ C_6H_6$$

The coefficients a, b, and c are calculated by performing mass balance of each element in the equation above.

Mass of each element in terms of the reaction coefficients are,

C: $m_C = (a + 6c) \times 12 = 12a + 72c$

H: $m_H = (2b + 6c) \times 1 = 2b + 6c$

O: $m_O = a \times 16 = 16a$

Assuming 1 kg of volatiles, the actual mass of each element is calculated and is substituted into the equations above to determine the reaction coefficients.

$m_O = wt\%_{O \text{ in } CxHyOz} \times 1 \text{ kg} = 0.3988 \text{ kg}$

$\Rightarrow 16a = 0.3988 \Rightarrow a = 0.02493$

$m_C = wt\%_{C \text{ in } CxHyOz} \times 1 \text{ kg} = 0.5109 \text{ kg}$

$$\Rightarrow 12a + 72c = 0.5109 \Rightarrow c = \frac{0.5109 - 12(0.02493)}{72} = 0.002941$$

$m_H = wt\%_{H \text{ in } CxHyOz} \times 1 \text{ kg} = 0.0903 \text{ kg}$

$$\Rightarrow 2b + 6c = 0.0903 \Rightarrow b = \frac{0.0903 - 6(0.002941)}{2} = 0.03633$$

With the coefficients a, b, and c being known, the thermal-cracking equation is rewritten as,

$$C_xH_yO_z \rightarrow 0.02493CO + 0.03633H_2 + 0.002941C_6H_6$$

Mass balance of each element is done to determine the values of x, y, and z.

$\Rightarrow x = 0.02493 + 6(0.002941) = 0.04258$

$\Rightarrow y = 2(0.03633) + 6(0.002941) = 0.09031$

$\Rightarrow z = 0.02493$

So, the volatiles' thermal-cracking equation becomes,

$$C_{0.04258}H_{0.09031}O_{0.02493} \rightarrow 0.02493\ CO + 0.03633\ H_2 + 0.002941\ C_6H_6$$

Normalize the coefficients to have the volatile in CH_mO_n form yields,

$$CH_{2.121}O_{0.5855} \rightarrow 0.5855\ CO + 0.8532\ H_2 + 0.06907\ C_6H_6$$

Enthalpy of Volatiles

The enthalpy of the volatiles is not known and thus needs to be calculated. A correct enthalpy value of the volatiles will ensure that energy is properly balanced in the volatiles thermal-cracking reaction.

The steps taken to find the enthalpy of the volatile, $CH_{2.121}O_{0.5855}$, are as follows.

(a) Calculate the volatiles' heating value

The volatiles' heating value is found by subtracting carbon's heating value from the coal's heating value as

$$HV_{CH2.121O0.5855} = HV_{coal} - HV_C$$

where,

HV_{coal} = 5,690 kcal/kg of coal ≈ 23.8 MJ/kg of coal

$$HV_C = 393{,}546 \frac{\text{kJ}}{\text{kmole of C}} \times \frac{1\ \text{MJ}}{1000\ \text{kJ}} \times 0.0396 \frac{\text{kmole of C}}{\text{kg of coal}} = 15.584\ \frac{\text{MJ}}{\text{kg of coal}}$$

Thus, the heating value of the volatiles is,

$HV_{CH2.121O0.5855}$ = (23.8 – 15.584) MJ/kg of coal = 8.216 MJ/kg of coal

Converting the volatiles' heating value in terms of mole number is,

$$HV_{CH2.121O0.5855} = 8.216 \frac{\text{kJ}}{\text{k g coal}} \times \frac{1\ \text{kg coal}}{0.0218357 \text{kmole volatiles}} = 376.264 \frac{\text{kJ}}{\text{k mole}}$$

(b) Calculate volatiles' enthalpy based on the volatile combustion reaction.

The chemical equation for the volatiles combustion is

$$CH_{2.121}O_{0.5855} + 1.2378O_2 \rightarrow CO_2 + 1.061H_2O\ (g)$$

The equation of the volatiles' heating value (at 25°C) is expressed as,

$$HV_{CH_{2.121}O_{0.585}} = \left[\left(1 \times h_{f,CH_{2.121}O_{0.585}}\right) + \left(1.2378 \times h_{f,O_2}\right)\right] - \left[\left(1 \times h_{f,CO_2}\right) + \left(1.061 \times h_{f,H_2O(g)}\right)\right]$$

Where,

$h_{f,CO2}$ = -393,546 kJ/kmole

$h_{f,H2O(g)}$ = -241,845 kJ/kmole

$h_{f,O2}$ = 0.

The equation is rearranged to give,

$$h_{f,\,CH_{2.12f}O_{0.585}} = HV_{CH_{2.12f}O_{0.585}} - \left(1.2378 \times h_{f,\,O_2}\right) + \left[\left(1 \times h_{f,\,CO_2}\right) + \left(1.061 \times h_{f,\,H_2O(g)}\right)\right]$$

Substituting the enthalpy values into the equation above gives,

$h_{f,CH_{2.121}O_{0.585}}$ = 376,264 – (1.2378 x 0) + [1 x (-393,546) + 1.061 x (-241,845)]

$h_{f,CH_{2.121}O_{0.585}}$ = 376,264 - 393,546 -256,597.54

$h_{f,CH2.121O0.585}$ = -273,879. 54 kJ/kmole

The value of -273,879.54 kJ/kmole is used as the enthalpy of the volatile ($CH_{2.121}O_{0.5855}$) at 25°C.

The molecular weight of the volatile ($CH_{2.121}O_{0.5855}$) = 12+1 x 2.121+16 x 0.5855

= 12+2.121+9.368

= 23.489

VITA

You Lu was born in Guizhou Province, China in 1986. He received his Bachelor of Science in Mechanical Engineering in 2009 from Central South University in Changsha, China. He then continued to pursue a Master of Science in Mechanical Engineering degree from the University of New Orleans. During his post-graduate program, he worked as a Research Assistant at the Energy Conversion and Conservation Center (ECCC) at the University of New Orleans under the supervision of Dr. Ting Wang. He received his Master of Science in Mechanical Engineering from the University of New Orleans in 2012.